Advancing the Use of Three-Dimensional Spheroids for Quantitative, Live-Cell, Fluorescence Microscopy in a High-Throughput Format

by

Elizabeth A. Leary

Sc.B., Brown University, Providence, RI, 2009

Submitted in partial fulfillment of the requirements for the degree of Doctor of Philosophy in Biomedical Engineering, a joint program in the Division of Biology and Medicine and School of Engineering at Brown University

Department of Molecular Pharmacology, Physiology, and Biotechnology

and

Center for Biomedical Engineering

PROVIDENCE, RHODE ISLAND

MAY 2018

This dissertation by Elizabeth A. Leary is accepted in its present form by the Biomedical Engineering program, a joint program in the Division of Biology and Medicine and the Division of Engineering as satisfying the dissertation requirements for the degree of Doctor of Philosophy

Date Jeffrey R. Morgan, Ph.D., Advisor

Recommended to the Graduate Council

Date Kim Boekelheide, M.D., Ph.D., Reader

Date Kareen Coulombe, Ph.D., Reader

Date Robbert Creton, Ph.D., Reader

Date Ulrike Mende, M.D., Reader

Date Randall Ruch, Ph.D., External Reader

Approved by the Graduate Council

Date Andrew Campbell, Dean of the Graduate School

CURRICULUM VITAE

NAME

Elizabeth Astrid Leary

EDUCATION

Brown University, Providence, RI
Ph.D., Biomedical Engineering, April 2018
Thesis Advisor: Jeffrey R. Morgan, Ph.D.
Thesis Title: Advancing the use of 3D Spheroids for Quantitative, Live-Cell, Fluorescence Microscopy in a High-Throughput Format

Brown University, Providence, RI
Sc.B., Biomedical Engineering, May 2009

PUBLICATIONS

Leary E, Rhee C, Wilks BT, Morgan JR. 2018. Quantitative Live-Cell Confocal Imaging of 3D Spheroids in a High-Throughput Format. SLAS Technology. PMID: 29412762.

Leary E, Rhee C, Wilks BT, Morgan JR. 2016. Accurate quantitative wide-field fluorescence microscopy of 3-D spheroids. Biotechniques 61(5):237-247. PMID: 27839509.

Leary E, Curran S, Susienka M, Manning KL, Blakely AM, Morgan JR. Micro-moulded non-adhesive agarose hydrogels to form multicellular microtissues – The 3D Petri Dish®. In Technology Platforms for 3D Cell Culture, S. Przyborski (Ed). 2017.

Kabadi PK, Vantangoli MM, Rodd AL, **Leary E**, Madnick SJ, Morgan JR, Kane A, Boekelheide K. 2015. Into the Depths: Techniques for in vitro three-dimensional microtissue visualization. Biotechniques 59(5):279-286. PMID: 26554505.

Curran S, Achilli TM, **Leary E**, Wilks BT, Vantangoli MM, Boekelheide K, Morgan JR. 2015. A 3D spheroid system to evaluate inhibitors of the ABCG2 transporter in drug uptake and penetration. TECHNOLOGY 1-10.

Hall SR, Jiang Y, **Leary E**, Yavanian G, Eminli S, O'Neill DW, Marasco WA. 2013. Identification and isolation of small CD44-negative mesenchymal stem/progenitor cells from human bone marrow using elutriation and polychromatic flow cytometry. Stem Cells Translation Medicine 2(8):567-578. PMID: 23847000

Havens AM, Shiozawa Y, Jung Y, Sun H, Wang J, McGee S, Mishra A, Taichman LS, Danciu T, Jiang Y, Yavanian G, **Leary E**, Krebsbach PH, Rodgerson D, Taichman RS. 2013. Human very small embryonic-like cells generate skeletal structures, in vivo. Stem Cells and Development 22(4):622-630. PMID: 23020187.

CONFERENCE ABSTRACTS and INVITED TALKS

Shah MK, **Leary E**, Morgan JR, Darling EM. 2018. Incorporation of Microparticles into a 3D Tumor Model of Melanoma. *Cellular and Molecular Bioengineering Conference.* Key Largo, FL.

Leary E, Morgan JR**.** 2017. Advancing the use of spheroids for live-cell, quantitative high content screening using confocal microscopy. High-Content Analysis and 3D Screening Summit. Cambridge, MA.

Leary E, Rhee C, Wilks B, Morgan JR. 2017. Advancing the use of 3D spheroids for quantitative, live-cell, confocal microscopy in a high-throughput format. *World Preclinical Congress.* Cambridge, MA.

Leary E, Rhee C, Wilks B, Morgan JR. 2017. Advancing the use of 3D spheroids for quantitative live-cell, high-throughput screening. *Cellular and Molecular Bioengineering Conference.* Hawai'i, HI.

Leary E, Morgan JR. 2014. Quantifying biological functions using fluorescent dyes in 3D spheroids. *Biomedical Engineering Society.*

RESEARCH EXPERIENCE

Brown University, Providence, RI
Graduate Research Assistant, September 2012 – present

NeoStem, Inc, Cambridge, MA
Research Assistant II, July 2009 – August 2012

Boston Biomedical Research Institute, Watertown, MA
Summer Intern, June 2008 – August 2008

TEACHING EXPERIENCE

Biomedical Engineering and Biotechnology Seminar (BIOL2230), Fall 2016, 2017
Guest Lecturer
Guest Lecture Title: "The Science of Giving a Great Presentation"

Techniques in Pathobiology, Spring 2016, 2017
Guest Lecturer
Guest Lecture Title: "Advancing the use of spheroids for high-throughput confocal microscopy"

Engineering Biomedical Systems, "Summer at Brown", June 2015
Teaching Assistant

Howard Hughes Medical Institute Summer Scholars Research Program, Summer 2013, 2014
Teaching Assistant

Techniques in Molecular and Cell Sciences (BIOL 2130), Fall 2013
Teaching Assistant

FELLOWSHIPS and AWARDS

Department of Education, pre-doctoral GAANN fellow, August 2016 – present

World Preclinical Congress Student Fellowship, June 2017

ACKNOWLEDGEMENTS

First and foremost, I would like to thank my advisor, Dr. Jeff Morgan, for your continued support, encouragement, and insightful feedback and conversations. I greatly appreciate your mentorship style, you have created a lab culture that enables myself and others to thrive. Through working with you over these past six years, you have “mold”-ed me into a better scientist, a better writer, and a better presenter.

I would also like to thank all of my committee members, Kim Boekelheide, Kareen Coulombe, Robbert Creton, and Ulrike Mende. Thank-you for your continued feedback and guidance throughout the years. Your thoughtful and thought-provoking questions have really challenged me to look critically into my scientific research. I would also like to thank my external reader, Dr. Randall Ruch – thank-you very much for joining my thesis committee, I am looking forward to the feedback and questions that your expertise will bring to the table!

Thank-you to all members of the staff, Jess, Kris, Krystal, Melody,Elly-thank-you for all of your help and support throughout the years. You all keep this department running like a well-oiled machine.

To all my fellow Morgan Lab members, both past and present, you guys are amazing! Toni-Marie, Jackie, and Sean, thank-you immensely for training me when I first started, you were always so helpful in answering my questions and showing me techniques. To my pal, Andrew Blakely, thank-you for always putting up with my shenanigans and for ALWAYS getting coffee(s) with me every day. Ben – your sense of humor, and wittiness keeps me laughing even while analyzing data; the data that I could NOT analyze without all of your coding help, so thank-you for always helping me solve computer-related problems!! To Andrew, Maryanne, Gianna, Blanche, Caitlin – thank-you for helping to make the Morgan lab a fun place to work.

Manisha, Jess, Kali, Hetal, Molly, Olivia, Sam, and Mike, (in no particular order), you all have made my second time here at Brown AMAZING. From our time spent at The Table, or the GCB, to getting lunches on Thayer, to girls trips (sorry mike…) and everything in between, you all have been a tremendous support system, and I will(/already) miss you guys soo much.

And to Ve, I am so lucky to have you as my best friend. You are an amazing person, friend, colleague, researcher, the list could go on and on, but alas I must send my thesis document into my committee members. I am so fortunate that we started here at Brown together! I know that neither one of us does emotions that well, so I was tempted to write my ode to you in wingdings, but instead I'll just keep it short and sweet. Thank-you for being an amazing friend, my time at Brown would NOT have been the same without you. I am so glad that I got to spend my last year here living with you. #BethridaForever.

Bethany – thank-you so much for being so incredibly caring, supportive, and helpful over these past few months! All the little things you do to take care of me (& monkey) really add up, you are amazing, and I am very fortunate to have you in my life!

And last, but CERTAINLY NOT least, I would like to thank my family for all of their support over the last 30-years. Mom and Dad – you two have always been and will continue to be my biggest supporters, I would not be the person I am today without your love and support. Danny – thank-you for being the best little brother I could ask for, you've always had my back and looked out for me, even as kids. To all my grandparents (both living and deceased), your unconditional love, support, and encouragement has taught me to strive to be the best version of myself. & Mom, I need to give you an extra special shout-out – you started my love for science at a very young age by making those school science projects so much fun!

Also, I would be remiss, if I did not also thank my little furball, Monkey. Thank-you for sitting right by my side throughout this whole process, (even though some days I had to bribe you with chicken to get you to sit still), you really are a great stress relief, and a very loyal pup!

TABLE of CONTENTS

CURRICULUM VITAE iv

ACKNOWLEDGEMENTS vii

TABLE of CONTENTS x

LIST of FIGURES xiv

LIST of TABLES xvii

1 Introduction 1

1.1 RELEVANCE FOR DEVELOPMENT OF SPHEROIDS AS A MODEL 2

1.2 TYPES of CELL SOURCES UTILIZED *IN VITRO* 13

1.2.1 Primary Cells 14

1.2.2 iPSC/ESC Derived 15

1.2.3 Cell Lines 17

1.3 INSTRUMENTATION NECESSARY to ACQUIRE 3D DATA 20

1.3.1 Brightfield Microscopy 20

1.3.2 Widefield Epi-Fluorescence Microscopy 21

1.3.3 Confocal Microscopy 23

1.3.4 Multi-photon Microscopy 26

1.3.5 Light Sheet Fluorescence Microscopy 26

1.4 FLUORESCENT PROBES ENABLE the MONITORING of BIOLOOGICAL PROCESSES THROUGHOUT SPHEROIDS 28

1.4.1 Measuring cellular responses to microenvironment 30

1.4.2 Modeling Movement throughout 3D spheroids 31

1.4.3 Limitations associated with the use of fluorescent probes 33

1.5 ADVANCEMENTS NECESSARY for 3D IMAGE QUANTITATION 34

1.6 SPECIFIC AIMS of this DISSERTATION 39

1.6.1 Aim 1. Develop accurate quantitative methods to analyze wide-field fluorescent images of 3D spheroids. 39

1.6.2 Aim 2. Develop quantitative analysis strategies to analyze confocal z-stacks of living 3D spheroids in a high-throughput format. 41

1.6.3 Aim 3. Develop a high-throughput quantitative assay to assess gap junction inhibition in 3D spheroids. 42

1.7 REFERENCES 45

2 Accurate Quantitative Wide Field Fluorescent Microscopy of 3D Spheroids. 64

2.1 ABSTRACT 65

2.2 INTRODUCTION 66

2.3 MATERIALS and METHODS 68

2.3.1 Micro-molded hydrogels, cell culture and spheroid formation 68

2.3.2 Labeling with fluorescent dyes, microscopy and image analysis 69

2.3.3 Calculation of prediction curves for relating volume/surface area, radii, and fluorescence. 71

2.3.4 Statistical Analysis 72

2.4 RESULTS and DISCUSSION 73

2.5 AUTHOR CONTRIBUTIONS 83

2.6 ACKNOWLEDGEMENTS 83

2.7 CONFLICT OF INTEREST 83

2.8 REFERENCES 84

2.9 SUPPLEMENTAL MATERIALS and METHODS 88

2.10 SUPPLEMENTAL FIGURES 89

3 Quantitative Live-Cell Confocal Imaging of 3D Spheroids in a High Throughput Format 97

3.1 ABSTRACT 98

3.2 INTRODUCTION 99

3.3 MATERIALS and METHODS 101

3.3.1 Micro-mold fabrication and hydrogel formation. 101

3.3.2 Cell culture, fluorescent dye labeling, and spheroid formation. 102

3.3.3 Microscopy and image analysis measurements. 103

3.3.4 Data analysis and derivation of ideal curves 104

3.4 RESULTS 107

3.4.1 Tri-axis positional control of spheroid formation in a 96-well plate for confocal imaging. 107

3.4.2 Cumulative fluorescent loss increases as function of spheroid radii. 110

3.4.3 Within spheroids, loss of the fluorescent signal is dependent upon the positional (x, y, z) location. 114

3.4.4 Ratio imaging corrects for loss of fluorescence throughout the *z*-depth. . 117

3.5 DISCUSSION ... 120

3.6 AUTHOR CONTRIBUTIONS ... 126

3.7 ACKNOWLEDGEMENTS ... 126

3.8 CONFLICT of INTEREST ... 127

3.9 REFERENCES ... 128

3.10 SUPPLEMENTAL FIGURES ... 133

4 Gap junction intercellular communication in 3D spheroids: Quantifying radial fluorescence ... 141

4.1 ABSTRACT ... 142

4.2 INTRODUCTION ... 143

4.3 MATERIALS and METHODS ... 145

4.3.1 Micro-mold fabrication and hydrogel formation. ... 145

4.3.2 Cell culture, spheroid formation, fluorescent dye labeling, and drug treatment. ... 146

4.3.3 Microscopy and image analysis measurements. ... 147

4.3.4 Data Analysis. ... 148

4.3.5 Statistical Analysis. ... 150

4.4 RESULTS ... 151

4.4.1 Spheroid fluorescence is dependent on the method of dye incorporation and location in the spheroid ... 151

4.4.2 CalceinRO outperforms calceinAM as an indicator of GJIC. ... 155

4.4.3 Spheroid size and calceinRO incubation time need to be optimized. ... 159

4.4.4 All tested methods of data analysis yielded statistical differences between +/- controls, but that does not imply ample separation with respect to Z-factor analysis. 167

4.5 DISCUSSION ... 171

4.6 AUTHOR CONTRIBUTIONS ... 177

4.7 ACKNOWLEDGEMENTS ... 178

4.8 CONFLICT of INTEREST ... 178

4.9 REFERENCES ... 179

4.10 SUPPLEMENTAL FIGURES ... 187

5 Conclusions, Discussion, & Future Directions 191

5.1 OVERVIEW 192

5.2 SUMMARY of MAJOR FINDINGS 196

5.2.1 Aim 1. Develop accurate quantitative methods to analyze wide-field fluorescent images of 3D spheroids 197

5.2.2 Aim 2. Develop quantitative analysis strategies to analyze confocal z-stacks of living 3D spheroids in a high-throughput format. 198

5.2.3 Aim 3. Develop a high-throughput quantitative assay to assess gap junction inhibition in 3D spheroids. 200

5.3 LIMITATIONS and POTENTIAL SOLUTIONS 202

5.3.1 Aim 1. Develop accurate quantitative methods to analyze wide-field fluorescent images of 3D spheroids 207

5.3.2 Aim 2. Develop quantitative analysis strategies to analyze confocal z-stacks of living 3D spheroids in a high-throughput format. 208

5.3.3 Aim 3. Develop a high-throughput quantitative assay to assess gap junction inhibition in 3D spheroids. 210

5.4 FUTURE DIRECTIONS 213

5.5 CONCLUDING REMARKS 216

5.6 REFERENCES 219

LIST of FIGURES

CHAPTER 1: Introduction

Figure 1-1. Spheroids can be formed from a variety of techniques…………..…………..4

Figure 1-2. Non adhesive hydrogels are created from micromolds………………………7

Figure 1-3. Non-adhesive hydrogels guide the process of microtissue self-assembly…...8

Figure 1-4. Time-lapse of variable sized spheroids self-assembling……………………10

Figure 1-5. 3D spheroids have potential recapitulate in vivo morphology.......................12

Figure 1-6. Embedding and histopathology of spheroids can be performed directly within agarose hydrogels……………………………………………………………………...22

Figure 1-7. Deconvolution improves visualization of epi-fluorescence z-stacks………..24

Figure 1-8. Tissue clearing enhances visualization throughout the z-depth of spheroids ……………………………………………………………………………………27

Figure 1-9. Light sheet fluorescence microscopy (LSFM) enhances visualization throughout the z-depth of spheroids when compared to confocal microscopy……….…29

Figure 1-10. Only utilizing fluorescent thresholding to identify surface of spheroid leads to inaccuracies…………………………………………………………………………37

Figure 1-11. Maximal projection images hide changes occurring throughout the 3D radius…………………………………………………………………………………..38

CHAPTER 2: Accurate Quantitative Wide Field Fluorescent Microscopy of 3D Spheroids.

Figure 2-1. Total Fluorescence intensifies with increasing spheroid radii regardless of whether calcein-AM was labeled in 2D or 3D……………………………………..….…74

Figure 2-2. Fluorescence normalization of calcein-AM is dependent upon the method of labeling. ……………………………………………………………………..................77

Figure 2-3. Increasing the concentration of calcein-AM diffused into spheroids improves the fit to surface area……………………………………………………………………..79

Figure 2-4. Surface area normalization enhances the ability to detect differences between different doses of calcein-AM diffusing into spheroids…………………………………81

Supplemental Figure 2-1. Spheroid height can be estimated from measuring spheroid length/width…………………………………………………………………………...89

Supplemental Figure 2-2. Volume- and surface area-based prediction lines are determined from fluorescent data…………………………………………………..90

Supplemental Figure 2-3. Time-course of calcein fluorescence in 3D spheroids………91

Supplemental Figure 2-4. Fluorescence of pre-labeled spheroids correlates with spheroid volume……………………………………………………………………………92

Supplemental Figure 2-5. Fluorescence of spheroids labeled by dye diffusion correlates with spheroid surface area………………………………………………………93

Supplemental Figure 2-6. Fluorescence of pre-labeled MCF-7 spheroids correlates with volume, while fluorescence of MCF-7 spheroids labeled by dye diffusion correlates with surface area…………………………………………………………………….....94

Supplemental Figure 2-7. Fluorescence of pre-labeled NHF spheroids correlates with volume, while fluorescence of NHF spheroids labeled by dye diffusion correlates with surface area……………………………………………………………………………95

Supplemental Figure 2-8. Increasing the concentration of calcein-RO diffused into spheroids improves the fit to surface area……………………………………………..96

CHAPTER 3: Quantitative Live-Cell Confocal Imaging of 3D Spheroids in a High Throughput Format.

Figure 3-1. Molding system to form micro-wells for four spheroids per well in a 96-well plate. ……………………………………………………………………………108

Figure 3-2. Spheroids of consistent size are formed within specific *x, y, z*-locations.…………………………………………………………………………..109

Figure 3-3. Loss of fluorescent signal occurs deeper within the z-depth for spheroids……………………………………………………………………………..111

Figure 3-4. Cumulative loss of total spheroid fluorescence increases as a function of spheroid radii…………...……………………………………………………………113

Figure 3-5. Fluorescent signal loss throughout the z-depth of spheroids exhibits a reproducible, exponential decay function…………………………………………..…..116

Figure 3-6. Cumulative loss of total spheroid fluorescence increases as a function of spheroid size…………………………………………………………………….....118

Figure 3-7. Ratio imaging reduces variation throughout the z-depth…………………..119

Supplemental Figure 3-1. Hypothetical maximal fluorescence derived from the cross-sectional area of confocal slices was used to determine the percent fluorescent loss for each spheroid………………………………………………………………….……..133

Supplemental Figure 3-2. Loss of fluorescent signal occurs deeper within the z-depth for spheroids labeled with CTV……………………………………………………….135

Supplemental Figure 3-3. Loss of fluorescent signal occurs deeper within the z-depth for spheroids labeled with CTR……………………………………………………….136

Supplemental Figure 3-4. Loss of fluorescent signal occurs deeper within the z-depth for spheroids labeled with CTDR……………………………………………………..137

Supplemental Figure 3-5. The loss of fluorescent signal within spheroids is dependent upon three axis positional (*x, y, z*) location……………………………………..…138

Supplemental Figure 3-6. Signal loss throughout the *z*-depth of spheroids exhibits a reproducible, exponential decay function for all dyes……………………………….140

CHAPTER 4: Gap Junction intercellular communication in 3D spheroids: Quantifying radial fluorescence.

Figure 4-1. Quantitation of GJIC is complicated by limitations of confocal imaging…152

Figure 4-2. Labeling cells with fluorescent dyes prior to spheroid formation yields uniform fluorescence throughout the spheroid…………………………………...….153

Figure 4-3. Calcein labeling of spheroids creates a gradient of fluorescence decreasing inwards from the spheroid surface……………………………………………….…154

Figure 4-4. CalceinRO is more effective than calceinAM as a reporter of GJIC………157

Figure 4-5. Spheroid size is integral in quantifying differences in fluorescent signal…162

Figure 4-6. The distinction between +/- CBX increases with time…………………….164

Figure 4-7. CBX inhibits calcein diffusion into the spheroid…………………………..168

Supplemental Figure 4-1. Individual confocal images were analyzed to measure fluorescence distribution across 2D radius……………………………………………..187

Supplemental Figure 4-2. Spheroids were rendered as hemispheres to measure fluorescence distribution across 3D radius……………………………………………..188

Supplemental Figure 4-3. CBX increases total fluorescence of calceinAM but not calceinRO labeled spheroids…………………………………………………………189

LIST of TABLES

CHAPTER 4: Gap Junction intercellular communication in 3D spheroids: Quantifying radial fluorescence.

Table 4-1. Statistically significant inhibition of GJIC does not imply good Z-factor scores.…………………………………………………………………...…………160

Table 4-2. The difference between positive and negative controls increases over time ………………………………………………………………………………………..166

Table 4-3. Statistically significant inhibition of GJIC does not imply good Z-factor scores…………………………………………………………………………………170

CHAPTER 1

Introduction

1.1 RELEVANCE FOR DEVELOPMENT OF SPHEROIDS AS A MODEL

Re-capitulating biological functions in an *in vitro* setting is a main objective in every biomedical field, ranging from developmental biology, cancer research, drug screening, toxicity testing, regenerative medicine, and tissue engineering [1-4]. *In vitro* models are used to model both healthy and diseased systems, as well as to evaluate the effects induced by drugs, compounds, substances, and toxicants [1-4]. *In vitro* models should recapitulate certain functionalities of the organ/tissue, possess similar responses to compound exposure, and ideally be predictive of *in vivo* environment [1-5]. In addition to satisfying biological parameters, *in vitro* models should also be straightforward to set-up, inexpensive, and adaptable to high throughput screening. Traditionally, *in vitro* models are composed of two-dimensional (2D) cell monolayers grown on plastic. 2D cell cultures are easy to use, easily adapted for high-throughput screening, relatively inexpensive, and easy to probe/access information from. However, despite their ease of use, 2D monolayers lack physiological relevance, as they possess low cell densities, no formation of gradients, abnormal cell morphology, and dominance of cell-plastic interactions over cell-cell interactions [1,6]. Furthermore, when cells are cultured in 2D, they start to lose their organ-specific phenotype [6,7]. For example, when liver cells are cultured on plastic, there is decreased production of liver-specific proteins and enzymes, such as albumin, CYP1A1, and CYP1A2 [8,9]. Kidney epithelial cells begin to dedifferentiate when cultured on plastic, and appear to become for fibroblast-like [10]. As the traditional 2D *in vitro* models fail to recapitulate the *in vivo* environment, a need arises for the development of better, more predictive models.

In response to this need for better *in vitro* models, three-dimensional (3D) cell culture models have been growing in number and importance. Many of these 3D approaches combine cells with a scaffold, either natural or synthetic, to achieve 3D architecture [1,7,11]. For these scaffold-based approaches, the scaffold comprises a large proportion of the mass of these structures, and interaction of cells with the scaffold is a critical component. In many cases, cell-scaffold interactions are more prevalent than cell-cell interactions. However, for most tissues *in vivo*, the opposite phenomenon occurs, with the extracellular matrix (ECM) comprises a relatively small proportion of the mass of the tissue, and cell-cell interactions predominating over cell-ECM interactions [7,11].

To overcome low cell densities plaguing scaffold-based 3D *in vitro* models, scaffold-free 3D spheroids can be utilized. In the absence of a scaffold for attachment, mono-dispersed cells will spontaneously aggregate to form a spheroid [12]. 3D spheroids can be formed from a multitude of methods, such as hanging drop, liquid overlay, spinner cultures, microfluidics, and micromolded nonadhesive hydrogels (**Figure 1-1, 1-2**) [12-14]. With the hanging drop method, droplets of monodispersed cells are pipetted onto a substrate and inverted, gravity induces cells to aggregate at the bottom of droplet, and subsequently self-assemble to form a single spheroid per drop **(Figure 1-1A) [**12,13]. With the liquid overlay technique, a tissue-culture plates are first coated with a nonadhesive hydrogel material, such as agarose, then monodispersed cells are added on top, and the application of gentle shaking encourages cells to aggregate together **(Figure 1-1C, D)** [12, 13]. With spinner cultures, monodispersed cells are added to a spinner flask and subject to constant agitation to prevent cell settling and encourage cells to aggregate via cell-cell collisions

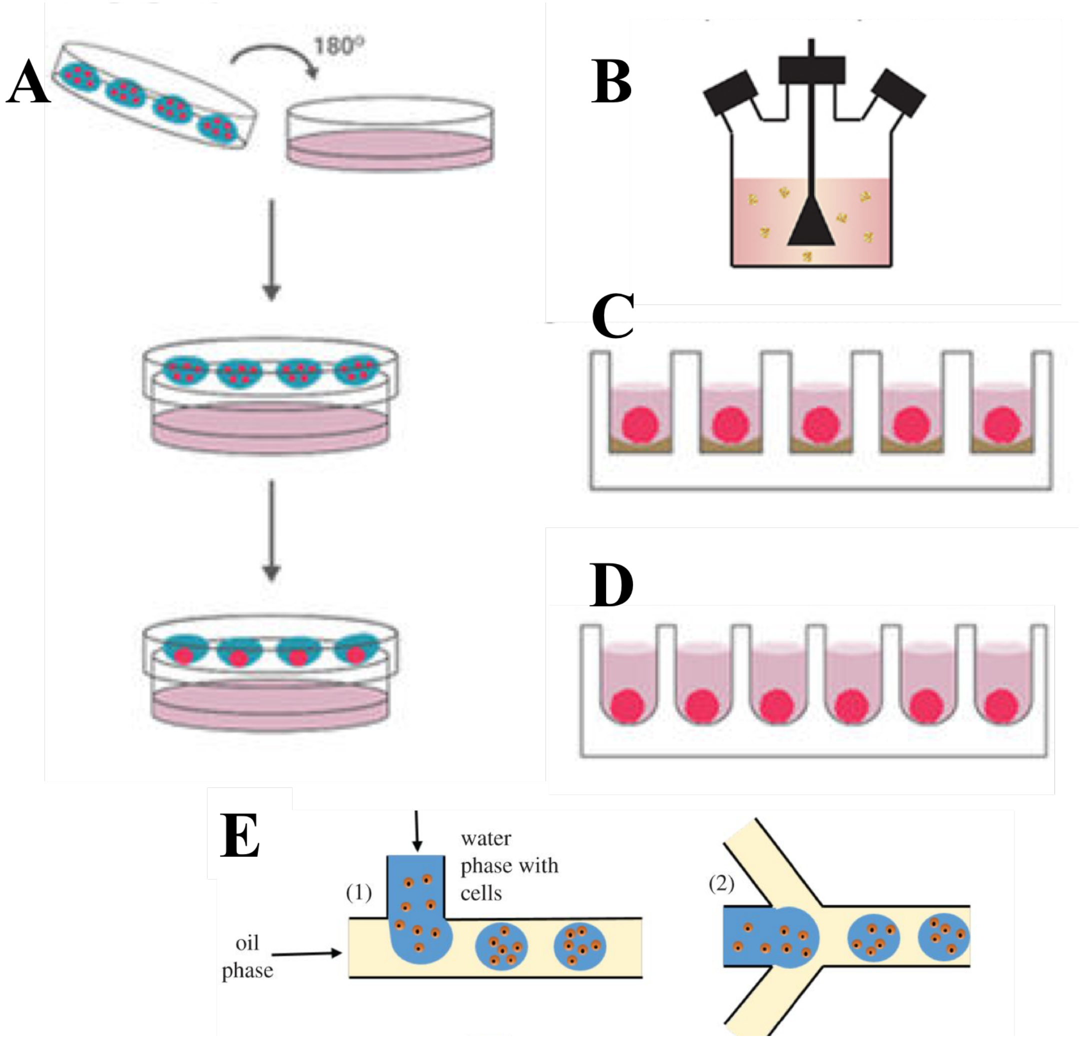

Figure 1-1. Spheroids can be formed from a variety of techniques.

Figure 1-1. Spheroids can be formed from a variety of techniques. Overall, the process of spheroid formation involves some type of force to aggregate cells together, and then in the absence of any other substrate to attach to, cells will attach to each other and self-assemble into spheroids. Each technique of spheroid formation utilizes a specific combination of force and nonadhesive substrate. For example, to form spheroids via the hanging drop technique, monodispersed cells are pipetted as droplets onto a substrate, and subsequently inverted, gravity forces cells to be in close contact at the bottom of droplet, and in absence of material to attach to, cells attach to one another to form spheroids (A – [modified from 13]). With spinner cultures, monodispersed cells are placed into a spinner flask, constant rotational flow forces cell-cell collisions and subsequently spheroid formation (B – [modified from 12]). With liquid overlay technique, a nonadhesive substrate, such as agarose, first coated onto a surface, prior to the addition of cells; gentle rotation of plate and gravity induces cells to come in contact with one another (C - [modified from 13]). A simplification of the liquid overlay technique, involves the use of nonadhesive round bottom wells, where gravity and the shape of well forces cells to be in contact with one another (D – [modified from 13]). With microfluidics, monodispersed cells are suspended in aqueous phase (blue area), as it approaches the oil phase (yellow area), monodispersed cells are segregated into droplets, where eventually the monodispersed cells will come into contact with one another and form spheroids (E) [modified from 14].

(**Figure 1-1B**) [12]. With microfluidics, monodispersed cells move through channels, where exposure to rotational flow induces cellular aggregation and spheroid formation (**Figure 1-1E**) [14]. Overall, each of these methods has their own set of advantages and disadvantages. For example, liquid overlay and hanging drop techniques are relatively straightforward to form spheroids, but media exchange is difficult, and have been traditionally plagued by non-uniformity in spheroid size, low throughput, and required secondary transport prior to probing biological functions [12,13]. However, more recently both hanging drop and liquid overlay techniques have been adopted for use with either 96- or 384-well plates, thus increasing throughput of spheroid-based assays [15,16]. Alternatively, spinner cultures are easily scalable to produce a large number of spheroids, however, spheroids are susceptible to shear-induced damage, and requires transfer prior to performing any biological studies [12].

Throughout this dissertation, we utilized the technique of micromolding agarose hydrogels, through a technology commercialized as the 3D Petri Dish® [17,18]. The 3D Petri Dish® is a micromold that consists of a rectangular platform upon which an array of rounded cylindrical micro-posts (**Figure 1-2A, E**) [18]. To form nonadhesive hydrogels, molten agarose is poured on top of 3D Petri Dish® and allowed to harden (**Figure 1-2B**). After solidifying, the hydrogel is removed from micromold and equilibrated with media (**Figure 1-2C, D, Figure 1-3A**) [18]. Molded into the agarose hydrogel are two key structures: a large chamber for seeding cells and series of small concave micro-recesses located below (**Figure 1-2E**) [18]. To form microtissues, a small volume of mono-dispersed cells is pipetted into the large seeding chamber (**Figure 1-3B**). Over the course

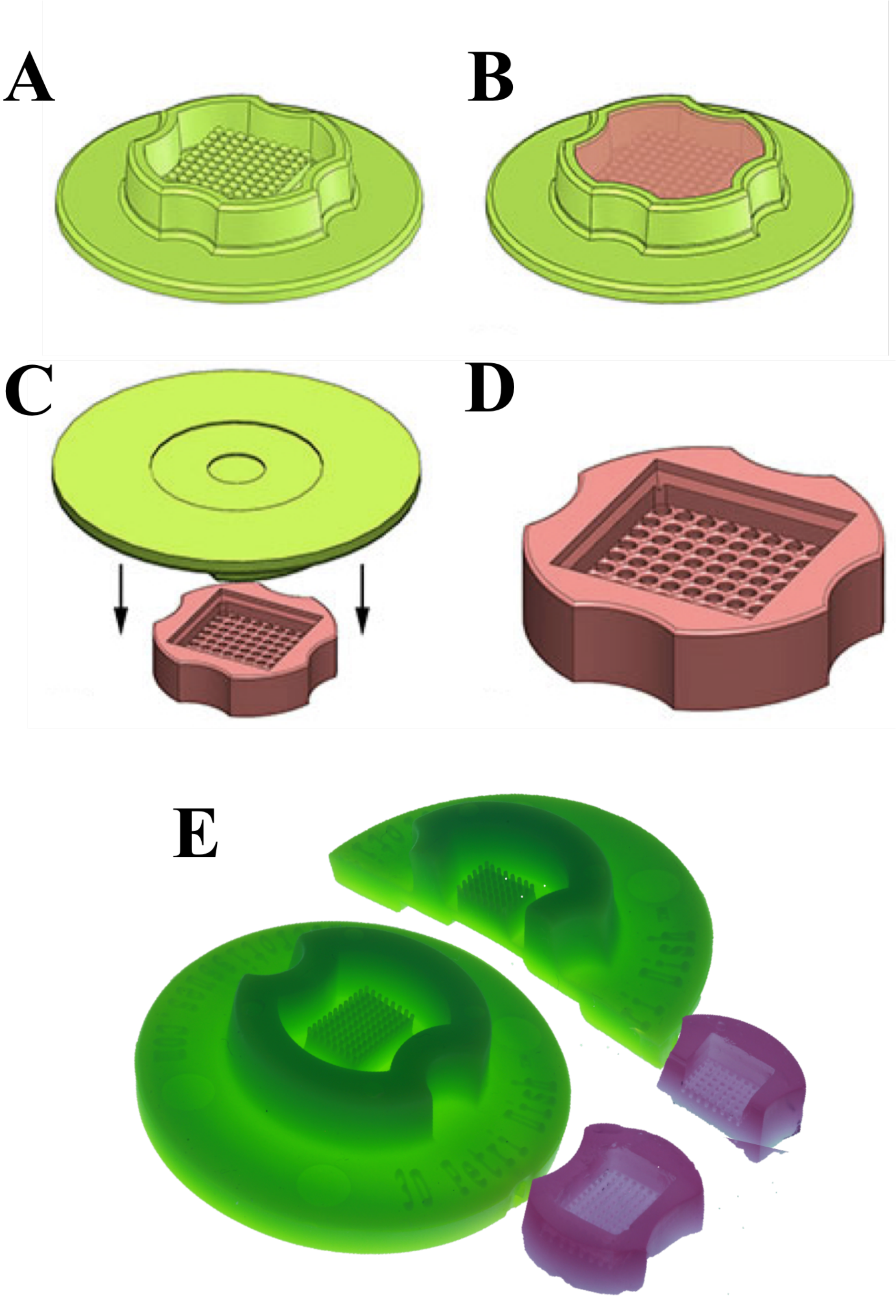

Figure 1-2. Non adhesive hydrogels are created from micromolds. Micromolds were designed to contain a rectangular block atop of which lay a series of small rounded microposts (A, E). To form hydrogels, molten agarose is pipetted on top of micromold (B). After allowing the agarose to solidify, hydrogels are removed from micromold (C). The resulting hydrogel will contain a rectangular loading dock, under which lay series of small round-bottom microrecesses (D, E). [modified from 18].

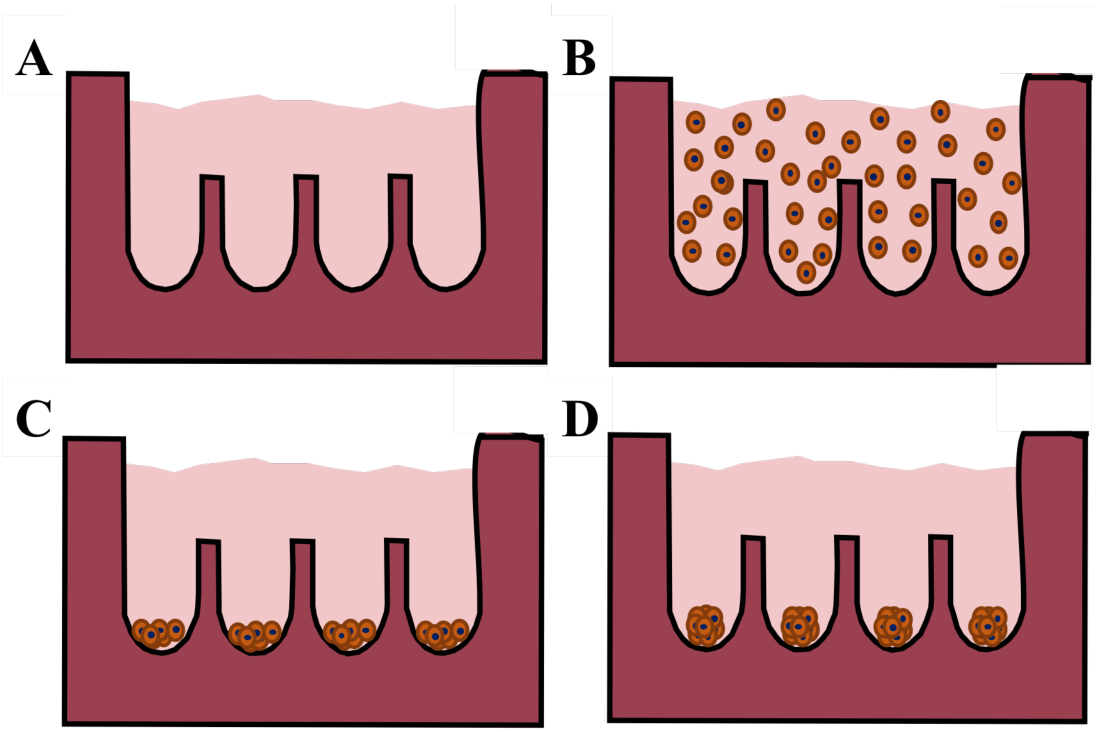

Figure 1-3. Non-adhesive hydrogels guide the process of microtissue self-assembly. Agarose hydrogels that have been previously equilibrated with media (A) were seeded with mono-dispersed cells by pipetting into the large chamber (B). After 30-minutes, cells have settled by gravity to the bottom of the micro-wells. (C). After 24 hours, cells have aggregated and self-assembled into microtissues (D). [modified from 18].

of 30-minutes, cells settle by gravity into the small micro-recesses below the seeding chamber (**Figure 1-3C**) [18]. The concave nature of micro-recesses ensures that cells are in close-contact with another. Furthermore, the non-adhesive nature of agarose prevents cellular attachment, thus over the course of 24-hours, cells aggregate and self-assemble into 3D spheroids (**Figure 1-3D, Figure 1-4**). Spheroid size can be easily controlled by altering the number of input cells, with higher seeding densities forming larger spheroids (**Figure 1-4**) [18]. Overall, this technology is advantageous for a variety of reasons, such as: (1) creation of a large number of spheroids of similar shape and size, (2) easy control of spheroid size by altering input number of cells, (3) media exchange without disturbing spheroids, and (4) spheroids can be probed directly within hydrogels [12,18]. Furthermore, throughout this dissertation, we showcase this technology's adaptability to high-throughput screening.

Regardless of the technique used, spheroids afford numerous advantages over both 2D monolayer and 3D scaffold-based *in vitro* models. Firstly, the cell density is much higher than both 2D monolayer and 3D scaffold-based approaches, and thus more comparable to *in vivo* tissues [12,14,19]. Due to this high cell densities, cell-cell interactions dominate as opposed to cell-substrate (scaffold or plastic) interactions, thus maximizing cell-cell communication [12, 20]. Furthermore, in 3D spheroids are able to excrete their own extracellular matrix proteins (ECM), exert forces over each other and ECM [19]. Cells are able to self-organize to undergo morphological changes according to biological principles [12,14,19]. For example, the breast cancer cell line, MCF-7, will form luminal structures when cultured as 3D spheroids, recapitulating the phenotype of the mammary

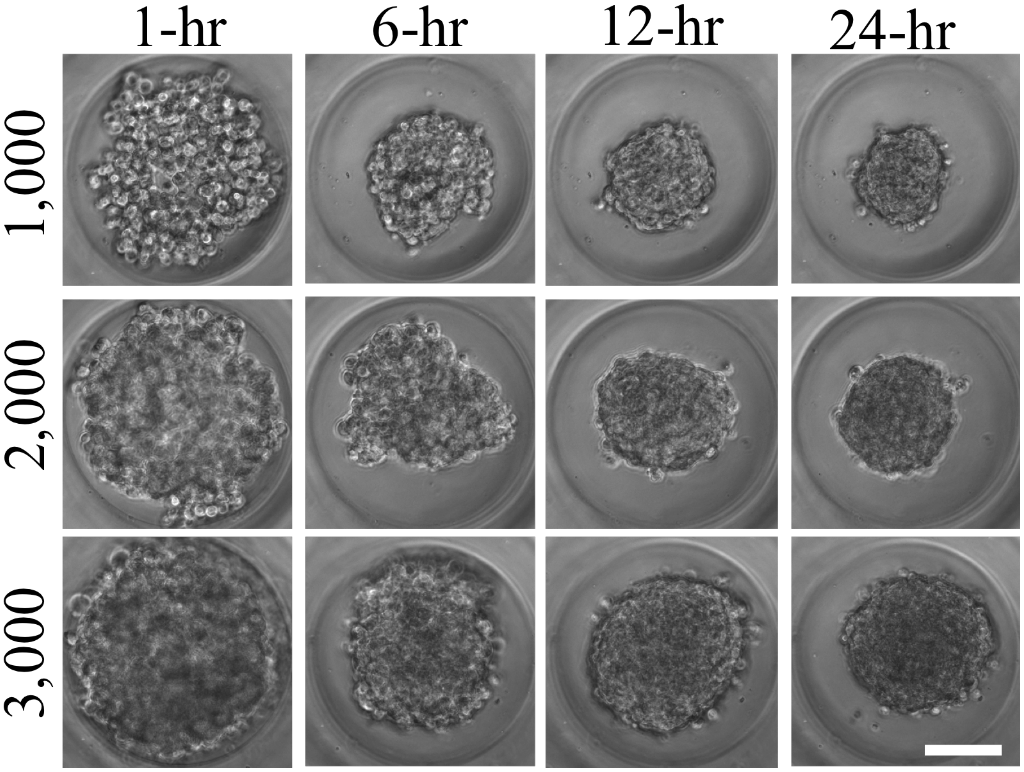

Figure 1-4. Time-lapse of variable sized spheroids self-assembling. Mono-dispersed cells of human ovarian granulosa cell line, KGN, were seeded into hydrogels at varying seeding densities: 1000- (top row), 2000- (middle row), 3000-cells per spheroid (bottom row). Images were acquired at 1-hour (left column), 6-hours (mid-left column), 12-hours (mid-right column), and 24-hours (right column) after seeding. Compact spheroids were formed within 24-hours, regardless of seeding density used. Higher seeding densities yielded larger spheroids. [modified from 18].

gland *in vivo* (**Figure 1-5**) [21]. Overall, cells cultured within 3D spheroids exhibit a more differentiated phenotype than cells cultured in 2D monolayers [8-10,21-24].

However, one of the major benefits to 3D spheroids is their ability to capture the complexity of *in vivo* environment with its multiple cell layers leading to the formation of gradients with respect to of pH, oxygen, nutrients, carbon dioxide, and ions [19,25,26]. Cells on the outer edge of spheroid will be exposed to very different conditions than cells in the center of the spheroid, with exacerbation of this differential by increasing spheroid radii. Therefore, throughout a single spheroid, there will be formation of different microenvironments throughout the 3D radius. Furthermore, these changes in the microenvironment can induce changes with respect to cellular processes with respect to proliferation, necrosis, apoptosis, viability, cellular communication [19,25-27]. If spheroid diameter is greater than 200-µm, cells in the spheroid center may not have enough access to nutrients and oxygen, thus leading to necrosis, meanwhile cells on outer edge of spheroid would remain viable [20,28,29]. Not only can we measure physiological changes that are naturally occurring within a 3D spheroid, but we can also measure changes in response to exposure/treatment with various substances. Additionally, upon exposure to a compound, cells within spheroid will be exposed to a concentration gradient concentration with the greatest exposure occurring along the spheroid perimeter. Therefore, we can measure the changes in the biological response as a function concentration gradient along the 3D radius.

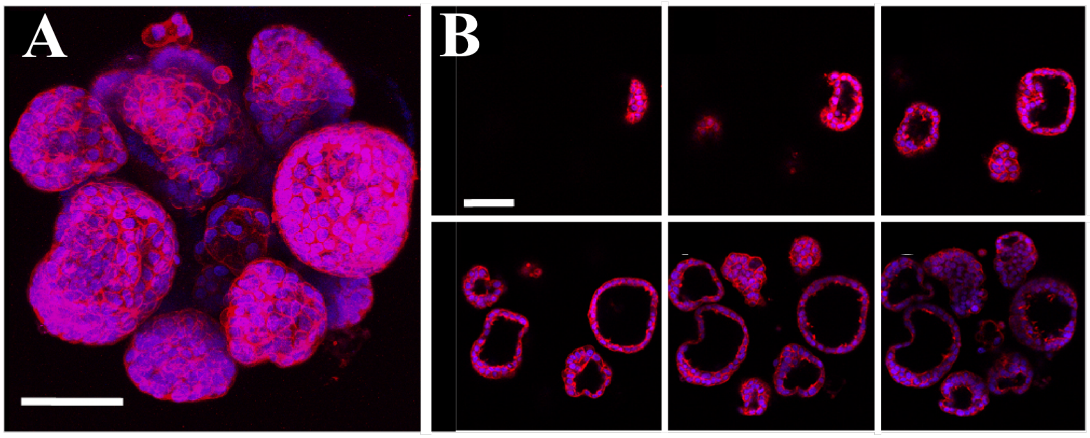

Figure 1-5. 3D spheroids have potential recapitulate *in vivo* morphology. Spheroids were formed from the breast cancer cell line, MCF-7, labeled with rhodamine phalloidin to stain F-action, and DAPI to stain the nucleus, and confocal z-stacks were acquired, and compiled to create a maximum projection image (A). MCF-7 cells form a series of spheroids within a single micro-well. To visualize throughout the 3D radius, representative confocal images were displayed every 15-μm, starting at a height of 0-μm (B). MCF-7 spheroids form luminal structures, thus mimicking the *in vivo* structure of mammary gland (B) [modified from 21].

Despite the numerous biological advantages that spheroids provide over traditional *in vitro* models, there are still numerous challenges remaining with respect to extracting information from 3D spheroids. For example, there are numerous commercially available instruments, probes, and kits to acquire information, as well as many validated open source or commercially available software programs to analyze the acquired data. However, all of these technologies have been optimized for use with 2D cell monolayers, and thus require further optimization and innovation for use with 3D spheroids. This dissertation specifically aimed to advance the use of 3D spheroids for quantitative, live cell, fluorescence microscopy.

1.2 TYPES of CELL SOURCES UTILIZED *IN VITRO*

A key component of developing *in vitro* models is determining an appropriate cell source to assess a biological function of interest. Cell sources are derived from either humans or other animals, such as rats, mice, hamsters, dogs. Furthermore, regardless of whether the cell source is human- or animal-derived, sources can be further classified as primary cells, induced pluripotent stem cell (iPSC)-derived, embryonic stem cell (ESC)-derived, or cell lines. Each type of cell source possesses a unique set of advantages and disadvantages. Additionally, utilizing these cell sources within 3D spheroids as opposed to traditional 2D cell monolayers, may yield additional cell source-specific challenges or improvements. Therefore, understanding the benefits and limitations of each cell source, especially with respect to 3D cell culture, is critical for developing biologically-driven *in vitro* models.

1.2.1 Primary Cells

Primary cells are isolated directly from *in vivo* tissues or organs: either from humans or animals [30-49]. Sources of primary tissue can be hypothetically isolated from any tissue *in vivo*, ranging from cardiac, hepatic, neural, renal, intestinal, skeletal, hematopoietic, and others [30-45]. Some primary tissue sources are commercially available, such as hepatocytes, respiratory epithelial cells, cardiomyocytes, astrocytes, endothelial cells from various vascular locations, various lineages of white blood cells, dermal fibroblasts or keratinocytes, arterial smooth muscle cells, renal epithelial cells, and others (www.ATCC.com, www.ThermoFisher.com, www.sigma-aldrich.com). Majority of commercially available primary tissue is human-derived, as opposed to animal-derived. Alternatively, acquisition of animal-derived sources requires researchers to isolate and process the desired tissue or organ directly from the animal [42-49]. Since tissues and organs are composed of multiple different cell types, either cell types can be utilized or tissues can be further processed to enrich for a single cell type prior to use [42-49]. There are multiple different techniques to enrich for single cells, ranging from fluorescence activated cell sorting, to magnetic activated cell sorting, to density-based gradients, as well as expansion on tissue culture plastic [46-49].

Overall, primary cells have been shown to better recapitulate the *in vivo* functions, phenotype, and morphology of the organ they have been isolated from. For example, primary human hepatocytes possess all key metabolizing enzymes and transporters, thus can accurately model metabolism, drug-drug interactions, and hepatoxicity [50,51]. Additionally, the use of primary human cardiomyocytes *in vitro* can accurately model the differential *in vivo* response to between torsadogenic and non-torsadogenic drugs [52]. Despite their biological advantages, there are numerous logistical disadvantages associated with the use of primary cells. For example, the isolation, enrichment, and preparation necessary to obtain a source of primary cells is relatively complex, time-consuming, potentially expensive. Alternatively, utilizing commercially available primary cells is relatively straightforward, however yields even greater expenses. Furthermore, most primary cells are unable to expand in culture past a few passages, thus limiting the ability to generate large cell numbers [53]. Therefore, primary cells can only be utilized for a small number of experiments prior to acquiring more sample. Given the large cell numbers necessary for high-throughput screening, especially with respect to use of multi-cellular spheroids, primary cells may not be a relevant cell source. Additionally, due to their lack of expansion capacity, multiple animal or human donors may be necessary, thus increasing the variability of experimental system. Furthermore, the availability of these cell sources is dependent upon the cell type and species of interest. For example, with respect to human-derived primary sources, tissue samples that are easily accessible, such as blood draws and skin biopsies, are more readily available than samples from other organ systems, such as hepatic, renal, cardiac or neural.

1.2.2 iPSC/ESC Derived

To overcome some of the availability issues plaguing primary cells, iPSC- of ESC-derived cell sources can be utilized. iPSCs and ESCs are both types of pluripotent stem cells that can differentiate down all three germ layers: mesoderm, ectoderm, and endoderm [54,55]. Both ESCs and iPSCs can be derived from either human or animals, have been shown to differentiate into a variety of different cell lineages, ranging from cardiomyocytes, to hepatocytes, to neurons [56-58]. The major difference between these two stem cells are where they are derived from, as ESCs are derived from the blastocyst cells of an embryo, whereas iPSCs are somatic cells that have been genetically reprogrammed back to a pluripotent state [54,55]. For iPSCs, the somatic cells can be isolated from any tissue of the body, however skin or blood are common sources due to the ease of obtaining samples [59-61]. Although the generation of iPSCs is complex, the process can be avoided, as there are many commercially available iPSC- and ESC-lines. Unlike primary cells, iPSCs and ESCs will continually proliferate until induced to differentiate into a specific cell lineage [54,55]. Therefore, despite the proliferative capacity associated with iPSCs and ESCs, the differentiation into tissue-specific cell sources prevents further proliferation, thus limiting the total number of cells that can be generated from a single differentiation run, although multiple runs can be performed simultaneously. Similar to primary cells, each differentiation run of iPSCs/ESCs may yield slightly different purities of cell type of interest, thus adding experimental variability to the system.

Additionally, iPSC technology affords unique opportunities to study any number of genetically-linked diseases [62,63]. For example, somatic cells can be isolated from any patient suffering from a disease, such as alzheimers or huntington’s, reprogrammed back into a pluripotent state, and differentiated into the cell type of interest, which in turn should possess characteristics of diseased state [62-66]. Although iPSCs and ESCs can produce cell types that are difficult to acquire from primary sources, these differentiated cells typically possess an immature phenotype. For example, iPSC-derived cardiomyocytes express an immature phenotype with respect to electrophysiology, force generation, and size [67,68]. Additionally, iPSC-derived hepatocytes express proteins associated with an immature phenotype, as well as lower levels of functional outputs, such as albumin production, urea production, and cytochrome P450 activity, when compared to primary human hepatocytes [69]. Whether or not these immature differentiated cell types are sufficient for *in vitro* modeling would be dependent upon what biological marker or function is being studied. Furthermore, maturity can be increased by extending length of culturing prior to assaying. For example, iPSC-derived cardiomyocytes develop a more mature phenotype with respect to gene expression profile, action potentials, and coordinated contraction, over the course of forty-five days in culture [70]. However, differentiating iPSCs or ESCs for months prior to utilizing them may not be a relevant, cost- or time-effective alternative. Overall, iPSC/ESC cellular differentiation is time-consuming, not reproducible, and low throughput. Therefore, until these limitations are addressed, this cell source will not be applicable to high-throughput screening.

1.2.3 Cell Lines

In order to circumvent some of these issues plaguing primary and iPSC/ESC derived cell sources, cell lines can be utilized. Cell lines are proliferative cultures developed from a single cell. Similar to both primary and iPSC/ESC sources, cell lines can be derived from animal or human origin. Cell lines are typically derived from cancer/tumor biopsies, such as cervical cancer cell line (Hela), the breast cancer cell line (MCF-7), liver cancer cell line (HepG2), ovarian granulosa tumor cell line (KGN) [71-74]. Alternatively, cell lines can be derived from transforming primary cell sources by viral transfection of either simian virus 40 (SV40) T antigen or telomerase reverse transcriptase protein (TERT) or adenovirus 5, such as human embryonic kidney cell line (HEK-293), thyroid follicular epithelial cell line (nThy-ori 3-1), normal prostrate cell line (PNT1A) [75-76].

Cell lines afford numerous advantages over primary or iPSC/ESC-derived sources. For example, cell lines can be stably passaged and cultured for an extended period of time, maintaining stable genotype and phenotype, thus reducing variable across multiple experiments [78]. Furthermore, cell lines can be easily expanded to obtain large numbers of cells, thus increasing its applicability for high-throughput screening, especially with respect to utilization of spheroid models [78]. Additionally, the majority of cell lines are commercially available, thus increasing the accessibility of their use. However, despite these logistical advantages, cell lines are also associated with various biological disadvantages. For example, these cell lines are either derived from cancerous tissue or genetically manipulated, which could alter their phenotype and functionality increasing disparities to *in vivo* environment [78]. Additionally, although cell lines can be used as a model for cancer, modeling other genetic-based diseases is more difficult. Overall, if a cell line cannot recapitulate the desired functions of the organ of interest, it lacks relevance as a viable cell source.

1.2.3.1 KGN - Cell Line

Throughout this thesis, we have predominantly utilized the human ovarian granulosa-like cell line, KGN. The KGN cell line was initially derived from a biopsy of granulosa tumor tissue, from a patient suffering from a reoccurrence of granulosa cell tumor, 9-years after initial diagnosis of granulosa cell carcinoma, stage III [71]. The KGN cell line has shown to be stably proliferate for over 100 passages, exhibit no contact inhibition of growth [71]. KGN cells exhibit a phenotype similar to noncancerous granulosa cells, as they possess steroidogenic activities, express a functional follicle stimulating hormone receptor, produce and regulate progesterone, and regulate aromatase activities [71]. KGN cells have been utilized for nearly two decades to study a range of biological processes, such as evaluating pathways of apoptotic induction, to studying diseases such as polycystic ovary syndrome, to assessing hormonal responses to chemical/toxicant exposure [71,79-82].

We have chosen to work with this cell source, for a variety reasons. Firstly, the central theme of this dissertation has been aimed at advancing the use of 3D spheroids for high-throughput, quantitative, live-cell, fluorescent assays for the eventual use of biologically driven assays. However, prior to developing these biologically driven assays, we must first gain a better understanding of how to best quantify the data we obtain from spheroids. Therefore, as opposed to choosing a more physiologically relevant cell source, such as primary or iPSC/ESC derived sources, we chose to utilize a cell line for its ease of use. Additionally, KGN cells will easily form compact spheroids, approximately of a spherical nature ($x = y = 0.9\ z$), and spheroid size can be easily controlled by altering the input number of cells. Furthermore, KGN cells express the membrane protein, connexin-43, which form gap junction channels between cells enabling intercellular communication. This facet will be integral for our third aim, where we developed a biologically driven assay assessing gap junction intercellular communication within 3D spheroids.

1.3 INSTRUMENTATION NECESSARY to ACQUIRE 3D DATA

A critical component of developing *in vitro* models utilizing 3D spheroids is identifying what outputs are necessary to acquire answers, and furthermore what instruments can provide the appropriate outputs. There are numerous different instruments that can image and capture information from 3D spheroids, answering questions about what is occurring overall, throughout the interior, and on the surface of spheroids. Each instrument has its own purpose, advantages, and disadvantages associated with its use. This dissertation specifically focuses on microscopy techniques that could visualize the spheroid's interior to capitalize on richness of biological content throughout.

1.3.1 Brightfield Microscopy

Brightfield microscopy is a simple technique where the sample is illuminated with white light, creating a bright field of view [83]. The specimen of interest is darker than remaining field of view due to attenuation of transmitted light through the sample. Brightfield microscopy is typically used to evaluate samples that are either stained with dye, naturally express pigmentation, or otherwise possess high contrast [83]. With respect to spheroids, brightfield microscopy can be used to visualize either a snap shot of the entire spheroid, or sections of spheroids. Performing brightfield microscopy on whole spheroids can only reveal features such as shape, size, sphericity in the (*x,y*)-dimension. Furthermore, brightfield alone cannot provide detailed information about what is occurring inside the spheroid, or on a single cell basis. However, to reveal more detailed information about spheroids, brightfield microscopy can be combined with histological sectioning [83]. Histological sectioning is a well-known pathology tool commonly used to characterize tissue biopsies. However, these techniques were adapted for use with 3D spheroids to enable the fixation, embedding, and sectioning directly within agarose hydrogels, thus enabling visualization of an array of spheroids (**Figure 1-6**) [84]. These sections of spheroids were then labeled with hematoxylin and eosin to look at nuclear and protein structures throughout cells (**Figure 1-6B, C**) [84]. Although histological sections can reveal biological changes throughout the spheroid, these techniques are time-consuming and low throughput. Furthermore, unless every section of spheroid was collected and analyzed, identifying where a section was located in the intact spheroid is difficult. Overall, brightfield microscopy is a simple, easy-to-use technique that comes standard with most high-throughput imaging systems. However, brightfield alone fails to provide quantitative data regarding biological changes throughout the 3D radius of spheroids.

1.3.2 Widefield Epi-Fluorescence Microscopy

To increase the amount of biological information that can be assessed from 3D spheroids, widefield epifluorescence microscopy can be utilized. Widefield epifluorescence microscopy can capitalize on the thousands of commercially available fluorescent dyes

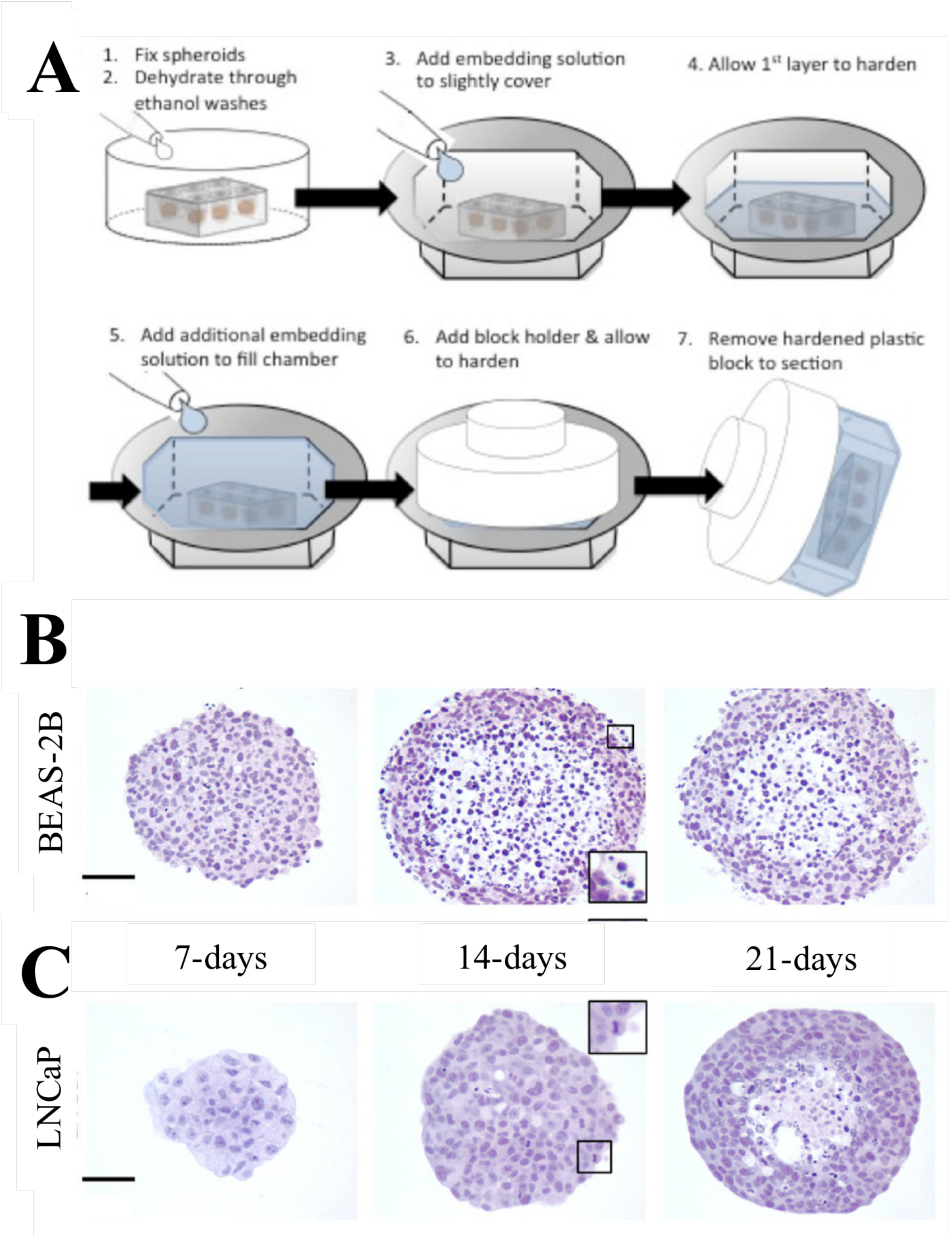

Figure 1-6. Embedding and histopathology of spheroids can be performed directly within agarose hydrogels. Arrays of spheroids can be embedded, sectioned, and imaged directly in agarose hydrogels through a two-step plastic embedding process, as shown in schematic (A). To highlight this process, both BEAS-2B (B) and LNCaP (C) spheroids were sectioned and stained with hematoxylin and eosin after culturing for the following time-points: 7-days (left column), 14-days (middle column), 21-days (right column). [modified from 84].

that probe a wide range of biological functions, which will be discussed further in the following section. With widefield epifluorescence microscopy, the fluorescently labeled sample is excited with a high intensity light source, which in turn creates an emission of light of a longer wavelength [85]. Through the use of filter sets, the appropriate excitation and emission wavelengths can be specified to only illuminate the wavelength of interest [85]. Widefield epifluorescence microscopy enables visualization of the entire spheroid, as well as the ability to optically section spheroids. Additionally, acquiring widefield fluorescent images is quick, easy, and adaptable to high-throughput screening. However, widefield epifluorescence microscopes illuminate the entire field of view at once and lacks the hardware to remove out-of-focus light, thus leading to blurry images [86]. Image stacks can be deconvolved to remove out-of-focus light, thus improving feature visualization (**Figure 1-7**) [86]. However, deconvolution increases image processing times, and not all deconvolution programs are compatible with further quantitative analysis [85,86]. Furthermore, even with deconvolution, accurate images can only be acquired within the first couple cell layers of spheroid.

1.3.3 Confocal Microscopy

To improve upon the out-of-focus light issue associated with widefield epifluorescence microscopy, confocal microscopy can be utilized. Similar to widefield epifluorescence, confocal microscopy relies on the use of fluorescently labeled samples. However, confocal microscopy utilizes hardware, such as slits, pinholes, or shutters, to physically block out-of-focus light, thus illuminating and capturing fluorescence from a single focal plane [87]. Acquiring confocal images obviates the need for deconvolution and improves

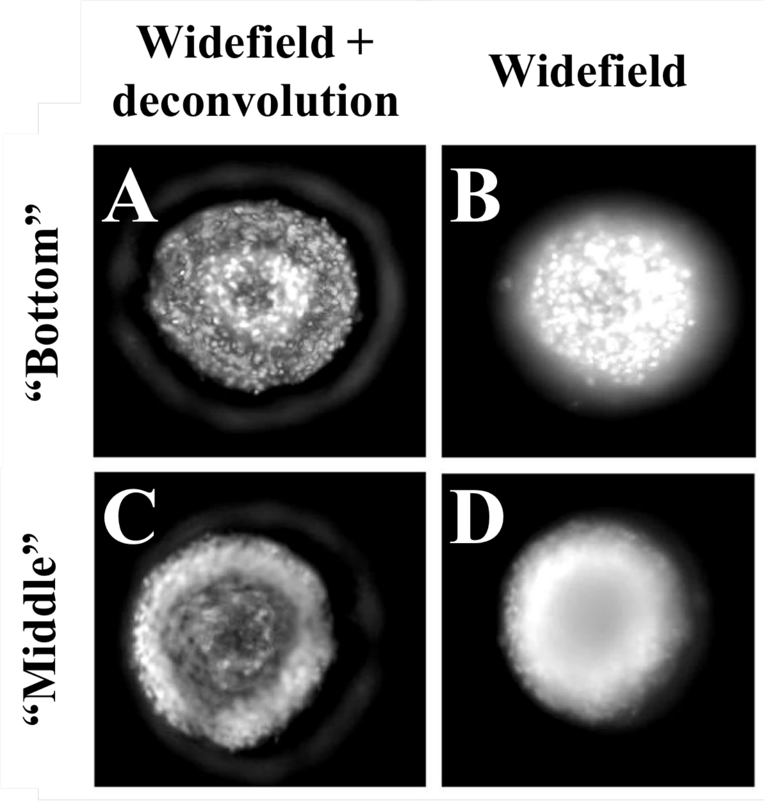

Figure 1-7. Deconvolution improves visualization of epi-fluorescence z-stacks. Panc-1 spheroids were stained with Hoechst33342, and widefield z-stacks were captured (20X, 0.70 NA). Representative epifluorescence images of the "bottom" (A,B) and "middle" (C,D) of spheroid were displayed both with (A,C) and without (B,D) performing deconvolution. Deconvolution reduces the blurriness of epifluorescence images by utilizing algortihms to remove the out-of-focus light. [modified from 86].

resolution in the *z*-dimension. Additionally, confocal microscopy utilizes high-powered lasers, as opposed to high energy light sources, to excite fluorophores of a specific wavelength, which could leave samples susceptible to phototoxicity and photobleaching [87]. Furthermore, there are two main types of confocal microscopy, point scanning and spinning disk, both operate on the same principles of blocking out-of-focus light, however, but the method of image acquisition is different [88]. With point scanning, a single pinhole is used to focus light on small spot (*x,y,z*), and scanned across the sample to build an image [87,88]. Alternatively, with spinning disk confocal, there are many spots of illumination across the sample leading to faster acquisition time [88]. Additionally, due to their fast acquisition, spinning disk confocal microscopes lead to less phototoxicity, thus better viability for live-cell imaging [88]. Overall, similar to wide-field epifluorescence, confocal microscopy can assess essentially any biological function due to large number of commercially available fluorescent probes. Additionally, there are now commercially available confocal microscopes adapted for high-throughput screening, such as Perkin Elmer's Opera Phenix, GE Healthcare's IN Cell Analyzer 6000, Thermo Fisher's CellInsight CX7, Molecular Devices' ImageXpress Velos, and others [89].

Additionally, acquiring confocal images of 3D spheroids is plagued with the inability to capture fluorescent signal deeper into the *z*-depth due to the light scattering properties of cells [90,91]. In response to these limitations, tissue clearing techniques have been developed that either (1) remove optically scattering substances, and/or (2) optically match the refractive indices of the tissue and surrounding media [84,90-93]. These techniques improve visualization into the spheroids, capturing signal up to 100-μm into the *z*-depth **(Figure 1-8)** **[**84,90**]**. However, tissue clearing requires samples to be fixed, thus making it incompatible for dynamic, live-cell assays.

1.3.4 Multi-photon Microscopy

Another alternative to improve visualization into a spheroid is through the use of multi-photon microscopy. Similar to epifluorescence and confocal microscopy, the sample should be labeled with fluorescent dyes, although there are also variant protocols, such as second harmonic generation, that enables visualization of fibers without the use of any fluorescent labels. With multiphoton microscopy, rather than exciting the respective fluorophore with a single photon of energy, the excitation is produced by two lower energy photons [94]. Therefore, only the point where the two photons meet will be excited, creating excellent resolution in the *z*-dimension, and thus obviating the need for pinholes or slits to remove out of focus light [94]. Additionally, multi-photon microscopy typically uses longer excitation wavelengths, thus increasing the penetration into the sample. Furthermore, since lower energy photons are excited at a precise point, there should be less phototoxicity associated with imaging compared to confocal microscopy [94]. However, multi-photon microscopes have not yet been converted to enable high-throughput applications, thus are limited by small sample sizes.

1.3.5 Light Sheet Fluorescence Microscopy

Light sheet fluorescent microscopy (LSFM) is another technique that enables the visualization throughout the 3D spheroid. With LSFM, the light path runs perpendicular

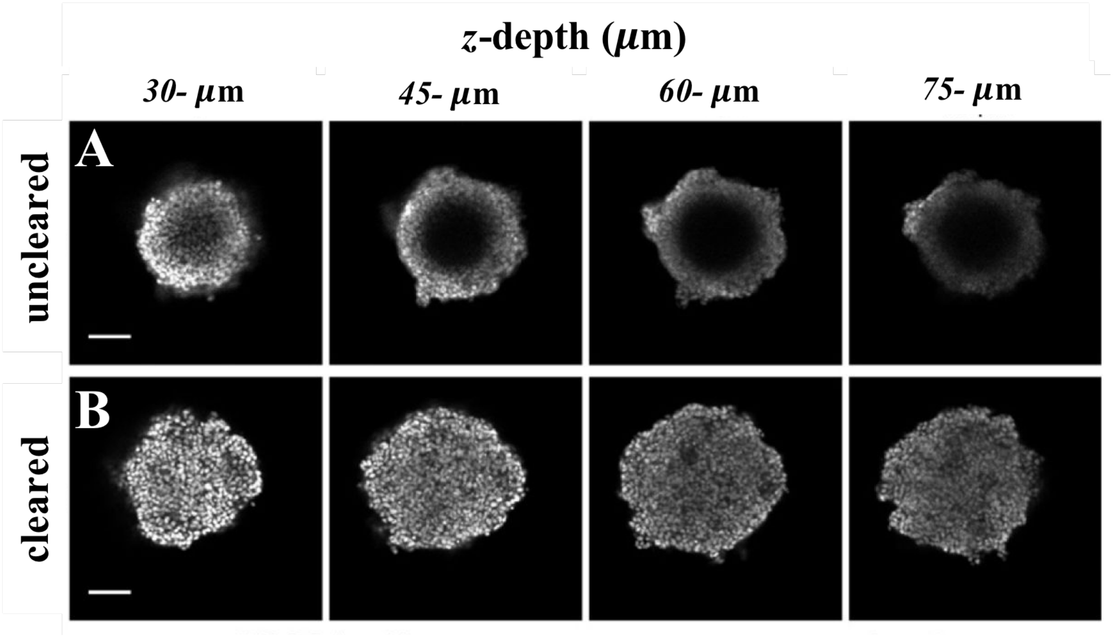

Figure 1-8. Tissue clearing enhances visualization throughout the *z*-depth of spheroids. To test the effect of clearing techniques on visualization throughout the *z*-depth, PLHC-1 spheroids, stained with the nuclear dye, DAPI, were fixed, and imaged either with (B) or without clearing (A) with formamide and polyethylene glycol. Representative confocal images every 15-µm throughout the *z*-depth are shown. When imaging un-cleared spheroids, signal loss was already apparent 30-µm into the *z*-depth, and the level of loss increased deeper into *z*-depth (A). Alternatively, with cleared samples, nuclei were clearly visualized at a depth of 75-µm into the spheroid (B). [modified from 84].

to its observation, unlike epifluorescence, confocal, and multiphoton microscopy which run in series [95,96]. Focusing a laser beam through a cylindrical lens, creates a thin (~100-nm) sheet of light, which decreases the amount of photo-damage to sample and reduces acquisition of out-of-focus light without the use of pinholes or slits [95,96]. LSFM outperforms confocal microscopy with respect to both the speed of image acquisition and visualization throughout the z-depth (**Figure 1-9**) [95]. Despite these advantages, sample preparation for LSFM is cumbersome, requiring sample to be mounted in a particular orientation, thus preventing its conversion to high-throughput screening [95-97].

1.4 FLUORESCENT PROBES ENABLE the MONITORING of BIOLOOGICAL PROCESSES THROUGHOUT SPHEROIDS

Another critical component of developing *in vitro* models utilizing 3D spheroids is understanding what the biological question is, and what tools are necessary to acquire answers. There are numerous different techniques and probes that can assess what is occurring throughout spheroids, spanning the fields of molecular biology, biochemistry, microscopy, and others. However, given the advancements towards high-throughput, high-content imaging, this dissertation focuses on utilizing fluorescent microscopy to develop *in vitro* spheroid-based models. Fluorescent microscopy has been successfully used in conjunction with 2D cell culture models for decades, thus there are hundreds of commercially available fluorescent dyes that probe a wide range of biological functions. Given the complexity of spheroids over 2D monolayers, utilization of these probes will require some optimization. However, a spheroid's complexity is also its key advantage,

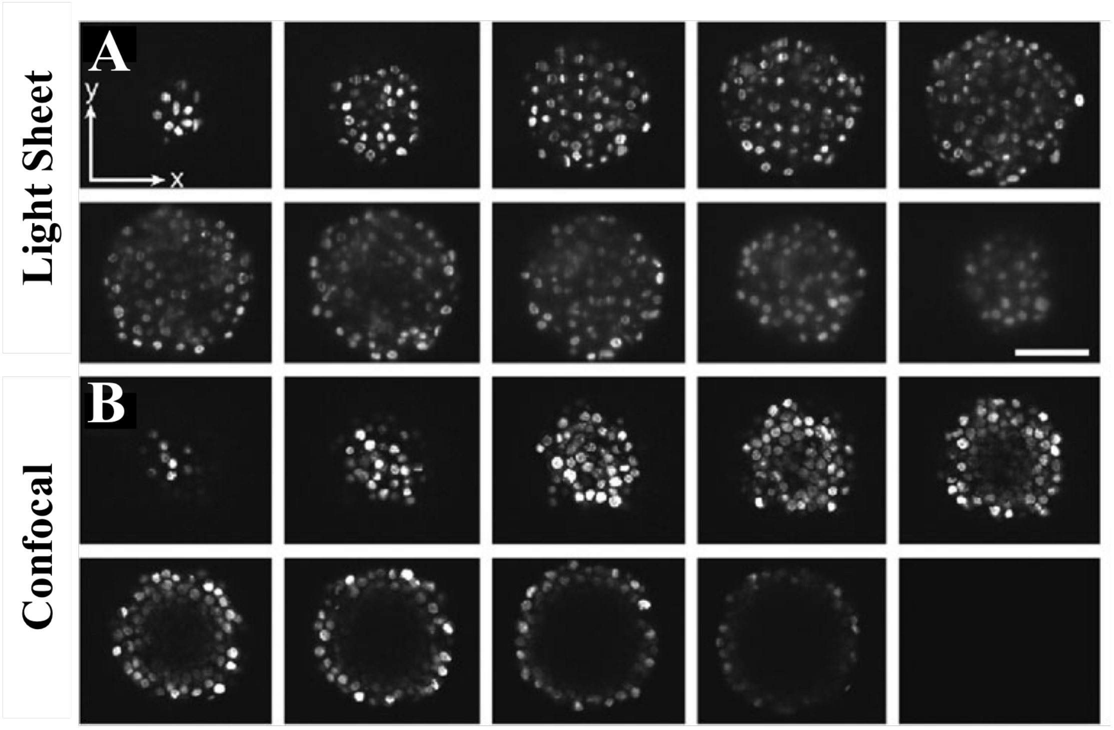

Figure 1-9. Light sheet fluorescence microscopy (LSFM) enhances visualization throughout the z-depth of spheroids when compared to confocal microscopy. Human pancreatic cancerous spheroids formed from BxPC3 cells were labeled with the nuclear dye DRAQ5, and assessed by either light sheet fluorescence microscopy (objective lens CZ 40X/0.8 NA water dipping) (A) or confocal microscopy (40X/0.8 NA water dipping objective) (B). *Z*-spacing for LSFM was 10-µm, meanwhile *z*-spacing for confocal was 5-µm. LSFM enabled better visualization of nuclei deeper into the *z*-depth [modified from 95].

as biological changes occurring throughout the entire spheroid can evaluated as a function of its 3D radius. Overall, the 3D nature of spheroids enables their ability to answer a multitude of questions that traditional 2D monolayers are not even equipped to ask.

1.4.1 Measuring cellular responses to microenvironment

A key advantage of utilizing spheroids for *in vitro* modeling are the complex biological changes that occur throughout the entire spheroid as a function of its 3D radius. The multiple cell layers that comprise a spheroid act as barriers to both diffusion and transport, thus creating gradients of nutrients, oxygen, ions, pH, carbon dioxide [7,19,25,26,98,99]. Due to the formation of these gradients, cells within the same spheroid will experience different microenvironments depending upon their location. Furthermore, these differences in microenvironments could induce differences in cellular behavior/function, thus creating different cell phenotypes along the 3D radius [7,99]. For example, cells on perimeter of spheroid will have easy access to the reservoir of nutrients and oxygen, thus should be viable [7,19,25,26,100]. However, cells in the center will have indirect access to nutrient and oxygen, and be dependent upon diffusion. Therefore, depending on the size of spheroid, cells in the center may undergo necrosis or apoptosis. Furthermore, this phenomenon is well characterized in the field of cancer biology, as the use of large multicellular tumor spheroids (>500-μm diameter) leads to the creation of multiple different zones: proliferation zone along the outer edge, quiescent zone in middle, and necrotic core [28,101]. There are numerous fluorescent dyes that will measure whether a cell is viable (calcein-AM, calcein-red-orange-AM, calcein-blue-

AM), apoptotic (resazurin, TUNEL), necrotic (propidium iodide, 7-aminoactinomycin D, ethidium homodimer), or proliferating (ki-67) [27,102,103]. A combination of these dyes enable the assessment of cytotoxicity throughout spheroids.

1.4.2 Modeling Movement throughout 3D spheroids

3D spheroids can serve as a platform to measure and monitor different types of movement throughout its radius. For example, uptake and penetration of various fluorescently labeled compounds, such as microbeads, nanoparticles, dyes, or drugs, into spheroids can be monitored over time to assess both (1) the overall amounts entering the spheroid, as well as (2) the distance traveled. Microbeads and nanoparticles are currently being evaluated for their use in drug delivery [102-104]. Therefore, tracking the uptake and penetration of fluorescent microbeads and nanoparticles into spheroids can act as a model to drug delivery for cancer biology [103,104]. Similar to the use nanoparticles/microbeads, certain cancer chemotherapeutics, like doxorubicin, are naturally fluorescent, thus their uptake and distribution can be modeled as well [105]. Additionally, when certain fluorescent dyes and cell types pairs are utilized, the uptake and penetration of fluorescent dyes into the yields information regarding efflux pumps or intercellular communication. For example, the nuclear dye, Hoechst 33342, is also a substrate for the efflux pump, breast cancer resistance protein (BCRP), meanwhile calcein-AM is a substrate for the efflux pump, p-glycoprotein (P-gp), and its fluorescent derivate, calcein, is a substrate for multi-drug resistance protein 1 (MRP1) [106-108]. Additionally, calcein can diffuse through gap junctions, thus acting as a model of gap junctional intercellular communication between cells [109]. Furthermore, by adding inhibitors or enhancers, the subsequent alterations in uptake and penetration can be assessed [107,108]. Finally, rather than simply model the movement of these fluorescent molecules throughout the spheroid, we can also monitor *how* cells respond to the movement of these compounds, by utilizing the methods detail in the previous section. For example, the potential toxicity of nanoparticles and drugs can be evaluated as they penetrate deeper into spheroids [110,111].

3D spheroids could also be used to track cellular movement throughout the 3D radius, whether it be an individual cell's movement or tracking populations of cells. Tracking an individual cell's movement throughout a 3D spheroid can model a number of biological phenomenon, such as a cancerous cell's ability to invade a healthy tissue, or endothelial cells undergoing angiogenesis [112,113]. Alternatively, by forming spheroids composed of multiple cell types, cells may self-sort into different architectures [108,114,115]. For example, when mixing normal human fibroblasts (NHFs) and rat hepatoma (H35) cells together, NHFs will migrate to the spheroid center, while H35 cells aggregate around the other edge [114]. For all cellular motility applications, cells should be labeled with fluorescent dyes prior to spheroid formation to track movement throughout the spheroid. Choosing what fluorescent dye to use for cell tracking study will be dependent upon the length of study, as CellTracker^{TM} dyes work well for short-term (3-6 generations), and Qtracker^{TM} probes possess longer retention times (6-10 generations), thus are better suited for long-term studies [108,114,115]. Both of these types of dyes come in a range of different excitation/emission properties from 353/466-nm up to 630/650-nm for CellTracker^{TM} dyes, and 488/525-nm up to 760/800-nm for Qtracker^{TM}. Alternatively, genetically engineered cell lines programmed to express fluorescent proteins, such as GFP, RFP, YFP, can also be utilized [116-118].

1.4.3 Limitations associated with the use of fluorescent probes

Despite the potential to answer a multitude of interesting questions, the use of fluorescent probes are not without limitations. A major limitation of fluorescent microscopy was already discussed in the previous section: inability to capture fluorescent signal deeper into the spheroid due to the light scattering properties of cells. However, the other main limitation deals with the delivery of fluorescent probes into spheroids. In 2D cell monolayers, every cell is exposed to the same reservoir of dyes [6,7]. However, with 3D spheroids, only cells in the outermost layer have immediate access to the reservoir of dyes [6,7]. The remaining cells within the spheroid must rely on diffusion to gain access to dye. This will result in a gradient of signal, with the brightest signal occurring at the perimeter of the spheroid. Although this phenomenon is useful to model how cell layers affect transport, this gradient of signal increases complexity of the system. For example, if a fluorescent signal does not exist deeper into the spheroid, that does not necessarily imply that the biological event is not occurring. Rather, a lack of signal could imply that the fluorescent dye has not penetrated that deep into the spheroid. The length of staining time and dye concentrations recommended per manufacturer's instructions have been most likely optimized for staining with 2D cell monolayers. Therefore, when adapting fluorescent dye for use with 3D spheroids, the dye concentration and staining times may need to be increased. The length of time that a particular dye needs will be dependent upon its molecular weight and chemical properties, as well as the size of spheroids. For examples, dyes will be able to penetrate throughout a smaller spheroid faster than a larger one, due to shorter radial distances necessary to reach the core. Additionally, lower molecular weight proteins should be able to diffuse faster than large molecular weight antibodies. Furthermore, with respect to chemical properties, if a dye can penetrate a 2D monolayer, it should also be able to penetrate at least the outer cell layer of spheroid. However, for dyes like calceinAM, cleavage by intercellular esterases, alter its chemical properties, thus preventing it from diffusing across the lipid bilayer. Overall, when developing 3D spheroid models, it is critical to understand the limitations of fluorescent probe use, and subsequently optimize the experimental system to address those limitations.

1.5 ADVANCEMENTS NECESSARY for 3D IMAGE QUANTITATION

Combining the ability to fluorescently label 3D spheroids and subsequently image with high-throughput confocal screening systems yield extensive datasets (100+GBs) that need to be analyzed and interpreted. The amount of data that can be acquired from high-throughput screening is too great to perform manual analysis upon, especially when attempting to quantify biological changes throughout the 3D radius. The advancements in instrumentation, which led to the development in high-throughput confocal imaging systems, have not yet been matched by advancements in technology to analyze these datasets [86,89]. Currently, there are some platforms, both open source and commercially available ones, that possess some features for 3D image analysis. ImageJ (FIJI), Vaa3D, BioImageXD, Icy, and TANGO are all open source programs that enable 3D rendering and visualization of spheroids [86,89]. These programs possess certain modules for 3D image analysis, such as surface and volume renderings, object counts. Furthermore, since these programs are open source, anyone can write and publish new algorithms for 3D image analysis, although support for these features is minimal. Alternatively, there are some commercially available systems, from such as Imaris, Amira, Harmony, Phaedra, Huygens, Metamorph, ImagePro [86,89]. Commercially available systems are more cost-prohibitive, however, typically come with more turnkey features and modules, as well as customer support for 3D image analysis.

None of the currently available software programs can handle the amounts and complexity of data obtained from performing high-throughput confocal imaging of 3D spheroids [86,89]. Some software programs possess some functions that are batch-able for large datasets [86,89]. However, these batch-able functions only provide basic data regarding the overall volume, surface, and shape of spheroids, thus failing to capitalize on the richness of biological content throughout the spheroid. Alternatively, the methods and modules available to quantify fluorescence throughout the spheroid tend to require user input and are not batch-able across the entire 96-well plate. Furthermore, most of these programs rely on thresholding fluorescent signal to identify regions of spheroid. However, given the loss of fluorescent signal throughout the *z*-depth of 3D spheroids, utilizing fluorescent signal alone may not be sufficient. For example, setting a high threshold based on the brighter signal, yields a spheroid surface that fails to capture entirety of the spheroid (**Figure 1-10E**). Alternatively, lowering the threshold will yield a more spherical object, however, a lower threshold encompasses more background signal, thus the surface identified will be an over-representation of the actual spheroid perimeter **(Figure 1-10C, D**).

Alternative approaches for 3D image analysis involves a simplification step by converting z-stacks to maximum projection images prior to performing quantitative analysis. However, maximum projections may not fully capture the changes occurring along the 3D radius, thus failing to capitalize upon the biological complexities of spheroids. Furthermore, depending upon the spheroid model, analyzing maximum projection images could yield misleading and inaccurate results. For example, when monitoring the uptake and distribution of a fluorescent dye within the spheroid, reducing the confocal z-stack to a maximum projection would yield similar results regardless of how far the dye penetrated (**Figure 1-11**).

Overall there are no turnkey programs that can measure biological changes as a function of 3D radius in a high throughput fashion. Until these advancements are achieved, spheroids will possess limited usefulness in high-throughput screening. However, even if batch-able software solutions already existed, there are other quantitative assessments that must be performed prior to developing high-throughput biological-based assays. This dissertation interrogated the effect of spheroid size and dye labeling methods with respect to obtaining quantitative fluorescent imaging.

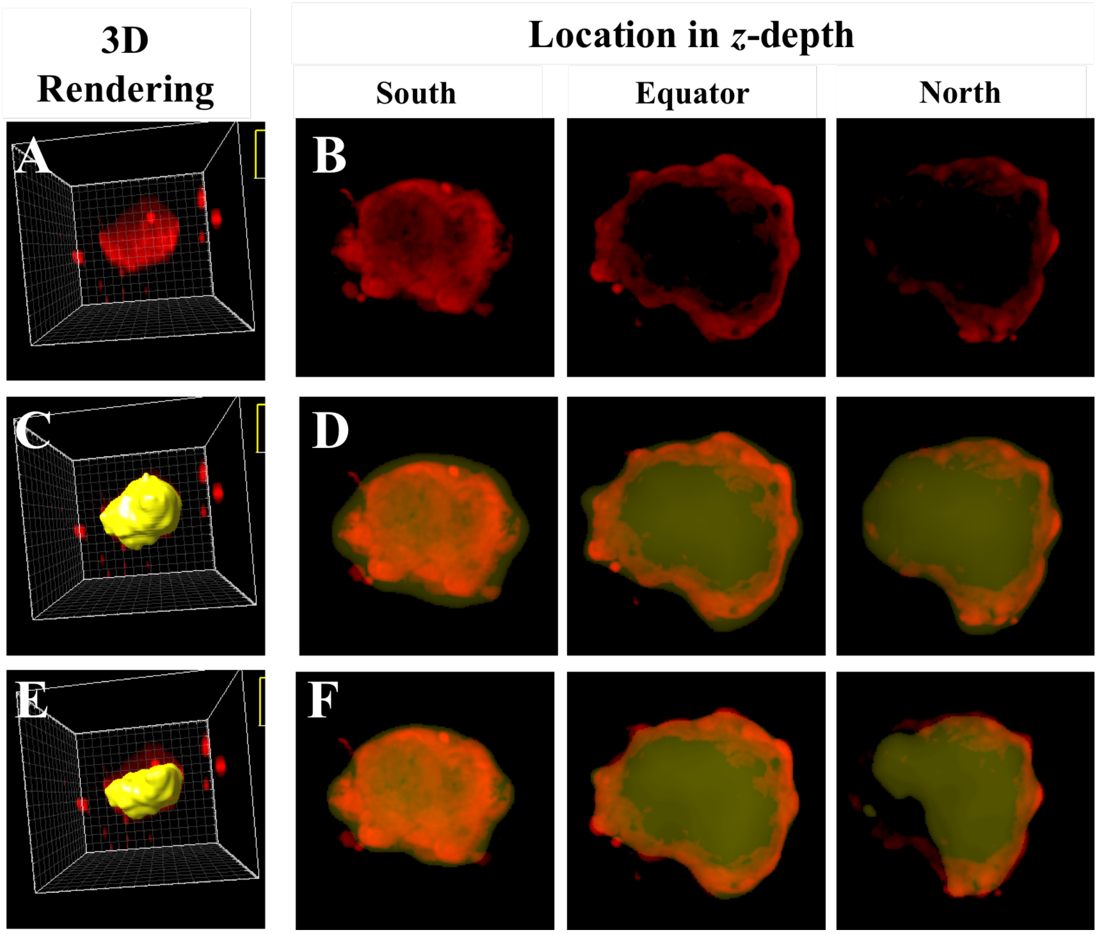

Figure 1-10. Only utilizing fluorescent thresholding to identify surface of spheroid leads to inaccuracies. Ovarian granulosa cells (KGN) were seeded into hydrogels to form spheroids, labeled with calcein-red-orange-AM, and confocal z-stacks were acquired. Confocal z-stacks were imported into the 3D image analysis program, Imaris, and rendered as 3D objects (A). To identify spheroids within Imaris, fluorescence thresholding limits must be set. Due to light scattering effects of cells, the fluorescence intensity throughout the spheroid will not be uniform, with brighter signals occurring south of the equator. To identify the entire spheroid region, the thresholding value should be lowered (C), as only thresholding the brightest signal leads to identification of lower spheroid portions (E). However, by lowering the fluorescent threshold, surface identification is expanded beyond the perimeter of the spheroid for slices below the equator (D – left column). Alternatively, setting higher thresholds lead to better fit to spheroids for slices south of the equator, however, fail to capture entirety of spheroid slices north of the equator (F).

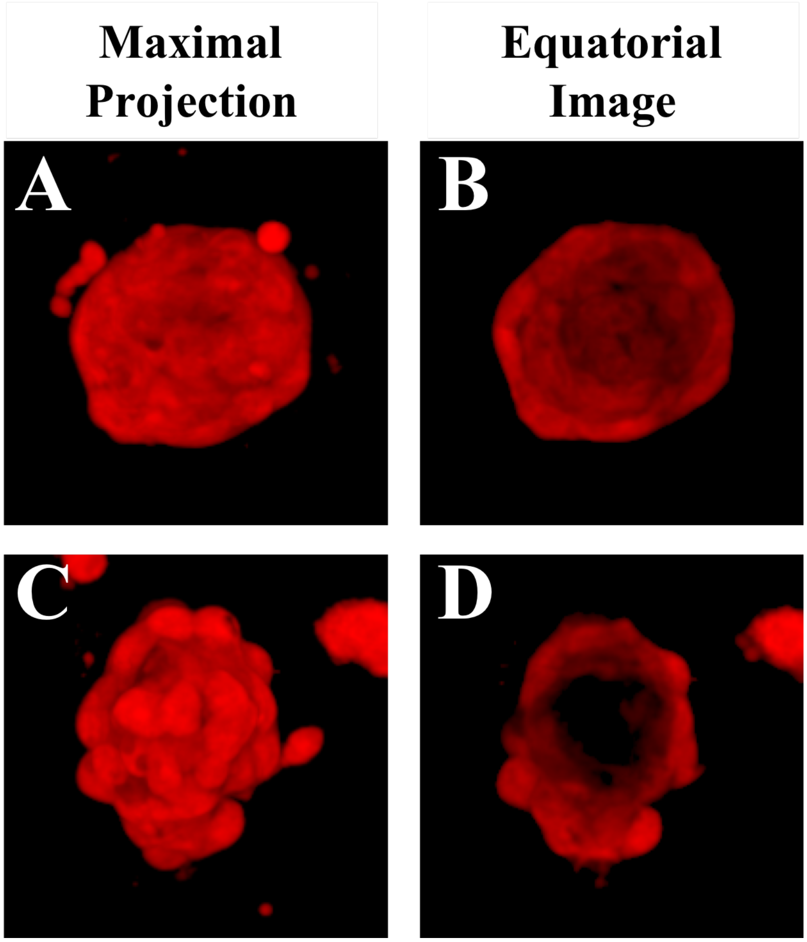

Figure 1-11. Maximal projection images hide changes occurring throughout the 3D radius. Ovarian granulosa cells (KGN) that express the gap junction protein, connexin-43, were seeded into hydrogels to form spheroids. Spheroids were treated with (C,D) or without (A,B) the gap junction inhibitor, carbenoxolone for 5-hours, and labeled with calcein-red-orange-AM for 70-minutes, and confocal z-stacks were acquired. Maximal projection images for spheroids treated with or without CBX reveal no qualitative differences in fluorescence pattern (A,C). However the equatorial confocal image shows differences in fluorescence patterns throughout the 3D radius, with carbenoxolone-treated spheroids possessing less fluorescence reaching the center (D) than the non-treated controls (B).

1.6 SPECIFIC AIMS of this DISSERTATION

Three-dimensional (3D) multicellular spheroids have been utilized for over a hundred years to study a range of biological processes [7,11,100,119-121]. Throughout this time-frame, spheroids have been shown to approximate the cell density found *in vivo*, have increased levels of cell-cell interactions and intercellular communication, as well as maintenance of the differentiated state, and recapitulation of organ-specific processes [21-24]. In response to these biological advantages, there are multiple commercially available technologies that have been developed to easily form and image large number of spheroids [16,20,29,86,89,122]. However, there has not been the same level of effort aimed at developing quantitative strategies and tools to analyze data acquired from 3D spheroids [86,89]. Therefore, through the following aims, we propose to evaluate and optimize the use of spheroids for quantitative-based assays.

1.6.1 Aim 1. Develop accurate quantitative methods to analyze wide-field fluorescent images of 3D spheroids.

The use of fluorescent dyes as a means to assess cell biology has been an integral component for range of biomedical/biological fields. Fluorescent dyes are commercially available, and are easy to use with traditional in vitro models, 2D cell monolayers. However, 2D monolayers fail to recapitulate the complexity of native tissues. Alternatively, 3D spheroids can be utilized to increase physiological relevance, however, their size and complexity yield novel challenges with respect to the use of fluorescent dyes, as well as their quantitation.

1.6.1.1 Approach.

To determine the most accurate method to quantify fluorescence, we formed an array of spheroids, of variable diameters ranging from 80-200-µm, that were labeled with calcein -AM via two different staining methods: (i – pre-label) by staining cells prior to self-assembly to create uniformly labeled spheroids, and (ii – diffusion-label) by diffusing dye into spheroids after self-assembly thus creating a gradient of signal. Time- lapse epi-fluorescence images were acquired and analyzed to measure spheroid fluorescence and radii. By evaluating fluorescence as a function of spheroid radii, we assessed whether the increase in fluorescent signal was better predicted by increase in spheroid volume or surface area.

1.6.1.2 Results.

Accurate normalization of spheroid fluorescence is dependent upon how the spheroid was labeled with dye. For pre-labeled spheroids, fluorescence was best normalized to spheroid volume, whereas for diffusion-labeled spheroids, fluorescence was best normalized to surface area.

1.6.1.3 Impact.

Utilizing the appropriate normalization strategy will reduce significant errors and enhance the sensitivity and robustness of spheroid-based assays. By enhancing this, spheroid-based assays may become more compatible with high-throughput screening, since fewer spheroids would be needed to discern the differences between experimental groups.

1.6.2 Aim 2. Develop quantitative analysis strategies to analyze confocal z-stacks of living 3D spheroids in a high-throughput format.

Creating *in vitro* models to accurately mimic *in vivo* functions of tissues and organs is critical for a wide range of biomedical fields, especially with respect to drug discovery and toxicity testing [89,123,124]. Traditional *in vitro* methods, involving the use of 2D cell monolayers, often fail to predict how the human body would react in response to a stimulus [89,125]. 3D spheroid models have been shown to better approximate the *in vivo* environment and recapitulate organ-specific functions. However, prior to developing biologically-driven 3D spheroid *in vitro* models, numerous challenges must be overcome, such as the ability to accurately obtain and quantify information throughout the 3D radius.

1.6.2.1 Approach.

To form spheroids in a high-throughput format, we developed and validated a micromold to mold agarose hydrogels, and subsequently form spheroids directly in a 96-well plate. To quantify fluorescent signal from 3D spheroids, cells were pre-labeled with fluorescent dyes and formed spheroids of variable size, with diameters ranging from 40-200-µm. Confocal *z*-stacks were acquired and analyzed to evaluate the total and positional fluorescent signal for spheroids of variable sizes.

1.6.2.2 Results.

With the novel micromold, four spheroids of reproducible size were formed in precise (*x,y,z*) locations within each well of 96-well plate. Spheroids larger than 50-µm in diameter experienced some degree of fluorescent loss further into *z*-depth. The total amount of fluorescent loss increased as a function of spheroid radii, with larger spheroid possessing a greater total amount of loss. Furthermore, unlike a planar specimen that will undergo uniform loss across each confocal slice of a *z*-stack, in a spheroid, the loss of fluorescence was far greater in the interior versus its outer edges due to its curvature. Additionally, within spheroids, fluorescent loss throughout the *z*-depth follows an exponential decay curve, and the rate of decay was dependent upon spheroid size.

1.6.2.3 Impact.

The use of spheroids for high-throughput screening affords numerous biological advantages due to their creation of complex microenvironments, which include gradients, barriers, polarity, cell-cell signaling [7]. However, prior to measuring these biological changes in 3D, it is crucial to understand both the pattern of and how to correct for variations in fluorescent signal throughout the z-depth induced by light scatter. This artifact of confocal imaging can be normalized through ratio imaging, thus enabling the development of biologically driven assays in 3D spheroids.

1.6.3 Aim 3. Develop a high-throughput quantitative assay to assess gap junction inhibition in 3D spheroids.

Gap junctions are transmembrane proteins that form channels between cells allowing for the passage of small molecules and ions [109,126,127]. Gap junctions are found in a variety of organ systems throughout the body and play a key role in regulating numerous cellular functions, such as proliferation, differentiation, apoptosis, signal propagation, and electrical coupling [126,128-134]. Traditional *in vitro* methods to assess whether a substance disrupts of gap junction intercellular communication (GJIC), such as scrape loading and microinjection, are low-throughput, require specialized techniques, and require use of 2D cell monolayers [109]. By developing a multicellular spheroidal model to assess GJIC, not only are we able to increase biological relevance through increased cellular interactions, but our technology is amenable to high throughput screening as well.

1.6.3.1 Approach.

GJIC will be assessed in 3D spheroids by monitoring the penetration of a fluorescent dye as it moves inwards. To develop a high-throughput assay to measure GJIC within 3D spheroids, we optimized a variety of parameters, such as spheroid size, calcein dye choice and labeling time, and method of quantification. To evaluate these optimizations, spheroids were treated with or without the gap junction inhibitor, carbenoxolone, and the separation between these positive and negative controls were quantified. To quantify GJIC, the spheroid was divided into a series of concentric rings, and the amount of fluorescence in each area was measured. To account for light scatter effects, spheroids were pre-labeled with CellTracker^{TM} fluorescent dyes, and ratio imaging was performed.

1.6.3.2 Results.

Gap junction intercellular communication and carbenoxolone-induced inhibition could be reliably measured within 3D spheroids. To achieve the greatest separation between spheroids treated with or without carbenoxolone, spheroids should be labeled with calcein-red-orange-AM (as opposed to calcein-AM) for at least 70-minutes prior to acquiring confocal z-stacks. Furthermore, spheroid radius is critical for quantifying GJIC, as both small spheroids (>30-µm radius) and larger spheroids (<50-µm radius) possess minimal quantifiable differences in GJIC when treated with or without carbenoxolone, albeit for different reasons. Finally, we determined an accurate and reliable method to quantify GJIC within spheroids.

1.6.3.3 Impact.

Gap junctions possess key communicatory throughout the body, and disruption of normal function can lead to various pathologies [126,131-134]. Therefore, knowing whether a compound, drug candidate, or environmental toxicant interferes with GJIC is crucial, and the development of this model will provide a high-throughput method to answer that question.

Furthermore, if we remove biological context of GJIC from this aim, we have essentially developed a high-throughput tool to reliably quantify fluorescent changes as a function of 3D radius. This tool can now be applied to answer a range of biological questions with different cell types and different fluorescent dyes.

1.7 REFERENCES

1. Pampaloni F, Reynaud EG, Stelzer EH. The third dimension bridges the gap between cell culture and live tissue. *Nature Reviews. Molecular Cell Biology.* 8(10):839-845, 2007.

2. Lancaster MA, Knoblich JA. Organogenesis in a dish: modeling development and disease using organoid technologies. *Science*. 345(6194):1247125, 2014.

3. Yamada KM, Cukierman E. Modeling tissue morphogenesis and cancer in 3D. *Cell.* 130(4):601-610, 2007.

4. Ong SM, Zhao Z, Arooz T, Zhao D, Zhang S, Du T, Wasser M, van Noort D, Yu H. Engineering a scaffold-free 3-D tumor model for in vitro drug penetration studies. *Biomaterials*. 31(6):1180-1190, 2010.

5. Maltman DJ, Przyborski SA. Developments in three-dimensional cell culture technology aimed at improving accuracy of in vitro analyses. *Biochemical Society Transactions*. 38(4):1072-1075, 2010.

6. Jaroch K, Jaroch A, Bojko B. Cell cultures in drug discovery and development: the need of reliable in vitro-in vivo extrapolation for pharmacodynamics and pharmacokinetics assessment. Journcal of Pharmaceutical and Biomedical Analysis. 147:297-312, 2018.

7. Knight E, Przyborski S. Advances in 3D cell culture technologies enabling tissue-like structures to be created in vitro. *Journal of Anatomy*. 227(6):746-756, 2015.

8. Terashima J, Goto S, Hattori H, Hoshi S, Ushirokawa M, Kudo K, Habano W, Ozawa S. CYP1A1 and CYP1A2 expression levels are differentially regulated in three-dimensional spheroids of liver cancer cells compared to two-dimensional monolayer cultures. *Drug Metabolism and Pharmacokinetics*. 30(6):434-440, 2015.

9. Luckert C, Schulz C, Lehmann N, Thomas M, Hoffmann U, Hammad S, Hengstier JG, Braeuning A, Lampen A, Hessel S. Comparative analysis of 3D culture methods on human HepG2 cells. *Archives of toxicology*. 91(1):393-406, 2017.

10. Buzhor E, Harari-Steinberg O, Omer D, Metsuyamin S, Jacob-Hirsch J, Noiman T, Dotan Z, Goldstein RS, Dekel B. Kidney spheroids recapitulate tubular organoids leading to tubulogenic potency of human kidney-derived cells. *Tissue Engineering Part A*. 17(17-18):2305-2319, 2011.

11. Pampaloni F, Reynaud EG, Stelzer EH. The third dimension bridges the gap between cell culture and live tissue. *Nature Reviews. Molecular Cell Biology.* 8(10):839-845, 2007.

12. Achilli TM, Meyer J, Morgan JR. Advances in the formation, use and understanding of multicellular spheroids. *Expert Opinions Biological Therapy*. 12(10):1347-1360, 2012.

13. Shoval H, Karsch-Bluman A, Brill-Karniely Y, Stern T, Zamir G, Hubert A, Benny O. Tumor cells and their cross-talk with endothelial cells in 3D spheroids. *Scientific Reports* 7:10428, 2017.

14. Cui X. Hartanto Y, Zhang H. Advances in multicellular spheroids formation. *Journal of the Royal Society Interface.* 14(127), 2017.

15. Horman SR, To J, Orth AP, Slawny N, Cuddihy MJ, Caracino D. High content analysis of three-dimensional tumor spheroids: investigating signaling pathways using small hairpin RNA. *Nature Methods*. 2013.

16. Tung YC, Hsiao AY, Allen SG, Torisawa YS, Ho M, Takayama S. High-throughput 3D spheroid culture and drug testing using a 384 hanging drop array. *The Analyst.* 136(3):473-478, 2011.

17. Napolitano AP, Dean DM, Man AJ, Youssef J, Ho CH, Rago AP, Lech MP, Morgan JR. Scaffold-free three-dimensional cell culture utilizing micromolded nonadhesive hydrogels. *Biotechniques.* 43(4):496-500, 2007.

18. Leary E, Curran S, Susienka M, Manning KL, Blakely AM, Morgan JR. Micro-moulded non-adhesive agarose hydrogels to form multicellular microtissues – The 3D Petri Dish®. In Technology Platforms for 3D Cell Culture, S. Przyborski (Ed). 2017.

19. Fennema E, Rivron N, Rouwkema J, van Blitterswijk C, de Boer J. Spheroid culture as a tool for creating 3D complex tissues. *Trends in Biotechnology*. 31(2):108-115, 2013.

20. Vinci M, Gowan S, Boxall F, Patterson L, Zimmermann M, Court W, Lomas C, Mendiola M, Hardisson D, Eccles SA. Advances in establishment and analysis of three-dimensional tumor spheroid-based functional assays for target validation and drug evaluation. *BMC Biology.* 10(29):10.1186/1741-7007-10-29, 2012.

21. Vantangoli MM, Madnick SJ, Huse SM, Weston P, Boekelheide K. MCF-7 Human Breast Cancer Cells Form Differentiated Microtissues in Scaffold-Free Hydrogels. *PLoS One*. 10(8):e0135426, 2015.

22. Sun T, Jackson S, Haycock JW, MacNeil S. Culture of skin cells in 3D rather than 2D improves their ability to survive exposure to cytotoxic agents. *Journal of Biotechnology*. 122(3):372-381, 2006.

23. Pickl M, Ries CH. Comparison of 3D and 2D tumor models reveals enhanced HER2 activation in 3D associated with an increased response to trastuzumab. *Oncogene*. 28(3):461-468, 2009.

24. Chang TT, Hughes-Fulford M. Monolayer and spheroid culture of human liver hepatocellular carcinoma cell line cells demonstrate distinct global gene expression patterns and functional phenotypes. *Tissue Engineering Part A.* 15(3):559-567, 2009.

25. Griffith LG, Swartz MA. Capturing complex 3D tissue physiology in vitro. *Nature Reviews Molecular Cell Biology*. 7(3):211-224, 2006.

26. Atala A, Kasper FK, Mikos AG. Engineering complex tissues. *Science Translational Medicine.* 4(160):160rv12, 2012.

27. Chen Y. Gao D, Liu H, Lin S, Jiang Y. Drug cytotoxicity and signaling pathway analysis with three-dimensional tumor spheroids in a microwell-based microfluidic chip for drug screening. *Analytica Chimica Acta*. 898:85-92, 2015.

28. Riffle S, Pandey RN, Albert M, Hedge RS. Linking hypoxia, DNA damage and proliferation in multicellular tumor spheroids. *BMC Cancer*. 17(1):338, 2017.

29. Kessel S, Cribbes S, Bonasu S, Qiu J, Chan LL. Real-time apoptosis and viability high-throughput screening of 3D multicellular tumor spheroids using the celligo image cytometer. *SLAS Discovery*. 23(2):202-210, 2018.

30. Chien PT, Lin CC, Hsiao LD, Yang CM. Induction of HO-1 by carbon monoxide releasing molecule-2 attenuates thrombin-induced COX-2 expression and hypertrophy in primary human cardiomyocytes. *Toxicology and applied pharmacology*. 289(2):349-359, 2015.

31. Malfa GA, Tomasello B, Sinatra F, Villaggio G, Amenta F, Avola R, Renis M. "Reactive" response evaluation of primary human astrocytes after methylmercury exposure. *Journal of neuroscience research*. 92(1):95-103, 2014.

32. Sharpe CC, Dockrell ME. Primary culture of human renal proximal tubule epithelial cells and interstitial fibroblasts. *Methods in molecular biology*. 806:175-185, 2012.

33. Zachos NC, Kovbasnjuk O, Foulke-Abel J, In J, Blutt SE, de Jonge HR, Estes MK, Donowitz M. Human Enteroids/Colonoids and Intestinal Organoids Functionally Recapitulate Normal Intestinal Physiology and Pathophysiology. *Journal of biological chemistry*. 291(8):3759-66, 2015.

34. Owens J, Moreira K, Bain G. Characterization of primary human skeletal muscle cells from multiple commercial sources. *In vitro cellular and developmental biology*. 49(4):695-705, 2013.

35. Hernandez CP, Morrow K, Velasco C, Wyczechowska DD, Naura AS, Rodriguez PC. Effects of cigarette smoke extract on primary activated T cells. *Cellular immunology*. 282(1):38-43, 2013.

36. Buhrke T, Krüger E, Pevny S, Rößler M, Bitter K, Lampen A. Perfluorooctanoic acid (PFOA) affects distinct molecular signalling pathways in human primary hepatocytes. *Toxicology*. 333:53-62.

37. Feng W, Guo J, Huang H, Xia B, Liu H, Li J, Lin S, Li T, Liu J, Li H. Human normal bronchial epithelial cells: a novel in vitro cell model for toxicity evaluation. *PLOS One*. 10(4):e0123520, 2015.

38. Sullivan MN, Francis M, Pitts NL, Taylor MS, Earley S. Optical recording reveals novel properties of GSK1016790A-induced vanilloid transient receptor potential channel TRPV4 activity in primary human endothelial cells. *Molecular Pharmacology*. 82(3):464-472, 2012.

39. García-Gareta E, Ravindran N, Dye JF. Apoptotic primary normal human dermal fibroblasts for in vitro models of fibrosis. *Analytical Biochemistry*. 470:22-24, 2014.

40. Rasmussen C, Thomas-Virnig C, Allen-Hoffmann BL. Classical human epidermal keratinocyte cell culture. *Methods of Molecular Biology*. 945:161-175, 2013.

41. Ždychová J, Čejková S, Králová Lesná I, Králová A, Malušková J, Janoušek L, Kazdová L. Co-cultivation of human aortic smooth muscle cells with epicardial adipocytes affects their proliferation rate. *Physiological Research*. 63:S419-427, 2014.

42. Boutin ME, Kramer LL, Livi LL, Brown T, Moore C, Hoffman-Kim D. A three-dimensional neural spheroid model for capillary-like network formation. *Journal of Neuroscience Methods*. 299:55-63, 2018.

43. Belostotskaya GB, Golovanova TA. Characterization of contracting cardiomyocyte colonies in the primary culture of neonatal rat myocardial cells: a model of in vitro cardiomyogenesis. *Cell Cycle*. 13(6):910-918, 2014.

44. Zhang J, Ren L, Yang X, White M, Greenhaw J, Harris T, Wu Q, Bryant M, Papoian T, Mattes W, Shi Q. Cytotoxicity of 34 FDA approved small-molecule kinase inhibitors in primary rat and human hepatocytes. *Toxicological letters*. 291:1138-148, 2018.

45. Kasimsetty SG, DeWolf SE, Shigeoka AA, McKay DB. Regulation of TLR2 and NLRP3 in primary murine renal tubular epithelial cells. *Nephron Clinical Practice*. 127(1-4):119-23, 2014.

46. Gaskill C, Majka SM. A high-yield isolation and enrichment strategy for human lung microvascular endothelial cells. *Pulmonary Circulation*. 7(1):108-116, 2017.

47. Katz G, Snow AL. Fluorescence-activated cell sorting-based quantitation of T cell receptor restimulation-induced cell death in activated, primary human T cells. *Methods in molecular biology*. 979:15-23, 2013.

48. Weiskirchen S, Tag CG, Sauer-Lehnen S, Tacke F, Weiskirchen R. Isolation and Culture of Primary Murine Hepatic Stellate Cells. *Methods in Molecular Biology*. 1627:165-191, 2017.

49. Hall SR, Jiang Y, Leary E, Yavanian G, Eminli S, O'Neill DW, Marasco WA. Identification and isolation of small CD44-negative mesenchymal stem/progenitor cells from human bone marrow using elutriation and polychromatic flow cytometry. *Stem Cells Translational medicine*. 2(8):567-578, 2013.

50. Moeller TA, Shukla SJ, Xia M. Assessment of Compound Hepatotoxicity Using Human Plateable Cryopreserved Hepatocytes in a 1536-Well-Plate Format. *Assay Drug Development and Technology*. 10(1):78-87, 2012.

51. Li AP. Evaluation of drug metabolism, drug-drug interactions, and in vitro hepatotoxicity with cryopreserved human hepatocytes. *Methods of Molecular Biology*. 640:281-294, 2010.

52. Nguyen N, Nguyen W, Nguyenton B, Ratchada P, Page G, Miller PE, Ghetti A, Abi-Gerges N. Adult Human Primary Cardiomyocyte-Based Model for the Simultaneous Prediction of Drug-Induced Inotropic and Pro-arrhythmia Risk. *Frontiers in physiology*. 8:e01073, 2017.

53. Cree IA, Andreotti PE. Measurement of cytotoxicity by ATP-based luminescence assay in primary cell cultures and cell lines. *Toxicology in vitro*. 11(5):553-556, 1997.

54. Takahashi K, Yamanaka S.Induction of pluripotent stem cells from mouse embryonic and adult fibroblast cultures by defined factors. *Cell*. 126(4):663-676, 2006.

55. Thomson JA, Itskovitz-Eldor J, Shapiro SS, Waknitz MA, Swiergiel JJ, Marshall VS, Jones JM. Embryonic stem cell lines derived from human blastocysts. *Science*. 282(5391):1145-1147, 1998.

56. Zhang J, Wilson GF, Soerens AG, Koonce CH, Yu J, Palecek SP, Thomson JA, Kamp TJ. Functional cardiomyocytes derived from human induced pluripotent stem cells. *Circulation Research.* 104(4):e30-41, 2009.

57. Song Z, Cai J, Liu Y, Zhao D, Yong J, Duo S, Song X, Guo Y, Zhao Y, Qin H, Yin X, Wu C, Che J, Lu S, Ding M, Deng H. Efficient generation of hepatocyte-like cells from human induced pluripotent stem cells. *Cellular Research*. 19(11):1233-1242, 2009.

58. Karumbayaram S, Novitch BG, Patterson M, Umbach JA, Richter L, Lindgren A, Conway AE, Clark AT, Goldman SA, Plath K, Wiedau-Pazos M, Kornblum HI, Lowry WE. Directed differentiation of human-induced pluripotent stem cells generates active motor neurons. *Stem Cells*. 27(4):806-11, 2009.

59. Park IH, Zhao R, West JA, Yabuuchi A, Huo H, Ince TA, Lerou PH, Lensch MW, Daley GQ. Reprogramming of human somatic cells to pluripotency with defined factors. *Nature*. 451(7175):141-146, 2008

60. Brown ME, Rondon E, Rajesh D, Mack A, Lewis R, Feng X, Zitur LJ, Learish RD, Nuwaysir EF. Derivation of induced pluripotent stem cells from human peripheral blood T lymphocytes. *PLoS One*. 5(6):e11373, 2010.

61. Revilla A, González C, Iriondo A, Fernández B, Prieto C, Marín C, Liste I. Current advances in the generation of human iPS cells: implications in cell-based regenerative medicine. *Journal of tissue engineering and regenerative medicine*. 10(11):893-907, 2016

62. Sterneckert JL, Reinhardt P, Schöler HR. Investigating human disease using stem cell models. *Nature Review Genetics*. 15(9):625-639, 2014.

63. Kim C. iPSC technology--Powerful hand for disease modeling and therapeutic screen. *BMB Reports*. 48(5):256-265, 2015.

64. Meneghello G, Verheyen A, Van Ingen M, Kuijlaars J, Tuefferd M, Van Den Wyngaert I, Nuydens R. Evaluation of established human iPSC-derived neurons to model neurodegenerative diseases. *Neuroscience*. 2015.

65. Zhang N, Bailus BJ, Ring KL, Ellerby LM. iPSC-based drug screening for Huntington's disease. *Brain Research*. 1638:42-56, 2016.

66. Zhang S, Lv Z, Zhang S, Liu L, Li Q, Gong W, Sha H, Wu H. Characterization of human induced pluripotent stem cell (iPSC) line from a 72year old male patient with later onset Alzheimer's disease. *Stem Cell Research*. 19:34-36, 2017.

67. Goversen B, van der Heyden MAG, van Veen TAB, de Boer TP. The immature electrophysiological phenotype of iPSC-CMs still hampers in vitro drug screening: Special focus on IK1. *Pharmacology and therapeutics*. 183:127-136, 2017.

68. Zhu R, Blazeski A, Poon E, Costa KD, Tung L, Bohele KR. Physical developmental cues for the maturation of human pluripotent stem cell-derived cardiomyocytes. *Stem Cell Research and Therapy*. 5:117, 2014.

69. Yu Y, Liu H, Ikeda Y, Amiot BP, Rinaldo P, Duncan SA, Nyberg SL. Hepatocyte-like cells differentiated from human induced pluripotent stem cells: relevance to cellular therapies. *Stem Cells Research.* 9(3):196-207, 2012.

70. Ivashchenko CY, Pipes GC, Lozinskaya IM, Lin Z, Xiaoping X, Needle S, Grygielko ET, Hu E, Toomey JR, Lepore JJ, Willette RN. Human-induced pluripotent stem cell-derived cardiomyocytes exhibit temporal changes in phenotype. *American Journal of Heart and Circulatory Physiology*. 305(6):H913-922, 2013.

71. Nishi Y, Yanase T, Mu Y, Oba K, Ichino I, Saito M, Nomura M, Mukasa C, Okabe T, Goto K, Takayanagi R, Kashimura Y, Haji M, Nawata H. Establishment and characterization of a steroidogenic human granulosa-like tumor cell line, KGN, that expresses functional follicle-stimulating hormone receptor. *Endocrinology*. 142(1):437-445, 2001.

72. Scherer WF, Syverton JT, Gey GO. Studies on the propagation in vitro of poliomyelitis viruses. IV. Viral multiplication in a stable strain of human malignant epithelial cells (strain HeLa) derived from an epidermoid carcinoma of the cervix. *Journal of experimental medicine*. 97(5):685-710, 1953.

73. Brooks SC, Locke ER, Soule HD. Estrogen receptor in a human cell line (MCF-7) from breast carcinoma. *Journal of biological chemistry*. 248(17):6251-6253, 1973.

74. Dearfield KL, Jacobson-Kram D, Brown NA, Williams JR. Evaluation of a human hepatoma cell line as a target cell in genetic toxicology. *Mutation research*. 108(1-3):437-449, 1983.

75. Berthon P, Cussenot O, Hopwood L, Leduc A, Maitland N. Functional expression of sv40 in normal human prostatic epithelial and fibroblastic cells - differentiation pattern of nontumorigenic cell-lines. *International Journal of Oncology*. 6(2):333-343, 1995.

76. Powell J, Wang X, Allard BL, Sahin M, Wang XL, Hay ID, Hiddinga HJ, Deshpande SS, Kroll TG, Grebe SK, Eberhardt NL, McIver B. The PAX8/PPARgamma fusion oncoprotein transforms immortalized human thyrocytes through a mechanism probably involving wild-type PPAR gamma inhibition. *Oncogene*. 23(20):3634-3641, 2004.

77. Aiello L, Guilfoyle R, Huebner K, Weinmann R. Adenovirus 5 DNA sequences present and RNA sequences transcribed in transformed human embryo kidney cells (HEK-Ad-5 or 293). *Virology*. 94(2):460-469, 1979.

78. Gurvinder Kaur and Jannette M. Dufour cell lines: valuable tools or useless artifacts. *Spermatogenesis*. 2(1):1-5, 2012.

79. Woods DC, Alvarez C, Johnson AL. Cisplatin-mediated sensitivity to TRAIL-induced cell death in human granulosa tumor cells. *Gynecologic oncology*. 108(3):632-640, 2008.

80. Tsutsumi R, Hiroi H, Momoeda M, Hosokawa Y, Nakazawa F, Koizumi M, Yano T, Tsutsumi O, Taketani Y. Inhibitory effects of cholesterol sulfate on progesterone production in human granulosa-like tumor cell line, KGN. *Journal of Endocrinolgy*. 55(3):575-581, 2008.

81. Ohno S, Yukinawa F, Noda M, Nakajin S. Mono-(2-ethylhexyl) phthalate induces NR4A subfamily and GIOT-1 gene expression, and suppresses CYP19 expression in human granulosa-like tumor cell line KGN. *Toxicolgical Letters*. 191(2-3):353-359, 2009.

82. Lu DF, Yang LJ, Wang F, Zhang GL. Inhibitory effect of luteolin on estrogen biosynthesis in human ovarian granulosa cells by suppression of aromatase (CYP19). *Journal of Agricultural and food chemistry*. 60(34):8411-8418, 2012.

83. Holgate JH, Webb J. Microscopy:Light Microscopy and histochemical methods. *Encyclopedia of Food Sciences and Nutrition*. 3917-3922, 2003.

84. Kabadi PK, Vantangoli MM, Rodd AL, Leary E, Madnick SJ, Morgan JF, Kane A, Boekelheide K. Into the depths: Techniques for in vitro three-dimensional microtissue visualization. *Biotechniques*. 59: 279-286, 2015.

85. Swedlow JR. Quantitative fluorescence microscopy and image deconvolution. *Methods in Cell Biology*. 114:407-426, 2013.

86. Martines NJ, Titus SA, Wagner AK, Simeonov A. High throughput fluorescence imaging approaches for drug discovery using in vitro and in vivo three-dimensional models. *Expert Opinion Drug Discovery*. 10(12):1347-1361, 2015.

87. Shotton DM. Confocal scanning optical microscopy and its applications for biological specimens. *Journal of Cell Science*. 94:175-206, 1989.

88. Oreopoulos J, Berman R, Browne M. Spinning-disk confocal microscopy: present technology and future trends. *Methods in Cell Biology*. 123:153-175, 2014.

89. Li L, Zhou Q, Voss TC, Quick KL, LaBarbera DV. High-throughput imaging: Focusing in on drug discovery in 3D. *Methods*. 96:97-102, 2016.

90. Boutin ME, Hoffman-Kim D. Application and assessment of optical clearing methods for imaging of tissue-engineered neural stem cell spheres. *Tissue Engineering Part C Methods.* 21(3):292-302, 2015.

91. Hama H, Kurokawa H, Kawano H, Ando R, Shimoguri T, Noda H, Fukami K, Sakaue-Sawano A, Miyawaki A. Scale: a chemical approach for fluorescence imaging and reconstruction of transparent mouse brain. *Nature Neuroscience*. 14:1481-1488, 2011.

92. Kuwajima T, Sitko AA, Bhansail P, Jurgens C, Guido W, Mason C. ClearT: a detergent- and solvent-free clearing method for neuronal and nonneuroanal tissue. *Development*. 140(6):1364-1368, 2013.

93. Ke MT, Fujimoto S, Imai T. SeeDB: a simple and morphology-preseriving optical clearing agent for neruonsal circuit reconstruction. *Nature Neuroscience.* 16(8):1154-1161, 2013.

94. Ustione A, Piston DM. A simple introduction to multiphoton microscopy. *Journal of Microscopy*. 243(3):221-226, 2011.

95. Pampaloni F, Ansari N, Stelzer EHK. High-resolution deep imaging of live cellular spheroids with light-sheet-based fluorescence microscopy. *Cell and Tissue Research*. 352(1):161-177, 2013.

96. Reynaud EG,Krzic U, Greger K, Stelzer EHK. Light sheet-based flourescence micrscopy: more dimensions, more photons, and less photodamage. *HFSP Journal*. 2(5):266-275, 2008.

97. Smyrek I, Stelzer EHK. Quantitative three-dimensional evaluation of immunofluorescence staining for large whole mount spheroids with light sheet microscopy. Biomedical Optics Express. 8(2):484-499, 2017.

98. Schmitz A, Fischer SC, Mattheyer C, Pampaloni F, Stelzer EH. Multiscale image analysis reveals structural heterogeneity of the cell microenvironment in homotypic spheroids. *Scientific Reports*. 7:43693, 2017.

99. Lancaster MA, Knoblich JA. Organogenesis in a dish: modeling development and disease using organoid technologies. *Science*. 345(6194):1247125, 2014.

100. Yamada KM, Cukierman E. Modeling tissue morphogenesis and cancer in 3D. *Cell.* 130(4):601-610, 2007.

101. Mehta G, Hsiao AY, Ingram M, Luker GD, Takayama S. Oppurtunities and challenges for use of tumor spheroids as models to test drug delivery and efficacy. *Journal of Controlled Release*. 164(2):192-204, 2012.

102. Probst CE, Zrazhevskiy P, Bagalkot V, Gao X. Quantum dots as a platform for nanoparticle drug delivert vehicle deisgn. *Advanced Drug Delivery Reviews*. 65(5):703-718, 2013.

103. Lei H, Hofferberth SC, Liu R, Colby A, Tevis KM, Catalano P, Grinstaff MW, Colson YL. *Journal of Thoracic Cardiovascular Surgery*. 149(5):1417-1424, 2015.

104. Tng DJ, Sing P, Lin G, Soehartono AM, Yang G, Yang C, Yin F, Tan CH, Yong KT. Synthesis and characterization of multifunctional hybrid-polymeric nanoparticles for drug delivery and multimodal imaging of cancer. *International journal of nanomedicine*. 10:5771-5786, 2015.

105. Baek N, Seo OW, Kim M, Hulme J, An SS. Monitoring the effects of doxorubicin on 3D-spheroid tumor cells in real time. *OncoTargets and Therapy*. 9:7207-7218, 2016.

106. berghien F, Loor F. Ranking of P-glycoprotein substrates and inhibitors by a calcein-AM fluorometry screening assay. *Anticancer Drugs*. 7(5):568-78, 1996.

107. Achilli TM, McCalla S, Meyer J, Tripathi A, Morgan JR. Multilayer spheroids to quantify drug uptake and diffusion in 3D. *Molecular pharmacolgy.* 11(7):2071-2081, 2014.

108. Curran S, Vantangoli MM, Boekelheide K, Morgan JR. Architecture of chimeric spheroids controls drug transport. *Cancer Microenvironment*. 8(2):101-109, 2015.

109. Abbaci M, Barberi-Heyob M, Blondel W, Guillemin F, Didelon J. Advantages and limitations of commonly used methods to assay the molecular permeability of gap junctional intercellular communication. *Biotechniques*. 45(1):63-68, 2008.

110. Hornung A, Poettler M, Friedrich RP, Weigel B, Duerr S, Zaloga J, Cicha I, Alexiou C, Janko C. Toxicity of mitoxantron-loaded superparamagnetic iron oxide nanoparticles in a HT-29 tumor spheroid model. *Anticancer Research*. 36(6):3093-3101, 2016.

111. Senyavina NV, Gerasimenko TN, Pulkova NV, Maltseva DV. Transport and toxicity of silver nanoparticles in HepaRG cell spheroids. *Bulletin of Experimental Biology and Medicine*. 160(6):831-834, 2016.

112. Blacher S, Erpicum C, Lenoir B, Paupert J, Moraes G, Ormenese S, Bullinger E, Noel A. Cell invasion in the spheroid sprouting assay: a spatial organization analysis adaptable to cell behavior. *PLoS One*. 9(5):e97019, 2014.

113. Carey SP, Starchenko A, McGregor A, Reinhart-King CA. Leading malignant cells initiate collective epithelial cell invasion in a three-dimensional heterotypic tumor spheroid model. *Clinical and Experimental Metastasis*. 30(5):615-630.

114. Achilli TM, McCalla S, Tripathi A, Morgan JR. Quantification of the kinetics and extent of self-sorting in three-dimensional spheroids. *Tissue Engineering Part C*. 18(4):302-309, 2012.

115. Pinaud F, Michalet X, Bentolila LA, Tsay JM, Doose S, Li JJ, Iyer G, Weiss S. Advances in fluorescence imaging with quantum dot bio-probes. *Biomaterials*. 27(9):1679-87, 2006.

116. Amsterdam A, Lin S, Hopkins N. The Aequorea victoria green fluorescent protein can be used as a reporter in live zebrafish embryos. *Developmental Biology*. 171(1):123-129, 1995.

117. Yamamoto N, Jiang P, Yang M, Xu M, Yamauchi K, Tsuchiya H, Tomita K, Wahl GM, Moossa AR, Hoffman RM. Cellular dynamics visualized in live cells in vitro and in vio by differential dual-color nuclear-cytoplasmic fluorescent-protein expression. *Cancer Research*. 64(12):4251-4256, 2004.

118. Zhang J, Campbell RE, Ting AY, Tsien RY. Creating new fluorescent probes for cell biology. *Nature Reviews Molecular Cell Biology*. 3(12):906-918, 2002.

119. Wilson HV. A new method by which sponges may be artificially reared. *Science*. 25:912-915, 1907.

120. Lancaster MA, Knoblich JA. Organogenesis in a dish: modeling development and disease using organoid technologies. *Science*. 345(6194):1247125, 2014.

121. Ong SM, Zhao Z, Arooz T, Zhao D, Zhang S, Du T, Wasser M, van Noort D, Yu H. Engineering a scaffold-free 3-D tumor model for in vitro drug penetration studies. *Biomaterials*. 31(6):1180-1190, 2010.

122. Mosaad EO, Chanmbers KF, Futrega K, Clements JA, Doran MR. The Microwell-mesh: A high-throughput 3D prostrate caner spheroid and drug-testing platform. *Scientific Reports*. 8(1):253, 2018.

123. Krewski D, Acosta, Jr. D, Andersen M, Anderson H, Bailar JC 3rd, Boekelheide K, Brent R, Charnley G, Cheung VG, Green S Jr, Kelsey KT, Kerkvliet NI, Li AA, McCray L, Meyer O, Patterson RD, Pennie W, Scala RA, Solomon GM, Stephens M, Yajer J, Zeise L. Toxicity testing in the 21st century: a vision and a strategy. *Journal of Toxicology and Environmental Health, Part B, Critical Reviews*. 13:51-138, 2010.

124. Elliott NT, Yuan F. A review of three-dimensional in vitro tissue models for drug discovery and transport studies. *Journal of Pharmaceutical Sciences*. 100(1):59-74, 2011

125. Bhadriraju K, Chen CS: Engineering cellular microenvironments to improve cell-based drug testing. Drug Discovery Today. 7:612–620, 2002.

126. Loewenstein WR. Junctional intercellular communication: the cell-to-cell membrane channel. *Physiological Reviews*. 61:829-913, 1981.

127. Alexander DB, Goldberg GS. Transfer of biologically important molecules between cells through gap junction channels. *Current Medicinal Chemistry*. 10:2045-2058, 2003.

128. Brink PR, Cronin K, Ramanan SV. Gap junctions in excitable cells. *Journal of Bioenergetics and Biomembranes*. 28:351-358, 1996.

129. Webb RJ, Marshall F, Swann K, Carroll J. Follicle-stimulating hormone induces a gap junction-dependent dynamic change in [cAMP] and protein kinase a in mammalian oocytes. *Developmental biology*. 246(2):441-454, 2002.

130. Kalimi GH, Lo CW. Gap junctional communication in the extraembryonic tissues of the gastrulating mouse embryo. *The Journal of Cell Biology*. 109:3015-3026, 1996.

131. Dere E, Zlomuzica A. The role of gap junctions in the brain in health and disease. *Neuroscience and Behavioral Reviews*. 36(1):206-217, 2012.

132. Dermietzal R, Spray DC. Gap junctions in the brain: where, what type, how many and why? *Trends in neuroscience*. 16(5):186-192, 1993.

133. Davis LM, Rodefeld ME, Green K, Beyer EC, Saffitz JE. Gap junction protein phenotypes of the human heart and conduction system. *Journal of Cardiovascular Electrophysiology*. 6(10):813-822, 1996.

134. Poelzing S, Rosenbaum DS. Altered connexin43 expression produces arrhythmia substrate in heart failure. *Journal of Physiology Heart*. 287(4)1762-1770, 2004.

CHAPTER 2

Accurate Quantitative Wide Field Fluorescent Microscopy of 3D Spheroids.

Elizabeth Leary [1, 2], Claire Rhee, Benjamin Wilks[1,2], Jeffrey R. Morgan [1, 2]

Biotechniques. 2016. 61(5):237-247. DOI: 10.2144/000114472

Author Affiliation:
[1] Department of Molecular Pharmacology, Physiology and Biotechnology
[2] Center for Biomedical Engineering
Brown University
175 Meeting Street
Providence, Rhode Island, USA 02912

2.1 ABSTRACT

Hundreds of commercially available fluorescent dyes are used to quantify a wide range of biological functions of cells in culture and their use has been a mainstay of basic research, toxicity testing and drug discovery. However, nearly all of these dyes have been optimized for use on cells cultured as two-dimensional monolayers. Three-dimensional culture systems more accurately recapitulate native tissues, but their size and complexity present a new set of challenges to the use of fluorescent dyes especially with regards to accurate quantitation. Using spheroids labeled with calcein-AM via two different staining methods, we performed time-lapse fluorescent microscopy. We determined the accurate method to quantify fluorescence as a function of whether spheroids were uniformly labeled with dye prior to spheroid formation or if the dye was diffused into the spheroid after its formation. For uniformly labeled spheroids, fluorescence was best normalized to volume, whereas for spheroids labeled via dye diffusion, fluorescence was best normalized to surface area. This framework for evaluating dyes can easily be applied to others. Utilizing the appropriate size-based normalization strategy enhanced the ability to detect statistically significant differences between experimental conditions.

KEYWORDS: spheroids, quantitative image analysis, live cell imaging, epi-fluorescence, calcein-AM

2.2 INTRODUCTION

Three-dimensional (3D) multi-cellular spheroids are increasingly being used for research, toxicity testing and drug discovery [1-3]. In general, spheroids more closely mimic the natural biological functions and complexities of native tissues and organs than cells cultured in 2D, a property important for phenotypic drug discovery [4-8]. Moreover, spheroids and other 3D technologies are helping to reduce the use of animals in research. For example, some researchers are looking to reduce the use of animals by developing cancer-based spheroid models to assist in the drug screening process [9,10]. One commonly used means of assessing these biological functions is the use of fluorescent reporter molecules coupled with quantitative fluorescent microscopy. Fluorescent reporters come in a large range of sizes and can report on a wide scope of diverse biological functions. For example, small fluorescent molecules such as calcein-AM are used to assess cell viability, while genetically engineered fluorescent fusion proteins are used to quantify the levels of selected gene expression. Moreover, fluorescent reporters are deployed via diffusion into a biological system (e.g., calcein-AM) or are embedded in and intrinsic to the biological system (e.g., fluorescent fusion protein) [11-13]. However, nearly all of these fluorescent reporters have been tested in and optimized for use in 2D monolayer cell culture. Unlike thin monolayers of cells where the *z* dimension is in the 5μm range, tissue engineered 3D constructs can have a *z* dimension of 100μm and greater [14]. This increased thickness presents unique challenges to the quantitative use of fluorescent reporters related to the penetration of light and fluorescent molecules into the tissue as well as depth of reliable imaging [15-18].

To investigate these issues, we formed an array of 3D multi-cellular spheroids on transparent nonadhesive agarose micro-molds that could be easily imaged using wide field fluorescent microscopy [19]. We tested the commonly used viability dye, calcein-AM, as a case study to evaluate how to quantify fluorescence from 3D spheroids. We added calcein-AM via two different methods: (1) by staining cells prior to self-assembly to create uniformly labeled spheroids, and (2) by diffusing into spheroids after self-assembly. To determine the accurate means of quantifying fluorescence for each scenario, we acquired time-lapse epi-fluorescence images of spheroids of variable sizes, ranging from 80-200μm in diameter. We have previously shown that the wide-field epi-fluorescent signal of a range of spheroid sizes is linear only up to diameters of about 205μm [20]. If a spheroid was uniformly stained with calcein-AM, the fluorescent signal was more accurately normalized to the volume of the spheroid regardless of size, whereas if calcein-AM was diffused into the spheroid, the fluorescent signal was more accurately normalized to surface area of the spheroid. We further validated these findings by testing a total of three cell types (KGN, MCF-7, NHF) and five fluorescent dyes (calcein-AM, calcein-red-orange-AM, Hoechst 33342, CellTracker^{TM} Red CMPTX, CellTracker^{TM} Green CMFDA). Overall, quantitative fluorescence of spheroids requires optimization and close attention to the means of staining, the range of spheroid sizes and the time of spheroid staining. Utilizing the appropriate normalization strategy will reduce significant error and can enhance the sensitivity and robustness of spheroid-based assays. By improving sensitivity and robustness, spheroid-based assays may become more applicable to high-throughput screening, since fewer spheroids are needed to discern differences between experimental groups. Furthermore, this method can be applied to numerous other fluorescent dyes to measure a variety of biological functions, thus making our approach applicable to a broad range of fields in basic research, as well as toxicity testing and drug discovery.

2.3 MATERIALS and METHODS

2.3.1 Micro-molded hydrogels, cell culture and spheroid formation

To create agarose hydrogels, 3D PetriDish® micro-molds (Microtissues, Inc, Providence, RI, USA), consisting of a series of 96 rounded cylindrical pegs atop a rectangular platform, were used. Sterile molten UltraPure Agarose (Fisher Scientific, Waltham, MA, USA) (2% weight/volume in water) was pipetted into the micro-mold, allowed to solidify, and released from the micro-mold directly into a 24-well plate. The resulting hydrogel contained a rectangular loading dock on top of a series of 96 round-bottom recesses. Hydrogels were equilibrated with serum-free DMEM supplemented only with 1% penicillin/streptomycin, degassed to remove air bubbles from recesses, and incubated overnight at 37°C with 10% CO_2.

All cell types, including human ovarian granulosa (KGN) cells, breast cancer (MCF-7) cells, and normal human fibroblast (NHF) cells, were grown in DMEM with 10% fetal bovine serum (FBS) (Fisher Scientific, Waltham, MA, USA) and 1% penicillin/streptomycin at 37°C with 10% CO_2. Cells were trypsinized using 0.05% trypsin, concentrated by centrifugation at 800 rpm for 6-minutes, and counted. Cells were washed once with serum-free DMEM and spun down at 800 rpm for 6-minutes. Cells were re-suspended in serum-free DMEM at one of the following concentrations: 1.33

$\times 10^6$ cells/mL, 2.67 x 10^6 cells/mL, or 4.00 x 10^6 cells/mL. 75μL of each cell suspension was pipetted into the loading dock of each hydrogel to form spheroids of approximately 1,000-, 2,000-, or 3,000-cells per spheroid. Cells settled by gravity to the bottom of the micro-wells. After 30-minutes, 1-mL of serum-free DMEM was added per well. Cells were given 24-hours to self-assemble into spheroids prior to performing imaging studies.

2.3.2 Labeling with fluorescent dyes, microscopy and image analysis

Spheroids were labeled with fluorescent dyes in one of two ways: staining cells as 2D monolayers prior to spheroid formation or staining the formed 3D spheroids. Five different fluorescent dyes were tested: calcein-AM (Life Technologies, Grand Island, NY, USA), calcein-RO (Life Technologies, Grand Island, NY, USA), Hoechst 33342 (Life Technologies, Grand Island, NY, USA), CellTracker^{TM} Green CMFDA (CTG) (Life Technologies, Grand Island, NY, USA), and CellTracker^{TM} Red CMPTX (CTR) (Life Technologies, Grand Island, NY, USA). When staining the cell monolayer, serum-containing medium was removed from the culture flasks. Fluorescent dyes were reconstituted in serum-free DMEM, and incubated with the cell monolayer for 30-minutes at 37°C with 10% CO_2. All five dyes were used to stain monolayers at the following concentrations: 5μM calcein-AM, 5μM CTR, 5μM CTG, 5μM calcein-RO, and 4μg/mL Hoechst 33342. After labeling, medium was exchanged with fresh serum-free DMEM, and incubated for 15-minutes at 37°C with 10% CO_2. After staining, the labeled cell monolayers were trypsinized, counted and seeded into micro-molded gels at various seeding densities. Cells were allowed to self-assemble into spheroids for 24-hours, prior to performing imaging studies.

To label formed spheroids by dye diffusion, cell monolayers were trypsinized, counted, and seeded into micro-molded hydrogels at various seeding densities. Un-labeled cells were allowed to self-assemble into spheroids for 24-hours, prior to staining with fluorescent dyes and performing imaging studies. Fluorescent dyes were reconstituted in serum-free DMEM, and 1-mL was added per well. All five dyes were used to stain spheroids at the following concentrations: 5μM calcein-AM, 5μM CTR, 5μM CTG, 5μM calcein-RO, and 4μg/mL Hoechst 33342. To determine the optimal concentration of calcein-AM and calcein-RO for diffusion into spheroids, the following concentrations were tested per dye: 1.25-μM, 2.5-μM, 5-μM.

Conventional inverted microscopy was used to acquire both phase contrast and time lapse fluorescent images of the spheroids. A Carl Zeiss Axio Vision Observer Z1 equipped with an AxioCam MRm camera (Carl Zeiss MicroImaging, Thornwood, NY, USA), an Xcite 120XL mercury lamp (Exfo Life Sciences Division, Mississauga, Ontario, Canada) and an incubation chamber were used. The following filter configurations were used for these dyes: excitation and emission cutoffs are 365-nm and 445/50-nm for Hoechst 33342, 545/30-nm and 620/60-nm for CTR and calcein-RO, and 470/40-nm and 525/50-nm for calcein-AM and CTG. ImageJ was used to measure spheroid length (x), and width (y). Total spheroid fluorescence was calculated by subtracting a background-matched control from the raw spheroid fluorescence for every spheroid at every time-point. Spheroid height (z) diameter was calculated to be a ratio of the average x, y-diameters (**Supplemental Figure 2-1, Supplemental Material and Methods**). The ratio was determined by using alternative micro-molds containing a single row of spheroids. These molds were imaged using conventional phase contrast microscopy to measure *x, y*-dimensions, and side-view microscopy to measure *x, z*-dimensions. To determine the relationship between height versus length/width, the length and width were averaged, and then plotted versus the height for a range of spheroid sizes. Spheroids of KGN cells had a height that was 89% of the average length and width over a diameter range of 100µm to 270µm (**Supplemental Figure 2-1D**). The height of spheroids of MCF-7 cells was 84% of its average length and width over a diameter range of 80µm to 290µm (**Supplemental Figure 2-1E**). Instead of assuming that spheroids were perfect spheres, we used these correction factors in our calculations of spheroid shape and fluorescence. Additionally, spheroids larger than 205µm in diameter were excluded from analysis, since we have previously shown that their fluorescent signal was no longer linear with respect to size (20). For each labeling and dye combination, total spheroid fluorescence data from all three seeding densities were pooled, and plotted as a function of their radii.

2.3.3 Calculation of prediction curves for relating volume/surface area, radii, and fluorescence.

Two different prediction lines were generated to relate the average spheroid radii and fluorescence against either spheroid volume or spheroid surface area. As spheroid radii increase, both spheroid volume and surface area increase, but at different rates. The increase in fluorescence with respect to radii was measured, and compared to the rates of increase in volume and surface area. The prediction lines for volume and surface area were derived from geometric principles, with volume represented as: $V = \frac{4}{3}\,\pi\, r^3$, and surface area represented as $SA = 4\,\pi\, r^2$, where "r" is the average of all x, y, and z radii of each spheroid. Volume and surface area are units of measurement (μm^3 and μm^2 respectively), thus to relate these values to fluorescence (A.U.), a conversion factor was used. Both volume and surface area conversion factors were derived for each dye, at every experimental time-point. To derive the conversion factors, fluorescence was plotted with respect to either volume or surface area, and the best-fit line was determined (**Supplemental Figure 2-2**). The slope of the best–fit line is the conversion factor that relates fluorescence to either volume (m_{vol}) or surface area (m_{SA}) (**Supplemental Figure 2**). With the appropriate conversion factors, the prediction line for increasing volume/surface area with respect to spheroid radii were defined with volume represented as $V = m_{vol}\left(\frac{4}{3}\,\pi\, r^3\right)$, and surface area represented as $SA = m_{SA}\,(4\,\pi\, r^2)$.

2.3.4 Statistical Analysis

To determine the relationship between fluorescent signal and spheroid size both correlation and Kolmogorov-Smirnov test (K-S test) were performed. Correlation between the observed fluorescent signal and either volume-based or surface area-based prediction lines were computed by the following equation: "$R^2 = 1 - \frac{SS_{res}}{SS_{tot}}$ "; where "$SS_{res} = \sum_i (y_i - f_i)^2$" and "$SS_{tot} = \sum_i (y_i - \bar{y})^2$"; "$y_i$" represented observed values, "f_i" represented predicted values, and "$\bar{y}$" represented the average observed value. Using MatLab, a two-sample K-S test at a 5% significance level was computed between observed fluorescent signal and either volume-based or surface area-based prediction lines. With a p-value of less than 0.05, we reject the null hypothesis that both sets of data were derived from the same continuous data set. With a p-value greater than 0.05, we fail to reject the null hypothesis.

To determine whether size-based normalization enhances the sensitivity of an assay, fluorescent measurements from four size-matched spheroids per condition, were analyzed and plotted three different ways: (1) average and standard deviation of raw fluorescent values, or normalized to (2) spheroid volume or (3) spheroid surface area prior to computing the average and standard deviation. A two-tailed Student's t-test was performed with a significance of 0.05 to compare experimental conditions. To compare the different methods of normalization, a coefficient of variation (CV) analysis was performed for each of the three methods. Lower CV values indicate less variation.

2.4 RESULTS and DISCUSSION

An array of multi-cellular spheroids suitable for time-lapse fluorescent microscopy were formed in micro-molded agarose gels. The resulting size of spheroids was controlled by altering the input number of mono-dispersed cells, with higher seeding densities yielding larger spheroids (**Figure 2-1A**). To ascertain biological information from these spheroids, fluorescent dyes could be used, however adapting their usage for 3D spheroids is more complex than 2D, especially with respect to quantification. In contrast to monolayers of cells where fluorescent signals are typically normalized to either field of view or number of cells, spheroids are 3D multi-cellular objects that possess unique length, width, and height radii, thus the method of normalization of fluorescence should reflect these

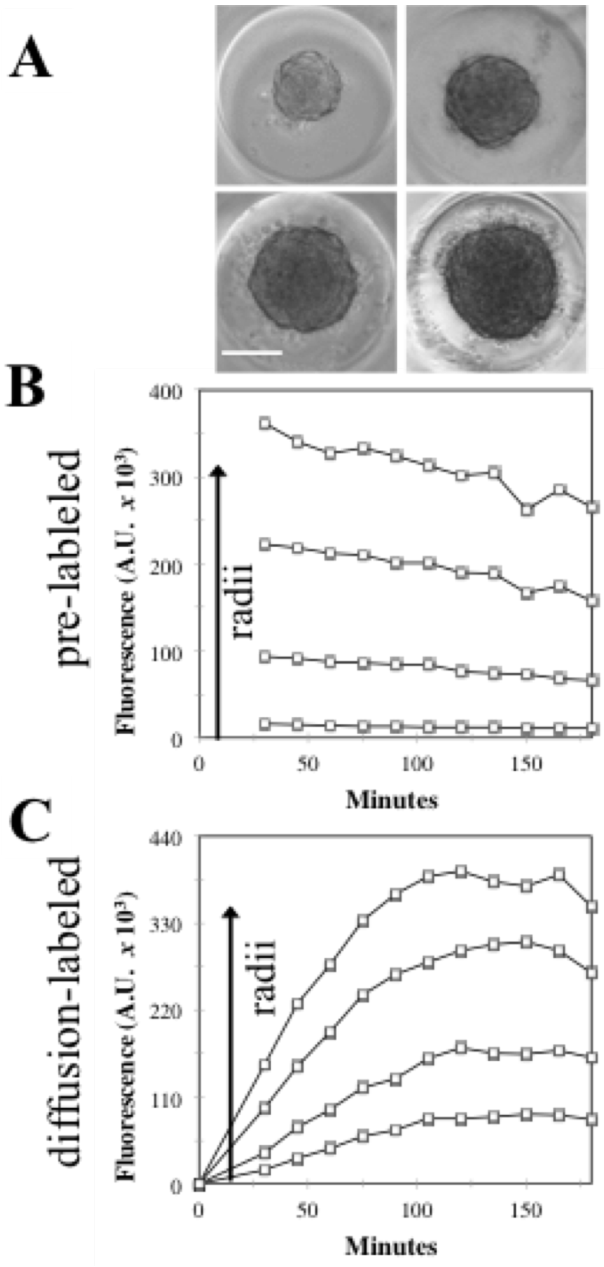

Figure 2-1. Total Fluorescence intensifies with increasing spheroid radii regardless of whether calcein-AM was labeled in 2D or 3D. Spheroids uniformly pre-labeled with 5μM calcein-AM and spheroids labeled by 5μM calcein-AM diffusion were prepared by seeding at hydrogels at the following seeding densities: 1,000-, 2,000-, and 3,000-cells/spheroid. Phase contrast images of spheroids of varying sizes were acquired every 15 minutes for a total of 3-hours. Total spheroid fluorescence as a function of time was quantified for individual spheroids that were pre-labeled (B) or labeled by diffusion into spheroids (C). Each line represents fluorescent data from a single spheroid (radii ~ 40μm, 60μm, 80μm, 100μm) (B, C). Scale bar is 100μm.

variables [14,21]. Without accounting for size, larger spheroids yield a greater fluorescent signal, which if not properly accounted for could generate inaccurate experimental conclusions. To illustrate the need for a size-based method of normalization of the fluorescent measurements, calcein-AM was incorporated into spheroids by either (1) staining individual cells prior to spheroid self-assembly, or (2) adding calcein-AM after spheroid self-assembly, thus staining the spheroid by inward diffusion of the dye. The fluorescent signal from pre-labeled spheroids was constant over 3-hours (**Figure 2-1B, Supplemental Figure 2-3A, B**). In contrast, the fluorescent signal from spheroids labeled by dye diffusion increased over time (**Figure 2-1C, Supplemental Figure 2-3C, D**). Regardless of how calcein-AM was incorporated, increasing spheroid radii yielded an increase in fluorescence **(Figure 2-1B, C)**. However, this increase in fluorescence did not imply biological differences, but rather the need for a size-based method to normalize fluorescence.

To eliminate size-based differences in fluorescence, there are two approaches: (1) only analyze spheroids within a narrow range of radii so that size doesn't matter, or (2) normalize signal by an appropriate size-based parameter, which increases the number of analyzable spheroids. We hypothesized that the size-based parameter used to normalize spheroid fluorescence was dependent on the method of dye labeling. When cells were pre-labeled with dye prior to spheroid formation, we predicted that as spheroid radii increased, total fluorescence would increase at a rate proportional to spheroid volume since every cell was evenly stained. In contrast, when spheroids were labeled by dye diffusion, we predicted that as spheroid radii increased, total fluorescence would increase at a rate proportional to spheroid surface area since the amount of dye that could diffuse inwards was dependent upon surface area. Therefore, to determine the best means to quantify fluorescence of spheroids, we stained spheroids of varying size (diameter = 80-200μm), using both labeling techniques with calcein-AM. Total spheroid fluorescence was measured and plotted as a function of average spheroid radii. These data were then fitted with a curve of the increase in spheroid volume as a function of spheroid radii or a curve of the increase in surface area as a function of spheroid radii. To quantify which curve better predicted the observed increase in fluorescence, correlation analysis and two-sample Kolmogorov-Smirnov test were performed (**Figure 2-2**). For spheroids uniformly pre-labeled with calcein-AM, the increase of fluorescence as a function of spheroid radii more closely matched the curve depicting the increase in volume as a function of spheroid radii (**Figure 2-2A**). This evidence for volume-based prediction line was supported both by a greater correlation value and by a p-value greater than 0.05 for volume-based, with which we fail to reject the null hypothesis that both datasets were derived from a continuous set of data (**Figure 2-2A)**. This was true for all time points tested over the 3 hour time lapse (data not shown). In contrast, for spheroids labeled by calcein-AM diffusion, the increase of fluorescence as a function of spheroid radii more closely matched the curve depicting the increase in surface area as a function of spheroid radii (**Figure 2-2B)**. Similarly, this match to the surface area-based prediction line was supported by a greater correlation value and by p-value greater than 0.05 (**Figure 2-2B**). The robustness of this hypothesis was further validated by testing four additional fluorescent dyes (calcein-RO, Hoechst 33342, CTR, CTG) in a variety of cell types (MCF-7, NHF)**(Supplemental Figures 2-4, 2-5, 2-6, 2-7)**. Therefore, we have shown

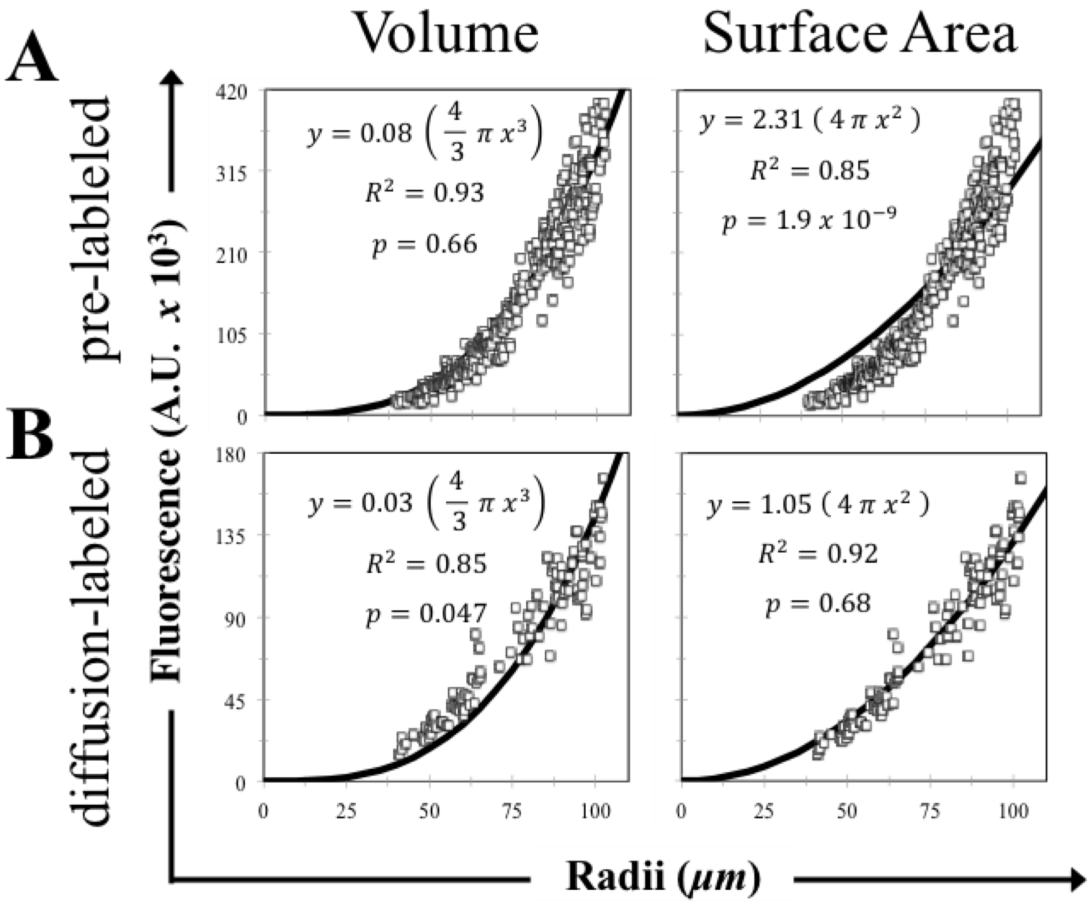

Figure 2-2. Fluorescence normalization of calcein-AM is dependent upon the method of labeling. Calcein-AM was incorporated into KGN spheroids via two different methods. To form pre-labeled spheroids, 5μM calcein-AM was added to 2D monolayers, then trypsinized and seeded into gels (A). Alternatively, for diffusion-based spheroid labeling, KGN cells were self-assembled into spheroids of varying sizes prior to the addition of 5μM calcein-AM (B). Fluorescent images were acquired 24-hours after self-assembly and total spheroid fluorescence was plotted as a function of radii. The data are plotted versus either a curve of the spheroid volume as a function of radii (left column) or spheroid surface area as a function of radii (right column). Each point represents a single spheroid. Correlation analysis and K-S tests were performed to determine which prediction line better matched the observed data. When calcein-AM was pre-labeled, the correlation between fluorescent signal and volume-based prediction line was greater than the correlation to surface area (A). Additionally, the p-value for all surface area-based prediction lines were less than 0.05, thus rejecting the null hypothesis that both sets of data were derived from a continuous data set (A). Alternatively, when calcein-AM was diffused into spheroids, the trends for correlation and K-S tests were reversed, with fluorescent signal better correlating with the surface area-based prediction line (B).

that regardless of differences in excitation/emission spectra, and where the dye resides intracellularly, the accurate means of normalization of the fluorescent measurement was dependent upon how the dye was incorporated into the spheroids. Volume versus surface area normalization is important for spheroids, because unlike thin 2D monolayers where diffusion occurs very rapidly, spheroids are multi-cell layers thick and are a significant barrier to diffusion of fluorescent dyes.

Although those other dye characteristics did not seem to affect the normalization method, we did determine that for diffusion-based labeling, concentration of and staining time for calcein-AM was very important. We diffused different concentrations of calcein-AM into spheroids in order to see whether the concentration would alter the fit to surface area. After forming spheroids of variable size, calcein-AM was diffused into spheroids for 3-hours at the following concentrations: 1.25-μM, 2.5-μM, 5-μM. For spheroids treated with the lower dye concentrations (1.25-μM, 2.5-μM), as radii increased, the fit diverged from the surface area prediction line (**Figure 2-3A, B)**. This divergence was exacerbated at later time-points in the experiment (**Figure 2-3A, B**). Utilizing a higher concentration of calcein (5-μM), the fit to surface area was better matched, and did not diverge as incubation time increased **(Figure 2-3C).** The fit to spheroid volume was worse for all time-points and concentrations of calcein-AM tested (data not shown). Calcein-RO also exhibited the same trends (**Supplemental Figure 2-8**). Overall, we determined that low concentrations and lengthy incubation times reduced the reliability of the model. Therefore, when adapting assays for their use in 3D spheroids, certain optimizations

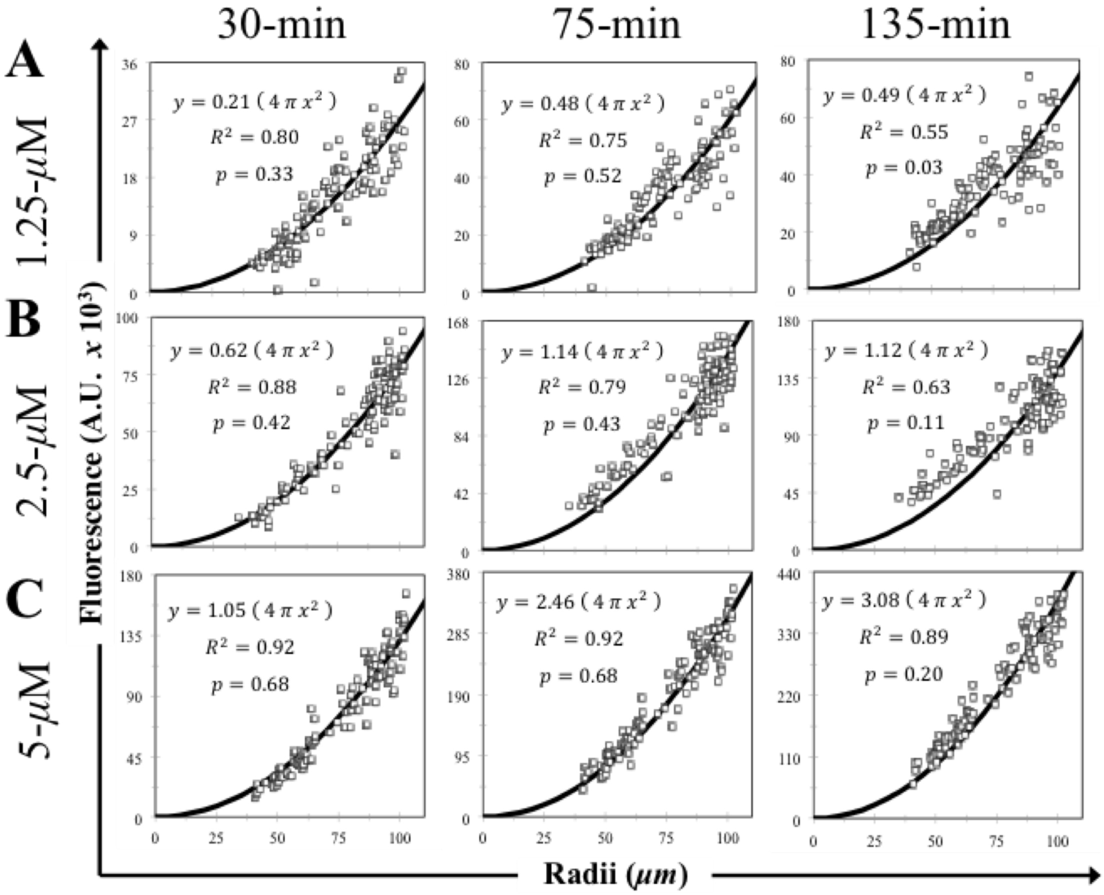

Figure 2-3. Increasing the concentration of calcein-AM diffused into spheroids improves the fit to surface area. KGN cells were self-assembled into spheroids of varying sizes prior to the addition of calcein-AM at the following concentrations: 1.25-µM (A), 2.5-µM (B), 5-µM (C). Fluorescent time-lapse images were acquired every 15-min for a total of 3-hours and subsequently analyzed to measure total fluorescence and spheroid radii. The increase in spheroid fluorescence with respect to radii was plotted at various time-points after the addition of dye: 30-min (left column), 75-min (middle column), and 135-min (right column). The data are plotted versus a curve of the spheroid surface area as a function of radii. Each point represents a single spheroid. Correlation analysis and K-S tests were performed to determine how the fit to surface area changed in response to altering dose and incubation time. The fit to surface area declined with lower dosages of calcein-AM and increased incubation times, as evidenced by lower correlation values. Furthermore, after 135-minutes of staining with 1.25-µM, the K-S value was less than 0.05, thus rejecting the null hypothesis that both sets of data were derived from a continuous data set (A).

made for 2D monolayers are not directly transferable to 3D spheroids and thus require further optimization.

To highlight the importance of choosing the appropriate size-based normalization method, we measured fluorescence of spheroids incubated with different calcein-AM concentrations (1.25-μM, 2.5-μM) over 3-hours (**Figure 2-4**). We plotted the data from four size-matched spheroids (radii: 50-95 μm) three different ways: (1) the average and standard deviation of raw fluorescent values, or normalized each spheroid by its (2) volume or (3) surface area prior to computing the average and standard deviation. To determine if time points were significantly different, a two-tailed t-test with significance 0.05 was performed. Significant differences between the concentrations throughout the entire experiment were detected when fluorescence was normalized by spheroid surface area, the appropriate normalization when a fluorescent dye is diffused into a spheroid (**Figure 2-4C**). We performed a coefficient of variation (CV) analysis to compare the variability amongst the three methods of analysis. For all time points tested, the surface area-normalized data had the lowest CV values, indicating the least amount of variation (**Figure 2-4D**). Therefore, by utilizing the correct normalization method, we can improve assay sensitivity to discern smaller, yet significant biological differences in experimental conditions. With improved sensitivity, we can analyze fewer spheroids, which will be critical for adapting spheroids for uses such as high throughput screening.

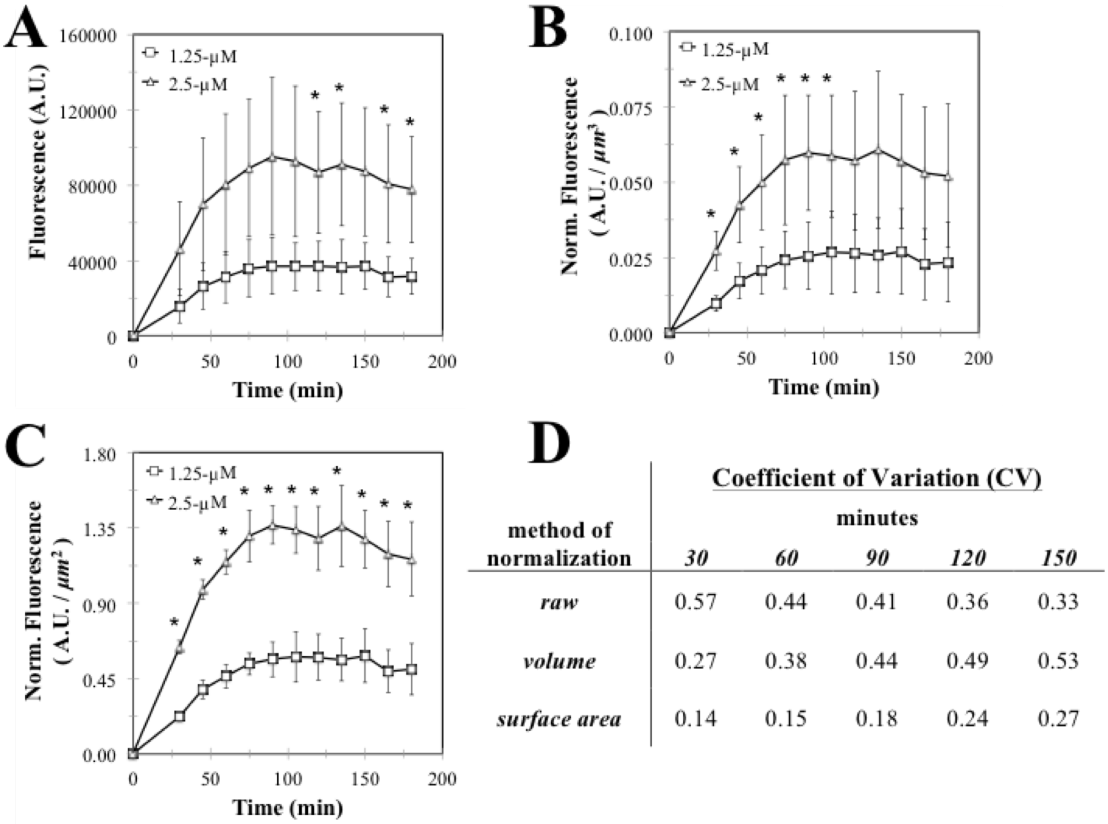

method of normalization	Coefficient of Variation (CV) minutes *30*	*60*	*90*	*120*	*150*
raw	0.57	0.44	0.41	0.36	0.33
volume	0.27	0.38	0.44	0.49	0.53
surface area	0.14	0.15	0.18	0.24	0.27

Figure 2-4. Surface area normalization enhances the ability to detect differences between different doses of calcein-AM diffusing into spheroids. KGN cells were self-assembled into spheroids of varying sizes prior to the addition of either 1.25-µM (white squares) or 2.5-µM calcein-AM (white triangles). Fluorescent time-lapse images were acquired every 15-min for a total of 3-hours and subsequently analyzed to measure total fluorescence and spheroid radii. 4 size-matched spheroids of variable radii (ranging from 50 - 95 µm) were analyzed for each concentration. Diffusion of calcein-AM into 4 size-matched spheroids of variable radii (range: 50 - 95 µm) was plotted as a function of time for each concentration. The diffusion of calcein was represented as the average and standard deviation of either the spheroids' raw fluorescence (A), volume-normalized fluorescence (B), or surface area-normalized fluorescence (C). A two-tailed Student's t-test with significance of 0.05 was performed for every time-point ("*" indicates statistically significant). Statistically significant differences were observed throughout the entire experiment when fluorescence was normalized by surface area (C), whereas only certain time-points were statistically significant when evaluating raw fluorescence (A) or volume-normalized fluorescence (B). The coefficient of variation (CV) was calculated for each method of analysis and for each time-point. The CV for surface area-normalized data was lower than both raw and volume-normalized data for all time-points (D).

There are thousands of commercially available fluorescent dyes that probe a diverse range of biological functions. However, these fluorescent dyes have been predominately developed for use with 2D monolayers only, and require careful optimization when adapted to 3D spheroids. For example, since spheroids possess a much larger z-dimension than 2D cell cultures, spheroid height must be taken into consideration when performing imaging studies. Previously, we have shown that only spheroids below 205μm in diameter can be reliably imaged via wide field fluorescence [20]. Furthermore, it is widely acknowledged that spheroids significantly greater than 200μm in diameter have diffusion limitations that can lead to cell death and necrosis in the spheroid core [22]. Also, as shown in this paper, dye concentrations and incubation times that are well suited for 2D are not necessarily accurate for spheroids and require optimization. Fluorescent images of 2D monolayers are typically normalized to cell number in a fixed field of view, but this method is not applicable to spheroids. For accurate quantitation of fluorescent images of spheroids, it is important to select the normalization method that matches the method of dye staining. Fluorescent images of uniformly labeled spheroids should be normalized by spheroid volume, while fluorescent images of spheroids labeled by inward diffusion of dyes should be normalized by spheroid surface area. Although we tested five fluorescent small molecule dyes, this method of validating and normalizing fluorescent signals from spheroids should be applicable to many other fluorescent dyes and possibly GFP reporter genes. However, GFP reporter assays are varied and can be complex (e.g., induction of GFP by a small molecule, diffusion of GFP encoding virus into a spheroid) so it would be important to perform validation studies and carefully consider the experimental design before choosing a normalization strategy. Furthermore, certain methods of labeling may not be appropriate for certain experimental designs. For example, forming spheroids from pre-stained cells may not be useful for experiments that extend over multiple days to weeks. Attention to the details of the biological/experimental system is crucial for developing a strategy for image analysis of spheroids. Overall, the correct method of normalization will reduce errors, improve sensitivity and can account for the natural variation in spheroid size.

2.5 AUTHOR CONTRIBUTIONS

E.L. and C.R. designed and performed the series of experiments. B.W. designed ImageJ analysis programs. J.R.M. supervised the project. All authors contributed towards writing the manuscript.

2.6 ACKNOWLEDGEMENTS

This work was funded in part by seed funds from Unilever, and the generous support of Donna McGraw Weiss '89 and Jason Weiss.

2.7 CONFLICT OF INTEREST

J.R.M has an equity interest in Microtissues, Inc. This relationship has been reviewed and managed by Brown University in accordance with its conflict of interest policies.

2.8 REFERENCES

1. Atala A, Kasper FK, Mikos AG. Engineering complex tissues. *Science Translational Medicine.* 4(160):160rv12, 2012.

2. Elliott NT, Yuan F. A review of three-dimensional in vitro tissue models for drug discovery and transport studies. *Journal of Pharmaceutical Sciences*. 100(1):59-74, 2011

3. Tung YC, Hsiao AY, Allen SG, Torisawa YS, Ho M, Takayama S. High-throughput 3D spheroid culture and drug testing using a 384 hanging drop array. *The Analyst.* 136(3):473-478, 2011.

4. Griffith LG, Swartz MA. Capturing complex 3D tissue physiology in vitro. *Nature Reviews Molecular Cell Biology*. 7(3):211-224, 2006.

5. Yamada KM, Cukierman E. Modeling tissue morphogenesis and cancer in 3D. *Cell.* 130(4):601-610, 2007.

6. Bartosh TJ, Yostalo JH, Mohammadipoor A, Bazhanov N, Coble K, Claypool K, Lee RH, Choi H, Prockop DJ. Aggregation of human mesenchymal stromal cells (MSCs) into 3D spheroids enhances their antiinflammatory properties. *Proceedings of the National Academy of Sciences of the United States of America*. 107(31):13724-13729, 2010.

7. Chang TT, Hughes-Fulford M. Monolayer and spheroid culture of human liver hepatocellular carcinoma cell line cells demonstrate distinct global gene expression patterns and functional phenotypes. *Tissue Engineering Part A.* 15(3):559-567, 2009.

8. Vantangoli MM, Madnick SJ, Huse SM, Weston P, Boekelheide K. MCF-7 Human Breast Cancer Cells Form Differentiated Microtissues in Scaffold-Free Hydrogels. *PLoS One*. 10(8):e0135426, 2015.

9. Lemmo S, Atefu E, Luker GD, Tavana H. Optimization of aqueous biphasic tumor spheroid microtechnology for anti-cancer drug testing in 3D culture. *Cellular and Molecular Bioengineering*. 7(3):344-354, 2014.

10. Vinci M, Gowan S, Boxall F, Patterson L, Zimmermann M, Court W, Lomas C, Mendiola M, Hardisson D, Eccles SA. Advances in establishment and analysis of three-dimensional tumor spheroid-based functional assays for target validation and drug evaluation. *BMC Biology.* 10(29):10.1186/1741-7007-10-29, 2012.

11. Weston SA, Parish CR. New fluorescent dyes for lymphocyte migration studies. Analysis by flow cytometry and fluorescence microscopy. *Journal of Immunological Methods.* 133(1):87-97, 1990.

12. Chalfie M, Tu Y, Euskirchen G, Ward WW, Prasher DC. Green fluorescent protein as a marker for gene expression. *Science*. 263(5148):802-805, 1994.

13. Singhvi R, Kumar A, Lopez GP, Stephanopoulos GN, Wang DI, Whitesides GM, Ingber DE. Engineering cell shape and function. *Science*. 264(5159):696-698, 1994.

14. Pampaloni F, Reynaud EG, Stelzer EH. The third dimension bridges the gap between cell culture and live tissue. *Nature Reviews. Molecular Cell Biology.* 8(10):839-845, 2007.

15. Pampaloni F, Ansari N, Stelzer EH. High-resolution deep imaging of live cellular spheroids with light-sheet-based fluorescence microscopy. *Cell and Tissue Research.* 352(1):161-177, 2013.

16. Boutin ME, Hoffman-Kim D. Application and assessment of optical clearing methods for imaging of tissue-engineered neural stem cell spheres. *Tissue Engineering Part C Methods.* 21(3):292-302, 2015.

17. Robertson FM, Ogasawara MA, Ye Z, Chu K, Pickei R, Debeb BG, Woodward WA, Hittelman WN, Cristofanilli M, Barsky SH. Imaging and analysis of 3D tumor spheroids enriched for a cancer stem cell phenotype. *Journal of biomolecular screening.* 15(7):820-829, 2010.

18. Schneckenburger H, Weber P, Wagner M, Schickinger S, Richter V, Bruns T, Strauss WS, Wittig R. Light exposure and cell viability in fluorescence microscopy. *Journal of microscopy*. 245(3):311-318, 2012.

19. Napolitano AP, Dean DM, Man AJ, Youssef J, Ho CH, Rago AP, Lech MP, Morgan JR. Scaffold-free three-dimensional cell culture utilizing micromolded nonadhesive hydrogels. *Biotechniques.* 43(4):496-500, 2007.

20. Achilli TM, McCalla S, Meyer J, Tripathi A, Morgan JR. Multilayer spheroids to quantify drug uptake and diffusion in 3D. *Molecular pharmacolgy.* 11(7):2071-2081, 2014.

21. Smith LE, Smallwood R, Macneil S. A comparison of imaging methodologies for 3D tissue engineering. *Microscopy Research and Technique*. 73(12):1123-133, 2010.

22. Casciari JJ, Sotirchos SV, Sutherland RM. Glucose diffusivity in multicellular tumor spheroids. *Cancer research*. 48(14):3905-3909, 1988.

2.9 SUPPLEMENTAL MATERIALS and METHODS

Micro-molded side-view hydrogels and side view microscopy. To create side-view hydrogels, wax molds, consisting of a single row of 21 rounded cylindrical pegs, were used (20). Acrylamide/bis-acrylamide solution (Fisher Scientific, Waltham, MA), 10% weight/volume ammonium persulfate (Sigma-Aldrich, St. Louis, MO), 0.5M Tris buffer (Fisher Scientific, Waltham, MA), and DMEM were added together and degassed. To initiate hydrogel polymerization, N, N, N', N'-tetramethylethlenediamine (Sigma-Aldrich, St. Louis, MO) was added to the mixture. The mixture was pipetted into the wax mold, allowed to polymerize, and released into a 12-well plate. Polyacrylamide hydrogels were equilibrated with serum-free DMEM supplemented only with 1% penicillin/streptomycin, degassed to remove air bubbles from recesses, and incubated overnight at 37°C with 10% CO_2. Cells were re-suspended in serum-free DMEM at one of the following concentrations: 2.8 x10^5 cells/mL, 5.6 x 10^5 cells/mL, or 8.4 x 10^5 cells/mL. 75μL of each cell suspension was pipetted into the loading dock of each hydrogel to form spheroids of approximately 1,000-, 2,000-, or 3,000-cells per spheroid. After 30-minutes, 4-mL of serum-free DMEM was added per well. Cells were given 24-hours to self-assemble into spheroids prior to imaging with an inverted microscope and a side view microscope. Side view images were obtained using a Mitutouo FS-110 microscope placed on its back, with a Nikon Coolpix 900 digital camera. Spheroid length (x) and height (z) were measured using ImageJ. For the derived relationship between spheroid height (z) and average length, width (x, y), the standard error of regression was computed, and the 95% prediction interval was determined.

2.10 SUPPLEMENTAL FIGURES

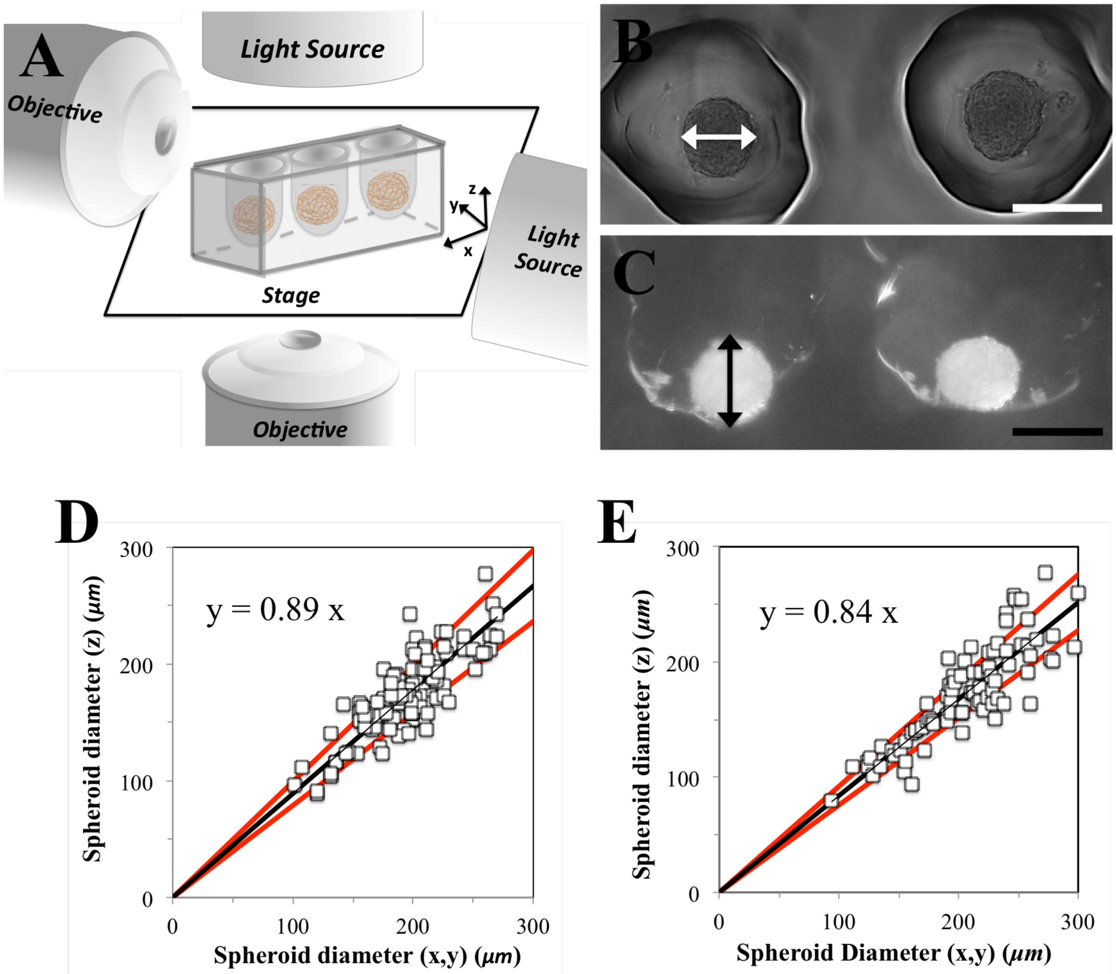

Supplemental Figure 2-1. Spheroid height can be estimated from measuring spheroid length/width. Spheroids of varying radii were self-assembled using hydrogels containing a single row of recesses (A). Spheroids were imaged using both a conventional inverted microscopy to obtain phase contrast images (*x, y*) and horizontal microscopy to obtain side-view brightfield images (*x, z*) (A). Length (x) and width (y) were measured from phase images (B), while height (z) was measured from side-view images (C). For each spheroid, the average length (*x*) and width (*y*) were determined and plotted against the measured height (*z*) (D, E). The best-fit-line (black line) and 95% confidence interval (red line) were computed and plotted. The height (*z*) was determined to be approximately 89% of its average length-width (*x, y*) for KGN spheroids (D) and 84% for MCF-7 spheroids (E). Arrows indicate measured diameters. Scale bar is 200μm.

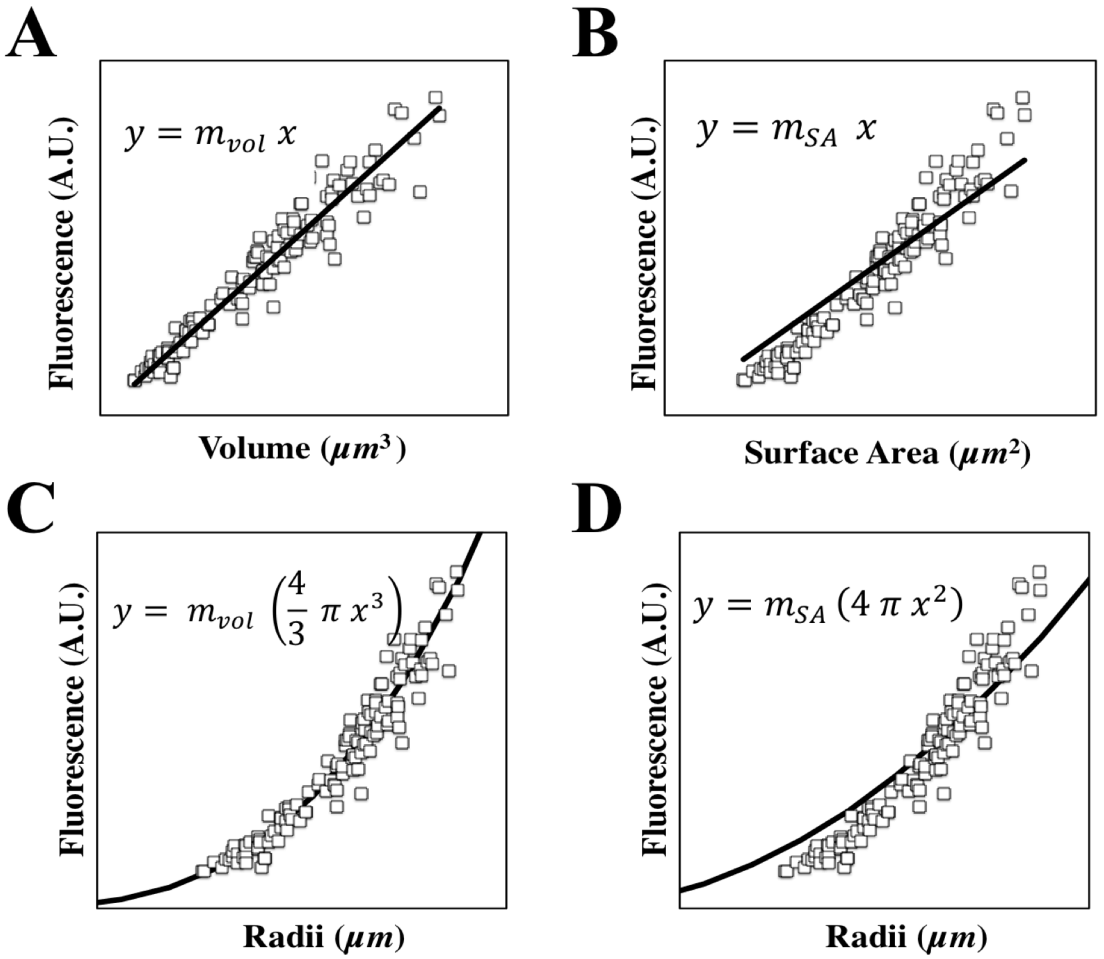

Supplemental Figure 2-2. Volume- and surface area-based prediction lines are determined from fluorescent data. Spheroids uniformly pre-labeled with dyes and spheroids labeled by dye diffusion were prepared in varying sizes. Total spheroid fluorescence was plotted versus either spheroid volume (A) or surface area (B), and the best-fit-line was computed. The slope, m_{vol}, of the best-fit line was the factor that converted spheroid volume as a function of radii to fluorescence ($F = m_{vol}\left(\frac{4}{3}\pi r^3\right)$) (C), likewise the slope, m_{SA}, converted surface area ($F = m_{SA}\,(4\pi r^2)$) (D).

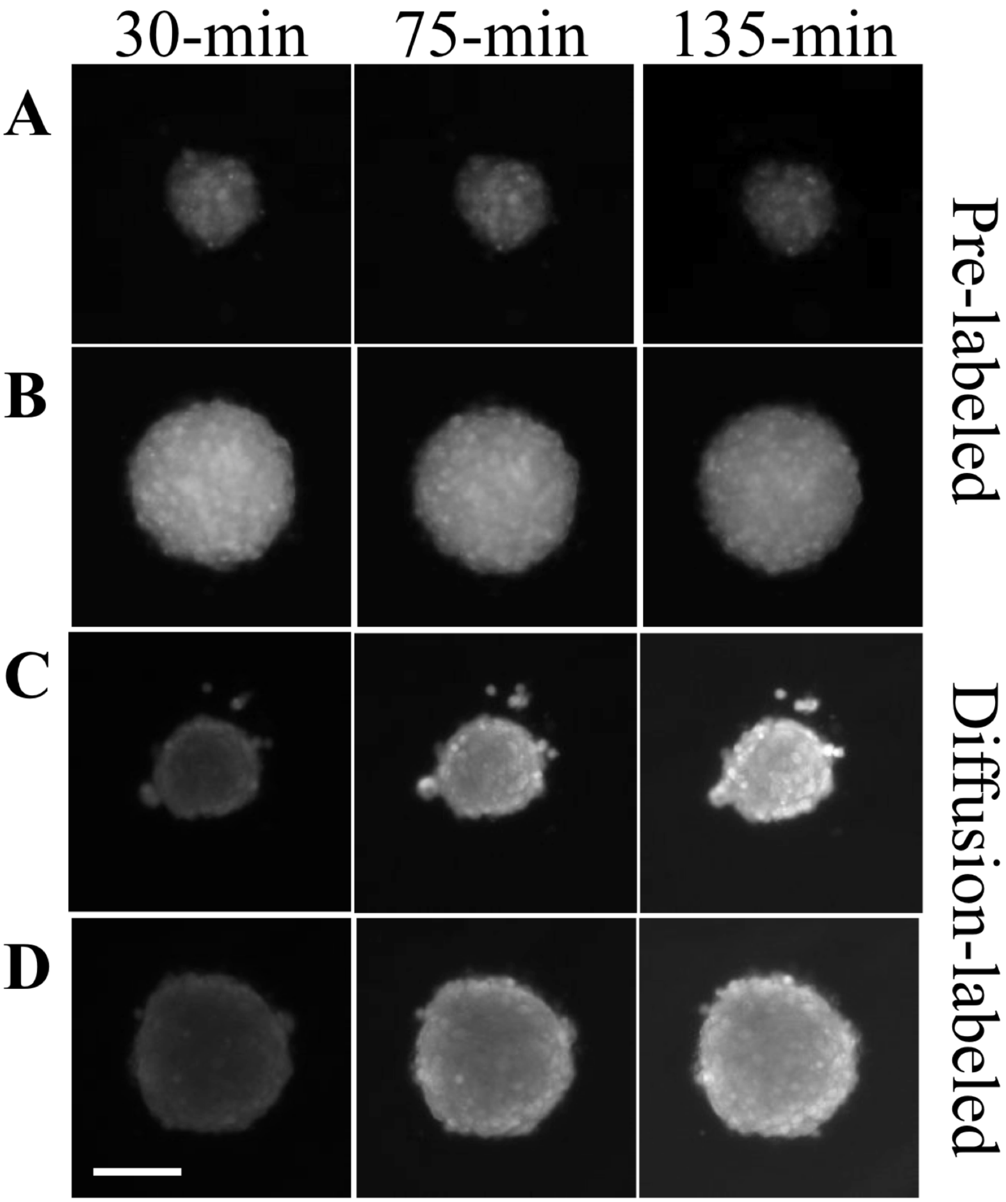

Supplemental Figure 2-3. Time-course of calcein fluorescence in 3D spheroids. Calcein-AM was incorporated into KGN spheroids via two different methods. To form pre-labeled spheroids, calcein-AM was added to 2D monolayers, which were then trypsinized and seeded into hydrogels at varying cell seeding densities (A, B). Alternatively, for diffusion-based spheroid labeling, cells were self-assembled into spheroids of varying sizes prior to the addition of calcein-AM (C, D). Regardless of staining protocol, spheroids were allowed to self-assemble for 24-hours prior to imaging. Fluorescent images were acquired every 15-minutes for a total of 3-hours. Panel of images represent small (radii ~ 50μm) (A, C) and large (radii ~ 100μm) (B, D) spheroids that were pre-labeled (A, B) or labeled by diffusion into spheroids (C, D) at 30- (left column), 75- (middle column), and 135-minutes (right column). Scale bar is 100μm.

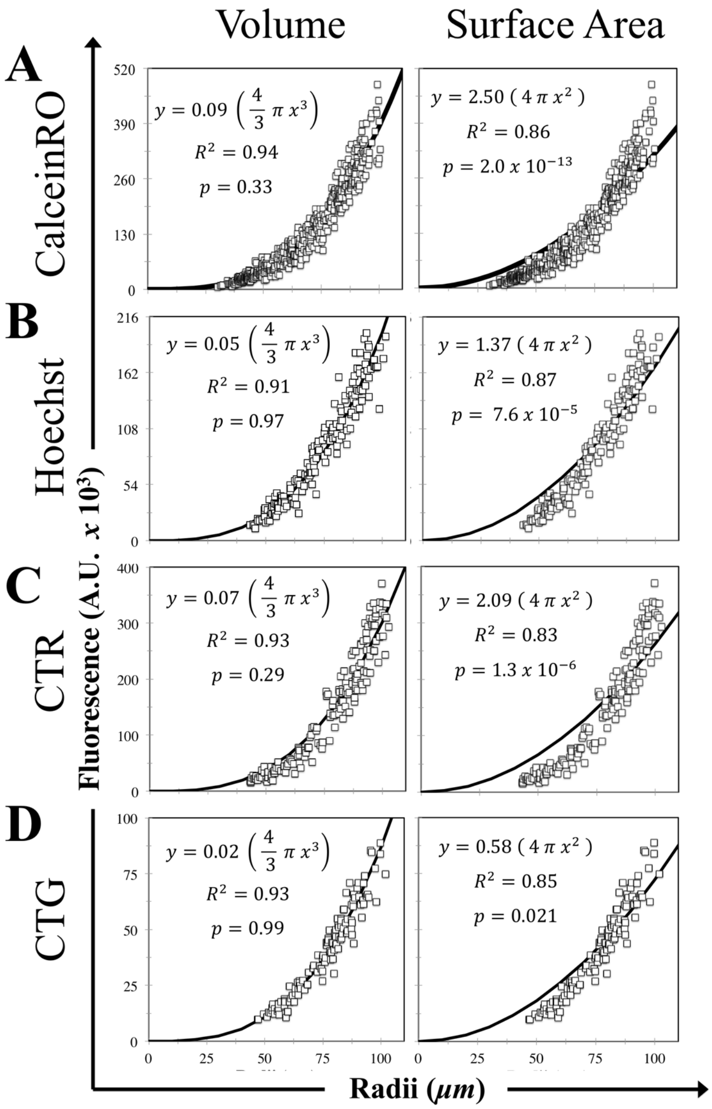

Supplemental Figure 2-4. Fluorescence of pre-labeled spheroids correlates with spheroid volume. KGN cells labeled with calcein-RO, Hoechst 33342, CTR, or CTG as a 2D monolayer were trypsinized and seeded into gels to form pre-labeled spheroids. Fluorescent images were acquired 24-hours after self-assembly and total spheroid fluorescence was plotted as a function of radii for spheroids stained with calcein-RO (A), Hoechst 33342 (B), CTR (C), and CTG (D). The data are plotted versus either a curve of the spheroid volume as a function of radii (left column) or spheroid surface area as a function of radii (right column). Each point represents a single spheroid. Correlation analysis and K-S tests were performed to determine which prediction line better matched the observed data. The correlation between fluorescent signal and volume-based prediction line was greater than the correlation to surface area for all four dyes. The p-value for all surface area-based prediction lines were less than 0.05, thus rejecting the null hypothesis that both sets of data were derived from a continuous data set.

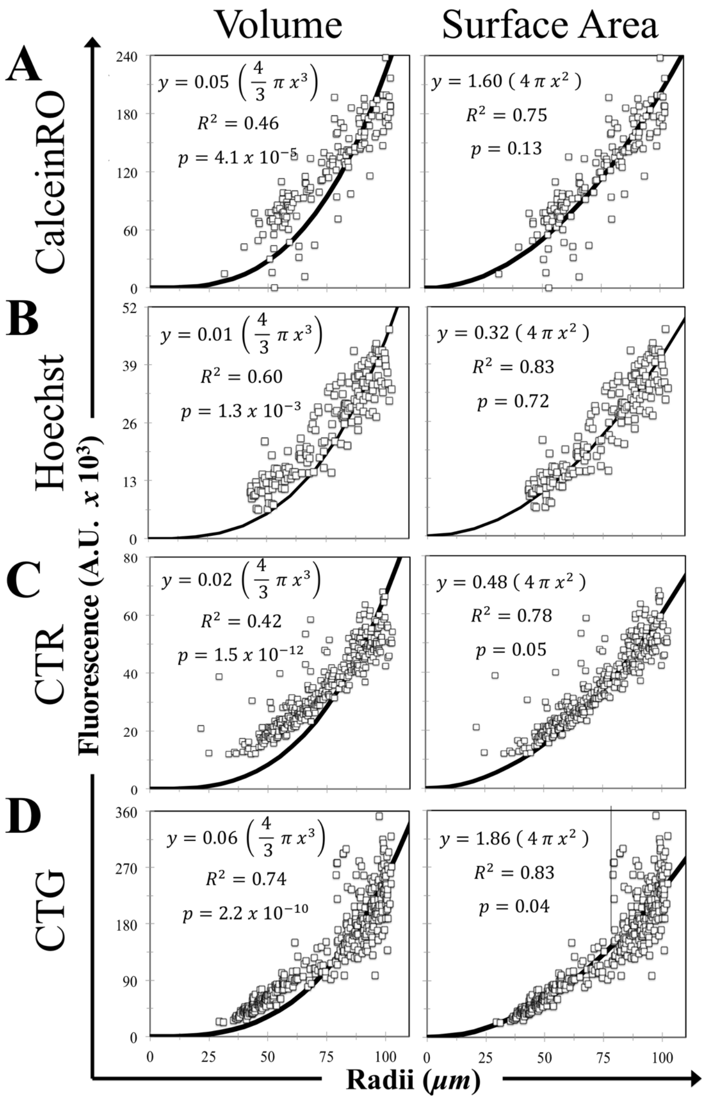

Supplemental Figure 2-5. Fluorescence of spheroids labeled by dye diffusion correlates with spheroid surface area. KGN cells were self-assembled into spheroids of varying sizes prior to the addition of the following dyes: calcein-RO (A), Hoechst 33342 (B), CTR (C), or CTG (D). Fluorescent time-lapse images were acquired every 15-min for a total of 3-hours and subsequently analyzed to measure total fluorescence and spheroid radii. The increase in spheroid fluorescence with respect to radii was plotted 30-minutes after the addition of dye. The data are plotted versus either a curve of the spheroid volume as a function of radii (left column) or spheroid surface area as a function of radii (right column). Each point represents a single spheroid. Correlation analysis and K-S tests were performed to determine which prediction line better matched the observed data. The correlation between fluorescent signal and surface area-based prediction line was greater than the correlation to volume for all four dyes. The p-value for all volume-based prediction lines were less than 0.05, thus rejecting the null hypothesis that both sets of data were derived from a continuous data set.

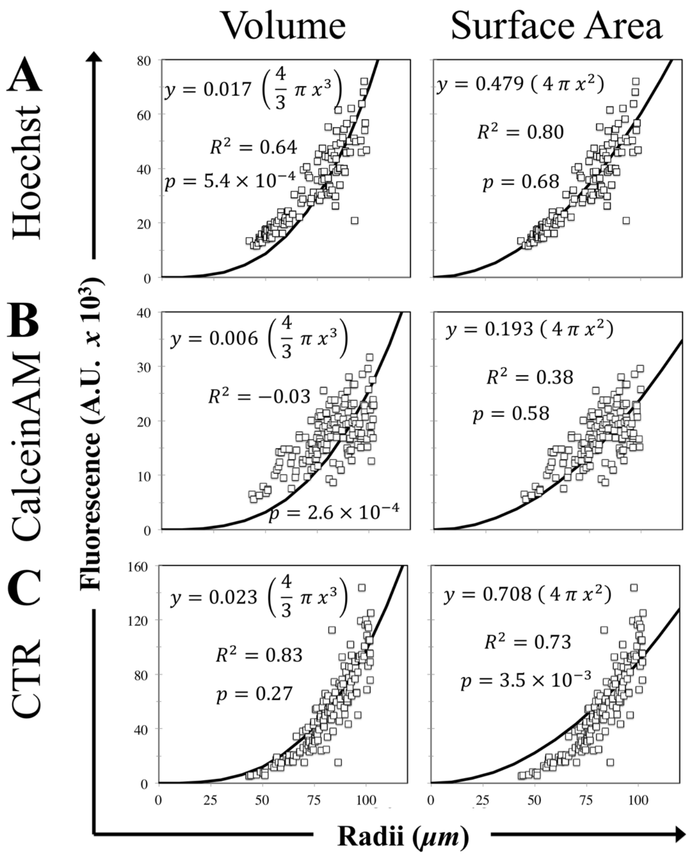

Supplemental Figure 2-6. Fluorescence of pre-labeled MCF-7 spheroids correlates with volume, while fluorescence of MCF-7 spheroids labeled by dye diffusion correlates with surface area. MCF-7 spheroids were either uniformly pre-labeled with CTR or labeled by diffusion of Hoechst 33342 or calcein-AM. Fluorescent images were acquired every 15-min for a total of 3-hours, and total spheroid fluorescence was plotted as a function of a range of spheroid radii for spheroids stained with Hoechst 33342 (A), calcein-AM (B), and CTR (C). The data are plotted versus a curve of the predicted spheroid volume as a function of radii (left column) and spheroid surface area as a function of radii (right column). Each point represents a single spheroid. Correlation analysis and K-S tests were performed to determine which prediction line better matched the observed data. The correlation between fluorescent signal and volume-based prediction line was greater than the correlation to surface area when the spheroids were uniformly pre-labeled, CTR (C). The p-value for surface area-based prediction line was less than 0.05, thus rejecting the null hypothesis that both sets of data were derived from a continuous data set (C). Alternatively, the correlation between fluorescent signal and surface area-based prediction line was greater when spheroids were labeled by dye diffusion, Hoechst 33342 (A) and calcein-AM (B). The p-value for volume-based prediction lines were less than 0.05, thus rejecting the null hypothesis that both sets of data were derived from a continuous data set (A, B).

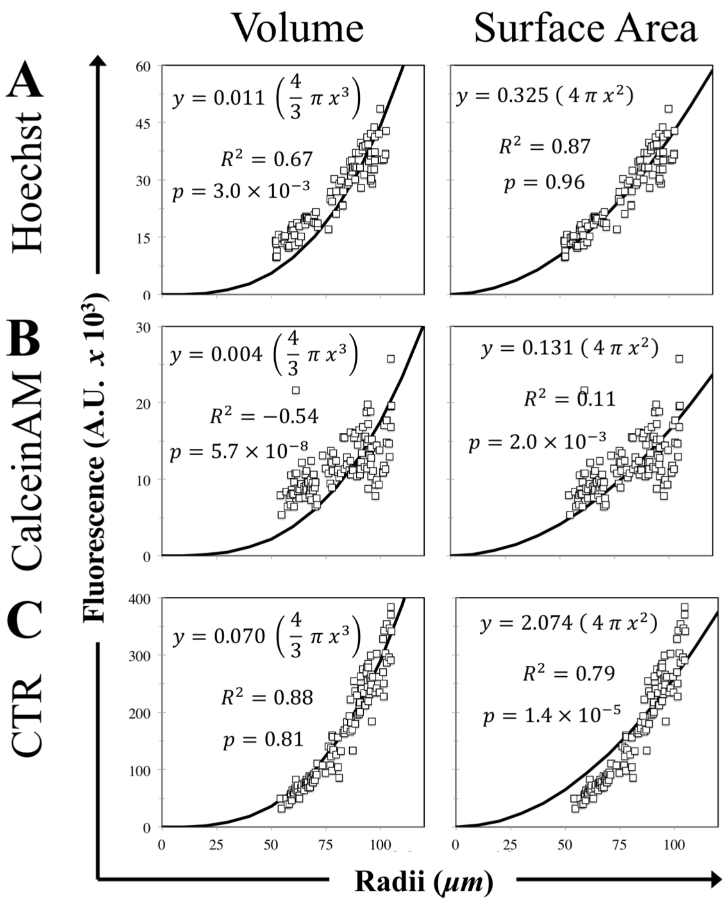

Supplemental Figure 2-7. Fluorescence of pre-labeled NHF spheroids correlates with volume, while fluorescence of NHF spheroids labeled by dye diffusion correlates with surface area. NHF spheroids were either uniformly pre-labeled with CTR or labeled by diffusion of Hoechst 33342 or calcein-AM. Fluorescent images were acquired every 15-min for a total of 3-hours. Total spheroid fluorescence was plotted as a function of a range of spheroid radii for spheroids stained with Hoechst 33342 (A), calcein-AM (B), and CTR (C). The data are plotted versus a curve of the predicted spheroid volume as a function of radii (left column) and spheroid surface area as a function of radii (right column). Each point represents a single spheroid. Correlation analysis was performed to determine which prediction line better matched the observed data. The correlation between fluorescent signal and volume-based prediction line was greater than the correlation to surface area when the spheroids were uniformly pre-labeled, CTR (C). The p-value for surface area-based prediction line was less than 0.05, thus rejecting the null hypothesis that both sets of data were derived from a continuous data set (C). Alternatively, the correlation between fluorescent signal and surface area-based prediction line was greater when spheroids were labeled by dye diffusion, Hoechst 33342 (A) and calcein-AM (B). Also, for spheroids labeled with Hoechst 33342, the p-value for volume-based prediction line was less than 0.05, thus rejecting the null hypothesis that both sets of data were derived from a continuous data set (A).

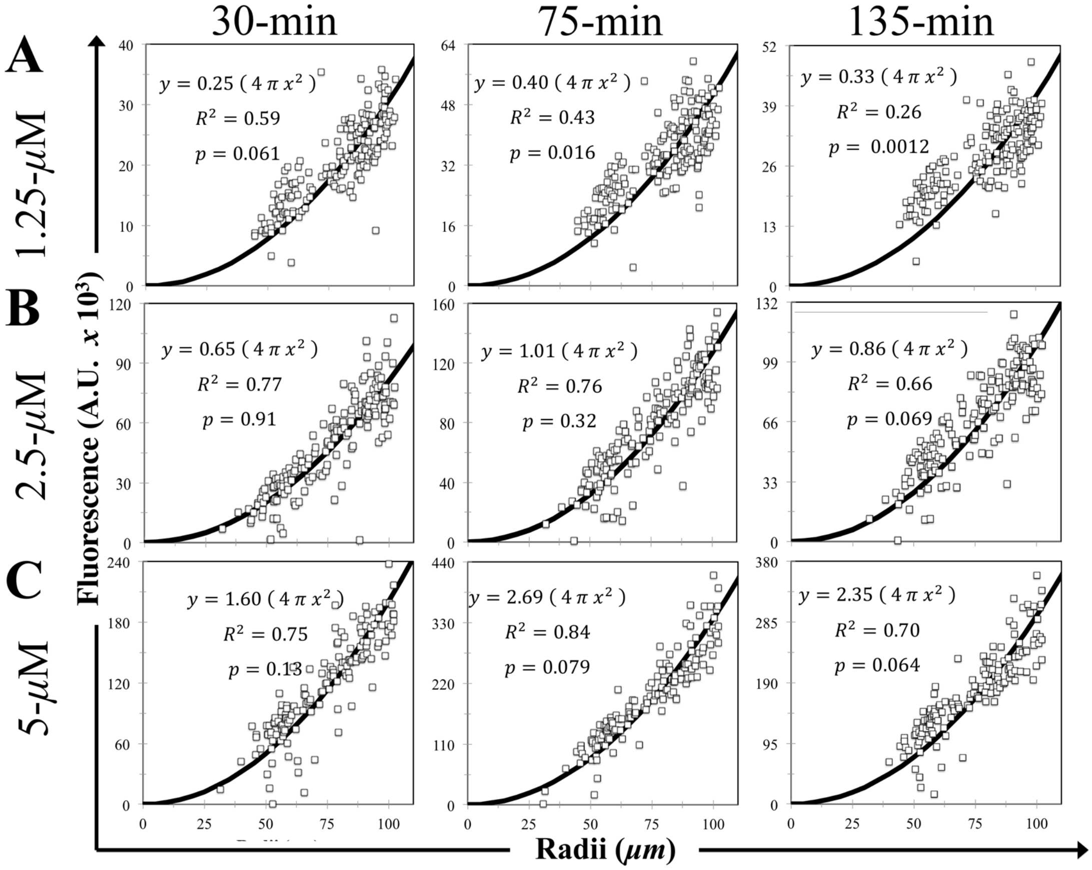

Supplemental Figure 2-8. Increasing the concentration of calcein-RO diffused into spheroids improves the fit to surface area. KGN cells were self-assembled into spheroids of varying sizes prior to the addition of calcein-RO at the following concentrations: 1.25-µM (A), 2.5-µM (B), 5-µM (C). Fluorescent time-lapse images were acquired every 15-min for a total of 3-hours and subsequently analyzed to measure total fluorescence and spheroid radii. The increase in spheroid fluorescence with respect to radii was plotted at various time-points after the addition of dye: 30-min (left column), 75-min (middle column), and 135-min (right column). The data are plotted versus a curve of the spheroid surface area as a function of radii. Each point represents a single spheroid Correlation analysis and K-S tests were performed to determine how the fit to surface area changed in response to altering dose and incubation time. The fit to surface area declined with lower dosages of calcein-RO and increased incubation times, as evidenced by lower correlation values.

CHAPTER 3

Quantitative Live-Cell Confocal Imaging of 3D Spheroids in a High Throughput Format

Elizabeth Leary [1, 2], Claire Rhee [1], Benjamin Wilks[1,2], Jeffrey R. Morgan [1, 2]

SLAS Technology. 2018. DOI: 10.1177/2472630318756058

Author Affiliation:
[1] Department of Molecular Pharmacology, Physiology and Biotechnology
[2] Center for Biomedical Engineering
Brown University
175 Meeting Street
Providence, Rhode Island, USA 02912

3.1 ABSTRACT

Accurately predicting the human response to new compounds is critical to a wide variety of industries. Standard screening pipelines (including both *in vitro* and *in vivo models*) often lack predictive power. Three-dimensional culture systems of human cells, a more physiologically relevant platform, could provide a high-throughput, automated means to test the efficacy and/or toxicity of novel substances. However, the challenge of obtaining high magnification, confocal z-stacks of 3D spheroids and understanding its respective quantitative limitations must be overcome first. To address this challenge, we developed a method to form spheroids of reproducible size at precise spatial locations across a 96-well plate. Spheroids of variable radii were labeled with four different fluorescent dyes and imaged with a high-throughput confocal microscope. 3D renderings of the spheroid had a complex bowl-like appearance. We systematically analyzed these confocal z-stacks to determine the depth of imaging, the effect of spheroid size and dyes on quantitation. Furthermore, we have shown that this loss of fluorescence can be addressed through the use of ratio imaging. Overall, understanding both the limitations of confocal imaging as well as the tools to correct for these limits are critical for developing accurate quantitative assays using 3D spheroids.

KEYWORDS: HTS High Throughput Screening, Data Analysis, Fabrication

3.2 INTRODUCTION

The ability to accurately model the complex responses of human tissues and organs in a laboratory setting is crucial for many fields including drug discovery and toxicity testing [1-5]. However, the current methods and models, which include both *in vitro* assays and *in vivo* animal testing, are often inadequate in their ability to predict how a compound will interact within the human body [1-3]. *In vitro* assays, which predominantly utilize two-dimensional (2D) cell monolayers, are relatively inexpensive, easy to perform, and have the potential to utilize human cells from various sources. However, 2D cell monolayers are limited due to significant differences with the *in vivo* environment including low cell densities, a predominance of cell-plastic interactions, a lack of diffusion gradients and, for certain cell types, dedifferentiation and a loss of organ-specific functions [6-8]. Alternatively, while animal models are able to recapitulate the complexity of the *in vivo* environment, they are expensive and time-consuming, thus limiting their usefulness to the evaluation of only very small numbers of compounds. Furthermore, animal models, due to species differences, often fail to predict the human response [9,10]. Three-dimensional (3D) multi-cellular spheroids have been proposed as an intermediate test bed [1,2,5,10]. Compared to animal testing, spheroids are inexpensive, easy-to-use, and have the potential to use human cells [1-3]. Furthermore, spheroids better approximate the cell density found *in vivo*, have increased levels of cell-cell interactions and intercellular communication, as well as maintenance of the differentiated state, and recapitulation of organ-specific processes [6-8, 11-14].

Despite the biological advantages of spheroids, there are numerous other issues that must be overcome to utilize spheroids as a high-throughput screening tool. For example, imaging of thin 2D monolayers is straightforward, whereas spheroids require more complex techniques to visualize the additional biology occurring within these relatively thick microtissues [2,15,16]. Histological techniques, such as cryo- and plastic sectioning, work well, but are time-consuming, low throughput, not appropriate for screening large number of spheroids, and not amenable to imaging live cells [15]. Alternatively, confocal and two photon microscopy optically section spheroids and can visualize living cells [17,18]. Furthermore, confocal microscopy has been configured as a high throughput instrument for purposes of high content imaging of large numbers of samples. However, due to light scattering, confocal microscopy has inherent limitations with respect to imaging thick tissues [15,18]. To overcome this limitation, tissue clearing methods that remove scattering substances and/or provide refractive index matching have been developed [18-21]. Although the depth of imaging is significantly improved, clearing can only be used on fixed non-living cells as part of an endpoint assay [18-21]. Endpoint assays are important, but not all assays can be performed as single point assays. Live-cell imaging enables users to examine dynamic changes over time, and gather more information.

To evaluate the usefulness of spheroids as a high-throughput screening tool, we developed a method to form spheroids directly within a 96-well plate, as well as examine the quantitative limitations associated with live-cell confocal imaging of spheroids. Through molding agarose hydrogels directly within a 96-well plate, we formed four spheroids of reproducible size that are located at precise *x, y, z*-locations across the entire plate. By varying the number of cells seeded per well, the size of the spheroids could be varied ranging 50 – 200 μm in diameter. To determine the depth of confocal imaging, spheroids were formed from cells that were uniformly labeled with four fluorescent dyes each with different excitation/emission wavelengths. Confocal *z* stacks were acquired and analyzed to evaluate the total and positional fluorescent signal for spheroids of variable sizes. As spheroid radii increased, the overall proportion of fluorescent signal retention was diminished. Furthermore, the fluorescent signal decreased as a function of *z* depth into spheroids of all sizes. Interestingly, loss of fluorescence across each *x, y* confocal slice of the spheroid was not uniform. Due to the curved nature of the spheroid, loss of fluorescence was least around the outer edges of the spheroid and greatest in the center of the spheroid, resulting in a bowl-like appearance in a 3D rendering of the spheroid. Unlike solid tissue blocks, the irregular spheroidal shape and subsequent bowl-like appearance makes it difficult to accurately model, quantitate, and correct the fluorescence throughout a 3D microtissue. However, we have shown that loss of the fluorescent signal can be addressed by ratio imaging. Overall, understanding and accounting for the fluorescent changes throughout confocal z-stacks of variable sized spheroids is critical for designing quantitative biological assays using spheroids.

3.3 MATERIALS and METHODS

3.3.1 Micro-mold fabrication and hydrogel formation.

Molds, designed using computer-assisted design (CAD) (Solidworks, Concord, MA), consisted of two main components: a base platform upon which lay a series of 4 rows by

8 columns of pegs (**Figure 3-1A**). The design of the peg consisted of three main components. Directly upon the base platform lay a cylinder shape designed to fit tightly within the inner diameter of a well, thus preventing shifting in the *x, y* direction. This cylinder was then funneled into a flat-top conical structure ending with a 2 row by 2 column array of conical-shaped micro-posts each positioned at the center of an imaging grid of the Opera Phenix. Molds were 3D printed (Phenomyx, LLC, Cambridge, MA).

To form hydrogels, 90-μL of sterile molten UltraPure Agarose (Fisher Scientific, Waltham, MA) (2% weight/ volume in phosphate buffered saline) was pipetted into each well and the mold was placed on top of the plate with the micro-posts submerged in agarose. After 10-minutes, the molten agarose solution solidified and the mold was removed. The resulting hydrogel that formed within each well contained a round loading dock above 4 micro-recesses (**Figure 3-1B**). To equilibrate the hydrogels, 150-μL of serum-free DMEM (Life Technologies, Grand Island, NY) supplemented with 1% penicillin/streptomycin was added to each well, and incubated for 24 hours at 37°C with 10% CO_2.

3.3.2 Cell culture, fluorescent dye labeling, and spheroid formation.

Human ovarian granulosa (KGN) cells were grown in DMEM with 10% fetal bovine serum (FBS) (Fisher Scientific, Waltham, MA) and 1% penicillin/streptomycin at 37°C with 10% CO_2. Once confluent, cell monolayers were labeled by first removing serum-containing medium from the culture flasks. Fluorescent dyes were reconstituted in serum-free DMEM, and incubated with the cell monolayer for 30-minutes at 37°C with 10% CO_2. Four dyes were used to stain monolayers: 2μM CellTracker^{TM} Red CMPTX (CTR) (Life Technologies, Grand Island, NY), 2μM CellTracker^{TM} Green CMFDA (CTG) (Life Technologies, Grand Island, NY), 2μM CellTracker^{TM} Violet (CTV) (Life Technologies, Grand Island, NY), and 2μM CellTracker^{TM} Deep Red (CTDR) (Life Technologies, Grand Island, NY). After labeling, medium was exchanged with fresh serum-free DMEM, and incubated for 15-minutes at 37°C with 10% CO_2. The labeled cell monolayers were harvested using 0.05% trypsin, concentrated by centrifugation at 120 *x g* for 6-minutes, and counted. Cells were washed once with serum-free DMEM and spun down at 120 *x g* for 6-minutes. Cells were re-suspended in serum-free DMEM at one of the following concentrations: 50,000-, 100,000-, 150,000-, 200,000-, 250,000-, 300,000-, 400,000-, 500,000-cells/mL A 20-μL aliquot of cell suspension was pipetted into the loading dock of each hydrogel to form four spheroids each composed of 250-, 500-, 750-, 1,000-, 1,250-, 1,500-, 2,000-, or 2.500-cells. After allowing the cell suspension to settle to the bottoms of the micro-recesses for 30-minutes, 150-μL of serum-free DMEM was added per well. Cells were allowed to self-assemble into spheroids for twenty-four hours prior to imaging.

3.3.3 Microscopy and image analysis measurements.

To image spheroids, the Opera Phenix^{TM} High Content Screening System (Perkin Elmer, Waltham, MA, USA), an inverted confocal microscope equipped with proprietary Synchrony^{TM} Optics consisting of a Nipkow spinning microlens disk in conjunction with a pinhole disk and 2 sCMOS cameras, was used. Fluorescent images for each dye were acquired using the 20x water objective in conjunction with 4 excitation lasers: 405-nm for CTV, 488-nm for CTG, 561-nm for CTR, and 640-nm for CTDR. Confocal z-slices of spheroids were acquired every 5-μm for a total of 500-μm.

Confocal z-slice images were analyzed via two different image analysis software programs: Imaris (Bitplane, Belfast, UK) and ImageJ (National Institutes of Health, Bethseda, MD, USA). With Imaris, confocal slices were rendered as 3D objects, and a mask of the outer spheroid surface was created. Total volume was measured for each spheroid, and its average radii was computed by the following equation: $r = \sqrt[3]{\frac{3}{4}\frac{Vol.}{\pi}}$. ImageJ was used to measure the following parameters at every confocal slice: cross-sectional area, total fluorescence of cross sectional area, average fluorescent intensity across the radii.

3.3.4 Data analysis and derivation of ideal curves.

To evaluate fluorescence, and its subsequent loss due to imaging limitations both the measured and maximum hypothetical fluorescence were computed per slice. The measured fluorescence for each slice was plotted as a function of its *z*-depth, and the area under the curve (AUC) was calculated (**Supplemental Figure 3-1B, D**). To calculate the hypothetical fluorescence, the following assumption was made: since all cells of the spheroid were evenly stained as a cell monolayer prior to spheroid formation, the signal was assumed to be homogenous throughout. Therefore, cross-sectional area should increase linearly with respect to fluorescence for each slice up until the equator. To determine the hypothetical signal, fluorescence was plotted as a function of cross-sectional area, and the best-fit line for the linear region of the curve was determined to be "$y = mx + b$" (**Supplemental Figure 3-1A**). The hypothetical values for each slice were computed by the following equation " $Fl_{hyp} = m\ (CSA) + b$ " (**Supplemental Figure 3-1B**). The hypothetical fluorescence was plotted as a function of its z-depth, and the AUC was calculated (**Supplemental Figure 3-1C**). The total loss of fluorescence for each spheroid was computed as the difference between the hypothetical and measured AUC normalized by the hypothetical AUC (**Supplemental Figure 3-1E**). Spheroids were binned based upon size into 10-µm bins, and the average and standard deviation for each dye was computed.

To evaluate alterations of fluorescent signal within a spheroid, the center of the spheroid was identified, then on each confocal slice a series of concentric rings was propagated outwards from the center point (**Supplemental Figure 3-5C**). The fluorescent values around each concentric circle were then averaged to yield the average fluorescent signal across the cross-sectional radii (x, y) (**Supplemental Figure 3-5C**). The average fluorescent signal was then plotted as a function of its cross-sectional radii for each confocal slice throughout the spheroid.

To evaluate the fluorescent loss throughout the z-dimension, the center of the spheroid was identified, and the average fluorescent intensity was computed along that central z-axis for each slice (**Figure 3-5B**). The average intensity of each point was normalized by the maximum fluorescent intensity along the central z-axis for each spheroid. This normalized average intensity was plotted as a function of z-depth. The best-fit exponential decay function was calculated from 50-μm past the peak signal for every spheroid, according to the following equation: "$y = Ce^{mx}$", where "y" is normalized average fluorescence, "x" is z-depth, "m" represents the rate of loss. Spheroids were binned based upon 10-μm sized bins, and the average and standard deviation of the slope of the exponential decay function each dye was computed and plotted as a function of spheroid radii.

To evaluate the ability of ratio imaging to mitigate fluorescent loss throughout the z-depth, the average fluorescence along the central *z*-axis was measured for spheroids pre-labeled with both CTG and CTDR as 2D monolayers. To perform ratio imaging, the CTG fluorescence was divided by the CTDR fluorescence at each *z*-slice and vice versa. Both the average and normalized fluorescence were plotted as a function of spheroid *z*-depth. The average and standard deviation of the fluorescence throughout the *z*-depth was computed for both pre-and post-normalization. To compare the effect of ratio imaging, a coefficient of variation (CV) analysis was performed for both pre- and post-normalization of the fluorescence throughout the *z*-depth. Lower CV values indicate less variation throughout the *z*-depth.

3.4 RESULTS

3.4.1 Tri-axis positional control of spheroid formation in a 96-well plate for confocal imaging.

To increase the throughput of spheroid formation, we designed a mold insert compatible with a 96-well plate. The micromold consisted of a series of pegs, where each peg was designed to fit within the dimensions of one well (Figure 1A). Furthermore, atop of each peg, were four conical shaped micro-posts, thus enabling the formation of four technical replicates per well. To minimize the imaging area and the number of confocal slices, the micro-pegs and were designed to fall within the same spatial location in every well. Therefore, after adding agarose into 96-well plate, the resulting hydrogel consisted of four micro-wells with the same *x, y, z* locations in every well (**Figure 3-1B**).

To evaluate the accuracy of the mold, spheroid formation was measured with respect to two different assessments: (1) the *x, y, z* location in each well, and (2) spheroid radii. Monolayers of KGN cells were labeled with CTR, trypsinized, counted, and seeded into hydrogels to form spheroids (~750 cells). After 24-hours, confocal slices were acquired using the 20X water objective and analyzed to measure *x, y, z*- position as well as spheroid radii. Spheroids formed in specific locations within the *x, y*- bounds of the 646-by 646-μm imaging grid system of the microscope (**Figure 3-2A**). Furthermore, spheroids formed within a 200 μm range of z-locations, approximately centered 650 μm from the bottom of plate (**Figure 3-2B)**. To assess reproducibility of size, we seeded plates with either the same or varying concentrations of monodispersed cells. When seeding ~750 cells per spheroid across the entire plate, the average radii was 54.2-µm +/-

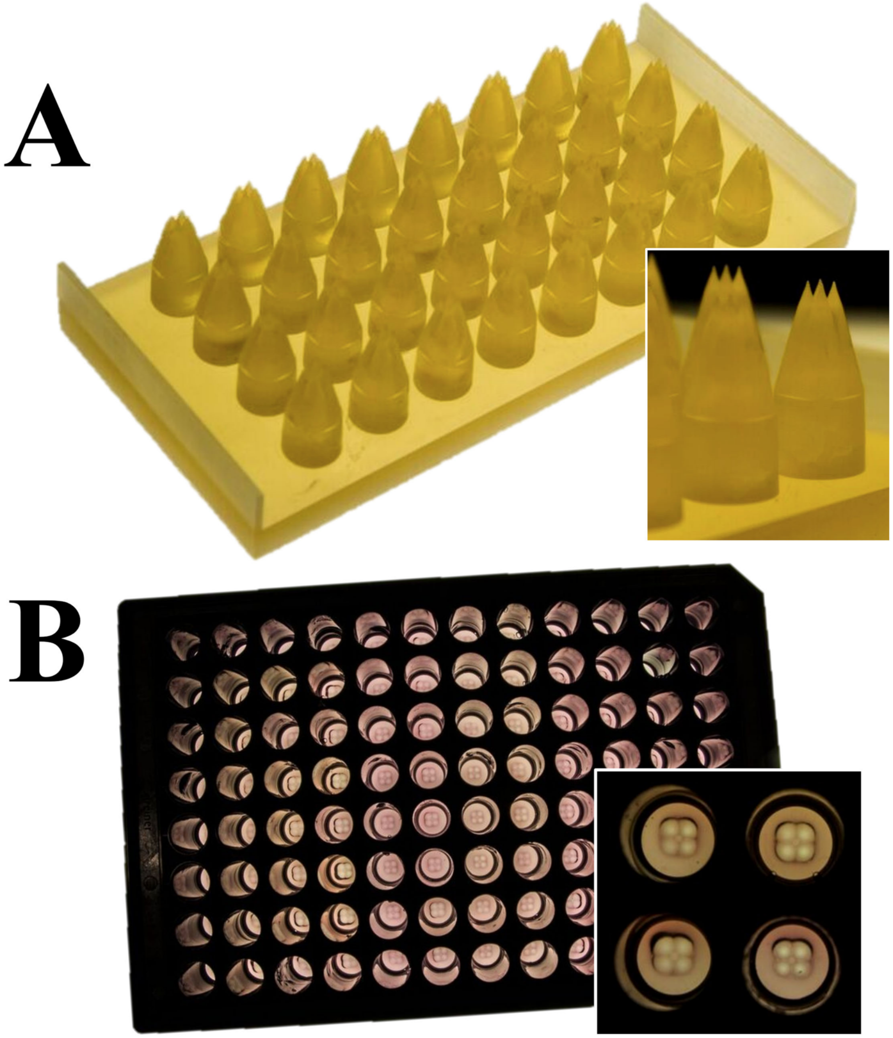

Figure 3-1. Molding system to form micro-wells for four spheroids per well in a 96-well plate. Molds designed in CAD, consisting of an array of 4 rows by 8 columns of pegs, with each peg containing 4 micro-posts, were 3D printed (A). To create hydrogels, molten agarose was pipetted into each well of a 96-well plate, and the mold placed atop. After the agarose gelled, the mold was removed, leaving a hydrogel containing a square loading dock atop of 4 micro-recesses for spheroid formation (B).

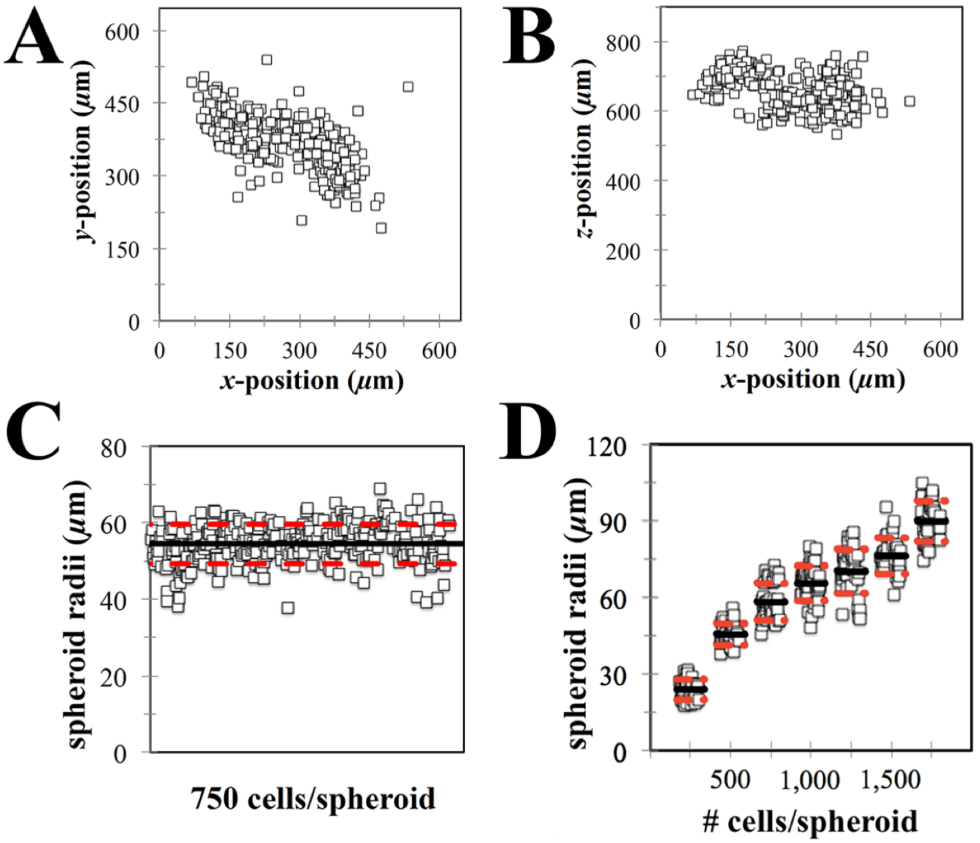

E

Seeding Density (cells/spheroid)	***750***	***250***	***500***	***750***	***1,000***	***1,250***	***1,500***	***2,000***
Average (µm)	54.2	24.0	45.6	58.3	65.6	70.2	76.4	90.0
St. Dev (µm)	5.2	4.0	4.2	7.2	6.7	8.7	6.9	7.9

Figure 3-2. Spheroids of consistent size are formed within specific *x, y, z*-locations. Molds were used to produce agarose hydrogels directly into the wells of a 96-well plate. Monodispersed cells were seeded into the hydrogels at either i.) a single seeding density for the entire plate (A, B, C, E), or ii.) multiple seeding densities (D, E). After 24 hours of self-assembly, confocal images of the spheroids were obtained using the 20X water objective and analyzed. All spheroids were located within the bounds of one of the 646- x 646-µm (*x, y*)-imaging grids used by the 20X objective (A). Spheroids were located within approximately a 200-µm range of *z*-height, centered approximately 650-µm from the bottom of the plate (B). When using a single cell seeding density to form spheroids, the average spheroid radii was 54.2 µm +/- 5.2 µm standard deviation (C, E). Alternatively when using multiple seeding densities, spheroid size increased in a dose-dependent manner with higher seeding densities yielding larger spheroids (D, E). Regardless of seeding density used, the standard deviation accounted for approximately 10% of the average (C, D, E).

5.2-μm, thus deviation was approximately 10% of the mean **(Figure 3-2C)**. Furthermore, when seeding varying concentrations, (~250- to ~2,000- cells/spheroid), the higher seeding densities yielded larger spheroids (**Figure 3-2D**). Regardless of the seeding density, the standard deviation was approximately 10% of its mean (**Figure 3-2D, E**).

3.4.2 Cumulative fluorescent loss increases as function of spheroid radii.

To assess the loss of fluorescence associated with live-cell confocal imaging of spheroids, we imaged spheroids over a range of sizes and tested four different fluorescent dyes. To form uniformly labeled spheroids, KGN cell monolayers were first labeled with four different fluorescent dyes: CellTracker^{TM} Violet (CTV), CellTracker^{TM} Green CMFDA (CTG), CellTracker^{TM} Red (CTR), CellTracker^{TM} Deep Red (CTDR). After labeling, monolayers were trypsinized, counted, seeded at various cell densities to form spheroids with diameters ranging from 50μm - 200μm. After self-assemlbing for 24-hours, confocal slices for each spheroid were obtained (20X water objective). Representative images for a 50-μm, 100-μm, and 150-μm diameter spheroids were reconstructed as orthogonal contrasts for the four dyes tested (**Figure 3-3, Supplemental Figures 3-2, 3-3, 3-4**). Since the cells were labeled as a monolayer prior to spheroid formation, hypothetically every cell in the spheroid should be evenly stained. Assuming there was no loss in fluorescence due to imaging limitations, the resulting spheroids should possess a homogenous signal throughout the entire spheroid. Qualitatively, for the four dyes tested, the signal was relatively homogenous throughout small spheroids (50-μm diameter). However, as radii increased, the signal decreased for confocal slices located deeper into the spheroid (**Figure 3-3, Supplemental Figures 3-2, 3-3, 3-4**).

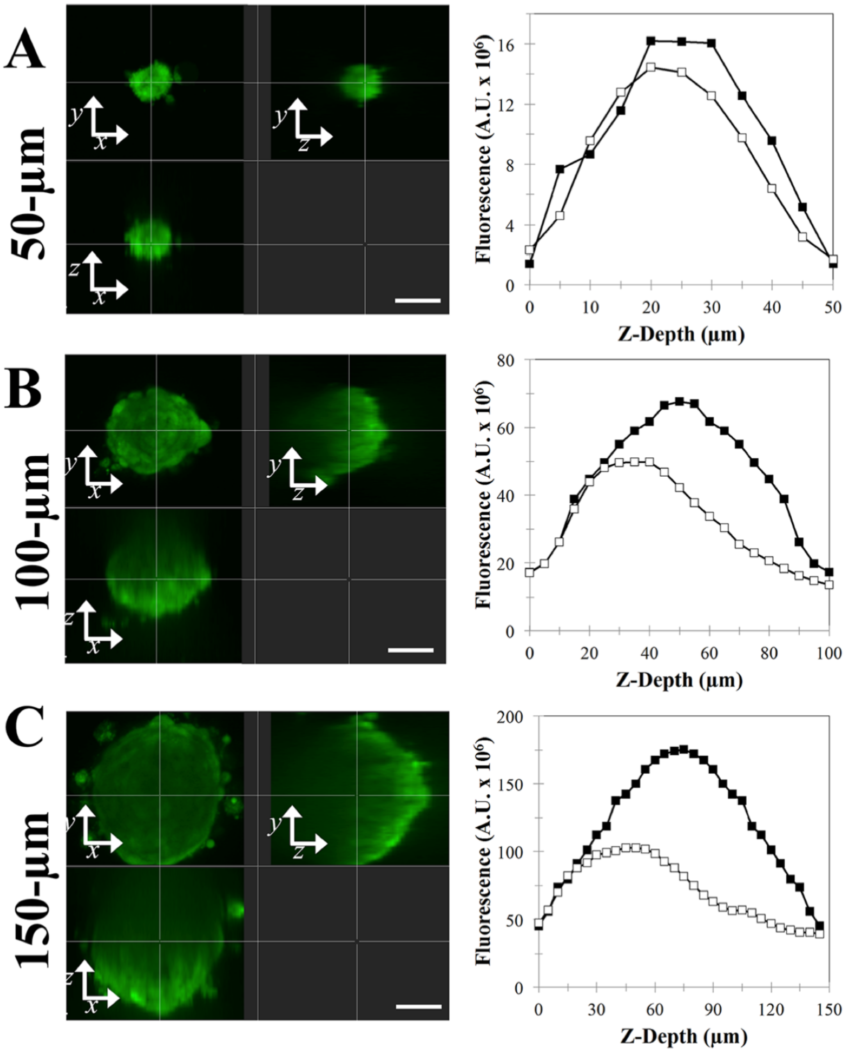

Figure 3-3. Loss of fluorescent signal occurs deeper within the z-depth for spheroids. KGN cell monolayers were labeled with CTG, trypsinized, counted, and seeded at varying cell numbers to form spheroids with diameters ranging from 50-μm to 200-μm. Confocal images were acquired, and orthogonal contrast images of representative spheroids of 50-μm (A), 100-μm (B), and 150-μm (C) diameters were rendered (left column). For each spheroid, the measured fluorescence at each confocal slice was plotted as a function of its *z*-depth (white squares). The data are plotted versus the hypothetical fluorescence for each confocal slice, which was calculated assuming no loss of fluorescent signal (black squares). Representative graphs for spheroids with a 50-μm (A), 100-μm (B), and 150-μm (C) diameters are shown (right column). For small spheroids (50-μm), the plot of measured and hypothetical fluorescence were mostly overlapping throughout the z-depth (A, right column) As spheroids increased in radii, the plots of measured fluorescence fell short of hypothetical fluorescence as z-depth into spheroid increased (B, C right column). (scale bar is 40-μm).

To understand this loss of fluorescence with increasing depth into larger spheroids, we quantified the total fluorescent signal loss for each spheroid and compared populations of spheroids of varying sizes. The actual and hypothetical fluorescence at every confocal slice was measured and plotted as a function of its *z*-depth (**Figure 3-3, Supplemental Figures 3-2, 3-3, 3-4**). Assuming no loss, the plot of actual fluorescence should match the plot of hypothetical fluorescence. For small spheroids (diameter of 50-μm), the plots for measured and hypothetical fluorescence were overlapping, indicating minimal loss for each of the following dyes: CTR, CTG, CTV, CTDR (**Figure 3-3A, Supplemental Figures 3-2A, 3-3A, 3-4A**). For medium and larger sized spheroids (diameters of 100-μm and 150-μm), the plots for measured and hypothetical fluorescence overlapped only through the lower portion of the *z*-depth. Beyond which, the plot of measured fluorescence falls short of the plot of hypothetical fluorescence (**Figure 3-3B, C, Supplemental Figures 3-2B, C, 3-3B, C, 3-4B, C**). Since all cells were homogenously labeled, the extent to which the plot of the measured fluorescence falls short of the plot of the hypothetical fluorescence is the loss due to imaging thick tissues.

To compare the effect of spheroid size on imaging, we quantified the difference between actual and hypothetical fluorescence for all dyes. The area under the curve (AUC) was calculated for actual and hypothetical fluorescence as a function of *z*-depth, and the percent loss was computed (**Supplemental Figure 3-1C, D, E)**. The percent loss was binned as a function of radii, then plotted for each of the dyes tested (**Figure 3-4**). The percent loss of fluorescence increased as spheroid radii increased (**Figure 3-4**).

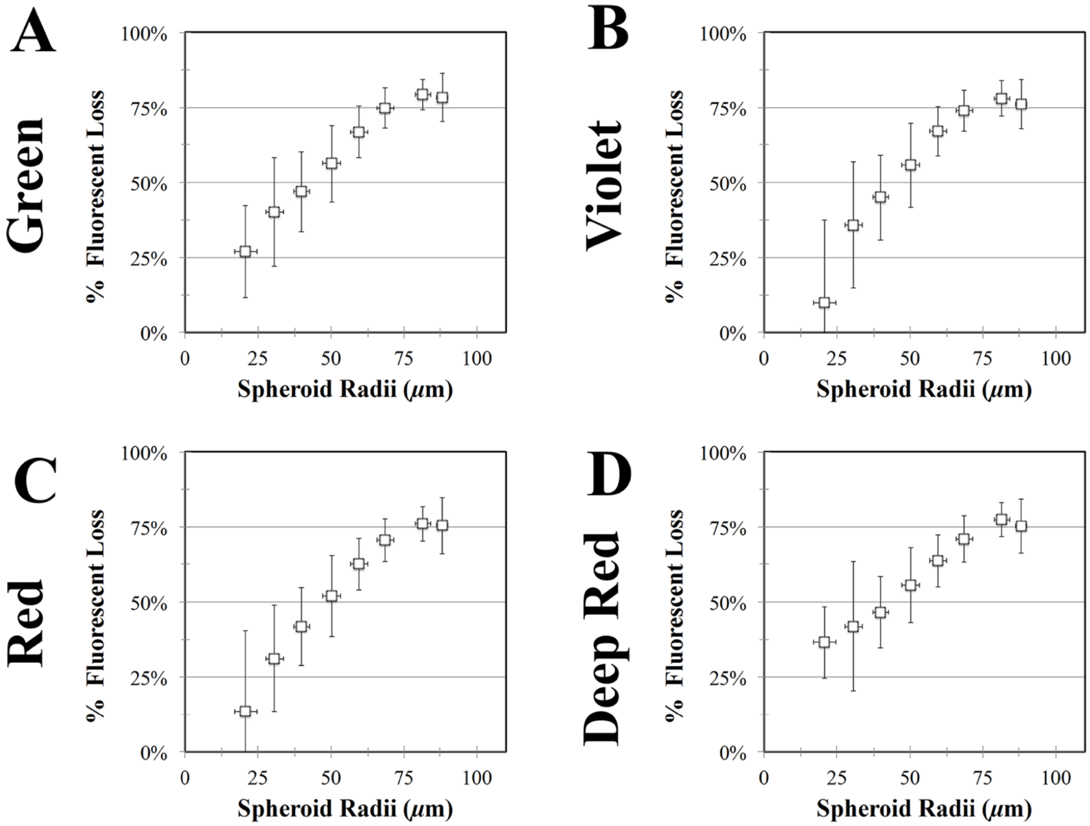

Figure 3-4. Cumulative loss of total spheroid fluorescence increases as a function of spheroid radii. KGN cell monolayers were labeled with four fluorescent dyes: CTR, CTV, CTG, CTDR. After staining, monolayers were trypsinized, counted, and seeded at varying cell numbers to form spheroids of range of sizes. Confocal images were analyzed to determine the actual fluorescence per confocal slice and hypothetical fluorescence per slice, and both were plotted as a function of *z*-depth. By calculating the area under the curves for both actual and hypothetical fluorescence, the cumulative fluorescent loss of each spheroid was determined. Spheroids were binned into 10-μm bins based on radii. The average percent loss of fluorescent signal was calculated for each range of radii and plotted as a function of radii for each of following fluorescent dyes: CTG (A), CTV (B), CTR (C), and CTDR (D). For the four dyes tested, as radii increased, cumulative fluorescent loss also increased.

3.4.3 Within spheroids, loss of the fluorescent signal is dependent upon the positional (x, y, z) location.

To assess where signal loss was occurring throughout the spheroid, we imaged spheroids over a range of radii and tested different fluorescent dyes. KGN cell monolayers were homogenously labeled with four different dyes (CTG, CTV, CTR, CTDR), trypsinzed, and seeded at varying cell densities to form spheroids with diameters ranging from 50μm - 200μm. After 24-hours, *z*-stacks were acquired, and the center point of each spheroid was identified. Representative confocal slices (x, y) were assessed at 30°north of, 30°south of, 60°south of, and the equator of a spheroid (~100μm diameter) stained with CTG (**Supplemental Figure 3-5B**). For confocal slices south of the spheroid equator (30° and 60°south), the fluorescent signal was relatively homogenous and bright across the entire slice (**Supplemental Figure 3-5B**). However, deeper into the *z*-depth (equator and 30°north), the fluorescent signal began to decrease preferentially in the center of each slice, whereas the outer edge of the spheroid retained a brighter signal (**Supplemental Figure 3-5B**). To quantify this pattern, the average fluorescence across the cross-sectional (*x, y*) radii was computed by averaging individual fluorescent values from a series of concentric rings (**Supplemental Figure 3-5C**). The average fluorescent signal was plotted as a function of its cross-sectional radii for the confocal slices 30° and 60°north of, 30° and 60°south of, and the equator for spheroids of variable radii (**Supplemental Figure 3-5C, D, E**). For smaller spheroids (~50μm diameter), the average fluorescent intensity across the cross-sectional radii was relatively constant across the confocal slice up until the equator, above which there was a decline in signal (**Supplemental Figure 3-5C**). For larger spheroids (~150μm diameter), fluorescent signal was relatively homogenous throughout the confocal slice corresponding to 30°south, however, fluorescence of the confocal slices deeper into the spheroid had a measurable decrease in the center as compared to the spheroid edge (**Supplemental Figure 3-5E**). Similar trends were observed for all dyes tested (data not shown). This pattern of fluorescent signal yields a “bowl-like” appearance in 3D renderings, with the brightest signal occurring along the bottom hemispheric edge of the spheroid (**Figure 3-5B**).

To compare the effect of spheroid size on this fluorescent loss throughout a spheroid, we first quantified the distance into live spheroids that could be imaged along the central *z*-axis (**Figure 3-5B**). For each spheroid and dye, the average intensity was first normalized by the maximum fluorescent signal along the central axis. The normalized signal was plotted as a function of its *z*-depth and the best-fit exponential decay curve was calculated from 50-μm past the peak signal (**Figure 3-5C, D, E**). Fluorescent dyes exhibited different staining patterns. For example, CTG staining was a homogenous uniform signal throughout the spheroid, whereas CTR staining was a more randomized punctate signal (**Figure 3-3 left column, Supplemental Figure 3-3 left column**). Dyes with a homogenous signal, also exhibited a reproducible exponential decline in fluorescent signal throughout the spheroid (**Figure 3-5**). Alternatively, dyes with a punctate signal exhibited a more variable sawtooth-like decrease in signal throughout (**Supplemental Figure 3-6B**). For all dyes, best-fit lines containing correlation values lower than 0.9 were excluded from further analysis.

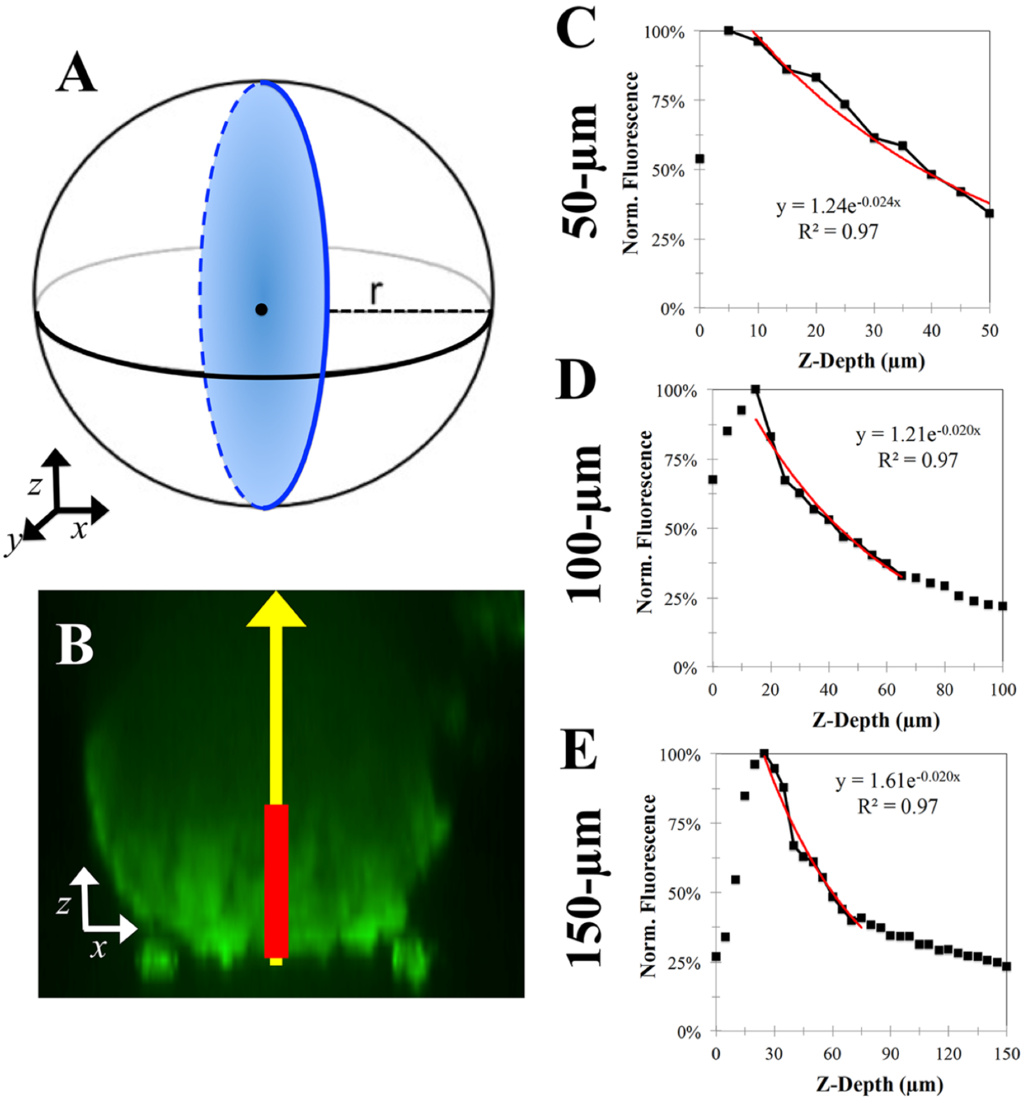

Figure 3-5. Fluorescent signal loss throughout the z-depth of spheroids exhibits a reproducible, exponential decay function. KGN cell monolayers were labeled with CTG, trypsinized, counted, and seeded at varying cell numbers to form spheroids with diameters ranging from 50-µm to 200-µm. After 24-hours, confocal images were acquired and cross-sectional images (*x, z*) were reconstructed (A,B). Fluorescent signal loss results in a reproducible "bowl"-like pattern throughout spheroids, where brightest signal occurred along outer spheroid edge up until the equator, where the signal was dimmer in central portions (B). To assess the distance into live spheroids that could be imaged, the average fluorescent intensity was measured along that central *z*-axis for each confocal slice (B, yellow line). For each spheroid, the average intensity was normalized by peak fluorescent signal, plotted as a function of its *z*-depth, and the best-fit exponential decay curve was calculated from 50-*µ*m past the peak signal (B, red line). Representative graphs for spheroids with a 50-µm (C), 100-µm (D), and 150-µm (E) diameters are shown.

To compare the effect of size on depth of imaging, we compared the slope of the exponential decay function from spheroids of variable radii. Slope was binned as a function of radii, then plotted for each dye (**Figure 3-6**). For the four dyes tested, the slope of the exponential decay function increased as radii increased, indicating that smaller spheroids possessed a steeper decline in signal throughout the *z*-depth when compared to larger spheroids (**Figure 3-6**).

3.4.4 Ratio imaging corrects for loss of fluorescence throughout the *z*-depth.

To determine if ratio imaging could be used to correct for loss throughout the z-depth, KGN cell monolayers were uniformly labeled with both CTR and CTDR, trypsinized, and seeded at varying cell densities to form spheroids of variable radii. After 24-hours, confocal *z*-stacks were acquired and fluorescence along the central z-axis was measured (**Supplemental Figure 3-5B**). Fluorescence of both CTG and CTDR were plotted as a function of *z*-depth (**Figure 3-7A, B**). Since the spheroid was uniformly with both dyes, fluorescence should hypothetically be the same throughout the *z*-depth, however, the signal of both dyes declined as a function of *z*-depth (**Figure 3-7A, B**). To normalize the attenuation, CTG fluorescence was divided by CTDR fluorescence at each confocal slice, and vice versa. This normalized signal was then plotted as a function of *z*-depth (**Figure 3-7C, D**). Once normalized, both dyes exhibit a more uniform signal throughout the *z*-depth (**Figure 3-7C, D**).

To confirm quantitatively that ratio imaging yielded a more uniform signal throughout, we performed a coefficient of variation (CV) analysis, according to the following

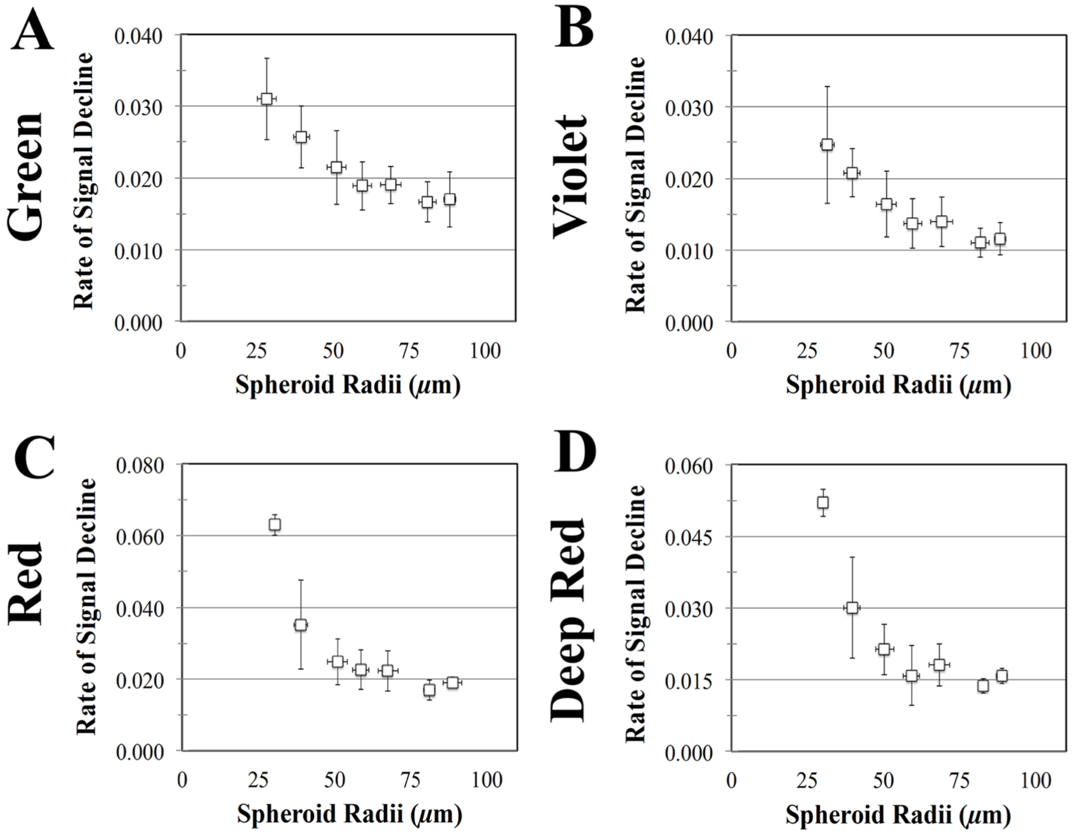

Figure 3-6. Cumulative loss of total spheroid fluorescence increases as a function of spheroid size. KGN cell monolayers were labeled with four fluorescent dyes: CTR, CTV, CTG, CTDR. After staining, monolayers were trypsinized, counted, and seeded at varying cell numbers to form spheroids of range of sizes. Confocal images were analyzed to determine the average fluorescent signal along the central *z*-axis, which was then normalized to peak fluorescence, and plotted as a function of *z*-depth for every spheroid. The best-fit exponential decay was calculated from 50-*μ*m past the peak signal. To evaluate the effect of spheroid size on the rate of loss, the slope of the exponential decay function was compared. Spheroids were binned into 10-μm bins based on radii. The average slope was calculated for each range of radii and plotted as a function of radii for each of following fluorescent dyes: CTG (A), CTV (B), CTR (C), and CTDR (D). For all dyes tested, the slope of the exponential decay function increased as a function of spheroid radii, which implied that the rate of signal loss was greater for small spheroids versus larger spheroids despite being the same cells and labeled with the same dye.

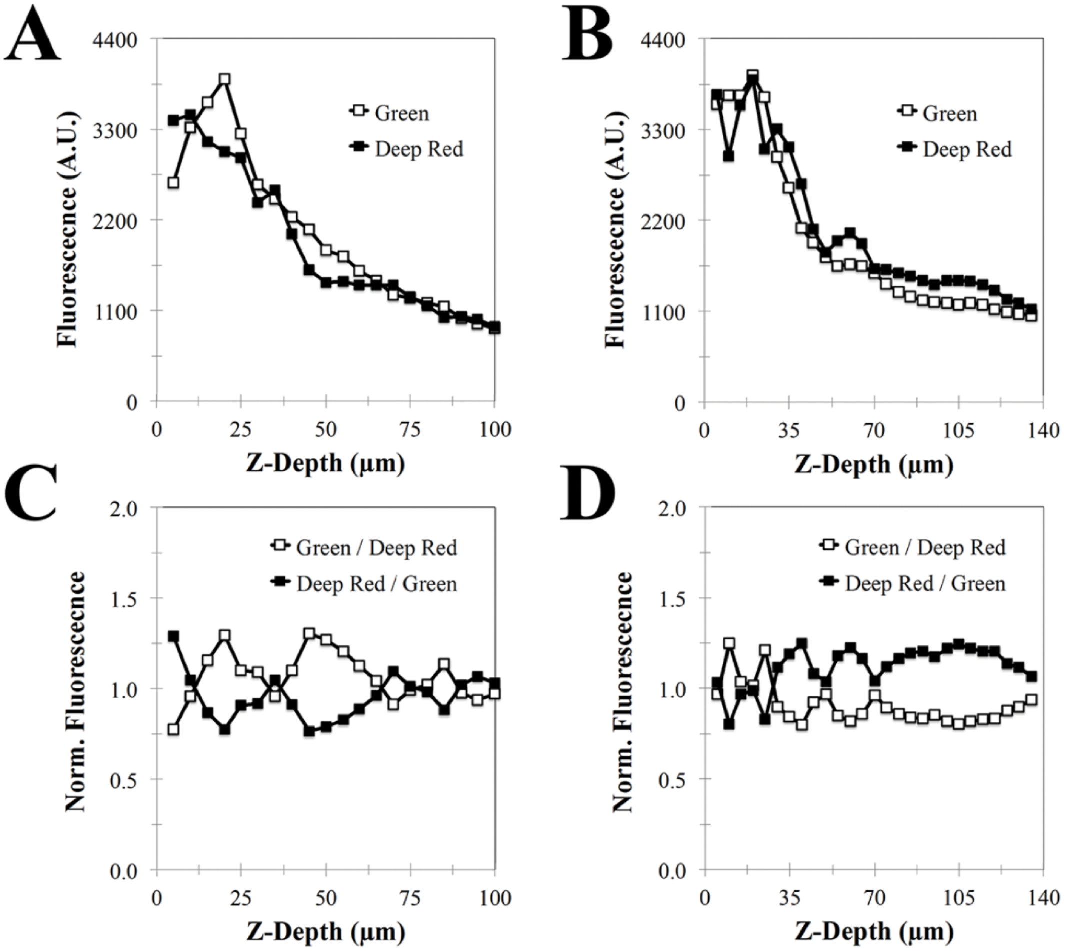

E

Fluorescent normalization	***spheroid A (radius = 50-um)***		***spheroid B (radius = 75-um)***	
	Green	*Deep Red*	*Green*	*Deep Red*
pre-	0.47	0.47	0.51	0.42
post-	0.13	0.13	0.12	0.11

Figure 3-7. Ratio imaging reduces variation throughout the z-depth. KGN cell monolayers were labeled with both CTG and CTDR, trypsinized, counted, and seeded at varying numbers to form spheroids. After 24-hours, confocal images were acquired and analyzed to measure the fluorescent signal along the central z-axis. Data from two representative spheroids are shown (A, C – 50μm radii; B, D – 75μm radii). The signal for both CTG (green) and CTDR (red) was plotted as a function of *z*-depth (A, B). To perform ratio imaging, the signal of each dye was divided by the other dye at each slice, and plotted as a function of its *z*-depth (C, D). To evaluate the effect of ratio imaging, the average and standard deviation of fluorescent signal along the central *z*-axis was computed. A CV analysis was performed for each spheroid for each dye both pre- and post-normalization (E). Lower CV values indicate less variation throughout the z-depth (E).

equation: $CV = \frac{st.dev.}{average}$. For every spheroid and each dye, the average and standard deviation of fluorescence throughout the entire z-depth was computed both pre- and post-normalization. Hypothetically, assuming there was no loss, fluorescence should be homogenously labeled throughout the *z*-depth, thus possessing a low standard deviation relative to the average. However, without normalization, fluorescence decreases throughout the *z*-depth for both CTG and CTDR, resulting in a CV of approximately 0.5 (**Figure 3-7E**). However, after normalization of the CTG signal to the CTDR signal and vice versa, the CV value was reduced to approximately 0.12 showing that variation in fluorescence throughout the z-depth can be reduced by ratio imaging.

3.5 DISCUSSION

Needed for drug discovery and toxicity testing are new, more predictive high throughput *in vitro* assays that more accurately mimic the biological complexity of human organs and tissues [1,2,5,22]. Multi-cellular spheroids are emerging as a possible solution, but challenges still remain with respect to work flow, spheroid formation, long term stability of spheroids and the high magnification imaging of spheroids necessary to acquire the quantitative high content information that spheroids can provide [1,2,5,10,23]. In addition to improved *in vivo*-like differentiation and function, much of this high content information is due to the fact that, like native tissues, spheroids have multiple cell layers that create gradients (e.g., oxygen, nutrients, metabolites) and barriers (e.g., drug transport, signaling) [4,6-8,24]. Biological activities in these microenvironments can be probed using a wide variety of fluorescent dyes along with confocal microscopy. But, to assess these activities as a function of radial position within a spheroid, it is critical that the images are high magnification to get accurate quantitative depictions.

In this paper, we aimed to increase assay throughput by designing and evaluating a mold system that formed spheroids directly within a 96-well plate, and then imaging the plate using a 20X water objective of a high-throughput confocal microscope. We acquired *z* stacks of living spheroids that were uniformly labeled with four different fluorescent dyes and quantified the loss of fluorescent signal as we imaged deeper into each spheroid. Unlike planar specimens where signal loss is a relatively simple function of *z*-depth, the curved nature of spheroids creates a more complex pattern. In 3D renderings, spheroids appear as bowl-like with a bright signal around the edges and a dampened signal in the interior. To better understand fluorescence signal distribution prior to developing biologically-driven assays, we quantified fluorescence of four dyes as a function of overall signal from entire spheroid, the rate of decrease throughout the z-depth, as well as the influence of spheroid size on these stacks of images. Furthermore, we used ratio imaging to demonstrate that loss throughout the *z*-depth can be compensated.

Prior to assessing fluorescence signal, we first designed and evaluated the mold's ability to form spheroids of reproducible size at precise locations. We molded four micro-wells into agarose in each well of a 96 well plate, thus forming four replicate spheroids per well that were placed at precise *x, y* and *z* locations within each well. The *x, y* locations corresponded to the centers of the four boxes in the imaging grid used by the 20X water objective. These *x, y* locations improve work flow by obviating the need to pre-scan a plate to find spheroid locations and/or having to stitch together adjacent images of spheroids that span grid lines. Placement of spheroids in a precise *z* location also improves work-flow since spheroids can be found at a predictable distance from the plane of initial focus. This fixed position reduces the number of confocal *z* slices needed to reliably image the entire spheroid. Moreover, the autofocus function can be used with our design because, unlike round bottom low attachment plates typically used to form spheroids in a high-throughput format, our mold is compatible with flat bottom well plates. Although agarose micro-wells are curved to aid in the self-assembly of spheroids, agarose has a refractive index nearly equal to that of water (1.334 vs. 1.3329 of water), thus should not scatter light more significantly than a water interface would [25]. Lastly, the agarose micro-wells have been shown to provide a stable cell culture platform for the long term, up to 4-week culture of spheroids of certain cell types [14,15,26].

We controlled spheroid size by altering the number of cells seeded into each well. When the same number of cells were seeded across an entire plate, the variation of spheroid radii was approximately 10% of its mean. Spheroid size could be controlled by altering the input number if cells, with higher seeding densities yielding larger spheroids. Over the range of sizes tested, variation of spheroid radii was also approximately 10% of the mean for all sizes. A number of factors probably contribute to variation in spheroid radii including pipetting errors and variation of the radius of the input cells (KGN cells 12 +/- 1μm). Control over spheroid size and uniformity of size are important because the biology of spheroids is often linked to their size. For example, spheroids with diameters significantly greater than 200μm often have necrotic cores with dead and dying cells due to the limitations of diffusion. For some cancer models, large spheroids with necrotic cores are thought to mimic the complexity of tumors *in vivo* [12,22,27]. But for other assays, such as those that use primary cells or that wish to replicate normal physiology, smaller spheroids are preferable with their high viability and lack of confounding influences associated with apoptotic/necrotic core.

Furthermore, the ability to perform confocal microscopy of an entire spheroid is dependent on their size. For small spheroids with diameters in the range of 50μm, we found there was minimal loss of fluorescence throughout the *z* stack. The entire spheroid could be imaged and for each slice the increase in cross-sectional area of the spheroid correlated with an increase in the total fluorescence. This was true for all four dyes tested. Depending on the assay, small spheroids may be sufficient. Our spheroids with 50μm diameters contain approximately 2-3 cell layers from the surface of spheroid to its edge. This number would vary depending on a number of factors including the oblate shape of the spheroid, the size of the cell type used and if the spheroid undergoes morphological changes such as the formation of luminal structures [15]. For assays using small spheroids that want to quantitate activity as a function of radius, an entire *z* stack could be obtained or a single confocal slice at about the equator may be sufficient for analysis.

Some assays may require larger spheroids with increased cell layers, however, we found that for spheroids with diameters above 50μm, there was an associated loss of signal. For all dyes tested, the signal loss increased as spheroid radii increased. Most importantly, this loss was not uniform throughout the spheroid. Unlike a planar specimen that will undergo uniform loss across each slice of a z-stack, in a spheroid, the loss of fluorescence was far greater in the interior versus its outer edges due to its curvature. Additionally, confocal slices beyond a certain z-depth into a spheroid are not accurate quantitative representations of fluorescence as a function of radial position within that slice, since the signal from interior portions would not differ from background noise. Furthermore, we hypothesized that regardless of size, the rate of loss throughout the central *z*-axis would exhibit an exponential decay function with similar rate of loss for first 50μm. However, even the rate of fluorescent decrease throughout the *z*-depth was dependent upon spheroid size, with smaller spheroids possessing a steeper rate than larger ones. This might imply that smaller spheroids scatter light more than large spheroids, despite possessing the same starting cell types and dyes. Therefore, to avoid differences between large and small spheroids, restricting spheroid size to a set range of radii would be beneficial when developing quantitative fluorescent assays.

This non-uniform overall fluorescent signal and its variable rate of loss complicates the ability to compensate for signal loss throughout a *z*-stack. To address the shortcomings associated with confocal imaging of large spheroids, there are various methodologies and approaches. For example, the depth of imaging in cleared samples is increased [19-22]. Although we have not tested it, we suspect that, like our live cell experiments, there is a reliable depth into cleared samples from which accurate radial information can be obtained from a given slice. However, utilizing this technique limits the type of assays that can be performed to fixed, end-point assays, since clearing is not compatible with live cell imaging. An alternative approach to acquiring live cell images deep within large spheroids could be the use of two photon microscopy, however we are not aware of a two photon microscope designed for high throughput automated imaging. Alternatively, one could limit spheroid size, 3D portions, or single confocal slices of spheroids to analyze only a set size and z-depth, where reliable quantitative information can be obtained. As shown by the data with small spheroids, this distance may be about 50μm. However, depending on the experimental assay, data from small spheroids or portions of spheroids may not be accurate quantitative depiction and require the use of larger spheroids. Additionally, to compensate for signal loss and reduce variability throughout the *z*-depth, one could utilize ratio imaging, however, ratio imaging does not overcome the physical limitations of confocal microscopy, and thus is still only effective for certain range of sizes.

Overall, the use spheroids for high throughput screening affords numerous advantages, including *in vivo*-like differentiation, function and architecture, as well as drug sensitivities comparable to tumors [6-7,27,29]. Moreover, spheroids have been formed from immortal cell lines as well as primary cells [14,15,26]. Additionally, since they are self-assembled from mono-dispersed cells, spheroids have been formed from mixtures of two or more cell types to make designer spheroids that can mimic even more complex tissue units [30]. Applications of spheroids, some of which have been adapted to high throughput formats, include toxicity testing, drug transport, and drug discovery [3,4,23,24]. Spheroids also create complex microenvironments that include gradients, barriers, polarity, cell-cell signaling as well as significant changes to cell physiology, morphology and differentiation [2,4,5]. These changes to the microenvironment will vary along the 3D radius of a spheroid. To accurately quantify these biological changes as a function of radii, the quantitative limitations of confocal imaging of spheroids must be understood. In this paper, we addressed some of the challenges of quantifying the bowl-like 3D image of spheroids. These studies set the stage for designing quantitative spheroid based assays for automated high throughput screening.

3.6 AUTHOR CONTRIBUTIONS

E.L. and C.R. designed and performed the series of experiments. B.W. designed ImageJ analysis programs. J.R.M. supervised the project. All authors contributed towards writing the manuscript.

3.7 ACKNOWLEDGEMENTS

This work was funded in part by seed funds from Unilever and the generous support of Donna McGraw Weiss '89 and Jason Weiss. Also, this work was funded under the US Department of Education, GAANN Award P200A150037. We thank Microtissues, Inc. for the mold used to make the 96 well plates.

3.8 CONFLICT of INTEREST

J.R.M has an equity interest in Microtissues, Inc. This relationship has been reviewed and managed by Brown University in accordance with its conflict of interest policies.

3.9 REFERENCES

1. Mazzoleni G, Di Lorenzo D, Steimberg N. Modelling tissues in 3D: the next future of pharmaco-toxicology and food research? *Genes and Nutrition.* 4(1):13-22, 2009.

2. Pampaloni F, Reynaud EG, Stelzer EH. The third dimension bridges the gap between cell culture and live tissue. *Nature Reviews Molecular Cell Biology*. 8(10):839-845, 2007.

3. Hirschhaeuser F, Menne H, Dittfield C, West J, Mueller-Klieser W, Kunz-Schughart LA. Multicellular tumor spheroids: an underestimated tool is catching up again. *Journal of Biotechnology*. 148(1):3-15, 2010.

4. Atala A, Kasper FK, Mikos AG. Engineering complex tissues. *Science Translational Medicine*. 4(160):160rv12, 2012.

5. Elliot NT, Yuan F. A review of three-dimensional in vitro models for drug discovery and transport studies. *Journal of Pharmaceutical Sciences*. 100: 59-74, 2011.

6. Chang TT, Hughes-Fulford M. Monolayer and Spheroid Culture of Human Liver Hepatocellular Carcinoma Cell Line Cells Demonstrate Distinct Global Gene Expression Patterns and Functional Phenotypes. *Tissue Engineering Part A*. 15(3): 559-567, 2008.

7. Chitcholtan K, Asselin E, Parent S, Sykes PH, Evans JJ. Differences in growth properties of endometrial cancer in three dimensional (3D) culture and 2D cell monolayer. *Experimental Cell Research*. 319(1):75-87, 2012.

8. Astashkina AI, Mann BK, Prestwich GD, Grainger DW. Comparing predictivie drug nephrotoxicity biomarkers in kidney 3D primary organoid culture and immortalized cell lines. *Biomaterials*. 33(18)4712-4721, 2012.

9. Knight A. Animal experiments scrutinised: systematic reviews demonstrate poor human and clinical toxicological utility. *ALTEX*. 24:320-325, 2007.

10. Krewski D, Acosta, Jr. D, Andersen M, Anderson H, Bailar JC 3rd, Boekelheide K, Brent R, Charnley G, Cheung VG, Green S Jr, Kelsey KT, Kerkvliet NI, Li AA, McCray L, Meyer O, Patterson RD, Pennie W, Scala RA, Solomon GM, Stephens M, Yajer J, Zeise L. Toxicity testing in the 21st century: a vision and a strategy. *Journal of Toxicology and Environmental Health, Part B, Critical Reviews*. 13:51-138, 2010.

11. Griffith LG, Swartz MA. Capturing complex 3D tissue physiology in vitro. *Nature Reviews: Molecular Cell Biology.* 7:211-224, 2006.

12. Yamada KM, Cukierman E. Modeling tissue morphogenesis and cancer in 3D. *Cell.* 130:601-610, 2007.

13. Bartosh TJ, Yostalo JH, Mohammadipoor A, Bazhanov N, Coble K, Claypool K, Lee RH, Choi H, Prockop DJ. Aggregation of human mesenchymal stromal cells (MSCs) into 3D spheroids enhances their antiinflammatory properties. *Proceedings of the National Academy of Sciences of the United States of America*. 107(31):13724-13729, 2010.

14. Vantangoli MM, Madnick SM, Huse SM, Weston P, Boekelheide K. MCF-7 human breast cancer cells form differentiated microtissues in scaffold-free hydrogels. *PLoS One*. 10:e0135426, 2015.

15. Kabadi PK, Vantangoli MM, Rodd AL, Leary E, Madnick SJ, Morgan JF, Kane A, Boekelheide K. Into the depths: Techniques for in vitro three-dimensional microtissue visualization. *Biotechniques*. 59: 279-286, 2015.

16. Mohapatra S, Nandi S, Chowdhury R, Das G, Ghosh S, Bhattacharyya K. Spectral mapping of 3D multi-cellular tumor spheroids: time-resolved confocal microscopy. *Physical Chemistry Chemical Physics*. 18(27):1881-1890, 2016.

17. Konig K, Uchugonova A, Gorjup E. Multiphoton fluorescence lifetime imaging of 3D-stem cell spheroids during differentiation. *Microscopy Research and Technique*. 74(1):9-17, 2011.

18. Boutin ME, Hoffman-Kim D. Application and assessment of optical clearing methods for imaging of tissue-engineered neural stem cell spheres. *Tissue Engineering Part C Methods*. 21(3):292-302, 2015.

19. Hama H, Kurokawa H, Kawano H, Ando R, Shimoguri T, Noda H, Fukami K, Sakaue-Sawano A, Miyawaki A. Scale: a chemical approach for fluorescence imaging and reconstruction of transparent mouse brain. *Nature Neuroscience*. 14:1481-1488, 2011.

20. Kuwajima T, Sitko AA, Bhansail P, Jurgens C, Guido W, Mason C. ClearT: a detergent- and solvent-free clearing method for neuronal and nonneuroanal tissue. *Development*. 140(6):1364-1368, 2013.

21. Ke MT, Fujimoto S, Imai T. SeeDB: a simple and morphology-preseriving optical clearing agent for neruonsal circuit reconstruction. *Nature Neuroscience.* 16(8):1154-1161, 2013.

22. Tung YC, Hsiao AY, Allen SG, Torisawa YS, Takayama S. High-throughput 3D spheroid culture and drug testing using a 384 hanging drop array. *Analyst*. 136(3):473-478, 2011.

23. Mehta G, Hsiao A, Ingram M, Luker GD, Takayama S. Opportunities and challenges for use of tumor spheroids as models to test drug delivery and efficacy. *Journal of Controlled Release*. 164:192-204, 2012.

24. Achilli TM, McCalla S, Meyer J, Tripathi A, Morgan JR. Multilayer spheroids to quantify drug upake and diffusion in 3D. *Molecular Pharmacology*. 11:2071-2081, 2014.

25. Jain A, Yang AH, Erickson D. Gel-based optical waveguides with live cell encapsulation and integrated microfluidics. *Optics Letter*. 37(9):1472-1474, 2012.

26. Dingle YT, Boutin ME, Chirilla AM, Livi L, Labriola NR, Jakubek LM, Morgan JR, Darling EM, Kauer JA, Hoffman-Kim D. Three-dimensional neural spheroid culture: An in vitro model for cortical studies. *Tissue Engineering Part C Methods*. 21(12):1274-1283, 2015.

27. Vinci M, Gowan S, Boxall F, Patterson L, Zimmermann M, Court W, Lomas C, Mendiola M, Hardisson D, Eccles SA. Advances in establishment and analysis of three-dimensional tumor spheroid-based functional assays for target validation and drug evaluation. *BMC Biology.* 10(29):10.1186/1741-7007-10-29, 2012.

28. Visser TD, Groen CA, Brakenhoff GJ. Absorption and scatter correction in fluorescence confocal microscopy. *Journal of Microscopy*. 163(2):189-200, 1990.

29. Robertson FM, Ogasawara MA, Ye K, Chu K, Pickei R, Debeb BG, Woodward WA, Hittelman WN, Cristofanilli M, Barsky SH. Imaging and analysis of 3D tumor spheroids enriched for a cancer stem cell phenotype. *Journal of Biomolecular Screening*. 15:820-829, 2010.

30. Curran S, Vantangoli MM, Boekelheide K, Morgan JR. Architecture of chimeric spheroids controls drug transport. *Cancer Microenvironment*. 8(2):101-109, 2015.

3.10 SUPPLEMENTAL FIGURES

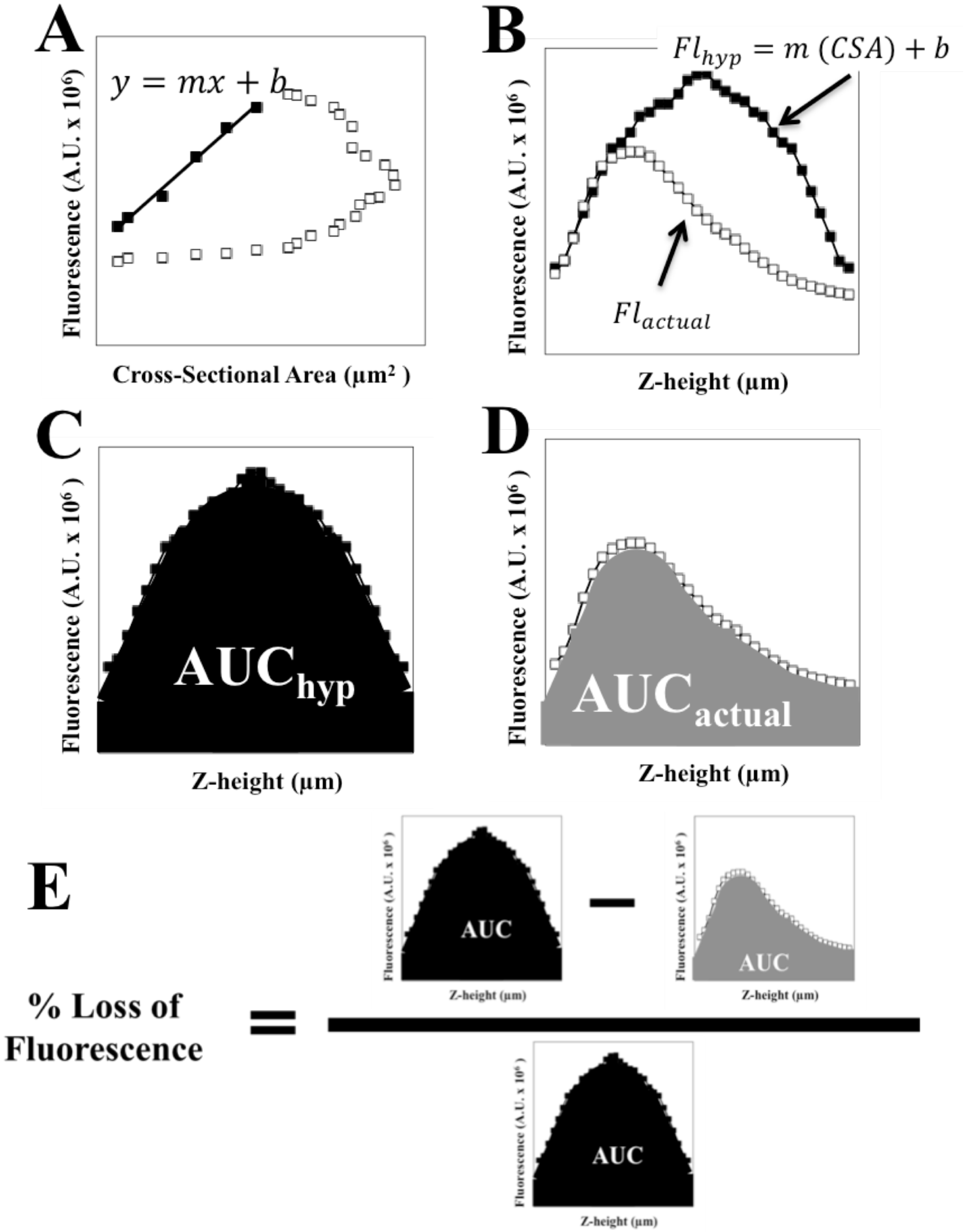

Supplemental Figure 3-1. Hypothetical maximal fluorescence derived from the cross-sectional area of confocal slices was used to determine the percent fluorescent loss for each spheroid.

Supplemental Figure 3-1. Hypothetical maximal fluorescence derived from the cross-sectional area of confocal slices was used to determine the percent fluorescent loss for each spheroid. KGN cell monolayers were labeled with four different fluorescent dyes (CTG, CTV, CTR, CTDR), trypsinized, counted, and seeded at various cell numbers to form spheroids with a range of diameters. After 24-hours of self-assembly, confocal images of the spheroids were obtained. The cross-sectional area and fluorescence of the spheroid within each confocal slice was measured. To compute the hypothetical maximal fluorescence for each spheroid, the measured fluorescence for each confocal slice was plotted versus its cross-sectional area (A). Assuming there was no fluorescent loss due to imaging limitations, the fluorescence of each confocal slice should increase proportionally to the increase in cross-sectional area until the spheroid equator, beyond which there would be a mirror decrease. However, fluorescent signal decreased as a function of z-depth for spheroids, therefore, fluorescence as a function of cross-sectional area was only linear for a portion of the curve. The best-fit line of the linear region was computed for every spheroid with each fluorescent dye tested (A). The hypothetical fluorescent signal was computed for every confocal z-slice of the spheroid through the use of the following equation: $Fl_{hypothetical} = m\,(CSA) + b.$ Both the measured and hypothetical fluorescence were then plotted as a function of their z-depth (B). To determine the total measured (D) and hypothetical (C) fluorescent signal of each spheroid, the area under the curve was calculated. The percent fluorescent loss of each spheroid was calculated according to the following equation: $\%\,Fl.Loss = \frac{(AUC_{hyp} - AUC_{actual})}{AUC_{hyp}}$ (E). This series of steps and calculations were performed for every spheroid for each of the four fluorescent dyes tested.

.

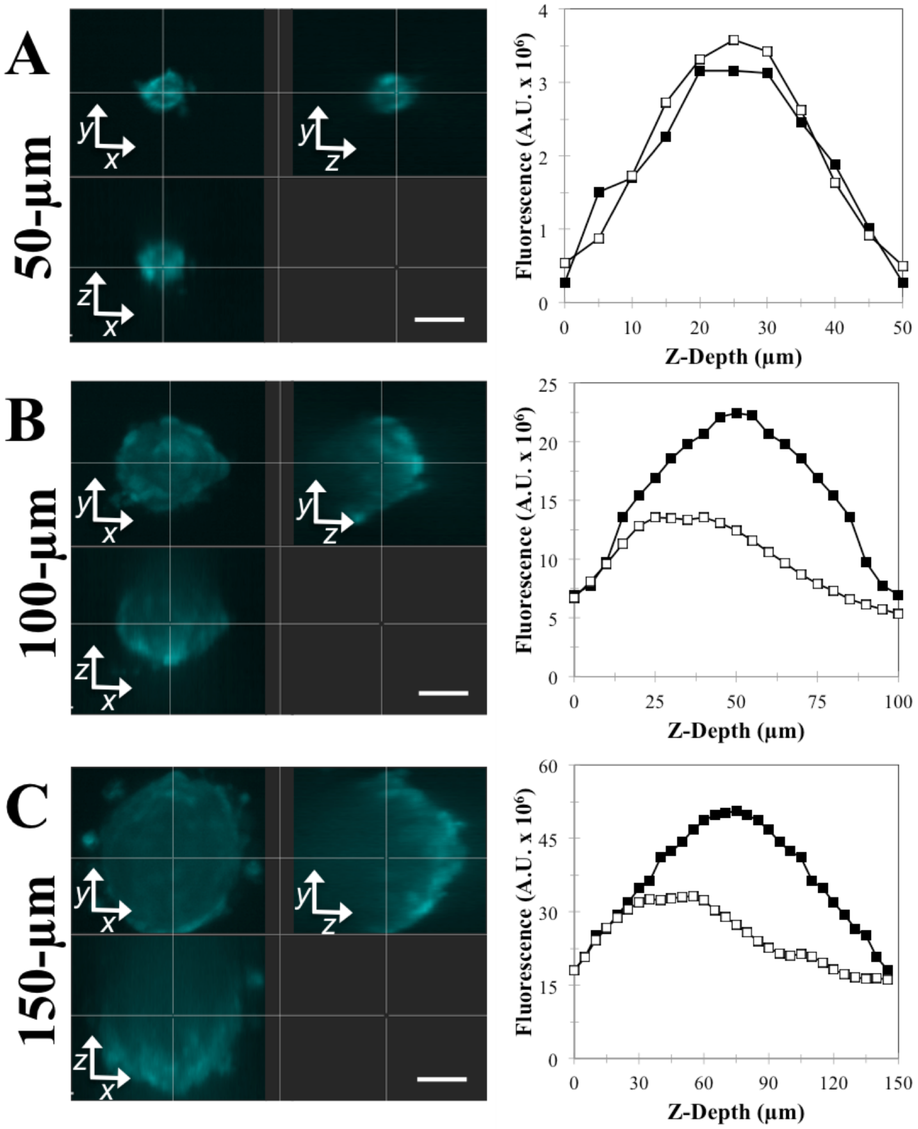

Supplemental Figure 3-2. Loss of fluorescent signal occurs deeper within the z-depth for spheroids labeled with CTV. KGN cell monolayers were labeled with CTV, trypsinized, counted, and seeded at varying cell numbers to form spheroids with diameters ranging from 50-*µ*m to 200-*µ*m. Confocal images were acquired, and orthogonal contrast images of representative spheroids of 50-*µ*m (A), 100-*µ*m (B), and 150-*µ*m (C) diameters were rendered (left column). For each spheroid, the measured fluorescence at each confocal slice was plotted as a function of its *z*-depth (white lines). The data are plotted versus the hypothetical fluorescence for each confocal slice, which was calculated assuming no loss of fluorescent signal (black lines). Representative graphs for spheroids with a 50-*µ*m (A), 100-*µ*m (B), and 150-*µ*m (C) diameters are shown (right column). For small spheroids (50-*µ*m), the plot of measured and hypothetical fluorescence were mostly overlapping throughout the z-depth (A, right column) As spheroids increased in radii, the plots of measured fluorescence fell short of hypothetical fluorescence as z-depth into spheroid increased (B, C right column). (scale bar is 40-*µ*m).

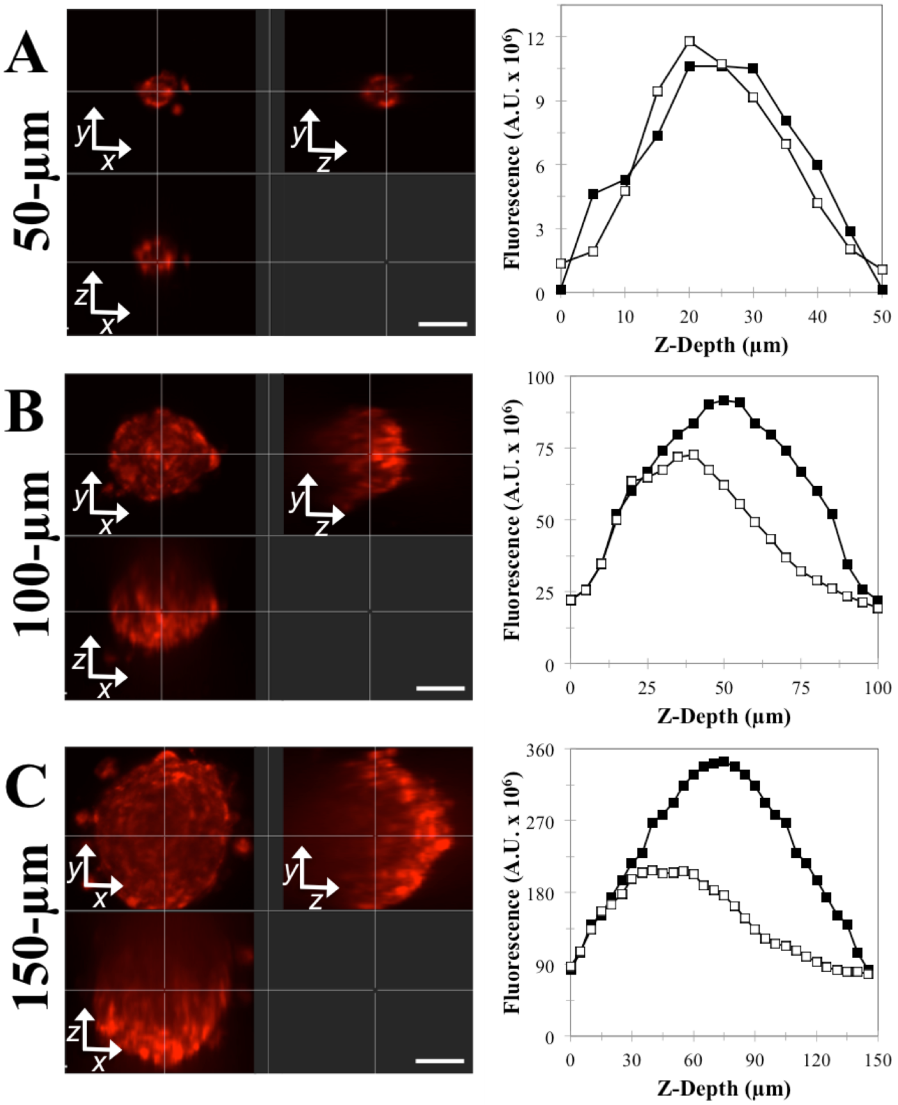

Supplemental Figure 3-3. Loss of fluorescent signal occurs deeper within the z-depth for spheroids labeled with CTR. KGN cell monolayers were labeled with CTR, trypsinized, counted, and seeded at varying cell numbers to form spheroids with diameters ranging from 50-*µ*m to 200-*µ*m. Confocal images were acquired, and orthogonal contrast images of representative spheroids of 50-*µ*m (A), 100-*µ*m (B), and 150-*µ*m (C) diameters were rendered (left column). For each spheroid, the measured fluorescence at each confocal slice was plotted as a function of its *z*-depth (white lines). The data are plotted versus the hypothetical fluorescence for each confocal slice, which was calculated assuming no loss of fluorescent signal (black lines). Representative graphs for spheroids with a 50-*µ*m (A), 100-*µ*m (B), and 150-*µ*m (C) diameters are shown (right column). For small spheroids (50-*µ*m), the plot of measured and hypothetical fluorescence were mostly overlapping throughout the z-depth (A, right column) As spheroids increased in radii, the plots of measured fluorescence fell short of hypothetical fluorescence as z-depth into spheroid increased (B, C right column). (scale bar is 40-*µ*m).

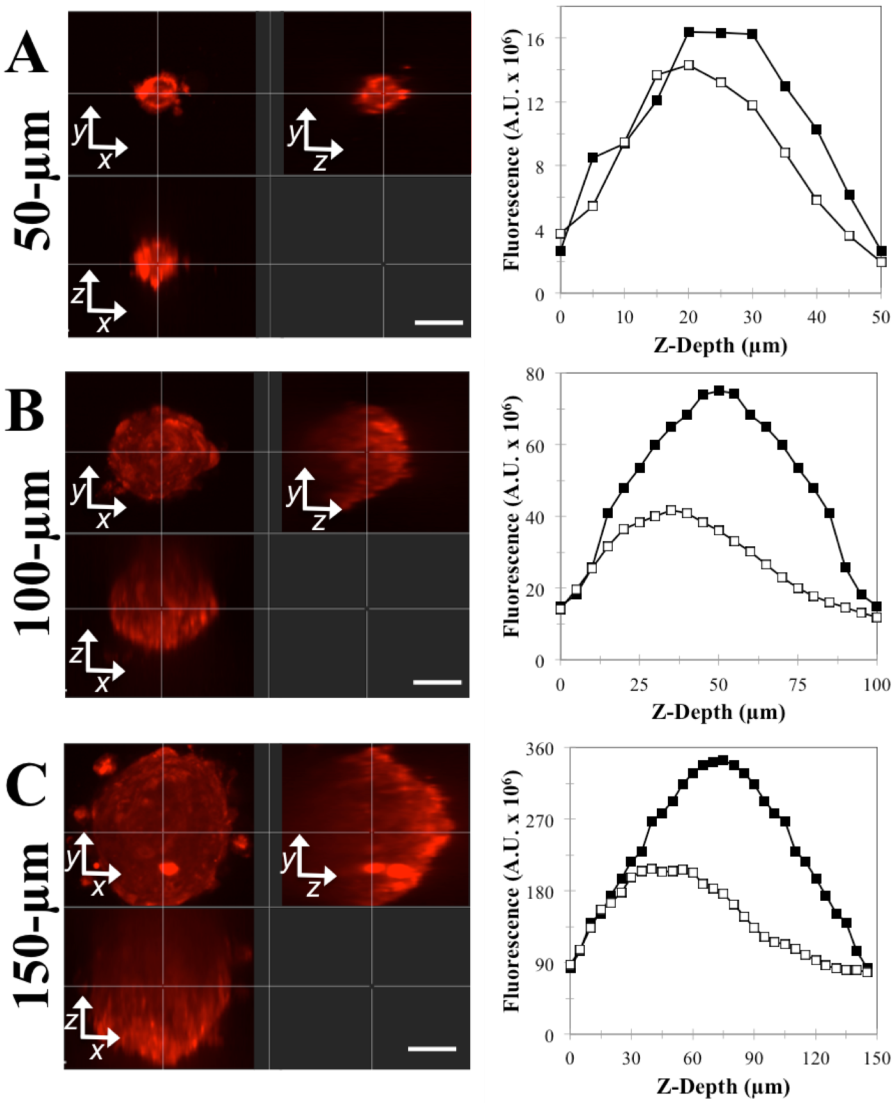

Supplemental Figure 3-4. Loss of fluorescent signal occurs deeper within the z-depth for spheroids labeled with CTDR. KGN cell monolayers were labeled with CTDR, trypsinized, counted, and seeded at varying cell numbers to form spheroids with diameters ranging from 50-*μ*m to 200-*μ*m. Confocal images were acquired, and orthogonal contrast images of representative spheroids of 50-*μ*m (A), 100-*μ*m (B), and 150-*μ*m (C) diameters were rendered (left column). For each spheroid, the measured fluorescence at each confocal slice was plotted as a function of its *z*-depth (white lines). The data are plotted versus the hypothetical fluorescence for each confocal slice, which was calculated assuming no loss of fluorescent signal (black lines). Representative graphs for spheroids with a 50-*μ*m (A), 100-*μ*m (B), and 150-*μ*m (C) diameters are shown (right column). For small spheroids (50-*μ*m), the plot of measured and hypothetical fluorescence were mostly overlapping throughout the z-depth (A, right column) As spheroids increased in radii, the plots of measured fluorescence fell short of hypothetical fluorescence as z-depth into spheroid increased (B, C right column). (scale bar is 40-*μ*m).

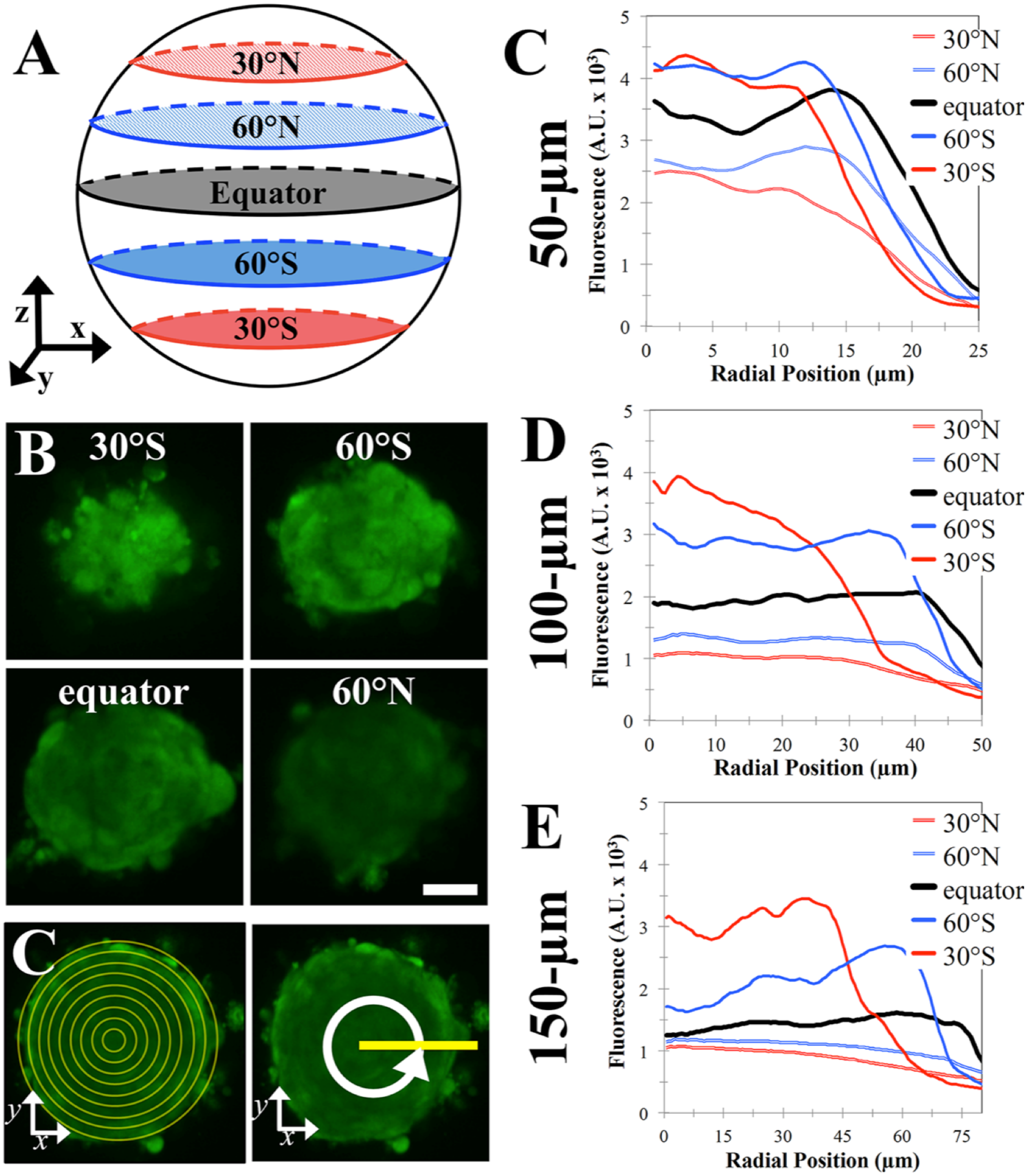

Supplemental Figure 3-5. The loss of fluorescent signal within spheroids is dependent upon three axis positional (*x, y, z*) location.

.

Supplemental Figure 3-5. The loss of fluorescent signal within spheroids is dependent upon three axis positional (*x, y, z*) location. KGN cell monolayers were labeled with CTG, trypsinized, counted, and seeded at varying cell numbers to form spheroids with diameters ranging from 50-µm to 200-µm. Confocal z-stacks were acquired, and confocal slices at the equator, 30°north, 60°north, 30°south, and 60°south were taken for further analysis (A). Representative confocal slices for an100μm diameter spheroid at equator, 30°south, 60°south, and 30°north were rendered (B). The fluorescent signal was relatively homogenous across confocal slices south of the equator, whereas at the equator there was a marked dampening of signal in the central portion compared to the outer edge (B). To quantify the difference in fluorescence across confocal slices, the average fluorescence across the cross-sectional (*x, y*) radii was computed by averaging individual fluorescent values from a series of concentric rings (C). The average fluorescent signal was plotted as a function of its cross-sectional radii for the confocal slices 30°north (dashed red lines), 60°north (dashed blue lines), 30°south (solid red lines), 60°south (solid blue lines), and the equator (black lines). Representative graphs for spheroids with a 50-µm (D), 100-µm (E), and 150-µm (F) diameters are shown. For smaller spheroids (~50μm diameter), the average fluorescent intensity across the cross-sectional radii was relatively constant for confocal slices up until the equator (C). For larger spheroids (~150μm diameter), even below the equator, the fluorescent signal was markedly decreased in the center as compared to edge (E). (scale bar is 30-µm).

.

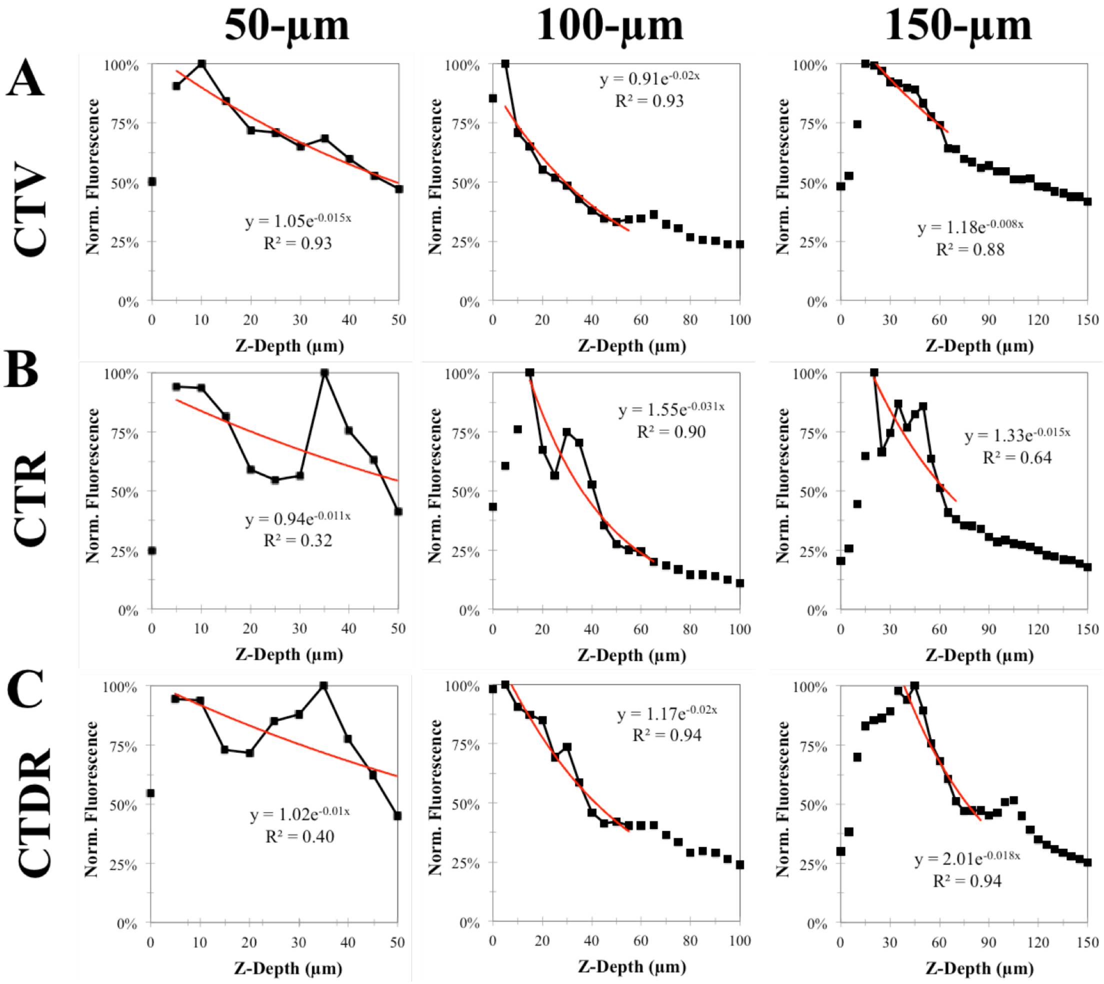

Supplemental Figure 3-6. Signal loss throughout the *z*-depth of spheroids exhibits a reproducible, exponential decay function for all dyes. KGN cell monolayers were labeled with CTV, CTR, CTDR, trypsinized, counted, and seeded at varying cell numbers to form spheroids with diameters ranging from 50-µm to 200-µm. After 24-hours, confocal images were acquired. To assess the distance into live spheroids that could be imaged by confocal microscopy, the average fluorescent intensity was measured along that central *z*-axis for each confocal slice. For each spheroid, the average intensity was normalized by peak fluorescent signal, plotted as a function of its *z*-depth, and the best-fit exponential decay curve was calculated from 50-*µ*m past the peak signal. Representative graphs for spheroids labeled with CTV (A), CTR (B), or CTDR (C) are shown at the following radii: 50-µm (left column), 100-µm (middle column), and 150-µm (right column)..

CHAPTER 4

Gap junction intercellular communication in 3D spheroids: Quantifying radial fluorescence

Elizabeth Leary [1, 2], David Reich, Jeffrey R. Morgan [1, 2]

Author Affiliation:
[1] Department of Molecular Pharmacology, Physiology and Biotechnology
[2] Center for Biomedical Engineering
Brown University
175 Meeting Street
Providence, Rhode Island, USA 02912

4.1 ABSTRACT

Connexins are membrane proteins that form gap junctions (GJ), which form direct channels of communication between cells in multiple organ systems. Since GJ are involved in many biological processes and disruption of gap junction intercellular communication (GJIC) has been linked to numerous pathologies, identifying compounds that interfere with GJIC is crucial. Traditional methods to study GJIC *in vitro* are low-throughput, performed in 2D cell monolayers, may induce cellular damage, and/or require the use of specialized skills. In this study, we have developed a method to assess GJIC in a high throughput format within 3D spheroids, a more physiologically relevant platform with increased cellular interactions and communication. Spheroids, four per well, were formed in a 96 well plate, and imaged using the 20X water objective of a high-throughput confocal microscope. We acquired *z*-stacks of living spheroids that were dynamically taking up fluorescent calcein dyes and distributing them via GJIC throughout its 3D radius. To account for the complexity of acquiring quantitative fluorescence from confocal *z*-stacks of spheroids, ratio imaging was utilized. We optimized the spheroid-based GJIC assay with respect to dye choice and labeling time, spheroid size, and means of fluorescent quantitation, by assessing the effect of treatment with and without carbenoxolone, a GJIC inhibitor. The 3D spheroid-based GJIC assay measured GJIC inhibition by quantifying the differences in fluorescence distribution across the 2D/3D radius.

KEYWORDS: Gap Junctions, Spheroids, Image Quantification, Confocal Microscopy

4.2 INTRODUCTION

Gap junctions (GJ) are channels that directly connect the cytoplasm of adjacent cells thus enabling intercellular communication (GJIC) [1]. GJ allow the passive diffusion of small, hydrophilic molecules, such as ions, metabolites, nutrients, and second messengers from one cell to the next [1,2]. GJ play key communicatory roles in a variety of organ systems, ranging from the brain to the heart [3-8]. For example, GJ facilitate electrical impulse propagation within the heart as well as neurons, help regulate vascular resistance, and coordinate follicular growth and maturation [4,5,8]. GJ dysregulation can lead to arrhythmias or tumor promotion [7,9,10]. GJIC can be modified by a variety of mechanisms, such as alterations in the functional state or channel permeability, or reduction in the overall number of channels [11]. Furthermore, GJIC can be negatively affected by a range compounds, from environmental toxicants, such as bisphenol A and cigarette smoke particulates, to pharmaceuticals, such as carbenoxolone and clotrimazole [12-16]. Different drugs and toxicants may alter GJIC via different mechanisms yielding different results. For example, certain drugs, such as carbenoxolone, mefloquine, and quinine, block gap junction communication, but its effects are reversible [15,17-19]. Whereas, other drugs, such as lipopolysaccharide, irreversibly block gap junctions [20,21]. Alternatively, other drugs, such as trimethylamine and quinolone, act to enhance GJIC [22,23]. Regardless of the mechanism, the altered level of communication between cells could lead to disturbances in homeostasis, which dependent upon the scenario may be beneficial or detrimental. For example, some GJ openers, such as quinolone, may lead to reduction in cancerous tumor growth, however, alternative GJ openers, such as trimethylamine, may induce seizures [22,23].

To study GJIC *in vitro*, there are variety of methods that assess the movement of fluorescent dyes between cells [1]. For example, microinjection, scrape loading, and electroporation load cells with membrane impermeable dyes and GJIC is measured by monitoring the passage of fluorescent signal to neighboring cells [24-31]. Gap-FRAP (fluorescence recovery after photobleaching) photobleaches a small area of fluorescently labeled cells and GJIC is measured by monitoring the recovery of the fluorescent signal from neighboring cells [32,33]. In a pre-loading assay, fluorescently labeled cells are added on top of unlabeled cell monolayers, and GJIC is measured by monitoring dye transfer to the monolayer [34,35]. Each of these techniques has its own advantages and disadvantages [1]. For example, microinjection, scrape-loading, electroporation, and gap-FRAP induce damage to the cells [24-33]. Overall, these techniques are time-consuming, low throughput, and some require specialized skills [1]. Furthermore, they all utilize cell monolayers to evaluate GJIC in two-dimensions (2D) [1].

In this paper, we used confocal microscopy to develop a method to assess GJIC in 3D spheroids in a high throughput format. Spheroids afford numerous advantages over 2D monolayer cultures, including improved physiological relevance and increased cell-cell interactions and communication [36-43]. To measure GJIC, spheroids were incubated with membrane permeable calcein derivatives that are converted by cellular esterases into impermeable fluorescent molecules, which can pass from cell-to-cell within spheroids via GJ [1,44]. Fluorescence within the labeled spheroids was assessed by acquiring a *z*-stack of images for each spheroid using a high throughput confocal microscope. The assay was optimized with respect to calcein derivative (calceinAM versus calein-red-orange-AM (calceinRO)), time of incubation with calcein prior to imaging, and spheroid size. To evaluate these optimizations, the effects induced by a well-known GJIC inhibitor at a dose known to block connexin-43, 100μM carbenoxolone (CBX), were compared to untreated spheroid controls [45,46]. Measurement of GJIC, required us to determine the best method to quantify calcein fluorescence as a function of spheroid radius from the *z*-stack of images. However, quantitation is complex due to the loss of fluorescence as a function of increasing depth as well as the spherical shape of the spheroid (**Figure 4-1**) [47-49]. To improve accuracy, we uniformly labeled cells prior to spheroid formation with different fluorescent dyes (CellTracker^{TM} Red CMPTX (CTR) or CellTracker^{TM} Green CMFDA (CTG)), and used ratio imaging for quantitation. We used these ratios to evaluate several different methods of quantifying fluorescence as function of spheroid radius and determined the best method by performing a Z-factor analysis.

4.3 MATERIALS and METHODS

4.3.1 Micro-mold fabrication and hydrogel formation.

Molds, designed using computer-assisted design (CAD) (Solidworks, Concord, MA), consisted of a base platform upon which lay a series of 6 rows by 8 columns of pegs, with each peg designed to fit within one well of 96-well plate (Sensoplate Plus, Grenier Bio One). Atop each peg were 4 conical-shaped micro-posts. Molds were milled out of aluminum (Proto Labs, Inc, Maple Plain, MN).

To form hydrogels, 90-μL of sterile molten UltraPure Agarose (Fisher Scientific, Waltham, MA) (2% weight/ volume in phosphate buffered saline) was pipetted into each well and the mold was inverted on top of the 96-well plate allowing the micro-posts to be submerged in agarose. The mold was removed after 10-minutes, after the molten agarose solidified. Each agarose hydrogel contained 4 micro-recesses where spheroids would be formed. Prior to spheroid formation, hydrogels were equilibrated with 150-μL of serum-free DMEM (Life Technologies, Grand Island, NY) supplemented with 1% penicillin/streptomycin for 24 hours incubating at 37°C with 10% CO_2.

4.3.2 Cell culture, spheroid formation, fluorescent dye labeling, and drug treatment.

Human ovarian granulosa (KGN) cells were grown in DMEM with 10% fetal bovine serum (FBS) (Fisher Scientific, Waltham, MA) and 1% penicillin/streptomycin at 37°C with 10% CO_2. Once confluent, cell monolayers were labeled with either 5μM CellTracker^{TM} Red CMPTX (CTR) (Life Technologies, Grand Island, NY) or 5μM CellTracker^{TM} Green CMFDA (CTG) (Life Technologies, Grand Island, NY). To label monolayers, serum-containing medium was removed from the culture flasks, and flasks were washed once with serum-free DMEM. Fluorescent dyes were reconstituted in serum-free DMEM, and incubated with the cell monolayer for 30-minutes at 37°C with 10% CO_2. After labeling, medium was exchanged with fresh serum-free DMEM, and incubated for 15-minutes at 37°C with 10% CO_2. The labeled cell monolayers were harvested using 0.05% trypsin, concentrated by centrifugation at 120 *x g* for 6-minutes, and counted. Cells were washed once with serum-free DMEM and spun down at 120 *x g* for 6-minutes. Cells were re-suspended in serum-free DMEM at a concentration of 200,000-cells/mL. A 20-μL aliquot of cell suspension was pipetted into the loading dock of each hydrogel to form four spheroids each composed of approximately 1,000-cells. After allowing the cell suspension to settle to the bottoms of the micro-recesses for 30-minutes, 150-μL of serum-free DMEM was added per well. Cells self-assembled into spheroids for twenty-four hours prior to the addition of a calcein dye. Spheroids labeled with CTR were incubated with 2.5μM calcein-AM (calceinAM) (Life Technologies, Grand Island, NY), while spheroids labeled with CTG were incubated with 2.5μM calcein-red-orange-AM (calceinRO) (Life Technologies, Grand Island, NY). To inhibit gap junction intercellular communication (GJIC), spheroids were incubated with 100μM carbenoxolone (CBX) for five hours prior to the addition of a calcein dye.

4.3.3 Microscopy and image analysis measurements.

To image spheroids, the Opera Phenix^{TM} High Content Screening System (Perkin Elmer, Waltham, MA, USA), equipped with proprietary Synchrony^{TM} Optics consisting of a Nipkow spinning microlens disk in conjunction with pinhole disk and 2 sCMOS cameras, was used. Fluorescent images for each dye were acquired using the 20x water objective in conjunction with two excitation lasers: 488-nm for CTG and calceinAM, 561-nm for CTR and calceinRO. Confocal z-stacks of spheroids were acquired every 5-μm for a total of 375-μm.

Confocal images were analyzed via two different image analysis software programs: Imaris (Bitplane, Belfast, UK) and ImageJ (National Institutes of Health, Bethesda, MD, USA). With Imaris, confocal images were rendered as 3D objects, and a mask of the outer spheroid surface was created (**Supplemental Figure 4-2B, C**). Total volume and center (x, y, z) position was measured for each spheroid, and its average radii was computed by the following equation: $r = \sqrt[3]{\frac{3}{4}\frac{Vol.}{\pi}}$. The 3D rendering was cropped to remove images north of the equator, as identified by the center *z*-position, thus forming a hemisphere (**Supplemental Figure 4-2D, E**). The outer surface underwent a distance transformation in order to create a series of concentric shells, eroding inwards in 5μm increments (**Supplemental Figure 4-2F**). The volume, calcein, and Celltracker^{TM} (CT) fluorescence were computed for every shell of the hemisphere (**Supplemental Figure 4-2G)**. With ImageJ, the spheroid's perimeter was identified by thresholding the calcein signal, subsequently eroded in 5μm increments creating a series of concentric shells for each confocal image (**Supplemental Figure 4-1B, C, D**). The same set of shells were applied to the corresponding CT signal for each confocal image of spheroid (**Supplemental Figure 4-1E**). The cross-sectional area, calcein, and CT fluorescence were computed for every shell at every image (**Supplemental Figure 4-1F)**.

4.3.4 Data Analysis.

To determine the staining patterns associated with the use of certain dyes and labeling methods, the "fluorescence per area" for each shell was calculated by dividing the total CT or calcein fluorescence of a given shell by the cross-sectional area of that shell. To evaluate this distribution across the spheroid radius, the "fluorescence per area" was plotted as a function of its radial location.

To determine the effects of inhibition of GJIC on the penetration of calcein inwards, two different approaches were evaluated: (1) the equatorial confocal image or (2) the southern hemisphere of the spheroid. For both approaches, the calcein fluorescence was normalized by the CT fluorescence for each shell. Additionally, each shell's radial position was normalized by the total number of shells, with a value of "1" indicating the outer shell of spheroid, and value of "0" indicating the spheroid center. For both the equatorial confocal image and the southern hemisphere of the spheroid, three different data analysis methods were computed:

(1) the ratio of calcein/CT fluorescence was plotted as a function of its normalized radial position for each confocal image, and the area under the curve was calculated.
(2) the ratio of the fluorescence of the center core to the outer shell at the equatorial confocal image was computed according to the equation below:

$$Ratio - core\!:outer\ shell = \frac{\left({}^{Fl_{core}}\!/_{Fl_{outer\ shell}}\right)_{calcein}}{\left({}^{Fl_{core}}\!/_{Fl_{outer\ shell}}\right)_{CT}}$$

(3) the ratio of the middle two shells to the outermost two shells was computed according to the following equation, where "n" is the outermost shell, "n-1" is the 2nd outermost shell, and so forth:

$$Ratio - middle\ shell{:}\ outer\ shell = \frac{\left(\frac{Fl_{n-3} + Fl_{n-4}}{Fl_n + Fl_{n-1}}\right)_{calcein}}{\left(\frac{Fl_{n-3} + Fl_{n-4}}{Fl_n + Fl_{n-1}}\right)_{CT}}$$

For all of these different methods of data analysis, the average and standard deviation was calculated for spheroids treated with or without the gap junction inhibitor, CBX.

4.3.5 Statistical Analysis.

To compare the effect of CBX on GJIC for all methods of data analysis, a two-tailed Student’s t-test was performed with a significance level of 0.05

To evaluate which method of data analysis provided the best separation between the positive control (CBX treatment) and negative control (no drug), we performed a Z-factor analysis, according to the equation below:

$$Z = 1 - \left(\frac{3(\sigma_{pos} + \sigma_{neg})}{|\mu_{pos} - \mu_{neg}|}\right)$$

Achieving a Z-factor values above 0.5 implies excellent separation between positive and negative controls, whereas achieving Z-factor less than zero implies too much overlap between positive and negative controls to be an effective assay at screening numerous compounds [50].

4.4 RESULTS

4.4.1 Spheroid fluorescence is dependent on the method of dye incorporation and location in the spheroid.

To assess gap junction intercellular communication (GJIC) within 3D spheroids, we measured the penetration of membrane permeable calcein dyes, calceinAM or calceinRO. Upon entering cells, calcein dyes are converted into membrane impermeable fluorescent molecules that can penetrate deeper into spheroids through functional gap junctions. To account for the limitations of confocal imaging of spheroids, we used ratio imaging by uniformly labeling cells with a CellTracker^{TM} (CT) dye prior to spheroid formation (**Figure 4-1**). Monolayers of KGN cells were labeled with a CT dye, either CTR or CTG, trypsinized, counted, seeded into hydrogels, and allowed to self-assemble into spheroids. After 24-hours, spheroids were incubated with a calcein dye (calceinAM was added to CTR-labeled spheroids, while calceinRO was added to CTG-labeled spheroids). After approximately 70-minutes of incubation, confocal images were acquired using the 20X water objective. Representative confocal images (*x, y*) were assessed at 30°south (30°S), 60°south (60°S), 60°north (60°N), and the equator of a spheroid either (1) uniformly labeled with a CT dye prior to spheroid formation (**Figure 4-2A, C**) or (2) labeled with a calcein dye via diffusion and GJIC into the spheroid (**Figure 4-3A, C**). The fluorescent signal of the CTR and CTG dyes was relatively homogenous across each confocal image (**Figure 4-2A, C**). Alternatively, the fluorescent signal of images from spheroids incubated with calceinAM or calceinRO, showed a gradient across each image, with the brightest signal occurring around the outermost cell layer (**Figure 4-3A, C**). For both

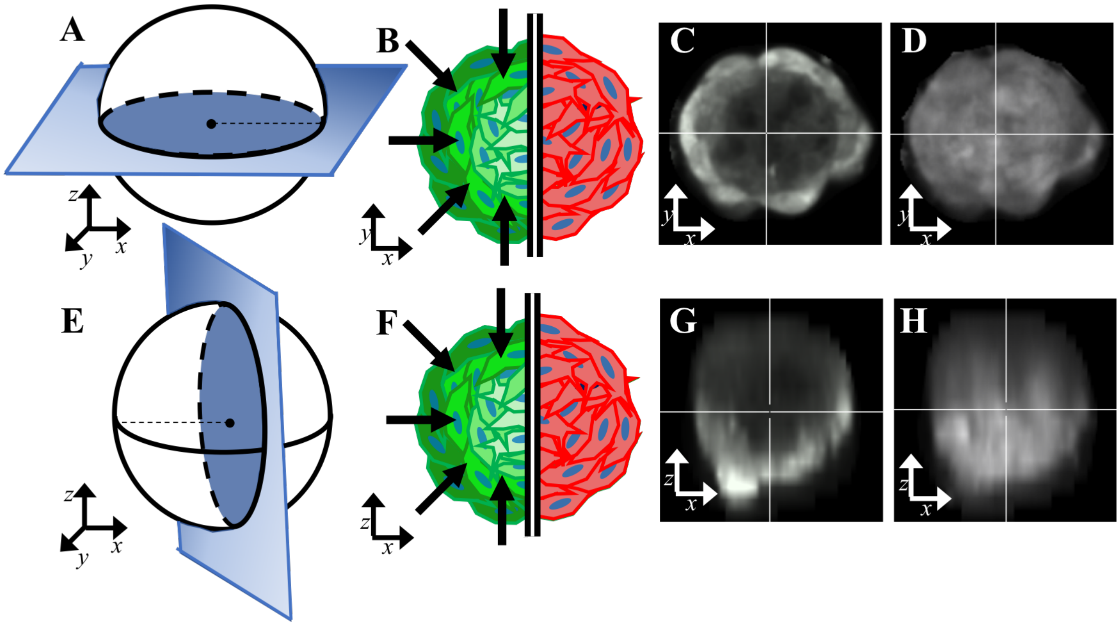

Figure 4-1. Quantitation of GJIC is complicated by limitations of confocal imaging. KGN spheroids were labeled with fluorescent dyes two different ways: (1) uniformly labeled by using a CT dye to label the individual cells used to form the spheroids, or (2) diffusion/GJIC driven by labeling spheroids with a calcein dye. For uniformly labeled spheroids, the diagram shows that fluorescence should hypothetically be uniform and equivalent at the (*x, y*) equator and the (*x, z*) plane (B, F - right side, shown in red). However, due to the limitations of confocal imaging, loss of fluorescence occurs with increasing *z*-depth. Fluorescence of the equatorial image (*x, y*) of a spheroid labeled with CT (D) is bright and uniform as are the images below the equator. But for images above the equator, fluorescence declines as shown by the (*x, z*) plane image of a spheroid labeled with CT (H). Alternatively, for spheroids labeled with calcein which is driven by diffusion/GJIC, the diagram depicts a gradient of fluorescence with the highest intensity near the spheroid surface. In theory, the equatorial plane (*x, y*) and the (*x, z*) plane should have a similar gradient pattern (B, F - left side, shown in green) because calcein should penetrate the spheroid evenly in all directions. The (*x, y*) equatorial image of a spheroid labeled with calcein shows this gradient (C), however the image of the (*x, z*) plane shows the gradient pattern only in the southern hemisphere, whereas in the northern hemisphere, there is no gradient and minimal fluorescence due to a loss of fluorescent signal deeper into the *z*-depth (G).

.

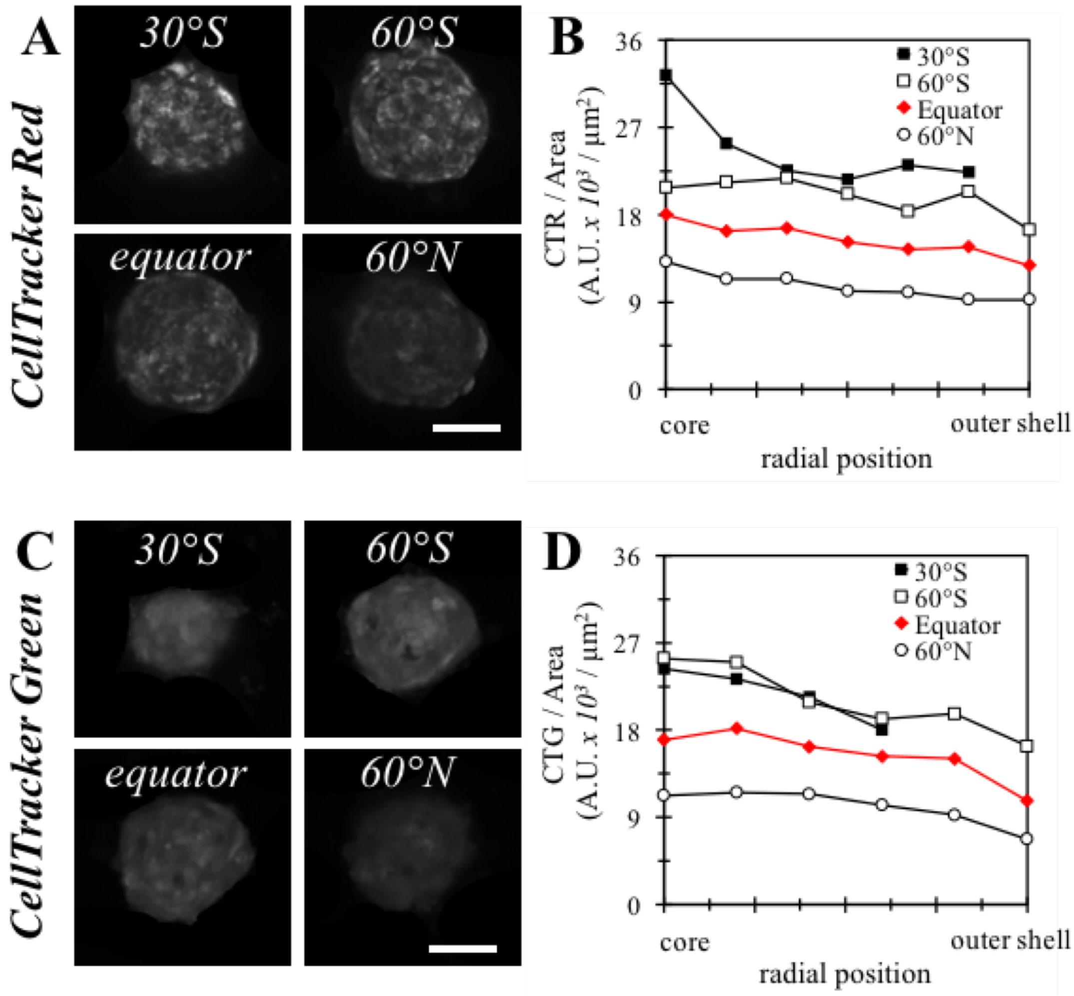

Figure 4-2. Labeling cells with fluorescent dyes prior to spheroid formation yields uniform fluorescence throughout the spheroid. KGN cell monolayers were labeled with either CTR (A, B) or CTG (C, D), trypsinized, counted, and seeded to form spheroids. After 24-hours, confocal *z*-stacks were acquired. Representative confocal images for at equator, 30°south, 60°south, and 60°north were rendered for either CTR (A) or CTG (C). For both dyes, the fluorescent signal was relatively homogenous across each of the confocal images, however, the overall signal began to dampen at confocal images deeper into the z-depth (equator, 60°north) (A,C). To quantify the fluorescence distribution across each confocal image, the perimeter of the spheroid was identified, and then eroded every 5μm to form a series of concentric shells. For each shell, the total fluorescence was divided by its cross-sectional area and plotted as a function of radial position (B, D). For both CTR and CTG, the average fluorescent signal across the radius is relatively even across for each confocal image (B, D). However, for both dyes, the overall fluorescent signal decreases in value for images deeper in the *z*-depth (B,D). (scale bar is 50μm).

.

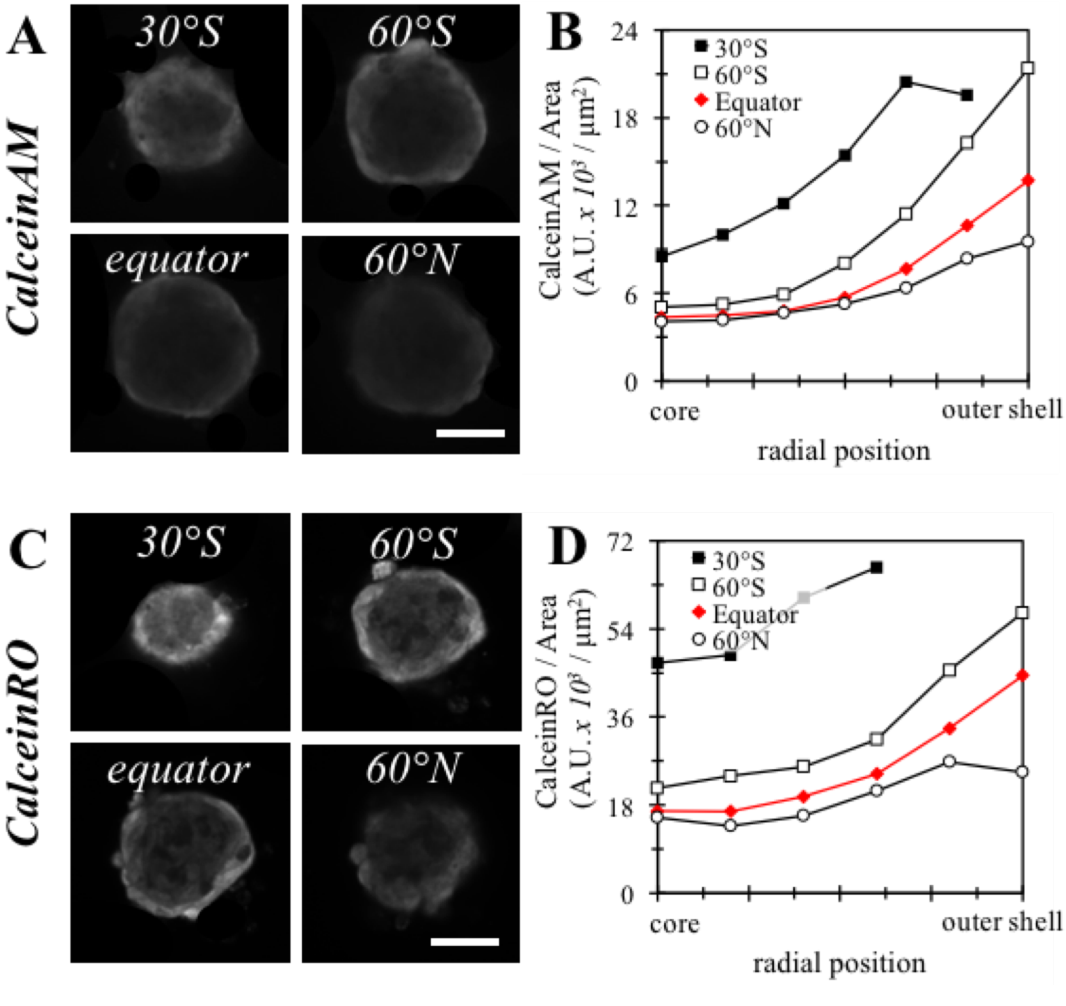

Figure 4-3. Calcein labeling of spheroids creates a gradient of fluorescence decreasing inwards from the spheroid surface. KGN cell monolayers were trypsinized, counted, and seeded to form spheroids. After 24-hours, spheroids were labeled with either calceinAM (A,B) or calceinRO (C,D) and confocal z-stacks were acquired. Representative confocal images for the equator, 30°south, 60°south, and 60°north were rendered for either calceinAM (A) or calceinRO (C). For both dyes, the fluorescent signal was brightest along the spheroid's perimeter, and decreased towards the center. Additionally, the overall signal began to dampen at confocal images deeper into the *z*-depth (equator, 60°north) (A,C). To quantify the fluorescence distribution across each confocal image, the perimeter of spheroid was identified, and then eroded every 5µm to form a series of concentric shells. For each shell, the total fluorescence was divided by its cross-sectional area and plotted as a function of radial position (B, D). For both caleinAM and calceinRO the fluorescent signal across the radius is greatest along the spheroid perimeter and decreases when moving towards the spheroid center (B, D). However, for both dyes, the overall fluorescent signal is decreased for images deeper in the *z*-depth (B,D). (scale bar is 50μm).

methods of staining, overall fluorescence decreased with *z*-depth, with the brightest images occurring south of the equator (30°S and 60°S) (**Figure 4-2A, C, Figure 4-3A, C**).

To quantify fluorescence along the spheroid's radius, the perimeter of the spheroid was detected a for each image using the calcein signal, and a series of concentric shells were formed by eroding inwards every 5-μm (**Supplemental Figure 4-1B, C, D**). The same set of shells were applied to the corresponding CT signal for each confocal image (**Supplemental Figure 4-1E**). For each shell, the total area and fluorescence of the CT and calcein dyes were measured, and the fluorescence per area was computed and plotted as a function of its radial location (**Figure 4-2B, D, Figure 4-3B, D**). For CT dyes, fluorescence per area was comparable for each shell due to the uniform labeling (**Figure 4-2B, D**). Alternatively, for calcein dyes, the fluorescence per area was greatest at the outer shell and decreased inwards toward the spheroid center (**Figure 4-3B, D**). Therefore, we can quantify calcein fluorescence as it penetrates inwards, and distinguish its staining pattern from a uniformly labeled CT fluorescent signal. These data also revealed that regardless of labeling method, fluorescence decreased significantly for confocal images north of the equator and so subsequent analyses were based only on the images of the southern hemisphere (**Figure 4-2B, D, Figure 4-3B, D**).

4.4.2 CalceinRO outperforms calceinAM as an indicator of GJIC.

To determine which calcein dye was better for assessing GJIC, we evaluated calceinAM versus calceinRO on spheroids treated with and without carbenoxolone (CBX) an inhibitor of GJIC. KGN cell monolayers were first labeled with a CT dye, either CTR or CTG, trypsinized, counted, and seeded into hydrogels to form spheroids. After self-assembling for 24-hours, spheroids were either incubated with or without CBX (+/- CBX) for five hours prior to the addition of a calcein dye. CalceinAM was added to spheroids labeled with CTR, while calceinRO was added to spheroids labeled with CTG. After approximately 80-minutes of incubation with the calcein dyes, confocal z-stacks were acquired and equatorial images were taken for further analysis. All spheroids possessed a gradient of calcein fluorescence with the brightest signal occurring around the perimeter (**Figure 4-4A, C)**. However, the gradient of fluorescence of spheroids treated with CBX experienced a sharper decline compared to untreated controls (**Figure 4-4A, C**).

To quantitatively compare the performance of the calcein dyes, we quantified calcein fluorescence as a function of radius for the equatorial images. The perimeter of the equatorial images was detected and a series of concentric shells were formed by eroding inwards every 5-μm for both the calcein and CT images (**Supplemental Figure 4-1B, C, D, E**). For each shell, calcein and CT fluorescence were measured, and the calcein signal was normalized to the CT signal to account for both minor differences in spheroid size and limitations of confocal microscopy. To account for differences in total fluorescence between spheroids, the ratio of calcein/CT was normalized to its maximum value and plotted as a function of normalized radial position (**Figure 4-4B, D**). When treated with CBX, the amount of fluorescence reaching the center for both calcein dyes was reduced (**Figure 4-4B, D**). However, for spheroids labeled with calceinRO, the difference

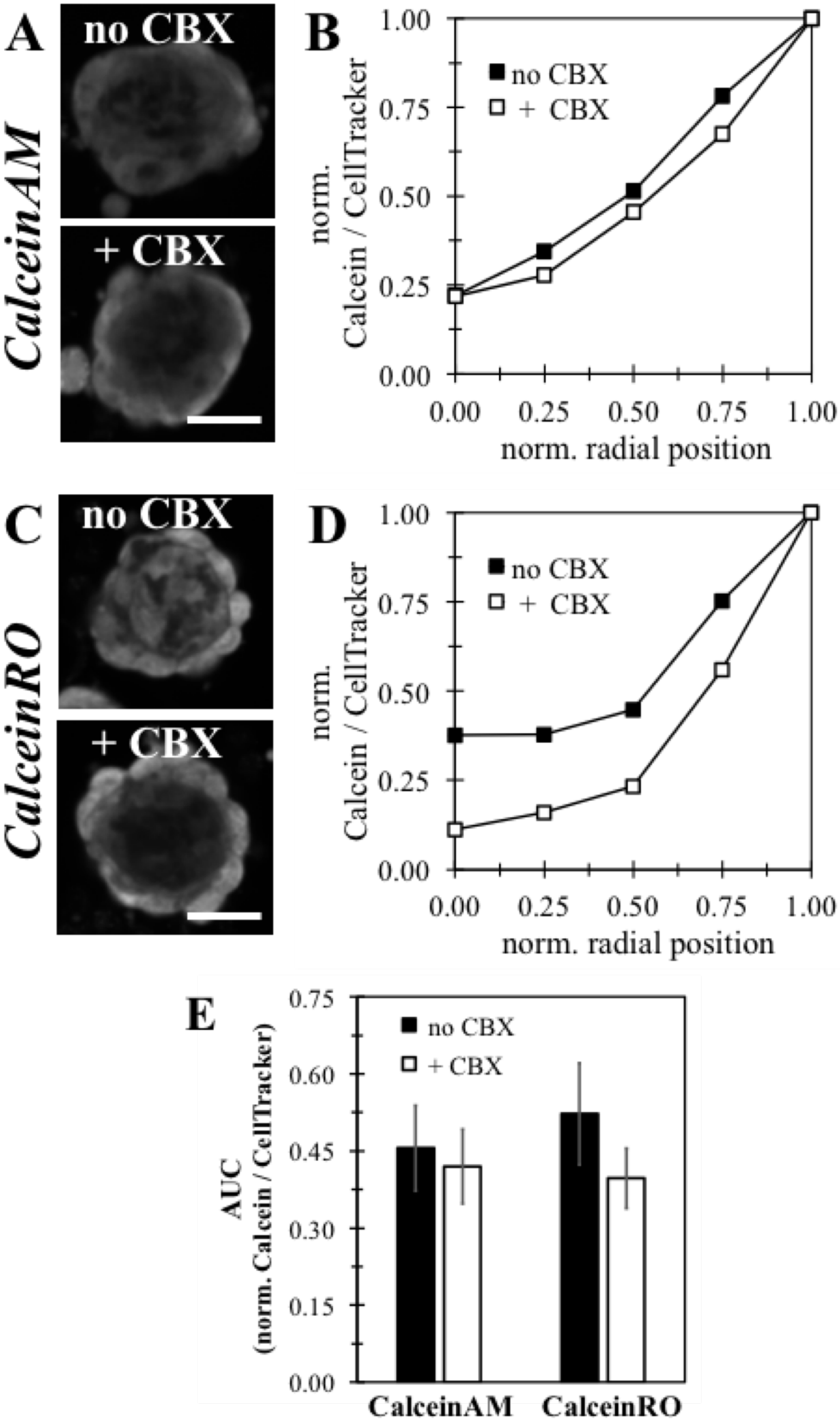

Figure 4-4. CalceinRO is more effective than calceinAM as a reporter of GJIC.

Figure 4-4. CalceinRO is more effective than calceinAM as a reporter of GJIC. KGN cell monolayers were labeled with either CTR or CTG, trypsinized, counted, and seeded into agarose hydrogels to form spheroids. After self-assembling for 24-hours, spheroids were incubated either with or without the gap junction inhibitor, CBX, for 5-hours prior to the addition of a calcein dye. CalceinAM was added to spheroids labeled with CTR, while calceinRO was added to spheroids labeled with CTG. Confocal *z*-stacks of spheroids were acquired and the equatorial image was taken for further analysis. Representative equatorial images were rendered for spheroids that were treated with CBX or without CBX and labeled with either calceinAM (A) or calceinRO (C). For both dyes, the fluorescent signal was brightest along the spheroid's perimeter, and decreased towards the center (A, C). Additionally, for spheroids treated with CBX, the decline in fluorescence appeared sharper (A, C). To quantify the fluorescence distribution across each confocal image, the perimeter of the spheroid was identified via calcein fluorescence, and then eroded every 5μm to form a series of concentric shells. The same set of concentric shells were applied to the CT channel. For each shell, the calcein fluorescence was divided by its CT fluorescence, normalized by its maximum ratio, and plotted as a function of its normalized radial position (B, D). Representative graphs for spheroids treated +/- CBX labeled with calceinAM (B) or calceinRO (D) were plotted. For both calceinAM and calceinRO, the spheroids treated with CBX (white squares) possessed a lower normalized fluorescent signal across the spheroid radius than their non-treated counterparts (black squares) (B, D). However, calceinRO labeled spheroids possessed a larger separation between the +/- CBX groups (D). To quantitatively compare the separation between +/- CBX for both calceinAM and calceinRO, the AUC was measured for each spheroid, and the average and standard deviation was computed for each dye (E). Spheroids labeled with calceinRO exhibited a greater and statistically significant separation between +/- CBX treatment than spheroids labeled with calceinAM (E). (scale bar is 50μm).

.

between control and CBX treatment was greater than spheroids labeled with calceinAM (**Figure 4-4B, D**). To quantify this difference in signal, we calculated the AUC and computed the average and standard deviation for spheroids treated +/- CBX for both calcein dyes (**Figure 4-4E, Table 4-1**). The difference in the AUC between +/- CBX-treatment was both greater and statistically significant for spheroids labeled with calceinRO versus calceinAM (**Figure 4-4E, Table 4-1**). To determine if CBX altered the total calcein dye taken up by spheroids, we examined the non-normalized data for spheroids labeled with calceinAM and calceinRO. Calcein/CT was plotted as a function of its radial position for the equatorial image (**Supplemental Figure 4-3A, C**). Furthermore, we quantified the effect CBX induced on overall fluorescent signal by summing the calcein and CT fluorescence of each shell, and normalizing the total calcein by total CT fluorescence for each equatorial image. CBX treatment did not significantly alter total fluorescence of spheroids labeled with calceinRO, however, CBX treatment did increase total fluorescence of spheroids labeled with calceinAM over non-treated controls (**Supplemental Figure 4-3, B, D, E**).

4.4.3 Spheroid size and calceinRO incubation time need to be optimized.

To evaluate the influence of spheroid size, we tested the effect of CBX on a range of sizes (radii 30-60μm). KGN cell monolayers were labeled with CTG, trypsinized, counted, and used to form spheroids which were either incubated with or without CBX for five hours prior to the addition of calceinRO. After approximately 80-minutes of incubation, confocal z-stacks were acquired, and equatorial images analyzed. Compared to spheroids with 60μm radii, fluorescence of smaller spheroids (30- and 45μm radii) was

	Drug Treatment	***n***	***Radii***		***Area Under the Curve (AUC)***			
			average	*st. dev*	*average*	*st. dev*	*difference*	*p-value*
calceinAM	no CBX	8	46.3	5.3	0.456	0.083	0.036	0.389
	+ CBX	7	44.0	7.2	0.420	0.073		
calceinRO	no CBX	6	42.6	9.9	0.522	0.099	0.125	0.026
	+ CBX	8	41.4	7.8	0.397	0.059		

Table 4-1. CalceinRO outperforms calceinAM at measuring CBX-mediated GJIC inhibition. KGN spheroids, prelabeled with either CTR or CTG, treated either +/- CBX, were labeled with calcein for 80-minutes prior to acquisition of confocal *z*-stacks (calceinAM was added to CTR-labeled spheroids, calceinRO was added to CTG-labeled spheroids). For each experimental group (+/- CBX, calceinAM or calceinRO), the total number of spheroids (*n*) was counted, and the average radius and its standard deviation was computed. To quantify the fluorescence distribution across the equatorial image, the perimeter of the spheroid was identified and eroded to form a series of concentric shells. For each shell, the calcein fluorescence was divided by its CT fluorescence, normalized by its maximum ratio, plotted as a function of its normalized radial position, and the AUC was calculated. The average and standard deviation was computed for spheroids treated +/- CBX, labeled with either calcein derivative. The difference between the averages and the statistical significance for +/- CBX-treated spheroids was computed for each dye. Spheroids labeled with calceinRO exhibited a greater and statistically significant separation between +/- CBX treatment than spheroids labeled with calceinAM.

.

higher and could qualitatively reveal the differences between treatment groups (**Figure 4-5A, C, E**). To quantify the fluorescent distribution throughout spheroids of variable radii, the perimeter of the equatorial images was detected and a series of concentric shells were formed. For each shell of the equatorial image, the ratio of calceinRO/CTG fluorescence was normalized by its maximum value and plotted as a function of its normalized radius (**Figure 4-5B, D, F**). For small and larger spheroids (30- and 60μm radii), the difference between control and CBX treatment was minimal (**Figure 4-5B, I)**. However, spheroids of intermediate size (45μm radii) showed a significant difference (**Figure 4-5D**).

To determine the optimal time of calceinRO labeling, KGN spheroids that were pre-labeled with CTG and treated +/- CBX, were incubated with calceinRO and confocal z-stacks were acquired at different times, starting 30-minutes after the addition of calceinRO. Acquiring confocal z-stacks (75 *z*-images, 2 fluorescent channels) for 4 spheroids per well takes approximately one minute, therefore, as opposed to evaluating a single spheroid over time, each well of 96-well plate represents a specific time point. Thirty minutes after the addition of calceinRO, fluorescence distribution across the radius appeared qualitatively similar for spheroids treated +/- CBX with minimal fluorescent signal reaching the center (**Figure 4-6A**). Over the time-course of 80-minutes, the level of calcein signal reaching the center increased for untreated spheroids, but appeared unchanged for spheroids treated with CBX (**Figure 4-6A**). To quantitatively evaluate the effect of calceinRO incubation time, the equatorial image of each spheroid was analyzed by forming concentric shells, measuring calcein and CT fluorescence, and computing the ratio of calceinRO/CTG fluorescence for each shell. This ratio was normalized by its

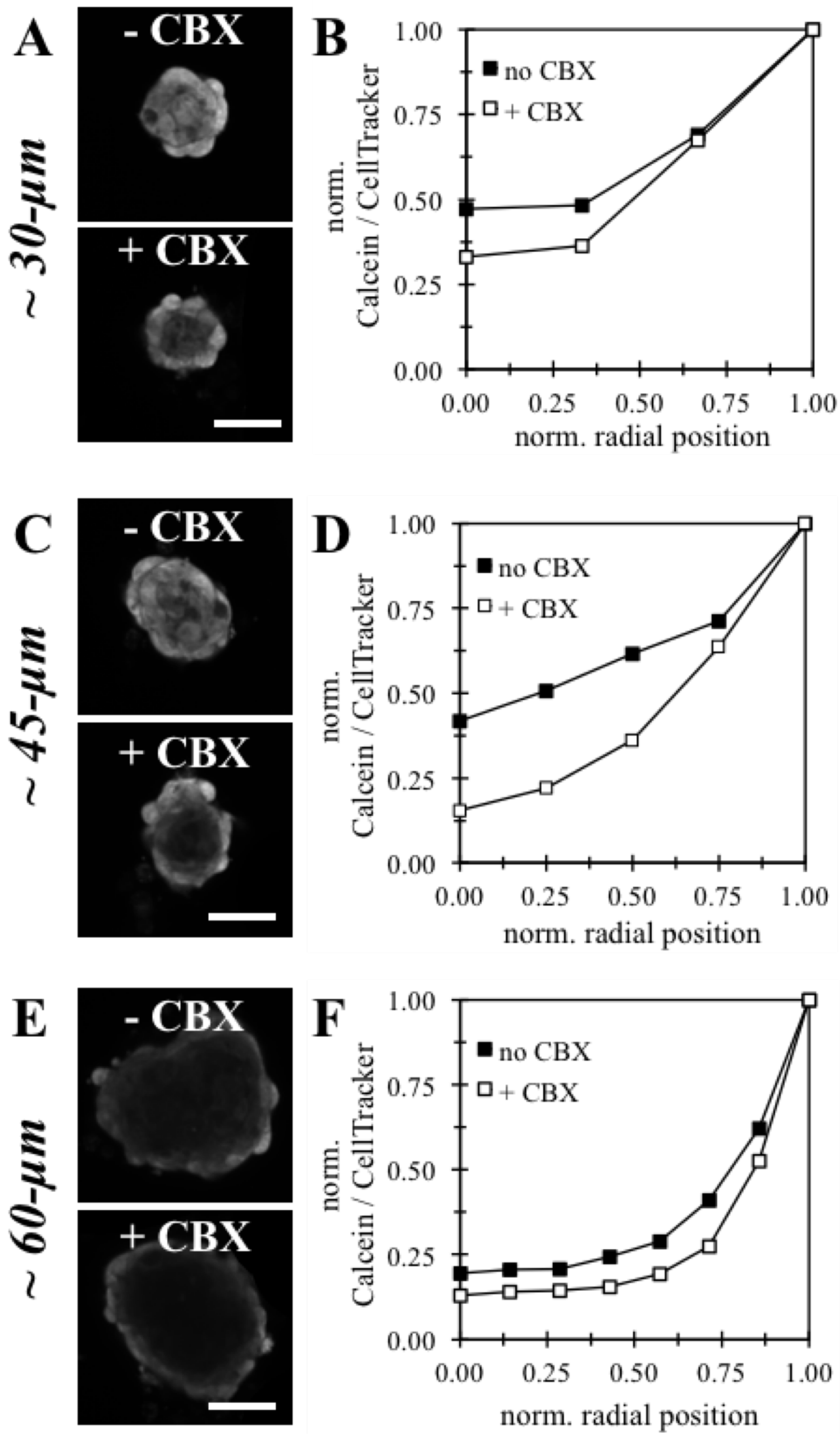

Figure 4-5. Spheroid size is integral in quantifying differences in fluorescent signal.

Figure 4-5. Spheroid size is integral in quantifying differences in fluorescent signal. KGN cell monolayers were labeled with CTG, trypsinized, counted, and seeded into agarose hydrogels to form spheroids. After self-assembling for 24-hours, spheroids were incubated either with or without the gap junction inhibitor, CBX, for 5-hours prior to the addition of calceinRO. After incubation with calceinRO for 80-minutes, confocal *z*-stacks of spheroids were acquired and the equatorial image was taken for further analysis. Representative equatorial images were rendered for spheroids that were treated with CBX or without CBX of variable radii ranging from 30μm (A), 45μm (C), to 60μm (E). Regardless of spheroid size, the fluorescent signal was brightest along the spheroid's perimeter, and decreased towards the center for both +/- CBX treatment (A, C, E). Additionally, for spheroids treated with CBX, the decline in fluorescence seemed sharper for spheroids under 50μm (A, C). However, for larger spheroids (60μm), the loss of fluorescent signal made it difficult to discern qualitative differences between +/- CBX (E). To quantify the fluorescence distribution across each confocal image, the perimeter of the spheroid was identified via calceinRO fluorescence, and then eroded every 5μm to form a series of concentric shells. The same set of concentric shells were applied to the CTG channel. For each shell, calceinRO fluorescence was divided by its CTG fluorescence, normalized by its maximum ratio, and plotted as a function of its normalized radial position (B, D, F). Representative graphs were plotted for spheroids treated +/- CBX for spheroids of variable radii ranging from 30μm (B), 45μm (D), to 60μm (F). For both small spheroids (30μm) and larger spheroids (60μm), there was minimal separation between CBX-treated spheroids (white squares) and non-treated groups (black squares) (B, F). For 45μm radius spheroids, there was a clear difference between +/- CBX treated spheroids (D). (scale bar is 50μm).

.

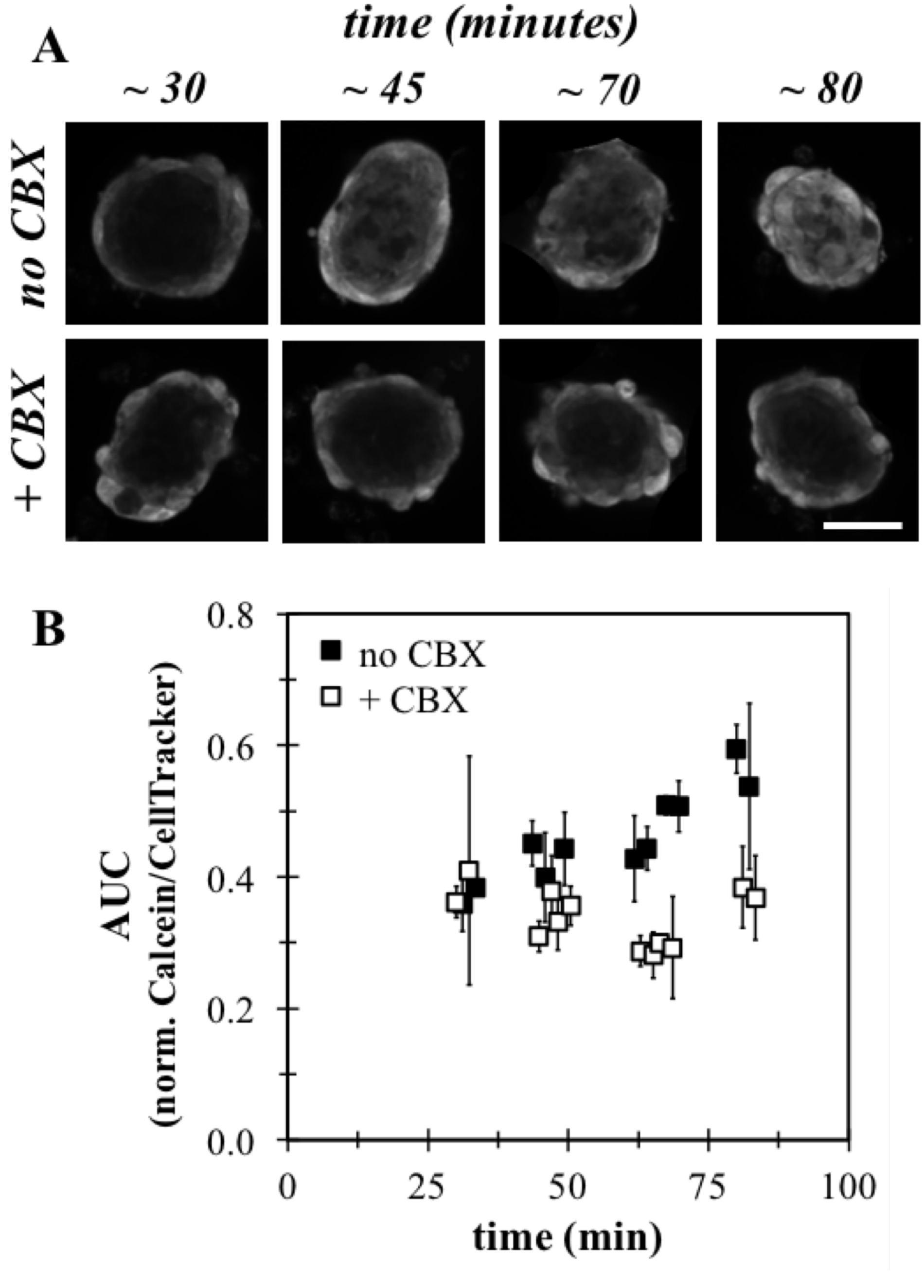

Figure 4-6. The distinction between +/- CBX increases with time.

.

Figure 4-6. The distinction between +/- CBX increases with time. KGN cell monolayers were labeled with CTG, trypsinized, counted, and seeded into agarose hydrogels to form spheroids. After self-assembling for 24-hours, spheroids were incubated either with or without the gap junction inhibitor, CBX, for 5-hours prior to the addition of calceinRO. Confocal *z*-stacks of spheroids were acquired and the equatorial image was taken for further analysis. Representative equatorial images were rendered for spheroids that were treated with CBX or without CBX at various time points (~30-, ~45-, ~70-, and ~80 minutes after the addition of calceinRO) (A). Regardless of time point, the fluorescent signal was brightest along the spheroid's perimeter, and decreased towards the center for both +/- CBX treatment (A). At early time points (30-minutes), spheroids treated +/- CBX appeared qualitatively similar with minimal fluorescent signal reaching the center (A). As incubation time with calceinRO increased, a greater fluorescent signal appeared from the center of non-treated spheroids, alternatively for CBX-treated spheroids, the fluorescent signal from the center did not appear to increase with time (A). To quantify the fluorescence distribution across each confocal image, the perimeter of spheroid was identified via calceinRO fluorescence, and then eroded every 5μm to form a series of concentric shells. The same set of concentric shells were applied to the CTG channel. For each shell, calceinRO fluorescence was divided by its CTG fluorescence, normalized to its maximum value, plotted as a function of normalized radii, and the AUC was calculated. The average and standard deviation was calculated for each well and plotted as a function of time (B). Thirty minutes after the addition of calceinRO, there was no difference in signal between CBX-treated spheroids (white squares) and no drug treatment (black squares) (B). As time progresses the separation between +/- CBX treated spheroids increased (B). (scale bar is 50μm).

.

Time (min)	Drug Treatment	***n***	***Radii***		***Area Under the Curve (AUC)***			
			average	*st. dev*	*average*	*st. dev*	*difference*	*p-value*
~ 32	no CBX	6	52.7	3.7	0.372	0.022	-0.014	0.541
	+ CBX	4	45.5	7.3	0.386	0.040		
~ 45	no CBX	7	49.1	6.9	0.429	0.060	0.080	0.023
	+ CBX	7	47.8	6.2	0.349	0.055		
~ 50	no CBX	3	51.6	7.6	0.443	0.044	0.097	0.039
	+ CBX	7	50.2	3.9	0.346	0.035		
~ 63	no CBX	7	47.6	3.2	0.434	0.051	0.149	0.000
	+ CBX	6	52.4	2.6	0.285	0.028		
~ 68	no CBX	8	40.5	3.3	0.508	0.027	0.214	0.001
	+ CBX	5	50.5	6.6	0.294	0.067		
~ 82	no CBX	5	39.2	7.8	0.572	0.081	0.194	0.003
	+ CBX	5	44.6	8.3	0.378	0.060		

Table 4-2. The difference between positive and negative controls increases over time. KGN spheroids, prelabeled with CTG, treated either +/- CBX, were labeled with calceinRO for varying incubation times prior to acquisition of confocal z-stacks. Time-points were grouped by columns across the 96-well plate, combining two wells per experimental group (+/- CBX). For each experimental group (+/- CBX, at varying time-points), the total number of spheroids (n) was counted, and the average radius and its standard deviation was computed. To quantify the fluorescence distribution across the equatorial image, the perimeter of the spheroid was identified and eroded to form a series of concentric shells. For each shell, the calcein fluorescence was divided by its CT fluorescence, normalized by its maximum ratio, plotted as a function of its normalized radial position, and the AUC was calculated. The average and standard deviation was computed for spheroids treated +/- CBX at each time point. The difference between the averages and the statistical significance for +/- CBX-treated spheroids was computed for each dye. The difference between +/- CBX treatment increased over time, with a peak occurring at ~68-minutes. With the exception of the first time-point (~32-minutes), all time-points were statistically significant from one another.

maximum value, plotted as a function of its normalized radius, and the AUC was calculated. The average and standard deviation of the AUC was computed for each well and plotted as a function of time (**Figure 4-6B**). At the beginning of the time series (~30-minutes) there was no difference in calceinRO distribution between control and CBX treated spheroids (**Figure 4-6B, Table 4-2**). As time progressed, the difference between control and CBX treatment increased with largest difference occurring after 70-minute incubation (**Figure 4-6B, Table 4-2**).

4.4.4 All tested methods of data analysis yielded statistical differences between +/- controls, but that does not imply ample separation with respect to Z-factor analysis.

To determine the best method to quantify GJIC, we tested two different approaches on the same data set. We analyzed confocal z-stacks of KGN spheroids prelabeled with CTG and incubated calceinRO for 70 minutes by either evaluating (1) just the equatorial image, or (2) the entire southern hemisphere of spheroid. For both approaches, the spheroid perimeter was detected and 5-μm concentric surfaces were applied to both the calceinRO and CTG fluorescent channels (**Supplemental Figure 4-1**, **Supplemental Figure 4-2**). The calceinRO/CTG signal for each shell of the equatorial image and the set of hemispheric images was then evaluated by three different methods: (a) normalizing to maximum value, plotting as a function of normalized radial position, and measuring the AUC, (b) calculating the ratio of fluorescence in the core normalized by outer shell, or (c) calculating the ratio of fluorescence in the middle shell normalized by outer shell (**Figure 4-7A, C, E**). These six calculations were done on every spheroid, and the

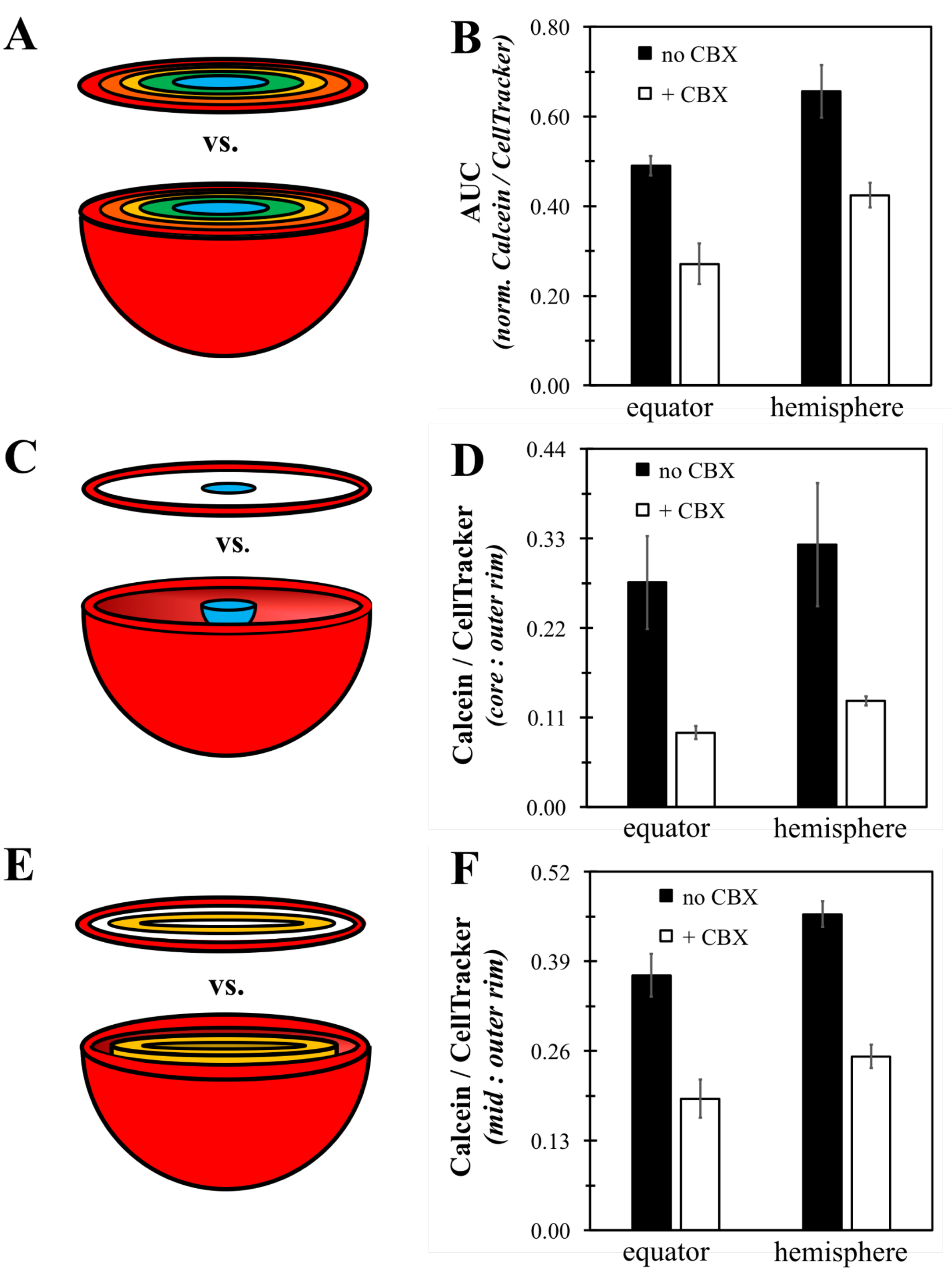

Figure 4-7. CBX inhibits calcein diffusion into the spheroid.

Figure 4-7. CBX inhibits calcein diffusion into the spheroid. KGN cell monolayers were labeled with CTG, trypsinized, counted, and seeded into agarose hydrogels to form spheroids. After self-assembling for 24-hours, spheroids were incubated either with or without the gap junction inhibitor, CBX, for 5-hours prior to the addition of calceinRO. After incubation with calceinRO for 70-minutes, confocal *z*-stacks of spheroids were acquired. Both the equatorial image and southern hemisphere of spheroid were taken for further analysis. To quantify the fluorescence distribution across the equatorial image and southern hemisphere, the perimeter of spheroid was identified, and then eroded every 5μm to form a series of concentric shells. The same set of concentric shells were applied to both the CTG and calceinRO signals. For each shell, calceinRO fluorescence was divided by its CTG fluorescence. For each spheroid, this normalized calceinRO/CTG fluorescence was then evaluated in three different ways: (1) further normalized by its maximum ratio, plotted as a function of its normalized radial position, and subsequently measuring the AUC (A, B), (2) calculating the ratio of core to outer shell fluorescence (C, D), (3) calculating the ratio of middle to outer shell fluorescence (E, F). For each method of data analysis, the average and standard deviation was calculated for spheroids treated with CBX (white bars) or without any drug (black bars) (B, D, F). For every method of analysis, CBX-treated spheroids had statistically significant lower amounts of calceinRO fluorescence penetrating inwards than their non-drug treated counterparts (B, D, F).

Drug Treatment	*n*	*Radii*	
		average	*st. dev*
no CBX	4	43.1	2.4
+ CBX	4	52.3	7.1

Data Analysis Method	Spheroid Portion	Drug Treatment	*Values*				
			average	*st. dev*	*difference*	*p-value*	*Z-factor*
AUC (norm. Calcein/CellTracker)	equator	no CBX	0.490	0.022	0.219	0.001	0.08
		+ CBX	0.271	0.045			
	hemisphere	no CBX	0.656	0.058	0.231	0.002	-0.11
		+ CBX	0.425	0.027			
core : outer shell (Calcein/CellTracker)	equator	no CBX	0.276	0.057	0.185	0.007	-0.06
		+ CBX	0.091	0.008			
	hemisphere	no CBX	0.322	0.076	0.192	0.014	-0.27
		+ CBX	0.130	0.006			
middle : outer shell (Calcein/CellTracker)	equator	no CBX	0.370	0.031	0.179	0.000	0.01
		+ CBX	0.191	0.028			
	hemisphere	no CBX	0.459	0.018	0.206	0.000	0.49
		+ CBX	0.252	0.017			

Table 4-3. Statistically significant inhibition of GJIC does not imply good Z-factor scores. KGN spheroids, pre-labeled with CTG, treated either +/- CBX, were labeled with calceinRO for 70-minutes prior to acquisition of confocal *z*-stacks. The total number of spheroids (*n*) was counted, and the average radius and its standard deviation was computed. Both the equatorial image and southern hemisphere of the spheroid were taken for further analysis. To determine the best method to quantify GJIC, the same data set was analyzed three different ways: (1) further normalized by its maximum ratio, plotted as a function of its normalized radial position, and subsequently measuring the AUC, (2) calculating the ratio of core to outer shell fluorescence, (3) calculating the ratio of middle to outer shell fluorescence. For each method of data analysis, the average and standard deviation was calculated for spheroids treated +/- CBX. Furthermore, the difference between the averages, the statistical significance, and Z-factor was computed

average, standard deviation, and statistical significance were calculated for spheroids treated +/- CBX (**Figure 4-7B, D, F, Table 4-3**). To compare analysis methods, a Z-factor analysis was performed. All six analysis methods showed that CBX inhibition of GJIC was statistically significant (**Table 4-3**). However, to be considered useful for a high throughput drug discovery screen, there must also be good separation between the control and treatment groups, as measured by the Z-factor, which evaluates the differences between the averages, and the variation about the mean. Of the six methods tested, the ratio of the middle shell to the outer shell of the hemispheric images yielded the largest Z-factor (**Table 4-3**).

4.5 DISCUSSION

Gap junctions perform a critical role in cellular communication throughout the body, and disruption of physiologic GJIC could lead to various pathologies [1,6-10]. To study GJIC *in vitro*, we have developed a 3D spheroid model that quantifies fluorescence distribution patterns throughout its radius. Although spheroids are biologically advantageous over traditional 2D monolayer approaches, acquiring accurate quantitative information from confocal *z*-stacks of 3D spheroids is more complex [39,43,47]. To address some of these imaging complexities, we utilized ratio imaging to normalize the uptake and distribution of calcein penetration into 3D spheroids. With this spheroid model, we acquired *z*-stacks of living spheroids that were dynamically taking up fluorescent calcein dyes and distributing them via GJIC throughout its 3D radius. We tested the ability of our system to detect CBX-mediated inhibition of GJIC. We optimized our model with respect to calcein dye choice and incubation time, spheroid size, and data analysis approach in order to enhance the separation between the positive and negative controls (+/- CBX).

Prior to assessing gap junction inhibition within 3D spheroids, we first assessed the ability of our system to quantify the penetration of calcein throughout spheroids. To do so, cells were first self-assembled into spheroids and then incubated with either calceinAM or calceinRO. When adding a fluorescent dye to spheroids, the dye must enter the outer cell layer prior to diffusing towards the spheroid center, thereby establishing a gradient of fluorescence from outer edge to core. When evaluating the diffusion of calcein dyes into spheroids, the greatest signal occurred at the edge of spheroid with a gradient of signal decreasing towards the center. However, a limitation of confocal microscopy of spheroids is the loss of fluorescent signal deeper into the *z*-depth [47-49]. We have previously shown that for larger spheroids (diameter $< 50\mu$m), loss is not uniform across the confocal image but rather is preferentially greater in the center of spheroid [47]. Therefore, when developing a gap junction assay that quantifies fluorescence along the 3D radius, these effects needed to be minimized and so spheroid size was restricted. Additionally, to ensure that this gradient of signal is due to calcein penetration and not signal loss due to the limitations of confocal imaging, we used ratio imaging by staining the cells used to form spheroids with a CT dye. By normalizing calcein fluorescence to CT fluorescence at each location in the spheroid we control for changes in fluorescence due to the limitations of confocal imaging of spheroids as well as small variations in spheroid size.

To develop a spheroid-based GJIC assay, we optimized several parameters; choice of calcein dye, time of incubation with calcein dye, spheroid size, timing of confocal imaging, and method of quantitative analysis. All were done with and without CBX treatment, a well-known inhibitor of GJIC [45,46]. We tested two calcein dyes, calceinAM and calceinRO. CalceinRO provided a greater separation between +/- CBX treatment groups compared to calceinAM. There could be a variety of attributes contributing to the better performance of calceinRO, ranging from differing excitation/emission spectra to differing chemical properties. However, calceinAM is a substrate for the efflux pump p-glycoprotein (P-gp), a pump expressed by KGN cells [44,51]. Moreover, we have previously shown that CBX inhibits P-gp in KGN spheroids [44]. For calceinAM-labeled spheroids, the addition of CBX increased the overall amount of fluorescence versus controls. But this was not the case for calceinRO-labeled spheroids treated with CBX, as the total fluorescence was comparable with and without CBX treatment. CBX treatment did inhibit GJIC in both calceinRO-labeled and calceinAM-labeled spheroids because the proportion of total calcein fluorescence in the outer shell of the spheroid was increased versus controls. These data suggest that calceinRO is not a P-gp substrate or a weak substrate, which may be part of the explanation as to why it outperformed calceinAM in our assay.

Assessing GJIC is a live cell assay, where the uptake and distribution of calcein throughout a spheroid is a dynamic process that starts when dye is added. Moreover, the acquisition of confocal *z*-stacks of two fluorescent channels (75 images per channel), for 4 spheroids per well, for an entire 96-well plate takes approximately 100-minutes.

Therefore, if a dynamic process is completed within minutes after addition of compound, then performing confocal microscopy of an entire 96-well plate would not be a relevant technique to use. Our previous research assessing GJIC in 3D spheroids indicated that calceinAM penetration and distribution throughout the spheroids occurred on a time-scale of hours, as opposed to minutes, thus confocal microscopy could be performed [44]. Alternatively, if confocal *z*-stacks are acquired too quickly after the addition of calcein dyes, then there may not be a detectable level of calcein present in the spheroid, let alone penetrating towards the spheroid center. Therefore, if calcein does not have adequate time to travel through gap junctions towards spheroid center, then +/- CBX treatment groups would exhibit the same staining patterns, and we would not be able to visualize or quantify differences between groups. We found that calceinRO should be incubated with spheroids for at least 70-minutes prior to imaging in order to provide adequate separation between +/- CBX treatment groups. Furthermore, since it requires approximately 1-minute to image one well, we need to either (1) dramatically reduce the amount of z-images needed per image location, or (2) account for the dynamic changes that could occur over 90-minutes and design the 96-well plate set-up accordingly. For example, our confocal microscope acquires images in a snake-like pattern moving from one column to the next across a 96-well plate. To account for dynamic changes that may occur across the plate, the positive control (+CBX) and negative control (no drug) should be included within each column. The images of the negative control (no drug) should be acquired first, while the positive control (+CBX) should be acquired last. Control spheroids possess the greatest amount of fluorescence reaching the core, and amounts will increase over time. Imaging the negative control 8-minutes prior to the positive control may reduce the difference between +/- controls, but it will ensure that differences are real, and not due to differences in the time of imaging.

Another critical parameter of the GJIC assay is spheroid size. For spheroids, we need to balance the need to increase physiological relevance with multiple cell layers with the physical limitations of instrumentation. If spheroid radius is too small, then treatment with a GJ inhibitor will have minimal effect since most cells of the spheroid will be in close proximity to the reservoir of calcein dye and will not be labeled via GJIC. Our studies indicate that spheroids with a radius under 30-μm are too small to observe differences between +/- controls. Alternatively, if a spheroid is too large (>60-μm) signal loss is extensive, thus differences between +/- controls are dampened. We found that maximum difference between positive and negative controls occurred with spheroids 40-45-μm in radius. Furthermore, when designing a strategy to measure inhibition of GJIC in 3D spheroids, we need to consider the role that spheroid size plays in fluorescence quantification. Due to the innate variability of cell type, as well as various pipetting errors throughout the experimental set-up, spheroid formation will yield of a range of spheroid sizes. With our technique, we aim to achieve a standard deviation approximately 10% of its mean. Therefore, an ideal quantification strategy would not be sensitive to minor deviations in spheroid radius.

To determine the best method of data analysis, we tested several computational methods focused on either the equatorial image or the stack of images comprising the southern hemisphere. Each approach has advantages and disadvantages. For example, evaluating the equatorial image is computationally simple, however, a single image may not be representative of the whole spheroid. Furthermore, given the range of spheroid sizes, their respective equators could be at different z-heights, making it susceptible to differing levels of fluorescent loss, thus adding more variability to the system. Alternatively, evaluating the images of the hemisphere is more computationally complex, but more representative of the spheroid and the effects of signal loss should be less versus the equatorial image. For the equatorial image and the hemispheric images, we also compared three different methods to quantify the normalized calcein fluorescent signal: (1) the AUC for normalized calcein as a function of radius, (2) the ratio of core to outer shell, or (3) the ratio of the middle shell to the outer shell. The AUC accounts for data from across the entire 2D or 3D radius of the spheroid, which should be beneficial, however difference in fluorescence patterns due to size changes can alter the AUC, leading to variability from spheroid to spheroid. Alternatively the ratio of core to outer shell, is a simplified approach, however, the core is more susceptible to fluorescent loss. Also, the distance traveled by calcein to the core is dependent upon the spheroid radius, thus increasing variability. However, the ratio of middle shell to outer shell circumvents some of these issues. With this method, calcein diffuses a fixed distance to reach the middle shell, whereas the distance to the core may vary depending on the size of the spheroid. Also, the middle shell is less affected by loss of fluorescent signal than the core. To compare these analysis methods, we performed a Z-factor analysis which examines the separation between the averages of +/- controls and the variability of the standard deviation about those means [50]. Although taking the ratio of the middle to outer shell in the southern hemisphere did not have the largest separation between the +/- CBX averages, its variation about their mean was small, thus contributing to a higher Z-factor than any other method of data analysis.

In this paper, we have developed a high throughput assay to measure GJIC within spheroids. Spheroids afford numerous biological advantages over more traditional approaches to study GJIC, including increased physiological relevance with multiple cell layers, increased cell-cell contacts and communication [39,43]. Despite their biological advantages, acquiring quantitative information from confocal *z*-stacks of spheroids is more complex than traditional 2D cell monolayers [47,48]. The spheroid-based GJIC assay substitutes calceinRO for calceinAM, is optimized for spheroid size, uses ratio imaging to correct for limitations of confocal imaging, and provides a quantitation method to analyze the data. Because GJ are involved in many biological processes and disruption of GJIC has been linked to numerous pathologies, this assay may be useful for identify drug candidates and environmental toxicants that interfere with GJIC.

4.6 AUTHOR CONTRIBUTIONS

E.L. and C.R. designed and performed the series of experiments. B.W. designed ImageJ analysis programs. J.R.M. supervised the project. All authors contributed towards writing the manuscript.

4.7 ACKNOWLEDGEMENTS

This work was funded in part by seed funds from Unilever and the generous support of Donna McGraw Weiss '89 and Jason Weiss. Also, this work was funded under the U.S. Department of Education, GAANN Award P200A150037, the National Science Foundation Award OIA1655221, and the National Institute of Environmental Health Sciences Award 1U01ES028184. We thank Microtissues, Inc. for the mold used to make the 96 well plates.

4.8 CONFLICT of INTEREST

J.R.M has an equity interest in Microtissues, Inc. This relationship has been reviewed and managed by Brown University in accordance with its conflict of interest policies.

4.9 REFERENCES

1. Abbaci M, Barberi-Heyob M, Blondel W, Guillemin F, Didelon J. Advantages and limitations of commonly used methods to assay the molecular permeability of gap junctional intercellular communication. *Biotechniques*. 45(1):63-68, 2008.

2. Alexander DB, Goldberg GS. Transfer of biologically important molecules between cells through gap junction channels. *Current Medicinal Chemistry*. 10:2045-2058, 2003.

3. Brink PR, Cronin K, Ramanan SV. Gap junctions in excitable cells. *Journal of Bioenergetics and Biomembranes*. 28:351-358, 1996.

4. Webb RJ, Marshall F, Swann K, Carroll J. Follicle-stimulating hormone induces a gap junction-dependent dynamic change in [cAMP] and protein kinase a in mammalian oocytes. *Developmental biology*. 246(2):441-454, 2002.

5. Kalimi GH, Lo CW. Gap junctional communication in the extraembryonic tissues of the gastrulating mouse embryo. *The Journal of Cell Biology*. 109:3015-3026, 1996.

6. Loewenstein WR. Junctional intercellular communication: the cell-to-cell membrane channel. *Physiological Reviews*. 61:829-913, 1981.

7. Dere E, Zlomuzica A. The role of gap junctions in the brain in health and disease. *Neuroscience and Behavioral Reviews*. 36(1):206-217, 2012.

8. Dermietzal R, Spray DC. Gap junctions in the brain: where, what type, how many and why? *Trends in neuroscience*. 16(5):186-192, 1993.

9. Davis LM, Rodefeld ME, Green K, Beyer EC, Saffitz JE. Gap junction protein phenotypes of the human heart and conduction system. *Journal of Cardiovascular Electrophysiology*. 6(10):813-822, 1996.

10. Poelzing S, Rosenbaum DS. Altered connexin43 expression produces arrhythmia substrate in heart failure. *Journal of Physiology Heart*. 287(4)1762-1770, 2004.

11. Herve JC, Bourmeyster N, Sarrouihe D. Diversity in protein-protein interactions of connexins: emerging roles. *Biochimica et Biophysica Acta.* 1662:22-41, 2004.

12. Cheng CY, Wong EW, Lie PP, Li MW, Siu ER, Yan HH, Mannu J, Mathur PP, Bonanomi M, Silvestrini B, Mruk DD. Environmental toxicants and male reproductive function. *Spermatogenesis*. 1(1):2-13, 2011.

13. Upham BL, Blaha L, Babica P, Park JS, SOvadinova I, Pudrith C, Rummel AM, Weis LM, Sai K, Tithof PK, Guzvic M, Vondracek J, Machala M, Trosko JE. Tumor promoting properties of a cigarette smoke prevalent polycyclic aromatic hydrocarbon as indicated by the inhibition of gap junctional intercellular communication via phosphatidylecholine-specific phospholipase C. *Cancer Science*. 99(4):696-705, 2008.

14. Kenny LC, Baker PN, Kendall DA, Randall MD, Dunn WR. The role of gap junctions in mediating endothelium-dependent responses to bradykinin in myometrial small arteries isolated from pregnant woman. *British Journal of Pharmacology*. 136(8):1085-1088, 2002.

15. Davidson JS, Baumgarten IM, Harley EH. Reversible inhibition of intercellular junctional communication by glycyrrhetinic acid. *Biochemical and Biophysical Research Communications*. 134:29-36, 1986.

16. Goldberg GS, Moreno AP, Bechberger JF, Hearn SS, Shivers RR, MacPhee DJ, Zhang YC, Naus CC. Evidence that disruption of connexon particle arrangements in gap junction plaques is associated with inhibition of gap junctional communication by a glycyrrhetinic acid derivative. *Experimental Cell Research*. 222(1):48-53, 1996.

17. Manjarrez-Marmolejo J, Franco-Perez J. Gap junction blockers: an overview of their effects on induced seizures in animal models. *Current Neuropharmacology*. 14(7):759-771, 2016.

18. Yamamoto Y, Suzuki H. Blockade by mefloquine of intercellular electrical coupling between vascular endothelial cells in the guinea-pig mesenteric arteries. *Journal of Smooth Muscle Research*. 44(6):209-215, 2008.

19. Nassiri-Asl M, Zamansoltani F, Zangivand AA. The inhibitory effect of trimethylamine on the anticonvulsant activities of quinine in the pentylenetetrazole model in rats. *Biological Psychiatry*. 32(6):1496-1500, 2008.

20. Liao CK, Wang SM, Chen YL, Wang HS, Wu JC. Lipopolysaccharide-induced inhibition of connexin43 gap junction communication in astrocytes is mediated by downregulation of caveolin-3. *The international journal of biochemistry and cell biology*. 42(5):762-770, 2010.

21. Bolanos JP, Medina JM. Induction of nitric oxide synthase inhibits gap junction permeability in cultured rat astrocytes. *Journal of Neurochemistry*. 66:2091-2099, 1996.

22. Shishido SN, Prasain K, Beck A, Nguyen TDT, Hua DH, Nguyen TA. Bioavailability and efficacy of a gap junction enhancer (PQ7) in a mouse mammary tumor model. *PLOS One*. 8(6):e67174, 2013.

23. Chang WP, Wu JJS, Shyo BC. Thalamic modulation of cingulate seizure activity via the regulation of gap junctions in mice thalamocingulate slice. *PLOS One*. 8(5):e62952, 2013.

24. Meda P. Probing the function of connexin channels in primary tissues. *Methods*. 20:232-244, 2000.

25. Liu J, Siragam W, Chen J, Fridman MD, Hamilton RM, Sun Y. High-throughput measurement of gap junctional intercellular communication. *American Journal of Physiology: Heart and Circulatory Physiology*. 306(12):1708-1713, 2014.

26. el-Fouly MH, Trosko JE, Chang CC. Scrape-loading and dye transfer. A rapid and simple technique to study gap junctional intercellular communication. *Experimental Cell Research*. 168:422-430, 1987.

27. Trosko JE, Chang CC, Wilson MR, Upham B, Hayashi T, Wade M. Gap junctions and the regulation of cellular functions of stem cells during development and differentiation. *Methods*. 20:245-264, 2000.

28. Opsahl H, Rivedal E. Quantitative determination of gap junction intercellular communication by scrape loading and image analysis. *Cell Communication and Adhesion*. 7:367-375, 2000.

29. Takano K, Ogawa M, Kawabe K, Moriyama M, Nakamure Y. Inhibition of gap junction elevates glutamate uptake in cultured astrocytes. *Neurochemical Research*. 43(1):50-56, 2018.

30. Raptis LH, Brownell HL, Firth KL, Mackenzie LW. A novel technique for the study of intercellular, junctional communication: electroporation of adherent cells on a partly conductive slide. *DNA and Cell Biology*. 13:963-975, 1994.

31. Geletu M, Guy S, Firth K, Raptis L. A functional assay for gap junctional examination; electroporation of adherent cells on indium-tin oxide. *Journal of Visualized Experiments*. (92):e51710, 2014.

32. Wade MH, Trosko JE, Schindler M. A fluorescence photobleaching assay of gap junction-mediated communication between human cells. *Science*. 232:525-528, 1986.

33. Kuzma-Kuzniarska M, Yapp C, Pearson-Jones TW, Jones AK, Hulley PA. Functional assessment of gap junctions in monolayer and three-dimensional cultures of human tendon cells using fluorescence recovery after photobleaching. *Journal of Biomedical Optics*. 19(1):015001, 2014.

34. Goldberg GS, Bechberger JF, Naus CC. A pre-loading method of evaluating gap junctional communication by fluorescent dye transfer. *Biotechniques*. 18:490-497, 1995.

35. Gittens JE, Mhawi AA, Lidington D, Ouellette Y, Kidder GM. Functional analysis of gap junctions in ovarian granulosa cells: distinct role for connexin43 in early stages of folliculogenesis. *American Journal of Physiology - Cell Physiology*. 284(4):880-887, 2003.

36. Chang TT, Hughes-Fulford M. Monolayer and Spheroid Culture of Human Liver Hepatocellular Carcinoma Cell Line Cells Demonstrate Distinct Global Gene Expression Patterns and Functional Phenotypes. *Tissue Engineering Part A*. 15(3): 559-567, 2008.

37. Chitcholtan K, Asselin E, Parent S, Sykes PH, Evans JJ. Differences in growth properties of endometrial cancer in three dimensional (3D) culture and 2D cell monolayer. *Experimental Cell Research*. 319(1):75-87, 2012.

38. Astashkina AI, Mann BK, Prestwich GD, Grainger DW. Comparing predictive drug nephrotoxicity biomarkers in kidney 3-D primary organoid culture and immortalized cell lines. *Biomaterials*. 33(18):4712-4721, 2012.

39. Griffith LG, Swartz MA. Capturing complex 3D tissue physiology in vitro. *Nature Reviews: Molecular Cell Biology.* 7:211-224, 2006.

40. Yamada KM, Cukierman E. Modeling tissue morphogenesis and cancer in 3D. *Cell.* 130:601-610, 2007.

41. Bartosh TJ, Yostalo JH, Mohammadipoor A, Bazhanov N, Coble K, Claypool K, Lee RH, Choi H, Prockop DJ. Aggregation of human mesenchymal stromal cells (MSCs) into 3D spheroids enhances their antiinflammatory properties. *Proceedings of the National Academy of Sciences of the United States of America*. 107(31):13724-13729, 2010.

42. Vantangoli MM, Madnick SM, Huse SM, Weston P, Boekelheide K. MCF-7 human breast cancer cells form differentiated microtissues in scaffold-free hydrogels. *PLoS One*. 10:e0135426, 2015.

43. Achilli TM, Meyer J, Morgan JR. Advances in the formation, use and understanding of multicellular spheroids. *Expert Opinions Biological Therapy*. 12(10):1347-1360, 2012.

44. Achilli TM, McCalla S, Meyer J, Tripathi A, Morgan JR. Multilayer Spheroids to Quantify Drug Uptake and Diffusion in 3D. *Molecular Pharmacolgy*. 11(7):2071-2081, 2014.

45. Sagar GDV, Larson DM. Carbenoxolone inhibits junctional transfer and upregulates connexin43 expression by a protein kinase A-dependent pathway. *Journal of Cellular Biochemistry*. 98:1543-1551, 2006.

46. Connors BW. Tales of a dirty drug: carbenoxolone, gap junctions, and seizures. *Epilepsy Currents*. 12(2):66-68, 2012.

47. Leary E, Rhee C, Wilks BT, Morgan JR. Quantitative Live-Cell Confocal Imaging of 3D Spheroids in a High-Throughput Format. *SLAS Technology*. 2018.

48. Boutin ME, Hoffman-Kim D. Application and assessment of optical clearing methods for imaging of tissue-engineered neural stem cell spheres. *Tissue Engineering Part C Methods.* 21(3):292-302, 2015.

49. Oreopoulos J, Berman R, Browne M. Spinning-disk confocal microscopy: present technology and future trends. *Methods in Cell Biology*. 123:153-175, 2014.

50. Zhang JH, Chung TD, Oldenburg KR. A simple statistical parameter for use in evaluation and validation of high throughput screening assays. *Journal of Biomolecular Screening*. 4(2):67-73, 1999.

51. berghien F, Loor F. Ranking of P-glycoprotein substrates and inhibitors by a calcein-AM fluorometry screening assay. *Anticancer Drugs*. 7(5):568-78, 1996.

4.10 SUPPLEMENTAL FIGURES

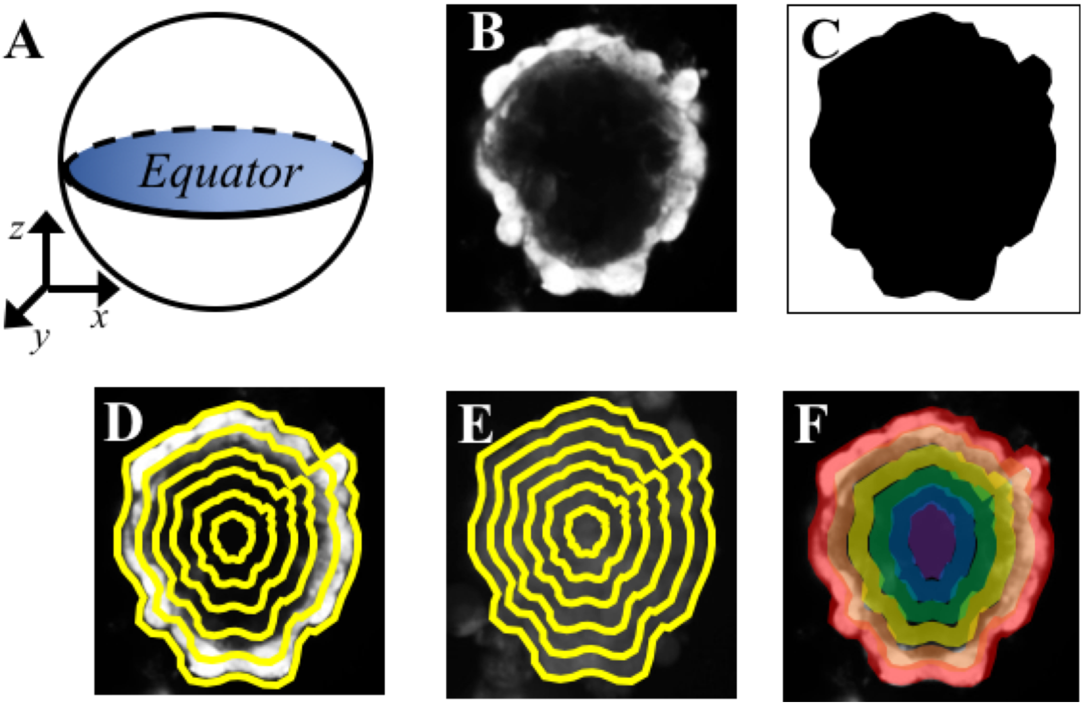

Supplemental Figure 4-1. Individual confocal images were analyzed to measure fluorescence distribution across 2D radius. Confocal *z*-stacks were acquired for spheroids labeled with both a CT and calcein dye, and the equatorial images were taken for analysis (A). The equatorial calcein image was imported into ImageJ and thresholded to identify the spheroid containing region (B, C). The outer perimeter of the spheroid was identified and subsequently eroded every 5μm to form a series of concentric shells (D). The same set of shells was applied to the CT fluorescent channel (E). For each shell, the area, the calcein signal, and the CT signal were measured (F).

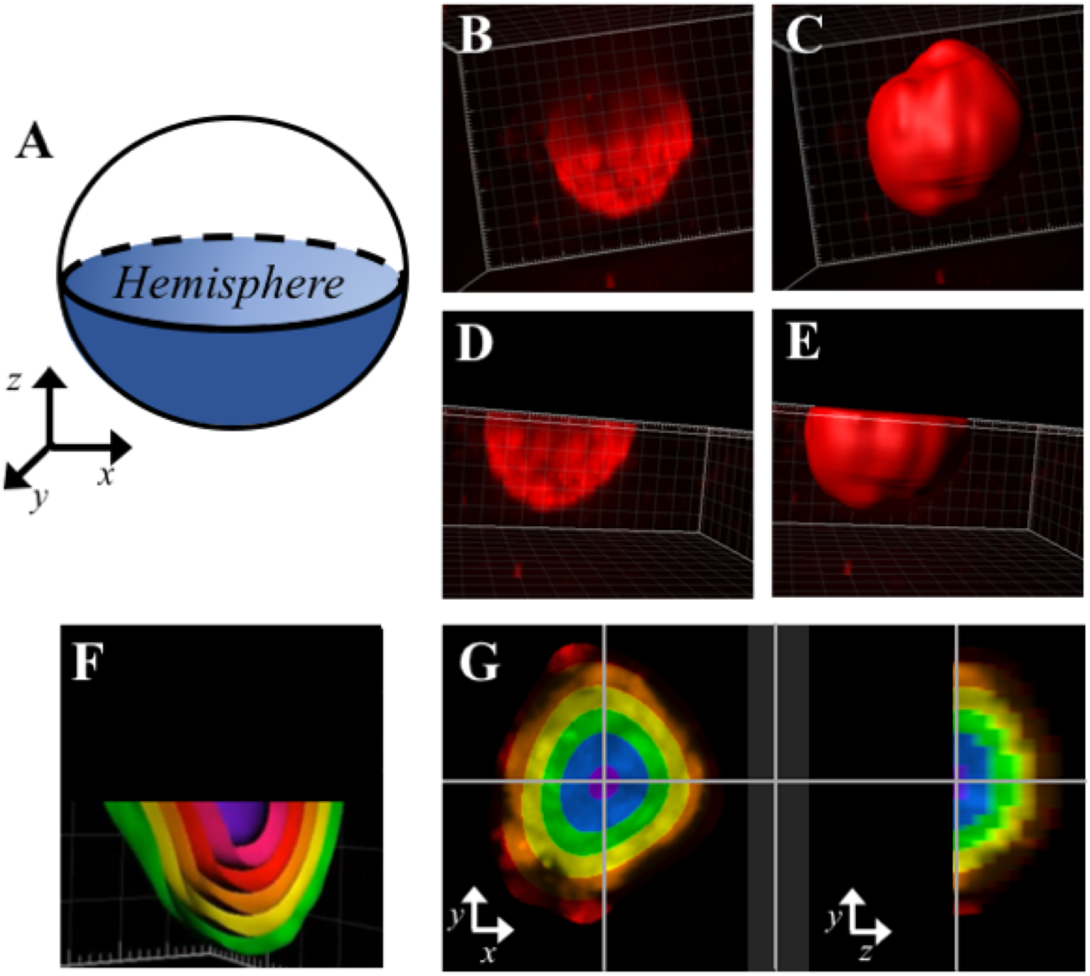

Supplemental Figure 4-2. Spheroids were rendered as hemispheres to measure fluorescence distribution across 3D radius. Confocal *z*-stacks were acquired for spheroids labeled with both a CT and calcein dye, and the southern hemisphere of the spheroid was analyzed (A). First, the entire *z*-stack was imported into Imaris, rendered in 3D (B), and the surface of the spheroid was identified (C). The center point of the spheroid (*x, y, z*), total volume, calcein-, and CT fluorescence were measured. To minimize the effects of fluorescent signal loss, the 3D rendering was cropped at the equator, leaving only the southern hemisphere (D, E). The outer surface of the spheroid was eroded every 5μm to form a series of concentric hemi-shells (F). The same set of shells were applied to both the CT and the calcein fluorescent channels. For each shell, the volume, the calcein signal, and the CT signal were measured (G).

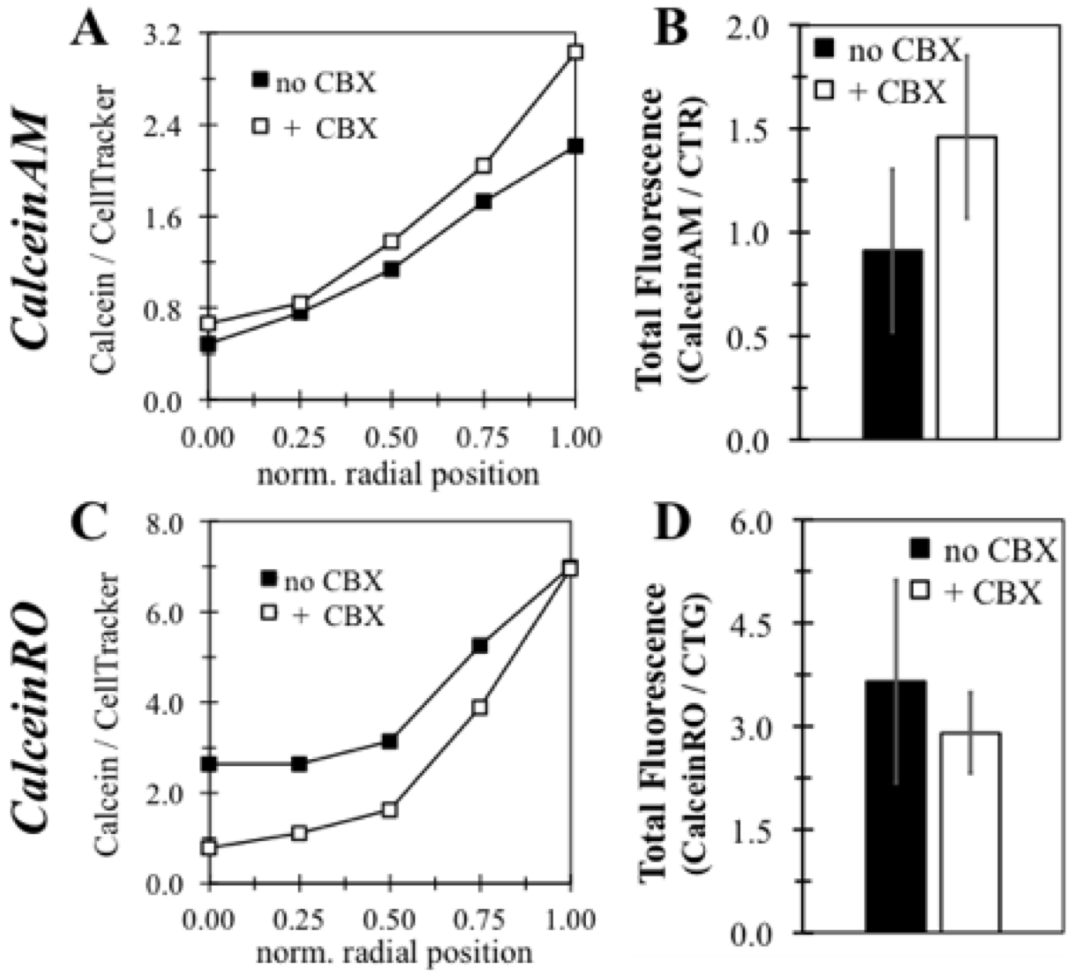

E

	Drug Treatment	*n*	*Radii*		*Total Fluorescence (Calcein/CT)*			
			average	*st. dev*	*average*	*st. dev*	*difference*	*p-value*
calceinAM	no CBX	8	46.3	5.3	0.912	0.392	-0.548	0.018
	+ CBX	7	44.0	7.2	1.459	0.392		
calceinRO	no CBX	6	42.6	9.9	3.655	1.475	0.747	0.284
	+ CBX	8	41.4	7.8	2.908	0.586		

Supplemental Figure 4-3. CBX increases total fluorescence of calceinAM but not calceinRO labeled spheroids.

Supplemental Figure 4-3. CBX increases total fluorescence of calceinAM but not calceinRO labeled spheroids. KGN cell monolayers were labeled with either CTR or CTG, trypsinized, counted, and seeded into agarose hydrogels to form spheroids. After self-assembling for 24-hours, spheroids were incubated either with or without the gap junction inhibitor, CBX, for 5-hours prior to the addition of a calcein dye. CalceinAM was added to spheroids labeled with CTR, while calceinRO was added to spheroids labeled with CTG. Confocal *z*-stacks of spheroids were acquired and the equatorial image was taken for further analysis. To quantify the fluorescence distribution across each confocal image, the perimeter of the spheroid was identified via calcein fluorescence, and then eroded every 5μm to form a series of concentric shells. The same set of concentric shells were applied to the CT channel. For each shell, the calcein fluorescence was divided by its CT fluorescence, and the calcein/CT signal was plotted as a function of its normalized radial position (A, C). Representative graphs for spheroids treated +/- CBX labeled with calceinAM (A) or calceinRO (C) were plotted. For calceinAM, spheroids treated with CBX (white squares) possessed a higher calceinAM/CTR fluorescent signal at the outer edge than their non-treated counterparts (black squares), with both lines converging to same value at spheroid center (A). However, for calceinRO, spheroids treated +/- CBX possessed a similar calceinRO/CTG signal at the outer edge, and then diverged with CBX-treated spheroids possessing an overall lower signal at spheroid center (C). To quantify the difference in fluorescent signal induced by CBX, the calcein and the CT fluorescence of each shell were summed, and the total calcein fluorescence was normalized by the total CT fluorescence. The total calcein/CT ratio was computed for each spheroid, and the average and standard deviation were calculated for spheroids treated +/- CBX (B, D, E). For calceinAM, spheroids treated with CBX had a statistically significant increase in overall fluorescent signal compared to non-treated counterparts (B, E). For calceinRO, untreated spheroids had a slightly higher overall fluorescent signal than CBX-treated spheroids, although the result was not statistically significant (D, E).

CHAPTER 5

Conclusions, Discussion, & Future Directions

5.1 OVERVIEW

In vitro models are integral tools in every biological field that possess a range of purposes from: examining physiology, modeling disease progression, as well as evaluating efficacy or toxicity of compounds [1-4]. Traditionally, *in vitro* modeling has predominantly utilized two-dimensional (2D) cell monolayers, which can be easily formed and assessed, relatively cheap, and adaptable to high-throughput screening. However, utilizing a single layer of cells attached to a plastic substrate fails to capture the complexity found *in vivo* [1]. To better mimic the *in vivo* environment, three-dimensional (3D) multicellular spheroids can be utilized. 3D spheroid models have been utilized for over hundred years to study a range of biological processes [2,5]. Throughout this time-frame, spheroids have been shown to approximate the cell density found *in vivo*, possess increased levels of cell-cell interactions and intercellular communication, as well as maintain a more differentiated state, and recapitulate organ-specific processes [2, 6-12]. Spheroids, with their multiple cell layers, will naturally form concentration gradients of nutrients, oxygen, carbon dioxide, and pH along its 3D radius [13,14]. These gradients give rise to variations within a single spheroid, thus individual cells will experience different microenvironments depending upon their location. This phenomenon cannot be recapitulated within 2D cell monolayers, as every cell experiences the same physiological conditions. Therefore, by probing with fluorescent dyes and microscopy, alterations in cellular behavior induced by changes in microenvironment can be assessed. Additionally, similar to the *in vivo* environment, the multiple cell layers within a spheroid form barriers to transport and diffusion [13,14]. By incubating spheroids with fluorescent compounds, uptake, diffusion, and distribution throughout spheroids can be modeled over time [4,15].

To further increase complexity, secondary compounds can be added that block or alter the uptake and distribution throughout. Overall, 3D spheroids can model complex biological processes in an *in vitro* setting.

A critical component in advancing the use of spheroids for quantitative *in vitro* modeling is determining the appropriate spheroid size. In order to quantify differences in biology throughout the spheroid, the radius must be large enough. If a spheroid is too small (1-3 cell layers), every cell within the spheroid could have protrusions reaching the outermost layer providing access to the reservoir of nutrients, dyes, compounds, thus preventing the formation of gradients. In order to achieve quantifiable differences within spheroids, multiple cell layers are necessary, with a larger number of cell layers yielding starker changes throughout. However, there is also an upper biological limit to spheroid size, as oxygen and nutrients can only diffuse 200-μm into the spheroid [15,16]. Creating spheroids larger than the diffusion limit will yield formation of apoptotic/necrotic cores, which could be useful for studying cancer biology, however, should be avoided for forming healthy tissues [3,15,17].

Furthermore, the key biological advantage of spheroids, its three-dimensionality, is also its potential downfall with respect to quantitative fluorescence microscopy. Acquiring quality images of thin, 2D cell monolayers is relatively straightforward regardless of the microscopy technique used. However, the increased tissue thickness of spheroids creates issues while imaging, with variable constraints dependent upon the type of microscopy performed. For example, for wide-field epifluorescence images, emitted fluorescent light can be captured for spheroids up to a height of 205-μm [18]. However, for confocal microscopy, fluorescent loss starts to occur immediately, with striking signal loss occurring approximately 50-μm into the *z*-depth [19,20]. This limit can be improved upon with tissue clearing techniques, which increase visualization up to approximately100-μm into a spheroid [19,20]. However, tissue clearing is not amenable to live cell imaging, thus limiting its usefulness to fixed, endpoint assays. Alternative microscopy techniques, such as multi-photon and light-sheet microscopy, also offer improved visualization into z-depth [21,22]. Overall, when developing quantitative spheroid assays, a delicate balance must be achieved between the biological need for multiple cell layers and the physical limitations of microscopy.

Additionally, spheroid size plays a role in dictating the total amount and subsequent distribution patterns of fluorescent signal throughout. In order to eliminate potential differences in fluorescent signal due to size, there are two options: (1) restrict spheroid size to be within a set range of radius, or (2) determine appropriate ways to normalize fluorescence data to analyze spheroids of different sizes. The process of spheroid formation will yield spheroids of variable radii, therefore, understanding how to normalize differences due to size is crucial to maximizing the usefulness of spheroids. Furthermore, fluorescent data obtained from different imaging systems may experience varying sensitivity to deviations of spheroid radius. Therefore, data obtained from each imaging system may possess different size-based inclusion criteria for fluorescent quantification. Understand the quantitative limitations of each technique is critical to maximize the usefulness of obtainable spheroid data. This dissertation aimed to develop quantitative analysis strategies for spheroids to better account for differences in fluorescent signal due to size.

In order for spheroids to be truly triumphant over 2D cell monolayers as an *in vitro* modeling tool, the technology must be amenable to high-throughput screening. Throughout the past decade, many commercially-available technologies have been developed to easily form and image spheroids in a high-throughput manner [23-25]. For example, many traditional techniques to form spheroids, such as hanging drop and liquid overlay, have been optimized for use with 96- and 384-well plates [23-25]. Additionally, confocal microscopy was adapted for use as high content, high throughput imaging systems, and there are many systems commercially available [26,27]. Despite these technological advances enabling the formation and image acquisition of spheroids in a high-throughput manner, there is still a lack of strategies and tools available to accurately quantify and interpret data from 3D spheroids [26,27]. For example, there are various open-source and commercially available software programs to analyze 3D data sets [26,27]. These programs either possess the ability to perform either (1) an in-depth analysis of a few spheroids, or (2) a high level, basic batch-able analysis of a large number of spheroids [26,27]. However, to fully capitalize on the complex biology of spheroids, an in-depth, batch-able 3D image analysis platform is necessary.

Developing high-throughput, quantitative, *in vitro* models using 3D spheroids can be distilled to combination of three tools: (1) probes to identify a biological event, (2) instrumentation to acquire data, and (3) software to analyze data. However, a successful spheroid model requires not only the utilization these tools, but rather demands a thorough understanding of both the physical and biological limitations associated with utilizing these tools with 3D spheroids. Overall, this dissertation aimed to advance the use of spheroids for quantitative, live-cell fluorescent imaging through examining, understanding, and accounting for the increased complexities of working with 3D spheroids.

5.2 SUMMARY of MAJOR FINDINGS

This dissertation laid the framework for developing high-throughput, fluorescent-based, quantitative, live-cell assays utilizing 3D spheroids. We evaluated two different forms of microscopy, epifluorescence and confocal, with respect to various fluorescent dyes. We evaluated how different fluorescent labeling methods would induce differences in fluorescent staining patterns in 3D, and subsequently require different quantitative analysis strategies. Our general experimental design involved the following steps: (1) pre-labeling 2D cell monolayers with fluorescent dyes, (2) tryspinizing and harvesting cells, (3) seeding into agarose hydrogels to form spheroids, (4) diffusion-labeling fluorescent dyes into 3D spheroids, and (5) acquire fluorescent images. Furthermore, we utilized a range of spheroid sizes to assess both (1) the induced differences in fluorescent signal, and (2) the respective limitations of our quantitative analysis strategies. Finally, by understanding these quantitative limitations, we developed a spheroid model to assess changes in fluorescent signal as a function of 3D radius.

5.2.1 Aim 1. Develop accurate quantitative methods to analyze wide-field fluorescent images of 3D spheroids.

First, we assessed how to best extract accurate quantitative data from wide-field epifluorescence images of 3D spheroids. To evaluate the role that dye incorporation has on fluorescent staining patterns and subsequent quantitative analysis, we labeled spheroids two different ways: (1 – pre-labeled) individual cells were labeled with fluorescent dyes as 2D monolayers prior to spheroid formation, thus creating uniform signal throughout, (2 – diffusion-labeled) fluorescent dyes were added after spheroids were formed, thus creating a gradient of signal throughout. Furthermore, to eliminate potential differences due to a dye's chemical properties, the same fluorescent dyes were utilized for both labeling methods. To evaluate the effect of size, spheroids of variable diameter (80-200-μm) were formed. Time-lapse epifluorescence images were acquired, and analyzed to measure total fluorescence and spheroid radii.

As spheroid radius increases, the overall fluorescent signal also increases, but that increase does not imply biological changes, but rather a need for fluorescent normalization. To determine how to best normalize fluorescence data, changes in spheroid surface area and volume as radii increased were modeled and compared to the corresponding fluorescent signal changes. For pre-labeled spheroids, fluorescent increase was best predicted by the increase in volume, whereas for diffusion-labeled spheroids, fluorescence was best predicted by the increase in surface area. Furthermore, utilizing the appropriate normalization strategy can significantly reduce errors and enhance the sensitivity and robustness of spheroid-based assays. Reduced variability and improved sensitivity increases compatibility with high-throughput screening, since fewer spheroids would be needed to discern the statistical differences between experimental groups.

5.2.2 Aim 2. Develop quantitative analysis strategies to analyze confocal z-stacks of living 3D spheroids in a high-throughput format.

Understanding how to accurately quantify wide-field epifluorescent images is useful for evaluating overall changes to spheroids, however, it fails to assess complex biological changes occurring throughout the 3D radius. Therefore, our second aim evaluated how to best assess quantitative data from 3D confocal z-stacks of spheroids. Since confocal microscopy of thick tissues is associated with light scatter induced fluorescent loss, extricating the gradient of signal induced by diffusion labeling from the gradient of signal induced by light scatter would be difficult. Therefore, to understand how light scatter effects fluorescent signal throughout 3D spheroids, spheroids were uniformly, pre-labeled with four different CellTracker^{TM} (CT) fluorescent dyes, or variable excitation/emission spectra. To evaluate the effect of size, spheroids of variable diameter (40-200-µm) were formed. Confocal z-stacks were acquired, and analyzed to measure the spheroid radius, and total and positional fluorescent signals throughout the z-depth.

Additionally, this experimental study was performed with a high-throughput confocal imaging system, thus requiring the adaptation of the 3D PetriDish technology for use with 96-well plate. Therefore, we developed a 3D printed micromold to mold agarose hydrogels, and subsequently form spheroids directly within a 96-well plate. Spheroid formation within the 96-well plate was validated with respect to spheroid size and positional (*x,y,z*) location. Spheroids formed within a designated (*x,y*) grid system of microscope, as well as within a 200-µm range of *z*-position. Furthermore, spheroid radius was controlled by altering input cell number. For each seeding density tested, standard deviation was approximately 10% of the mean radius.

Furthermore, with respect to fluorescence quantification, spheroids larger than 50-µm in diameter experienced some degree of fluorescent loss further into *z*-depth. To determine the total amount of fluorescent loss throughout the spheroid, the hypothetical fluorescence, assuming no loss of signal, for each confocal slice was calculated and compared to the measured values, throughout the *z*-depth of each spheroid. The total amount of fluorescent loss increased as a function of spheroid radii, with larger spheroids possessing a greater amount of loss. Furthermore, unlike a planar specimen that will undergo uniform loss across each confocal slice, the curvature of spheroid yields an uneven loss of signal across each slice with increased signal retention along the outer perimeter. Furthermore, we found that the rate of fluorescence loss throughout the *z*-depth will be different depending on spheroid size, with smaller spheroids possessing a higher rate of loss. This non-uniformity in signal loss both (1) across individual confocal slices and (2) throughout the *z*-depth increases the difficulty to compensate for fluorescent signal loss throughout. Ratio imaging can be used to normalize both (1) the differences in fluorescent distribution due to size and (2) the non-uniform fluorescent loss throughout the spheroid. Furthermore, utilizing ratio imaging reduces the variation in fluorescent signal throughout the z-depth.

5.2.3 Aim 3. Develop a high-throughput quantitative assay to assess gap junction inhibition in 3D spheroids.

Throughout the previous aim, we have determined the limitations of acquiring quantitative data from confocal *z*-stacks of spheroids. With this broader understanding of how light scatter affects the fluorescence of uniformly labeled dyes, more complex assays designed to evaluate biological changes as a function of 3D radius can be developed. When designing biologically driven assays, we set the following constraints based off our previous research:

(1) an uniformly, pre-labeled control fluorescent dye should be included in order to perform ratio imaging as a means to normalize light scatter effects

(2) images further than 50-µm into the *z*-depth are not appropriate for quantitative analysis, thus can image either entire spheroids, for radii ~25-µm, or the southern hemisphere of spheroids, for radii ~50um

Given the biological need for increased number of cell layers, only analyzing the southern hemisphere of a 50-µm radius spheroid would be more physiologically relevant than analyzing the entirety of a 25-µm radius spheroid.

To demonstrate the ability to measure biological changes along the 3D radius through fluorescent quantification, we developed a model to study gap junction intercellular communication (GJIC) within 3D spheroids. Gap junctions (GJs) are transmembrane proteins that form channels between cells allowing for the passage of small molecules and ions [28]. GJIC was assessed by monitoring the penetration of calcein fluorescent dyes towards the center of spheroid. To quantify the penetration inwards, the spheroid was divided into a series of 5-µm concentric shells. Furthermore, ratio imaging was performed by normalizing the calcein fluorescence by a uniformly, pre-labeled CT fluorescence, prior to any other quantification steps. To develop a model of GJIC within spheroids, we optimized a variety of parameters, including: spheroid size, fluorescent dye choice and labeling time, and method of fluorescent quantification. To evaluate the performance of each optimization the difference between spheroids treated with or without the gap junction inhibitor, carbenoxolone (CBX), was assessed. In order to maximize separation between spheroids treated with or without CBX, spheroids should be labeled with calcein-red-orange-AM (calceinRO), as opposed to calcein-AM (calceinAM), for at least 70-minutes prior to acquiring confocal z-stacks. Furthermore, in addition to microscopy-related size constraints, additional size constraints must be accounted for when developing biological based assays. For example, when spheroid size was too small (>30-µm radius), quantifiable differences between spheroids treated with or without CBX was minimal, implying that every cell within the spheroid may have access to the reservoir of calcein thus minimizing the effect of CBX. To accurately quantify GJIC within spheroids, we should aim to form spheroids approximately 40-µm radius.

Furthermore, to assess how best to quantify GJIC within spheroids, the same dataset containing spheroids treated with and without CBX was analyzed multiple different ways. Two different portions of spheroid (equatorial confocal image versus southern hemisphere) were analyzed in three different ways: (1) comparing the ratio of core to outer shell, (2) comparing the ratio of middle to outer shells, (3) comparing the distribution across all shells by plotting fluorescence as function of radial location and measuring the area under the curve. Calculating the ratio of the middle to outer shells in the southern hemisphere yielded (1) a good separation of means between spheroids treated with and without CBX and (2) proved to be least sensitive to minor deviations in spheroid radius, as evidenced by low standard deviations. Biologically, this outcome is logical because (1) calcein must travel a set distance to reach the middle shell as opposed to variable distances to reach the core, (2) the middle shell is less susceptible to fluorescent loss than the core, especially with respect to analysis of the southern hemisphere.

5.3 LIMITATIONS and POTENTIAL SOLUTIONS

This dissertation provides guidance for the development of high-throughput, quantitative assays of 3D spheroids for both wide-field epifluorescence and confocal microscopy. Specifically, we evaluated the effect of both spheroid size and method of dye labeling on the resulting distribution, acquisition, and quantification of fluorescent signal. Although this simplified experimental approach provided general framework for quantitation of fluorescence from 3D spheroids, moving towards developing more biologically relevant assays requires further optimization and validation, as evidenced by the development of GJIC assay in chapter 4. Although we have made significant advancements towards developing quantitative, live-cell, fluorescent assays in 3D spheroids, more optimizations and modifications could be performed to increase the relevance and applicability of the model.

First of all, the entirety of the experimental study (fluorescent labeling, spheroid self-assembly, image acquisition) was completed within 30-hours. Given the short experimental time-frame, the cellular retention of fluorescent dyes was high, thus yielding bright fluorescent signals. However, some *in vitro* models, especially those composed of primary or stem-cell derived cells, may require a week or more of maturation prior to assessing biological functions [12, 29-31]. In that time-frame, the retention of fluorescent dyes would diminish, preventing the acquisition of accurate fluorescent signals. Some commercially available fluorescent dyes, such as Qtracker dyes, are designed for longer retention times, up to 5-14 days in culture [32]. However, performing ratio imaging using a pre-labeled control dye from week(s) prior may not be the most effective solution. We have previously shown that for wide-field epifluorescent images of spheroids, the signal of a diffusion-labeled dye can be accurately normalized by spheroid surface area. However, given the complexity of quantifying fluorescence in confocal *z*-stacks of spheroids, that simplified approach would not account for all the parameters that need to be normalized. Therefore, alternative approaches need to be assessed and developed. For example, utilizing cell lines that have been genetically engineered to express certain fluorescent dyes, such as GFP or RFP, should yield a uniformly labeled fluorescent signal that would not dampen with increased culture time [33-35]. However, the process of engineering stable fluorescent cell-lines is time-consuming, and not necessarily compatible with all cell types [35]. Alternatively, the experimental design can be altered to add two different fluorescent dyes (dye of interest, and control dye) once the spheroid has matured. The control dye should be able to passively diffuse throughout the entire spheroid, and not be dependent upon any transport mechanism to either enter the spheroid or penetrate deeper. Additionally, the control dye should be able to maintain a stable fluorescent expression over the remainder of the experiment. Labeling all spheroids with the control dye first for a set period of time, in theory, will result in a similar signaling pattern throughout all similarly-sized spheroids. Therefore, the dye of interest, with its variable expression throughout, can be normalized by the control dye. To ensure that normalizing performed by a diffusion-labeled dye is an effective alternative strategy to pre-labeling, a comparative analysis of these techniques could be performed after a day in culture with multiple control dyes.

Additionally, our studies predominantly utilized fluorescent cytoplasmic dyes, which in theory should be evenly stained throughout the cell. However, we did not fully investigate the compatibility of our quantitative strategies with dyes that target a particular organelle, such as the cell membrane, nucleus, mitochondria, endoplasmic reticulum, or others. These particular dyes will express a different, more punctate, regional staining pattern within each cell, as opposed to the more uniformly labeled cytoplasmic dyes. We hypothesize that the same set of principles should apply, however, validating that these specialized intercellular markers would also be subject to the same set of quantitative principles would be necessary prior to development of novel biological assays.

Furthermore, we optimized our assay development to perform live-cell imaging to measure dynamic changes occurring within spheroids over time. Although measuring dynamic changes can provide interesting insights over time, accommodating those dynamic changes into development of quantitative assays can be complex. For example, repeated imaging over time can lead to both phototoxicity of cells or photobleaching of fluorescent signal, especially with respect confocal z-stacks [36,37]. In this dissertation, we only performed a time-lapse of spheroids during our first aim, where a single epifluorescent image was acquired per time-point, for a total of 11 time-points. After acquiring these 11 images, there was no evidence of phototoxicity or photobleaching, however, with such a small number of images that is not surprising. Furthermore, for the second and third aims, when confocal z-stacks of spheroids were acquired, we only evaluated a single time-point per spheroid, consisting of 75 z-slices. However, we did not examine how repeated imaging over time would affect cell viability or fluorescent signal retention. When designing quantitative fluorescent based assays in 3D spheroids, it is important to understand how frequently and how many images can be safely acquired prior to either a loss of fluorescent signal or viability, both of which could contribute to misleading results. There are two approaches that can be utilized to avoid phototoxicity/photobleaching while still obtaining dynamic results: (1) determine the limits for experimental system (cell type, fluorescent dye choice) and subsequently reduce the number of z-images or time-points to avoid those limits, or (2) utilize the 96-

well plate format, compare spheroids across the plate as different time-points. Determining which approach to use will be dependent upon the dynamic range of the experimental assay. For example, since it takes approximately ~100-minutes to image the entire 96-well plate (4 spheroids per well, 2 fluorescent channels, 75 z-slices), shorter time-points can be evaluated by comparing spheroids across the plate, however, longer dynamic ranges would need to be evaluated with time-lapse experiments.

Finally, live cell imaging has the potential to answer a multitude of questions, regarding dynamic changes over time, however, live cell imaging also will possess the most stringent constraints with respect to spheroid size. If a single time-point is sufficient to answer a biological question, then end-point assays can be utilized instead. With end-point assays, spheroids can be fixed and imaged at a later date, assuming the model is compatibility with fixation. Furthermore, with endpoint assays, tissue clearing techniques can be incorporated into the experimental design, thus improving visualization into the *z*-depth, and subsequently enabling the formation of larger spheroids (up to 100-μm radius). Ultimately when first designing novel quantitative assays using 3D spheroids, performing live-cell microscopy may be necessary to understand the dynamic changes occurring within the experimental system over time. However, once these dynamic changes are characterized and understood, the assay could be adapted to an endpoint assay to capitalize on the benefits of tissue clearing.

In addition to these general limitations applicable to all aims of this dissertation, there were also specific limitations and potential improvements to each aim, which are detailed in the following sections.

5.3.1 Aim 1. Develop accurate quantitative methods to analyze wide-field fluorescent images of 3D spheroids.

Our first aim determined how best to quantify the total fluorescent signal from wide-field epi-fluorescent images of 3D spheroids. We only validated our quantitative strategies with respect to low magnification (5X) images. We hypothesize that regardless of the objective used, the overall quantitative strategies should apply. However, do higher magnification objectives possess the same size-based constraints with respect to capture of emitted fluorescent light? For example, with wide-field, epifluorescence, low magnification (5X) images, emitted fluorescent light can be reliably captured for spheroids up to a height of 205-µm [18]. However, are there different size-based constraints when utilizing higher magnification objectives (10X, 20X)? We could test these potential constraints by forming spheroids of variable radii, pre-labeled with various fluorescent dyes, within our specialized side-view micromold. The side-view micromold allows for traditional (*x,y*) visualization, but also enables acquisition of brightfield (*x,z*) images [18]. By comparing the relationship between spheroid (*z*) height and peak fluorescence intensity, we could asses which height correlated to a loss of fluorescent capture for each objective [18]. Furthermore, this aim only evaluated the overall fluorescent signal from a single image, thus failing to capitalize on the richness of biological content throughout spheroids. There are methods to acquire *z*-stacks of epifluorescence spheroids, yet our quantitative approaches only evaluated the central plane. Utilizing wide-field epifluorescence microscopy to acquire *z*-stacks yields blurry images due to capture of out-of-focus light. There are methods to remove out-of-focus light by deconvolution [26-27,38]. However, rather than fully delve into the complexities of epifluorescence microscopy, we altered our approach to evaluate confocal z-stacks of spheroids.

5.3.2 Aim 2. Develop quantitative analysis strategies to analyze confocal z-stacks of living 3D spheroids in a high-throughput format.

Our second aim advanced the use of spheroids for live-cell, quantitative, confocal microscopy in a high-throughput format by: (1) developing a 3D printed micromold to form spheroids directly within 96-well plate, and (2) assessing the quantitative limitations of confocal z-stacks of spheroids. With the 3D printed micromold, we could form four spheroids per well in every well of 96-well plate. The placement of spheroids fell with the designated (*x,y*) grid system associated with microscope, as well as relatively precise *z*-range (~575-775-µm). However, even though spheroid centers fall within a ~200-µm range, the actual *z*-range that must be imaged will have to encompass the entirety of spheroid, not just the center, thus needs to account for spheroid radius. Assuming an average spheroid radius of 50-µm, at least 300-µm *z*-range must be imaged to capture entirety of spheroid. Therefore, only 33% of acquired images will contain intersect spheroids. By reducing variability in the *z*-position of spheroids, we can reduce acquisition time and amount of non-spheroid data. Reducing the acquisition time, enhances the ability to perform faster time-lapse imaging, whereas reducing the amount of non-spheroid data decreases file size lessening the burden of file storage and data analysis. Since the publication of Aim 2, the micromold construction has switched from 3D printed polymeric material to a milled metal (either aluminum or stainless steel). In theory, the metal micromolds should be more resilient and less susceptible micro-post breakage than the 3D printed polymeric prototypes, and thus lead to a reduction in variability about the *z*-position of spheroids. To ascertain if milled metal micromolds outperformed 3D printed micromolds, a study directly comparing the efficacy of 3D printed versus milled metal micromolds could be completed.

Additionally, our paper showcased the use of ratio imaging to compensate for fluorescent loss associated with confocal imaging of 3D spheroids. Overall, with ratio imaging, fluorescent signal loss was compensated for throughout the *z*-depth, however, there were still variability in normalized signal from slice to slice. To perform ratio imaging, a small circular region (radius = 1 pixel = 0.645-µm), encompassing 9 datapoints, was evaluated at the same (*x,y*) position throughout the *z*-depth. In theory, pre-labeling cells as a 2D monolayer ensures all cells are exposed to the same amounts of dye, however, in practice, every cell within a spheroid will not possess the same fluorescent signal. Therefore, analyzing too small portion of spheroid could lead to high variation from one image to the next. By increasing the sampling area, minor cell-cell differences in fluorescent signal can be accounted for. For the final aim of this dissertation, we altered our ratio imaging approach to normalize the fluorescent signal of one dye by another for either 5-µm wide concentric rings (*x,y*) or 5-µm wide concentric hemishells (*x,y,z*).

Overall, we provided general guidelines on how to assess quantitative limitations of confocal microscopy of spheroids. However, every cell type will have different scattering properties, and furthermore, different fluorescent dyes may have specific properties. Therefore, when developing new biologically driven assays in 3D spheroids, it is critical to first understand its respective quantitative limitations. Our techniques to assess quantitative limitations of confocal z-stacks are widely applicable to a broad range of applications, however, our specific results are only applicable to KGN cells labeled with these particular fluorescent dyes.

5.3.3 Aim 3. Develop a high-throughput quantitative assay to assess gap junction inhibition in 3D spheroids.

Our third aim capitalized on the work completed by the previous two aims by developing a quantitative, live-cell, confocal assay to measure gap junction intercellular communication (GJIC) in 3D spheroids. Despite our demonstrated ability to quantify drug-induced inhibition of GJ, there is still room to improve upon this model. First and foremost, we determined that the optimal method for assessing GJIC within spheroids is evaluating the ratio of middle to outer shells in the set of southern hemispheric images. However, analyzing the southern hemisphere of spheroid is time-consuming approach, requiring approximately 15-minutes to analyze a single spheroid which translates to 96-hours for an entire 96-well plate. In comparison, experimental set-up and image acquisition combined takes less than 5-hours. The lack of an efficient data analysis pipeline will prevent the translation of this GJIC assay into a high-throughput screening tool. Currently, 3D image analysis software programs cannot perform an in-depth analysis of 3D confocal z-stacks as a batch-able process. To overcome this limitation, we are currently collaborating with experts, from the Center for Computation and Visualization at Brown University, to develop image analysis pipelines that will require minimal user input and be run on computing clusters to enhance processing time.

Furthermore, to develop a quantitative GJIC assay in 3D spheroids, we have optimized a series of parameters to maximize separation between spheroids treated with positive (CBX) and negative control (no drug) treatments. We focused on obtaining maximal separation with respect to positive and negative controls, however we did not assess assay sensitivity yet. We can estimate the sensitivity of our assay through performing modified a power analysis, where a sample size (n) of 4, yields a degree of freedom (DOF) of 3, and to achieve a two-tailed significance level ($\propto$) of 0.05, the critical *t*-value is 3.182. Based on our current results from analyzing the ratio of middle to outer shells in the southern hemispheric images, we can estimate the standard deviation (StDev) to be approximately 0.02, and the mean for the negative control ($\bar{X}_{neg}$) is 0.459. Therefore, according to the following equation, we can calculate the minimum value ($\bar{X}$) necessary to measure statistically significant differences over the control sample:

$$t = \frac{\bar{X}_{neg} - \bar{X}}{StDev/\sqrt{n}} \quad \rightarrow \quad \bar{X} = \bar{X}_{neg} - t\left(\frac{StDev}{\sqrt{n}}\right)$$

According to this analysis, a reduction in GJIC as low as 7% to a value of 0.427 should, in theory, yield statistically significant results over the non-drug treated control spheroids. In comparison, our positive control (CBX-treated) reduces GJIC by 45% to a value of 0.252. These theoretical calculations provide insight regarding the approximate level of difference necessary to achieve statistical differences between the negative control and experimental samples. However, this sort of analysis cannot reveal the concentration of CBX that would induce that level of GJIC. To determine the concentration of CBX needed to significantly reduce GJIC, a concentration response of CBX can be performed.

Additionally, when evaluating the ratio of middle to outer shells in the southern hemisphere, our positive control (CBX) treatment only reduces GJIC by 45%. Adding drugs/compounds to inhibit GJIC within 3D spheroids may not result in a complete blockage of communication. To determine if this reduction in GJIC could be enhanced, the following modifications to the experimental design can be assessed: (1) test higher concentrations of CBX (>100-μM), (2) treat spheroids for longer periods of time with CBX (>5-hours) prior to adding calceinRO, (3) incubate with calceinRO for longer periods of time prior to imaging (>80-minutes), or (4) test other commonly used gap junction inhibitors, such as mefloquine, heptanol, and/or and oleamide [39-42]. Alternatively, spheroids do not form perfect onion-like layers composed of a single layer of cells, but rather may contain cellular projections that pass through multiple layers. Therefore, to determine whether the incomplete blockage of GJIC is due to spheroid architecture or drug treatment, comparing the effect of drug treatment (+/- CBX) on cell lines that either express or lack GJs. Ideally, the two cell lines (+/- GJs) would be derived from the same cell line to eliminate any background in system due to different cell sources. For example, cell lines, such as SKOV-3, that normally express low levels of GJIC can be stably transfected to express connexin proteins [43]. In theory, CBX treatment should have no effect on GJ- spheroids. Treating GJ+ spheroids with CBX will decrease GJIC compared to control spheroids. Furthermore, if the level of GJIC in CBX-treated GJ+ spheroids is similar to the level of communication in GJ- spheroids, then the architecture of spheroid enables some calcein penetration. Alternatively, if the level of GJIC in CBX-treated GJ+ spheroid is greater than the level of communication in GJ-spheroids, that implies CBX induced a partial inhibition of GJIC within spheroids.

5.4 FUTURE DIRECTIONS

The primary goal of this dissertation was to develop quantitative, live-cell assays using 3D spheroids that measure dynamic changes in response to stimuli. We specifically advanced the use of spheroids for high-throughput, quantitative, fluorescent microscopy, both epifluorescence and confocal. Based on the current advancements, the future of this project can advance in a multitude of directions, ranging from enhancement of throughput, to GJIC assay improvement, to developing novel assays with different cell types and fluorescent dyes.

Despite increasing the throughput of the 3D PetriDish technology from use in 12- and 24-well plates to compatibility with 96-well plates, there is still much room for improvement. Firstly, all experimental steps, from agarose hydrogel formation to data analysis, require user input and attention. However, each step can be adjusted and optimized to minimize user input and maximize throughput. For example, the various pipetting steps, which include agarose hydrogel formation and equilibration, cell seeding, media exchanges for both drug treatment and dye addition, can be automated with robotic liquid handling systems. Previous pilot studies performed in our lab, has already demonstrated the feasibility of seeding cells into agarose hydrogels. To automate all of these steps, we may want to make extra accommodations, such as the addition of temperature controlled areas to prevent agarose from solidifying prior to hydrogel formation. Temperature and carbon dioxide control may also be useful to maintain cell viability during seeding and media exchange steps. In addition to experimental automation, there must also be a similar level of automation applied to the data analysis. As mentioned previously, current data analysis protocols require approximately 96-hours to analyze an entire 96-well plate, meanwhile experimental set-up and data acquisition is less than 5-hours. To increase throughput of data analysis, need to create a data analysis pipeline that will be batch-able and require very little user input. Also, given the total size (100+ GB) of images, standard computers will not be able to handle these file, thus a switch to utilizing computer clusters to increase processing power will be necessary. Once the experimental and analysis throughput has been maximized, we can also begin to increase the throughput of the technology by adapting the micromold for use with a 384-well plate.

In addition to technological advancements, we can also advance the robustness, relevance, and reliability of the GJIC assay. Through the development of this model, we only assessed a single cell line, ovarian granulosa cells (KGN), that are known to express connexin-43. However, we can easily adapt this model to other cell types that have been shown to express GJIC *in vitro*/*in vivo*, such as cell lines (NHF, AC16 ventricular cell line, HUVEC), or primary cells (lung fibroblasts, hepatocytes), or iPSC/ESC derived cells (iPSC-neural networks, iPSC-cardiomyocytes, hESC-hepatocytes) [44-50]. Furthermore, all these different cell sources will express differing amounts and types of connexin proteins. For example, hepatic cells express connexin-32 and -26, while cardiomyocytes express connexin-43, -40, -45, -46, and neurons and astrocytes express connexin-32 [44,51,52]. By utilizing multiple different cell types, from multiple different sources throughout the body, with varying levels and types of connexin proteins, we can assess the robustness of our model at assessing. Also, the validity of our model could be assessed by testing other well-known gap junction inhibitors, such as mefloquine, heptanol, oleamide [39-42]. Additionally, the sensitivity of this model could be assessed by performing concentration responses with all those well-characterized gap junction inhibitors. Upon understanding how well-known gap junction inhibitors behave in our GJIC model, we can begin to assess how other drugs and chemicals of commerce that are linked to GJIC fare, such as BPA, 1-methylantracene, PCB-153 [53-55]. And eventually we can then begin to screen toxicants, chemicals, and compounds with unknown effects.

After assessing the limitations of acquiring quantitative fluorescence images of 3D spheroids, we ultimately chose to develop a model to study GJIC within those spheroids. However, if we were to remove the biological context from our GJIC assay, we essentially developed a method to accurately quantify fluorescent changes along the 3D radius of spheroids. Therefore, we essentially created a tool to answer any biological question so long as the following constraints are met: (1) the cell type(s) of interest will form a spheroid, (2) there exists a fluorescent probe to measure biology, and (3) the desired biological phenomenon will occur within a medium-sized spheroid (radius < 50-

μm) to avoid limitations associated with confocal microscopy. For example, the uptake and distribution of fluorescently labeled microbeads or nanoparticles into spheroids can be used as a model for drug delivery [56]. Alternatively, cellular cytoxicity upon exposure to drug/compounds can be monitored as a function of 3D radius in either physiological or pathophysiological derived spheroids [57]. However, studying the development of necrotic cores in cancerous spheroids would most likely be impossible with live-cell confocal imaging. This case study would satisfy the first two constraints, as numerous cancerous cell lines have been shown to form spheroids, and there exists a wide array of commercially available fluorescent dyes to probe necrosis, apoptosis, and viability. However, the formation of the necrotic core would occur in large spheroids (diameter ~ 500-μm), which is greater than the limit from which accurate quantitative analysis of confocal *z*-stacks can be completed [58]. However, within these larger cancerous tissues, the cellular proliferation within the outer zone could be evaluated.

5.5 CONCLUDING REMARKS

Through this dissertation, we have advanced the use of 3D spheroids for high-throughput analyses by developing micromold technology that is compatible with the 96-well plate format, and developing quantitative strategies to reliably measure fluorescent signal from spheroids. Spheroids provide a more physiologically relevant platform for modeling healthy and diseased tissues, as well as testing drug/compound efficacy and toxicity. However, the 3D nature of spheroids increases the complexity of assay development, at every step throughout the experimental design and analysis. These complexities can be overcome by first designing experiments to understand the biological and physical limitations of the model prior to developing biologically-based assays. Furthermore, one of the most critical components for assay development is choosing the appropriate spheroid size. If a spheroid is too large, issues regarding both cellular viability and image acquisition can arise. Alternatively, if a spheroid is too small, it will lack one if its key advantages: biological changes as function of 3D radius.

Understanding of how to utilize spheroids properly can yield the measurement of a wide range of biological functions throughout the 3D radius. Combining this understanding with the high-throughput adaption of both fluorescent imaging systems and spheroid formation techniques, positions spheroids at the forefront of the next generation of drug screening and toxicity testing. For example, the development of more physiologically relevant spheroid *in vitro* models, could potentially evaluate and predict a novel compound's efficacy, toxicity, off-target effects prior to performing animal studies and human clinical trials. More predictive *in vitro* models would reduce the total expenditure, time, and amount of unsuccessful trials necessary to successfully develop a new drug. Alternatively, combining the use of spheroids with induced pluripotent stem cell (iPSC) technology, could create both normal and genetically-linked disease models, to study both the progression and treatment of disease [59]. Furthermore, a single source of iPSCs can be induced down multiple different lineages, thus creating a series microtissues of different organs all from the same donor. Therefore, from a single patient, microtissues of organs both affected and un-affected by the disease could be generated, and studied to evaluate disease progression and treatment options for a personalized medicine approach. This personalized medicine approach is also applicable for cancer patients, as a biopsy can be used to generate a series of tumor microtissues, where the efficacy of various cancer chemotherapeutics can be tested. Furthermore, if iPSCs are also generated from the same patient, the off-target toxicity of these various chemotherapeutics can be simultaneously assessed. Numerous drugs and compounds either fail clinical trials or are later removed from the market due to safety concerns for a small population of people. However, with a personalized medicine approach, the efficacy and toxicity would not have to be compromised, but rather could determine the best treatment regimen for a particular patient.

Overall, spheroids possess the potential to model any number of biological phenomenon that occur in an *in vivo* environment. To successfully utilize spheroids as an *in vitro* model, simply need to understanding what cell source, fluorescent probe, microscope, and quantitative limitations and assessments are necessary to provide answers.

5.6 REFERENCES

1. Pampaloni F, Reynaud EG, Stelzer EH. The third dimension bridges the gap between cell culture and live tissue. *Nature Reviews. Molecular Cell Biology*. 8(10):839-845, 2007.

2. Lancaster MA, Knoblich JA. Organogenesis in a dish: modeling development and disease using organoid technologies. *Science*. 345(6194):1247125, 2014.

3. Yamada KM, Cukierman E. Modeling tissue morphogenesis and cancer in 3D. *Cell.* 130(4):601-610, 2007.

4. Ong SM, Zhao Z, Arooz T, Zhao D, Zhang S, Du T, Wasser M, van Noort D, Yu H. Engineering a scaffold-free 3-D tumor model for in vitro drug penetration studies. *Biomaterials*. 31(6):1180-1190, 2010.

5. Wilson HV. A new method by which sponges may be artificially reared. *Science*. 25:912-915, 1907.

6. Fennema E, Rivron N, Rouwkema J, van Blitterswijk C, de Boer J. Spheroid culture as a tool for creating 3D complex tissues. *Trends in Biotechnology*. 31(2):108-115, 2013.

7. Maltman DJ, Przyborski SA. Developments in three-dimensional cell culture technology aimed at improving accuracy of in vitro analyses. *Biochemical Society Transactions*. 38(4):1072-1075, 2010.

8. Wang W, Itaka K, Ohba S, Nishiyama N, Chung UI, Yamasaki Y, Kataoka K. 3D spheroid culture system on micropattterned substrates for improved differentiation

efficiency of multipotent mesenchymal stem cells. *Biomaterials*. 30(14):2705-2715, 2009.

9. Sun T, Jackson S, Haycock JW, MacNeil S. Culture of skin cells in 3D rather than 2D improves their ability to survive exposure to cytotoxic agents. *Journal of Biotechnology*. 122(3):372-381, 2006.

10. Pickl M, Ries CH. Comparison of 3D and 2D tumor models reveals enhanced HER2 activation in 3D associated with an increased response to trastuzumab. *Oncogene*. 28(3):461-468, 2009.

11. Chang TT, Hughes-Fulford M. Monolayer and spheroid culture of human liver hepatocellular carcinoma cell line cells demonstrate distinct global gene expression patterns and functional phenotypes. *Tissue Engineering Part A.* 15(3):559-567, 2009.

12. Vantangoli MM, Madnick SJ, Huse SM, Weston P, Boekelheide K. MCF-7 Human Breast Cancer Cells Form Differentiated Microtissues in Scaffold-Free Hydrogels. *PLoS One*. 10(8):e0135426, 2015.

13. Griffith LG, Swartz MA. Capturing complex 3D tissue physiology in vitro. *Nature Reviews Molecular Cell Biology*. 7(3):211-224, 2006.

14. Atala A, Kasper FK, Mikos AG. Engineering complex tissues. *Science Translational Medicine.* 4(160):160rv12, 2012.

15. Mehta G, Hsiao AY, Ingram M, Luker GD, Takayama S. Oppurtunities and challenges for use of tumor spheroids as models to test drug delivery and efficacy. *Journal of Controlled Release*. 164(2):192-204, 2012.

16. Casciari JJ, Sotirchos SV, Sutherland RM. Glucose diffusivity in multicellular tumor spheroids. *Cancer research*. 48(14):3905-3909, 1988.

17. Vinci M, Gowan S, Boxall F, Patterson L, Zimmermann M, Court W, Lomas C, Mendiola M, Hardisson D, Eccles SA. Advances in establishment and analysis of three-dimensional tumor spheroid-based functional assays for target validation and drug evaluation. *BMC Biology.* 10(29):10.1186/1741-7007-10-29, 2012.

18. Achilli TM, McCalla S, Meyer J, Tripathi A, Morgan JR. Multilayer spheroids to quantify drug uptake and diffusion in 3D. *Molecular pharmacolgy.* 11(7):2071-2081, 2014.

19. Boutin ME, Hoffman-Kim D. Application and assessment of optical clearing methods for imaging of tissue-engineered neural stem cell spheres. *Tissue Engineering Part C Methods.* 21(3):292-302, 2015.

20. Kabadi PK, Vantangoli MM, Rodd AL, Leary E, Madnick SJ, Morgan JF, Kane A, Boekelheide K. Into the depths: Techniques for in vitro three-dimensional microtissue visualization. *Biotechniques*. 59: 279-286, 2015.

21. Dmitriev RI, Zhdanov AV, Nolan YM, Papkovsky DB. Imaging of neurosphere oxygenation with phosphorescent probes. *Biomaterials*. 34(37):9307-9317, 2013.

22. Schmitz A, Fischer SC, Mattheyer C, Pampaloni F, Stelzer EH. Multiscale image analysis reveals structural heterogeneity of the cell microenvironment in homotypic spheroids. *Scientific Reports*. 7:43693, 2017.

23. Tung YC, Hsiao AY, Allen SG, Torisawa YS, Ho M, Takayama S. High-throughput 3D spheroid culture and drug testing using a 384 hanging drop array. *The Analyst.* 136(3):473-478, 2011.

24. Widder M, Lemke K, Kekec B, Forster T, Grodrian A, Gastrock G. A modified 384-well device for versatile use in 3D cancer cell (co-)cultivation and screening for investigations of tumor biology in vitro. *Engineering in Life Sciences*. 18(2):132-139, 2018.

25. Mosaad EO, Chanmbers KF, Futrega K, Clements JA, Doran MR. The Microwell-mesh: A high-throughput 3D prostrate caner spheroid and drug-testing platform. *Scientific Reports*. 8(1):253, 2018.

26. Li L, Zhou Q, Voss TC, Quick KL, LaBarbera DV. High-throughput imaging: Focusing in on drug discovery in 3D. *Methods*. 96:97-102, 2016.

27. Martines NJ, Titus SA, Wagner AK, Simeonov A. High throughput fluorescence imaging approaches for drug discovery using in vitro and in vivo three-dimensional models. *Expert Opinion Drug Discovery*. 10(12):1347-1361, 2015.

28. Abbaci M, Barberi-Heyob M, Blondel W, Guillemin F, Didelon J. Advantages and limitations of commonly used methods to assay the molecular permeability of gap junctional intercellular communication. *Biotechniques*. 45(1):63-68, 2008.

29. Dingle YT, Boutin ME, Chirila AM, Livi LL, Labriola NR, Jakubek LM, Morgan JR, Darling EM, Kauer JA, Hoffman-Kim D. Three-dimensional neural spheroid culture: an in vitro model for cortical studies. *Tissue Engineering Part C Methods*. 21(12):1274-1283, 2015.

30. Chandrasekaran A, Avci HX, Ochalek A, Rosingh LN, Molnar K, Laszlo L, Bellak T, Teglasi A, Pesti K, Mike A, Phanthong P, Biro O, Hall V, Kitiyanant N, Krause KH, Kobolak J, Dinnyes A. Comparison of 2D and 3D neural induction methods for the generation of neural progenitor cells from human induced pluripotent stem cells. *Stem Cell Research*. 25:139-151, 2017.

31. Vorrink S, Zhou Y, Ingelman-Sundberg M, Lauschke VM. Prediction of drug-induced hepatotoxicity using long-term stable primary hepatic 3D spheroid cultures in chemically defined medium, *Toxicological Science*. 2018.

32. Lin S, Xie X, Patel MR, Yang YH, Li Z, Cao F, Gheysens O, Zhang Y, Gambhir SS, Rao JH, Wu JC. Quantum dot imaging for embryonic stem cells. *BMC Biotechnology*. 7:67, 2007.

33. Amsterdam A, Lin S, Hopkins N. The Aequorea victoria green fluorescent protein can be used as a reporter in live zebrafish embryos. *Developmental Biology*. 171(1):123-129, 1995.

34. Yamamoto N, Jiang P, Yang M, Xu M, Yamauchi K, Tsuchiya H, Tomita K, Wahl GM, Moossa AR, Hoffman RM. Cellular dynamics visualized in live cells in vitro and in vio by differential dual-color nuclear-cytoplasmic fluorescent-protein expression. *Cancer Research*. 64(12):4251-4256, 2004.

35. Zhang J, Campbell RE, Ting AY, Tsien RY. Creating new fluorescent probes for cell biology. *Nature Reviews Molecular Cell Biology*. 3(12):906-918, 2002.

36. North AJ. Seeing is believing? A beginners’ guide to practical pitfalls in image acquisition. *Journal of Cell Biology*. 172(1):9-18, 2006.

37. Schneckenburger H, Weber P, Wagner M, Schickinger S, Richter V, Bruns T, Strauss WS, Wittig R. Light exposure and cell viability in fluorescence microscopy. *Journal of microscopy*. 245(3):311-318, 2012.

38. Swedlow JR. Quantitative fluorescence microscopy and image deconvolution. *Methods in Cell Biology*. 114:407-426, 2013.

39. Zibara K, Awada Z, Dib L, El-Saghir J, Al-Ghadban S, Ibrik A, El-Zein N, El-Sabban M. Anti-angiogenesis therapy and gap junction inhibition reuce MDA-MB-231 breast cancer cell invasion and metastasis in vitro and in vivo. *Scientific Reports*. 5:12598, 2015.

40. Seemann N, Welling A, Rustenbeck I. The inhibitor of connexin Cx36 channels, mefloquine, inhibits voltage-dependent Ca2+ channels and insulin secretion. *Molecular and Cellular Endocrinology*. 17:30610, 2017.

41. Manjarrez_marmolejo J, Franco-Perez J. Gap Junction Blockers: An overview of their effects on induced seizures in animal models. *Current Neuropharmacolgy*. 14(7):759-771, 2016.

42. Nguemo F, Saric T, Pfannkuche K, Watzele M, Reppel M, Hescheler J. In vitro model for assessing arrhythmogenic properties of drugs based on high-resolution imedance measurements. *Cellular Physiology and Biochemistry*. 29(5-6):819-832, 2012.

43. Fernstrom MJ, Koffler LD, Abou-Rjaily G, Boucher PD, Shewach DS, Ruch RJ. Neoplastic reversal of human ovarian carcinoma cells transfected with connexin43. *Experimental and Molecular Pathology*. 73(1):54-60, 2002.

44. Maes M, Yanguas SC, Willebroards J, Vinken M. Models and methods for in vitro testing of hepatic gap junctional communication. *Toxicology in vitro*. 30:569-577, 2015.

45. Makinen ME, Yla-Outinen L, Narkilahti S. GABA and gap junctions in the development of syncrhonized activity in human pluripotent stem-cell derived neural networks. *Frontiers in Cellular Neuroscience*. e00056, 2018.

46. Qin J, Chang M, Wang S, Liu Z, Zhu W, Wang Y, Yan F, Li J, Zhang B, Dou G, Liu J, Pei X, Wang Y. Connexin-32 mediated cell-cell communication is essential for hepatic differentiation from human embryonic stem cells. *Scientific Reports*. 6:37388, 2016.

47. Trovato-Salinaro A, Trovato-Salinaro E, Failla M, Mastruzzo C, Tomaselli V, Gili E, Crimi N, Condorelli DF, Vancheri C. Altered intercellular communication in lung fibroblast cultures from patients with idiopathic pulmonary fibrosis. *Respiratory Research*. 7(1):122, 2006.

48. Bao B, Jiang J, Yanase T, Nishi Y, Morgan JR. Connexon-mediated cell adhesion drives microtissue self-assembly. *FASEB J*. 25(1):255-264, 2011.

49. Davidson MM, nesti C, Palenzuela L, Walker WF, Hernandez E, Protas L, Hirano M, Isaac ND. Novel cell lines derived from adult human ventricular cardiomyocytes. *Journal of Molecular and Cellular Cardiology.* 39(1)133:147, 2005.

50. Van Rijen H, van Kempen MJ, Analbers LJ, Rook MB, van Ginneken AC, Gros D, Jongsma HJ. Gap junctions in human umbilicial cord endothelial cells contain multiple connexins. *American Journal of Physiology*. 272(1 Pt 1):C117-130, 1997.

51. Davis LM, Rodefeld ME, Green K, Beyer EC, Saffitz JE. Gap junction protein phenotypes of the human heart and conduction system. *Journal of Cardiovascular Electrophysiology*. 6(10), 1995.

52. Dermietzal R, Spray DC. Gap junctions in the brain: where, what type, how many and why? *Trends in neuroscience*. 16(5):186-192, 1993.

53. Cheng CY, Wong Ew, Lie PP, Li MW, Su L, Siu ER, Yan HH, Mannu J, Mathur PP, Bonanomi M, Silvestrini B, Mruk DD. Environmental toxicants and male reproductive function. *Spermatogenesis*. 1(1):2-13, 2011.

54. Upham BL, Blaha L, Babica P, Park JS, SOvadinova I, Pudrith C, Rummel AM, Weis LM, Sai K, Tithof PK, Guzvic M, Vondracek J, Machala M, Trosko JE. Tumor promoting properties of a cigarette smoke prevalent polycyclic aromatic hydrocarbon as indicated by the inhibition of gap junctional intercellular communication via phosphatidylecholine-specific phospholipase C. *Cancer Science*. 99(4):696-705, 2008.

55. Sovadinova I, Babica P, Boke H, Kumar E, Wilke A, Park JS, Trosko JE, Upham BL. Phosphatidylcholine specific PLC-induced dusregulation of gap junctions, a robust cellular response to environmental toxicants and prevention by resveratrol in a rat liver cell model. *PLoS One*. 10(5):e0124454, 2015.

56. Labriola NR, Mathiowitz E, Darling EM. Fabricating polyacrylamide microbeads by inverse emulsification to mimic the size and elasticity of living cells. *Biomaterials Science*. 5(1):41-45, 2016.

57. Kessel S, Cribbes S, Bonasu S, Qiu J, Chan LL. Real-time apoptosis and viability high-throughput screening of 3D multicellular tumor spheroids using the celligo image cytometer. *SLAS Discovery*. 23(2):202-210, 2018.

58. Zanoni M, Piccinin F, Arienti C, Zamagni A, Santi S, Polico R, Bevilacqua A, Tesei A. 3D tumor spheroid models for in vitro therapeutic screening: a systematic approach to enhance the biological relevance of data obtained. *Scientific Reports*. 6:19103, 2016.

59. Liu C, Oikonomopoulos A, Sayed N, Wu JC. Modeling human diseases with induced pluripotent stem cells: from 2D to 3D and beyond. *Development*. 145(5), 2018.